ENGINEERING, FINANCIAL AND NET ENERGY PERFORMANCE, AND RISK ANALYSIS FOR PARABOLIC TROUGH SOLAR POWER PLANTS

A Dissertation

by

JUN LUO

Submitted to the Office of Graduate and Professional Studies of
Texas A&M University
in partial fulfillment of the requirements for the degree of

DOCTOR OF PHILOSOPHY

Chair of Committee,	Thomas Lalk
Co-Chair,	Michael Schuller
Committee Members,	Michael Pate
	Sy-Bor Wen
Head of Department,	Andreas A. Polycarpou

August 2014

Major Subject: Mechanical Engineering

ABSTRACT

An investigation was conducted to determine how technology innovations, potential risks, plant configuration and size, operating strategy, and financial incentives affect the electricity output, financial payback, and net energy performance of a concentrating solar power plant.

A set of engineering performance, financial and net energy models were developed as tools to predict a plant's engineering performance, cost and energy payback. The models were validated by comparing the predicted results to operational data from an actual solar power plant. The models were used to analyze the effect of several combinations of design and operating parameters on the amount and cost of electrical output. In addition, they were used to assess the risk of particular component failures and their effect on plant engineering and financial performance, and to conduct an analysis to predict energy payback.

The results show some fundamental conclusions. First, the electricity production could be improved by adjusting plant configuration, increase the storage system size and increase the scale of plant. Second, the cost of electricity generated from a CSP plant will be higher (as much as 400%) than that of fossil fuel based power plants. Several methods could be used to lower the cost, such as constructing large plants, adopting new material and innovation components. However, the cost reduction will not be enough. Survival and future development of CSP plants may rely on external support, which

might include incentives or supportive policies. Third, generally a CSP plant will have a positive net energy with an energy payback of approximately 5 years. Last, flex hoses are the most vulnerable components in the solar field. Performming regular maintenance work should be necessary to maintain the solar field's performance level.

DEDICATION

First, I would like to appreciate Professor Thomas Lalk for his careful guidance, great support and prestigious contributions during the completion of this research.

I also want to express my deepest gratitude to Professor Michael Schuller. During my stay in Texas A&M University, he provided me with good advice, both on the technical content and form of this research. It's an honor to be your advisee and student.

Moreover, I'd like to thank my colleague and staff in SERC. We have a wonderful time together.

In addition, I need to show special thanks to my wife and my parents, for their extremely valuable help, continuous care, patience, encouragement, unconditional love and full support.

Finally, I would like to thank mechanical energy department of Texas A&M University, Department of Energy, and NSSPI. I am grateful for their financial support, without which it would be impossible for me to study in the United States.

NOMENCLATURE

Δ	change of …
A	area
C	cost
CSP	concentrating solar power
D	distance
DNI	direct normal irradiance
E	modulus of elasticity, energy
f	factor
g	gravity
h	height
h(*T*)	enthalpy at temperature *T*
HCE	heat collection element
HTF	heat transfer fluid
k	thermal conductive
L	length
LCOE	levelized cost of energy
m	mass
N	number
Nu	Nusselt number
P	pressure, power

Pr	Prandtl number
q	energy flow rate per unit area
Q	energy flow rate
r	radius
Ra	Rayleigh number
Re	Reynolds number
RH	relative humidity
S	area
SCA	solar collector assemblies
SM	solar multiple
T	temperature
t	time/thickness
TES	thermal energy storage
V	volume
α	linear expansion coefficient
β	volumetric thermal expansion coefficient
ε	emissivity, tensile strength
θ	altitude angle
λ	longitude, in degree
μ	dynamic viscosity
ρ	density
σ	Stefan-Boltzmann Constant

φ	latitude, in degree

Subscript

&	or
@	at … condition
absb	absorber
accu	accurate
adj	adjunct
Aux	auxiliary
avg	average
avil	available
bal	balance
btm	bottom
CF	cash flow
col	collector
COND	conduction
CONV	convection
depr	depreciation
dgn	design situation
dp	dew point
DSCR	debt service coverage ratio
dsct	discount

esc	escalation
enlp	envelope
env	environment
elec	electricity
err	error
filled	filled material
geo	geometry
grd	ground
high	high temperature
HL	heat loss
HTF	heat transfer fluid
i,o	inside/outside
lbr	labor cost
ld	load
in	inlet
ins	insulation
lm	log mean
max	maximum
min	minimum
opt	optical
out	outlet
pb	power block

pmt	payment
rad	radiation
ref	reference condition
refl	reflected
res	resident
rvu	revenue
salv	salvage
SCA	solar collector assemblies
scale	scaling factor
SF	solar field
sky	sky temperature
stag	stagant
std	standard
ST	storage
surf	surface
ThE	thermal energy
thml	thermocline
ut	unit price
vac	vacuum
void	void factor

TABLE OF CONTENTS

Page

Page

LIST OF FIGURES

Page

Page

Page

Page

Page

Page

Page

LIST OF TABLES

Page

Page

1. INTRODUCTION

1.1 Background

In the last several decades, one of the most controversial topics in the energy industry is the increasing energy demands and requesting for reducing greenhouse gases and other pollutants coming with energy production [1]. The world energy consumption and production of major greenhouse gases are increasing simultaneously, as shown in Figure 1.

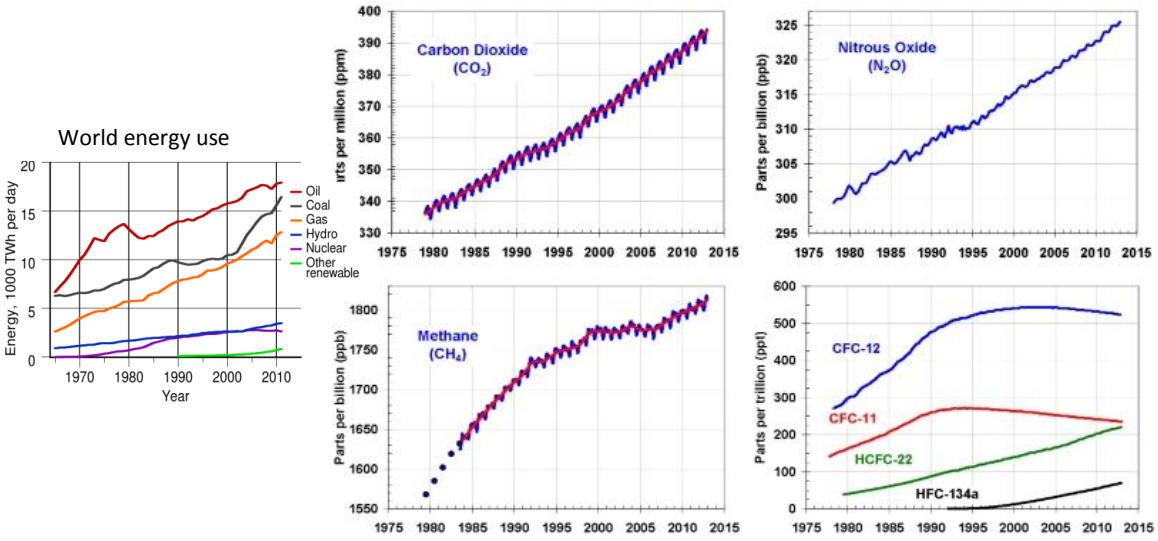

Figure 1: World's energy use and global average abundances of the major, well mixed, long-lived greenhouse gases trends [2] [3]

Fossil based energy such as oil, coal and natural gas has been the main energy source; it provided 77% of primary energy production during 2011 [4]. However, fossil energy is

not renewable, and typically needs millions of years to regenerate. The estimation of reserve depletion with current consumption rate is as follows: oil in 56 years, natural gas in 55 years and coal in 119 years [5]. Moreover, combustion of fossil fuel releases water vapor (the main greenhouse gas), CO_2 and other air pollutants such as NO_x, SO_x, volatile organic compounds, and heavy metals elements [6]. Some of the formed CO_2 is converted by photosynthesis or absorbed by the ocean. The rest stays in atmosphere and accumulates over time, from 280 *ppm* in pre-industrial time to 360 *ppm* with an accelerating rate at three to five *ppm* per year presently. The greenhouse effect has already caused a 1.4 $^{\circ}F$ increase of globally averaged combined land and ocean surface temperature in the last 100 years, and additional warming of 2 to 11.5 $^{\circ}F$ over the 21st century is anticipated[7]. In addition, NO_x, SO_x, and other gases are the primary reason for the destruction of the protective ozone layer, and the formation of acid rain and smog.

Due to economic development, technologic advancement and population growth, the world energy consumption is expected to have a 56% increase from 2010 to 2040. According to the current fossil energy reserves and projected consumption rates, it will deplete in less than 150 years at most [8].

Because of the intense greenhouse gas emission, depleting fossil energy and increasing energy price, governments are thinking about future energy strategies, including improving energy use efficiency to cut consumption, using environmentally benign energy conversion technologies and adopting alternative energy solutions.

Nuclear energy used to be the most promising alternative energy solution due to its advantages such as low greenhouse gas emission, large capacity and low lifetime cost. However, the nuclear accidents and their serious, intractable consequences resulted in a reconsideration of nuclear safety and energy policy in many countries. The public shows strong concern about nuclear safety. Resulting from Three Mile Island accident and the Chernobyl disaster, the installed nuclear capacity stagnated for almost 20 years, as shown in Figure 2.

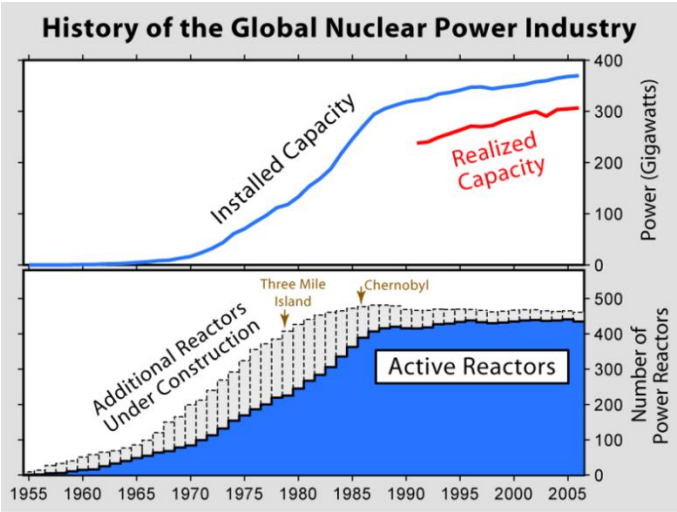

Figure 2: History of the global nuclear power industry[1]

The recent Fukushima Daiichi nuclear disaster caused Germany to decide to close all its reactors by 2022 [9], and Italy banned nuclear power as well [10]. Other countries also

[1] Picture retrived on March 2013, from website: http://en.wikipedia.org/wiki/File:Nuclear_Power_History.png, presented data is from the International Atomic Energy Agency, principally "Nuclear Power Reactors in the World"

suspended or cancelled planned power reactors. Due to the safety concerns, International Energy Agency (IEA) halved the original estimation of additional nuclear generating capacity to be built by 2035 [11], partly due to diminishing public acceptance of nuclear energy, but also to the increased costs of nuclear security improvements and of insurance premiums for accident-related damages [12].

Another way of fulfilling future energy demand is by adopting renewable energy such as solar and wind. The public has a strong desire to promote renewable energy to ensure sustainable energy growth without sacrificing the environment. However, even though renewable energy has been rapidly increasing, it still only contributes to marginal market share currently [13]. The main reason prohibiting it from development is its high cost, as shown in Figure 3, which is a plot of the levelized cost of energy (LCOE) for various energy sources (LCOE is one of the utility industrial metrics for the cost of electricity produced by a generator. It is the price at which electricity should be generated to break even over the entire lifespan of the project). This high cost may be offset by technology advancement, incentives or public support (public support for renewable energy may promote utilities to adopt more renewable energy, and they may be willing to accept higher electricity cost). IEA estimated that solar energy may contribute approximately half of the world's power by 2060, and the rest would be supplied by wind, hydropower and biomass plants[14].

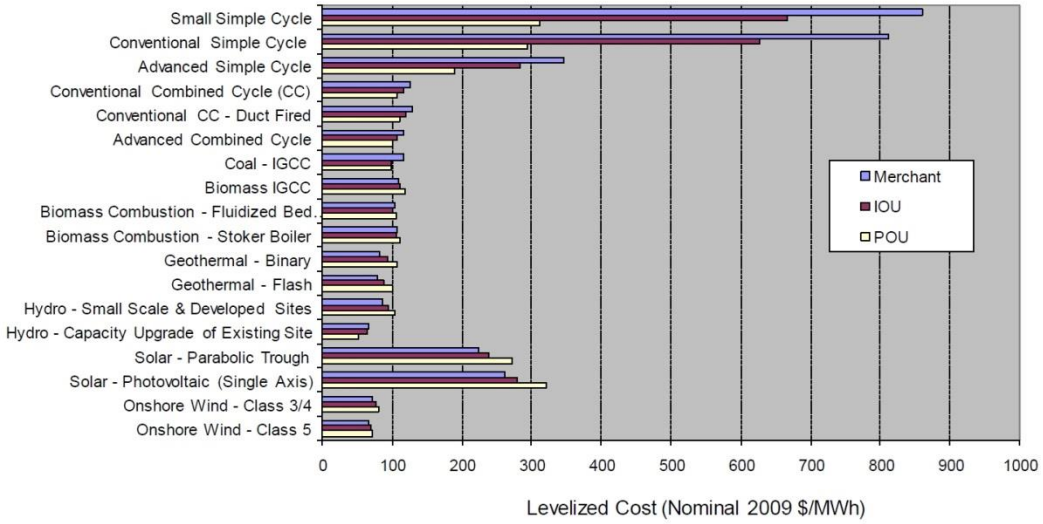

Figure 3: Summary of the average levelized costs – in-service 2009 (Merchant (financed by private investors), IOU (investor-owned utilities) and POU (publicly owned utilities) are investment types) [15]

Renewable energy has been quickly developing in recent years. It accounted for nearly half of the estimated 208 GW of new electricity capacity installed throughout the world in 2011[16], and it comprised 20.3% of the global electricity production share, increased from 19.4% in 2010. The non-hydro parts, mainly solar, wind, and biomass, represented most of the change, was rising from 3.3% to 5.0% during that period.

Wind and solar energy are regarded as the most promising renewable energy [17], and encountered rapid growth in last ten years. Solar energy is by far the most abundant available energy source. It is the only energy source which is capable of providing 1000 times of the energy human need. Moreover, solar energy is clean, inexhaustible and widely distributed. The adoption of solar energy will have enormous long-term benefits

such as reducing pollution, mitigating climate change and even keeping fossil fuel in the low price range. Figure 4 shows the global technical potential (the achievable energy generation with system performance, topographic limitations, environmental, and land-use constraints [18]) for different renewable energy sources.

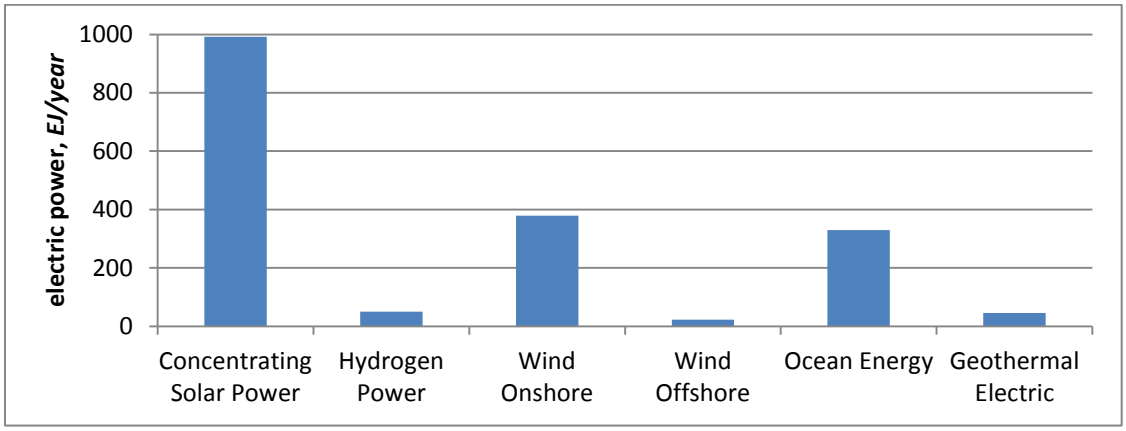

Figure 4: Global technical potential for renewable energy technologies on the long term [19]

Figure 5 shows the distribution of solar energy incident on the U.S. and the world. The strip between latitudes 15˚N and 35˚N has the most favorable conditions for solar energy applications. It has more than 3000 hours of annual sunshine, and limited cloud cover or rainfall. The next favorable belt lies between the equator and latitude 15˚N. It has about 2500 hours of sunshine per year, with uniform solar intensity, and slight seasonal variation. However, the high humidity and frequent cloudy weather result in a high

proportion of scattered radiation. The belt between latitude 35˚N and 45˚N is less favorable than the previous two belts. Though the average solar intensity is almost the same as the other two, it has remarkable seasonal variation in both solar radiation intensity and daylight time. Especially in the winter season, the solar radiation is much lower than the rest of the year. The remaining area is the most inappropriate for solar energy application, because near half of the total radiation is diffused, along with frequent and extensive cloud coverage [20].

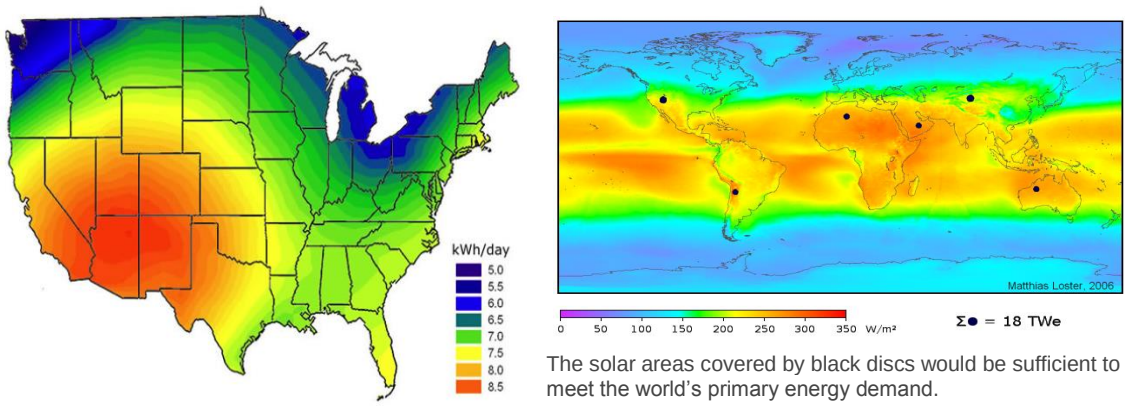

Figure 5: Solar energy distribution in the U.S [21] (left) and the world (right)[2]

Humans have harnessed solar energy for a long time. But it is until recent decades, people began to actively use solar energy. The most common way to convert it to

[2] Orignial Pictures retried on April 2013, from website: http://www.ez2c.de/ml/solar_land_area/

electricity is by using solar photovoltaic (PV) or concentrating solar power (CSP) methods, as shown in Figure 6.

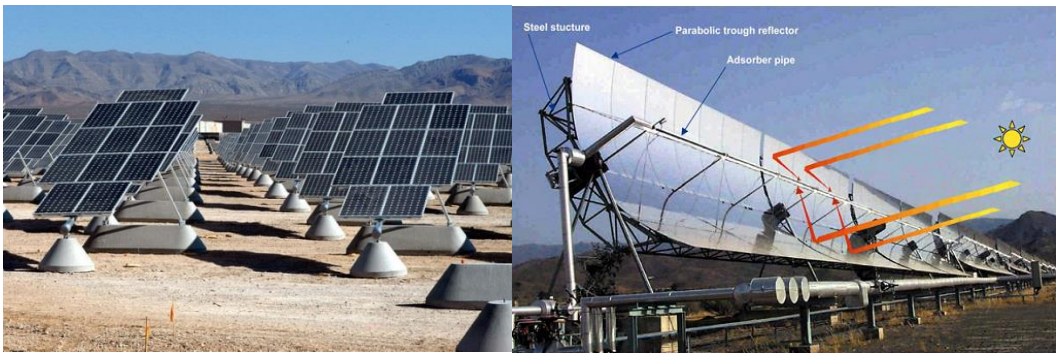

Figure 6: Typical parabolic trough (left) and PV (right) Systems[3]

A PV system converts solar energy into electricity directly by using one or more solar panels. The system can be easily scalable. It could be as small as only providing electricity to a single family, or large enough to supply electricity to a small town. A large scale PV system may contain some auxiliary equipment such as an electricity storage system, a solar tracker system or an energy management system to improve conversion efficiency. Current available solar panels have a sunlight-to-electricity

[3] Image retrived on July 2013, from Wikipedia, website address: http://en.wikipedia.org/wiki/File:Nellis_AFB_Solar_panels.jpg

efficiency ranging from 10% to 20%[4], and this number is continuing to increasing with development.

CSP is another approach to convert solar energy to electricity through thermal energy. It concentrates large portion of incoming sunlight to a small area by using mirrors or lenses. The solar radiation is converted to thermal energy of the collector and subsequently transferred to the working medium and finally converted to electricity by heat engines and electrical power generators.

CSP and PV are complementary technologies, because CSP has the ability to use thermal storage to balance fluctuating PV production and to generate baseload electricity. However, they are competitive in some markets as well, due to both of them utilizing solar to generate electricity.

There are several different solar concentrating types, as shown in Figure 7. A Power tower solar thermal system uses thousands of tracking mirrors to focus solar radiation to the tower, which is located in the center of a heliostat field. A dish design CSP system employs a large, parabolic dish to reflect sunlight to the point above the dish. A parabolic trough system adopts long curved mirrors to concentrate sunlight to the collectors.

[4] Conclusion derived from comparison of different products' data sheets. For example, E20/435 solar panel from Sunpower Company is claimed to have 20% efficiency. Resource website: http://us.sunpowercorp.com/cs/BlobServer?blobkey=id&blobwhere=1300271295172&blobheadername2=Content-Disposition&blobheadername1=Content-Type&blobheadervalue2=inline%3B+filename%3D11_318_sp_e20_435_ds_en_w_ltr.pdf&blobheadervalue1=application%2Fpdf&blobcol=urldata&blobtable=MungoBlobs

Figure 7: Power tower, dish type and parabolic trough collectors

1.2 Parabolic Trough Type CSP Plant

Parabolic trough technology is the most proven, economic, mature and reliable technology in all solar thermal electric technologies [22]. It dominates the global CSP market and accounts for 90% of CSP plants[23]. Figure 8 is a scheme of a general parabolic trough type CSP plant.

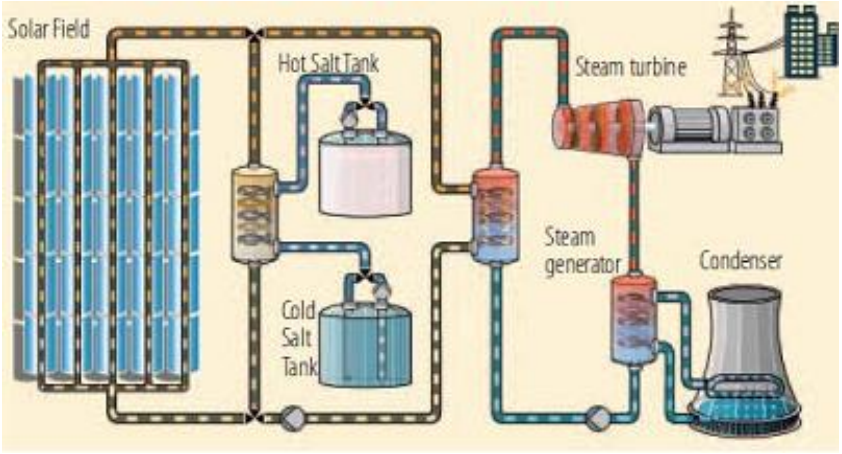

Figure 8: Schematic of parabolic trough type CSP plant [24]

This power plant includes three major subsystems: the solar field subsystem collects solar energy, the storage system stores and allows thermal energy to be extracted, and thereby regulates power generation, the power generation system converts thermal energy to electricity, and the pipelines connect these three subsystems.

The field constitutes for most area of a CSP plant. The most important components of field are parabolic trough-shaped mirrors, which reflect and concentrate sunlight onto the thermal energy collectors that are located at the troughs' focal line. HTF circulates in the tubes, heated by the concentrated sunlight, and its outlet temperature is constantly controlled. Then the heated HTF is pumped to pipeline subsystem for future distribution.

The pipeline system is a network that connects the other systems. It received thermal energy carried by heated HTF from solar field, stores or extracts energy from storage system and supplies energy to power block. It distributes energy between these systems according to specified operation requirements and control strategy. Heat exchangers or direct mass exchange methods are used to exchange energy between the pipeline and other systems.

The thermal storage system works as a buffer or a warehouse between the solar field and the power block, such that thermal energy can be stored or extracted from storage. It stabilizes the thermal energy input to power block in the day time, and extends the power block's operation at night. The using of a thermal storage system is a low cost and effective way to eliminate energy flow variation in transient weather conditions, smooth

and increase electricity production, and improves the flexibility and stability for both baseload and peak load power production.

The power block consists of turbines, generators, and condensers. It is similar to that used in fossil fuel power plants [25]. Thermal energy transported by HTF is transferred to water to generate high temperature steam. The steam expands in a turbine and turning the blades to generate electricity.

Table 1 shows a comparison between a fossil fuel thermal energy system and a solar thermal energy system in financial and energy investments.

Table 1: Comparison of financial and energy investment procedures between fossil thermal energy and CSP type solar thermal energy

Item	Fossil Thermal	Solar Thermal
Fuel extraction	Yes	No
Fuel transportation	Yes	No
Fuel refining/concentrating sunlight	Yes	Yes
Fuel energy to thermal energy	Yes	Yes
Thermal energy storage	No	Yes
Thermal energy to electricity	Yes	Yes
Emission control	Yes	No
Waste disposal	Yes	No
Electricity transmission	Yes	Yes
Operation	Yes	Yes
Salvages	Yes	Yes

Solar thermal energy receives energy from sunlight, and does not involve fuel mining, transportation and associated financial and energy cost. Also, the conversion procedure from solar radiation to thermal energy does not involve combustion. No greenhouse gas, pollutant or solid waste is produced. Therefore no relevant cost and energy investment is required. Solar thermal energy needs to concentrate solar radiation to raise its conversion efficiency, which is similar to fossil thermal's fuel refining procedure. Both of them have a comparable thermal energy to electricity conversion process, electricity transmission, operation, and salvaging procedures, all of them associated with financial and energy costs. In addition, solar thermal energy is usually equipped with a storage system to buffer the collected thermal energy, thus incurring investment that fossil thermal energy does not have. The comparison indicates solar thermal is less complicated by its very nature, and has much less pollution. Solar thermal's characteristics have proved its capability of fulfilling future energy requirements without sacrificing environmental quality.

However, previous research shows solar thermal's electricity cost is high and energy payback period is long [26]. There are two primary reasons: first, though the fuel of solar energy is regarded as free, its energy density (about 1000 W/m^2) is low. It requires using large land area and extensive collection systems (concentrating troughs, mirrors, steel structures, and pipes) to collect enough solar energy, all of them come with large amount of financial and energy costs. Second, solar radiation is periodic and fluctuant; it varies with a number of factors including locations, elevation, weather, seasons and time of day. Therefore, operating CSP plants have lower equipment utilization than fossil energy.

Third, a fossil thermal power has a higher thermal to electricity efficiency because of its higher operating temperature. Last, fossil power is close or already reaches its optimal size (1000 *MW*), while solar thermal plant's size is still less than 100 *MW*. So fossil thermal power has lower cost of the equipment compared with solar thermal energy.

Parabolic trough is a proven technology. The first commercial plants began operating since 1984, and still operational today [27]. The success of recent projects in Spain and United States will be important in determining the future role of CSP. If the CSP industry can demonstrate sharp cost reduction and well performed operating plants, a large wave of the projects in regions outside of the United States and Spain can be expected to occur, and more countries will be interested in establishing a domestic CSP industry. If cost reduction is not significant as expected, the outlook of CSP is unclear [28].

Thus, the research described here is primarily focusing on improvements of a CSP plants' financial and net energy payback from two aspects: first, optimize the configuration of the system, to determine the best one that has lowest electricity cost; second, identify potential cost savings from multiple methods such as scaling up or innovation technology. Moreover, it also discussed potential risks associated with CSP plants, influence of incentives, and influence of different operating strategies.

1.3 Literature Review

Previous work done in the area of trough type CSP technology can be divided into three categories: (i) general power plant's performance modeling; (ii) HCE modeling and

experiments; (iii) Storage system operating modeling and simulation. The following section on general power plant performance modeling addresses studies conducted to provide a method to estimate the annual electricity generation and lifetime LCOE in different locations and varying site configurations. HCE modeling and experiments discuss the work done by researchers who used models and experiment to predict the performance characters of HCE. Storage modeling describes the prediction of working conditions of two-tank and thermocline thermal energy storage systems. Literature pertaining to experimental work is not addressed as the proposed work primarily related to numerical modeling.

1.3.1 General Power Plant Performance Modeling

The most widely used model to simulate CSP plant – The System Advisor Model (SAM) is being developed by the National Renewable Energy Laboratory (NREL) and the Department of Energy (DOE) since 2003[29]. The first version was published in 2007 and several new versions were published thereafter. It is a software package capable of simulating several kinds of alternative energy systems. For CSP, SAM makes performance prediction by empirical or physical modeling in its latest version. The program is used to calculate the cost of electricity based on information including the project location, system specifications, installation and operating costs, financing configuration, applicable tax credits, and incentives.

Other than SAM, several proprietary parabolic trough type CSP plant's performance simulation programs have been developed. The operating company of SEGS developed

an hourly based simulation program specific to its plant to estimate the performance and fulfill its own need [30].Flabeg Solar International (FSI) developed a performance simulation model to conduct design studies and advertise CSP plants [31]. Also, the German Aerospace Center has established a solar power performance model [32]. However, all of these simulation programs are confidential and not disclosed.

1.3.2 HCE Model and Experiments

Research in the solar field of CSP focuses primarily on HCEs and concentrating troughs, since trough modeling is mainly focusing on designing, structure strength and reflection, this literature review will concentrate on HCE models.

Several models have been developed since 1970. Ratzel, et al. established an analytical and numerical receiver model to simulate receiver's conductive and convective heat losses [33]. Thomas, et al. developed a set of regression equations based on the result of a numerical heat transfer model [34]. Forristall accomplished a detailed numerical model to estimate the heat transfer of receivers [22]. Garcia-Valladares, et al. developed a detailed numerical model with three dimensional heat transfer analysis [35]. Odeh and his grounp's research include predicting the thermal performance of a collector which used water instead of oil to absorb the collected thermal energy. Also, they developed a model to study the performance variation caused by adjusting the field arrangements under Australian conditions [36, 37].Ricardo, et al. developed a one dimensional numerical model which considers the thermal interaction between the neighboring surfaces [38].

Several experimental results are also available for reference. Ulf Herrmann provided the experimental performance of the SKAL-ET collectors, which were used in the Andasol-1 power plant [39]. F. Nburkholder, et al. published detailed heat loss testing results of the PTR70 Parabolic Trough Receiver [40].

1.3.3 Storage Model

Research in storage system focuses on improving TES' performance, and reducing the system's cost. Also, some papers discuss storage system's heat loss characteristics during operation.

Ulf Herrmann developed a regression empirical heat loss model from measured data for two tanks system [41]. Joseph E. Kopp used constant heat loss values in his thesis [42]. And the SAM program used fixed heat loss values or results from a zero dimension model for empirical or physical type simulations. These results indicate that the heat loss is relatively small in comparison with the stored thermal energy, and can be neglected from rough calculation.

1.3.4 Cost Model

Previous research in the cost analysis of CSP plant mainly emphasizes its three systems: solar field system, storage system, and power block system. H. price used scaling equations to estimate the cost for the solar field [29]. Documentation of SAM program published a linear or linear like method to estimate the price for CSP plant, and showed a detailed budget list for a purposed 110MW CSP plant in State of Arizona [43]. B. Kelly, et al. estimated the cost of a two-tank thermal storage system by summing up material

and labor costs [44]. Sargent & Lundy LLC Consulting Group developed a regression model from previous data to estimate the unit electricity cost for power blocks [45].

1.3.5 Net Energy Analysis of CSP plant

Previous research in the net energy analysis of CSP plant primarily concentrated on determining whether it's an energy sink or producer, and comparing the energy returns from different alternative energies. Teresita Larrain conducted a net energy analysis of hybrid CSP plants in Chile [46]. A comparative analysis of energy cost between photovoltaic, concentrating solar, and wind electricity generation was conducted by Michael Dale [47].Charles A. S. Hall also performed lifetime analysis and compared the energy return among traditional fossil and alternative energies [48]. For standalone CSP, though some rough estimated energy return data are available, no known detailed and comprehensive analysis has been performed, and no result is disclosed.

1.4 Goal and Objective

The goal of this research is: to determine how electricity production, financial payback and net energy performance improvements of a CSP plant can be achieved in the near future;

Instead of using the existing simulation models, a numerical model is developed based on the following reasons:

1. Both steady status and transient status are considered in the performance model;

2. A storage tank sizing and insulation module is used to determine the storage system's physical size and insulation thickness in the performance model;
3. Different operation strategies are used in the performance model;
4. A detailed cost estimation method is used in the financial model;
5. The net energy analysis and risk assessment are conducted;

The objective is: to determine how technology innovations, such as using thermocline storage system instead of two-tank storage system, potential risks, plant configuration and size, operating strategy, and incentives affect the electricity output, net energy performance and economic payback of a CSP plant.

The tasks listed below were completed to achieve the above objective:

1. To predict a CSP plant's operation characteristics, a numerical model was developed consisting of models to calculate the performance, such as the electricity production and efficiency; predict the financial payback, for example, the investment and LCOE, and estimate energy payback, for instance, lifetime energy return and payback period. The flow chart of the numerical model is shown in Figure 9.

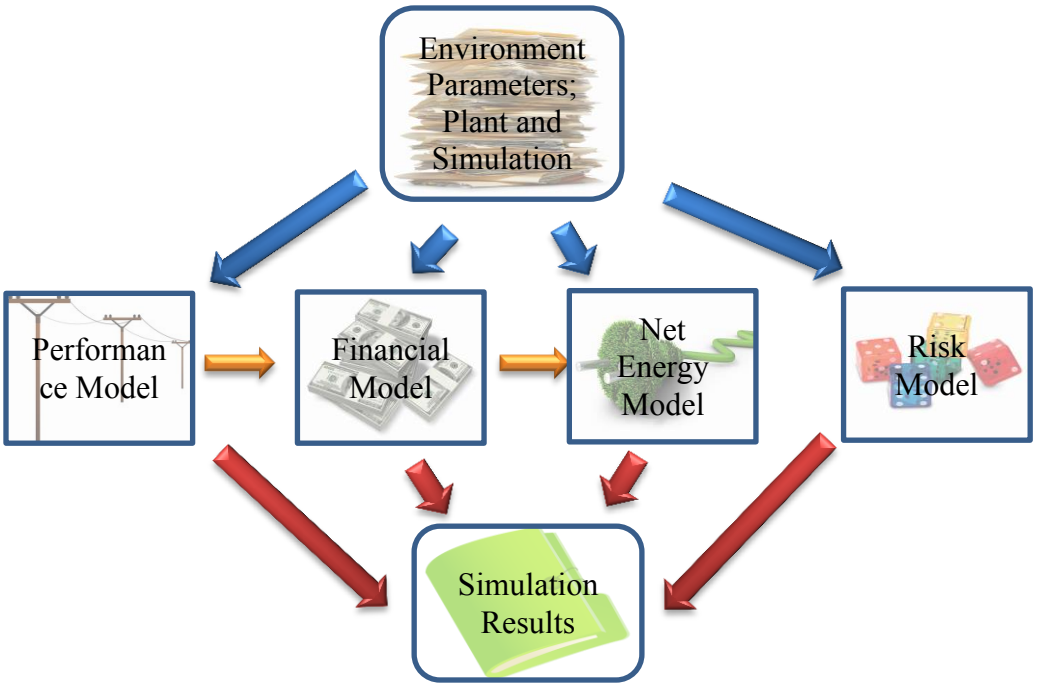

Figure 9: Flow chart of the numerical model

2. To validate this model by comparing numerical predictions against published experimental or operational data.
3. To analyze performance of an existing CSP plant with optimizations.

The performance, economic and net energy models of CSP plants are described in Chapters 2 to 4. The validation of the developed models is in Chapter 5. The next chapter is the analysis of several different cases. Conclusions and recommendations resulting from these results are summarized in Chapter 7.

2. DEVELOPMENT OF THE PERFORMANCE MODEL

2.1 Introduction

The numerical model was developed to evaluate a CSP plant's operation and performance with capability of changing a range of design and operating parameters. It consists of three routines: the preprocessing, calculation and post processing routines. The preprocessing routine serves to predict the performance under reference design conditions and provide the input for the calculation routine. The calculation routine simulates and estimates hourly operation performance for a certain period of time, typically one year. The simulation results, from the calculation routine, are sent to the post processing routine, which is a prerequisite step for the summary of the performance and financial analysis. The program flow chart illustrating the relationship among the three routines is shown in Figure 10 and each routine is explained below.

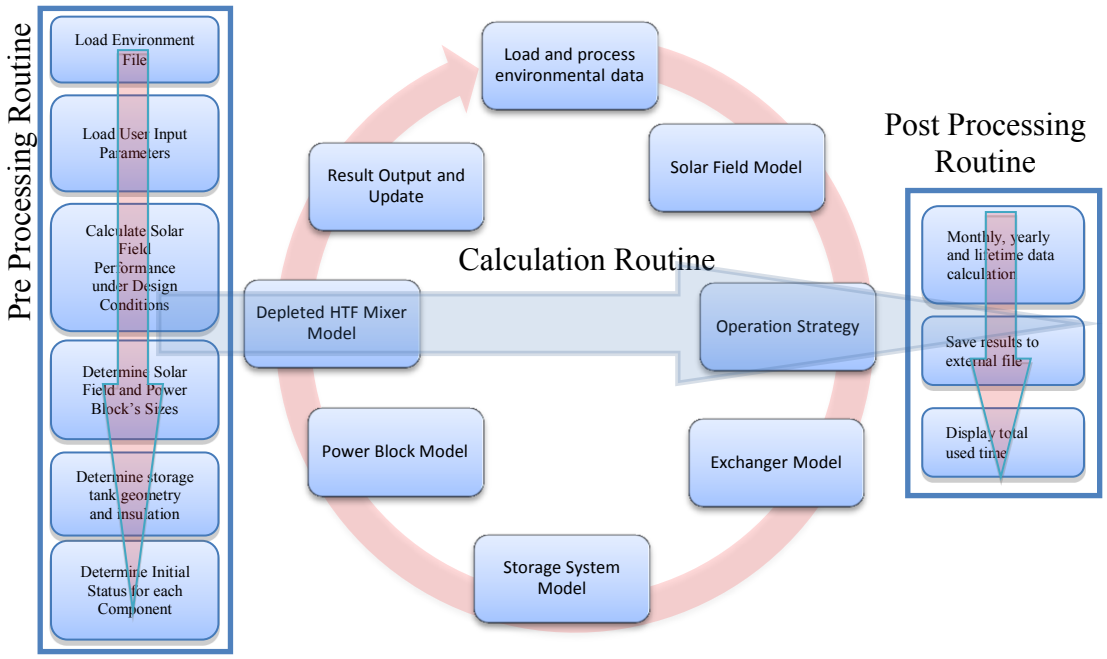

Figure 10: Flow chart of the performance model

2.2 Preprocessing Routine

The preprocessing routine has several functions. They include:

1. Loading the time varying environmental, CSP plant's configuration, and model simulation parameters, which may be different at each calculation step;
2. Determine the performance of the CSP plant under design conditions;
3. Determine the sizes of the solar field and the power block;
4. Determine the geometric size of the storage system;
5. Determine the initial conditions for the calculation routine.

2.2.1 Environmental Parameters

The performance model allows for changing the following environmental parameters: latitude, longitude, elevation, DNI, ambient temperature, dew temperature, ground temperature, wind speed and relative humidity.

The NOAA (National Oceanic and Atmospheric Administration) has monitored and recorded climate conditions in United States for decades with different methods, including land based stations, radar, weather balloons and satellites. These data (hourly, daily, monthly, yearly) are available from its national climatic data center website[5].

Several other websites that also provide weather data include:

The energy website[6] which maintains weather data for international locations;

The national solar radiation data base[7] and the solar prospector website[8] which provide weather data for U.S locations.

Hourly based weather data is the most detailed weather data available. The calculation routine's time step is limited by availability of climate data. Appendix A shows the procedure to derive the needed weather data.

[5] Available at website: http://www.ncdc.noaa.gov/.
[6] Available at website: http://apps1.eere.energy.gov/buildings/energyplus/cfm/weather_data.cfm.
[7] Available at website: http://rredc.nrel.gov/solar/old_data/nsrdb/1991-2005/tmy3/
[8] Available at website: http://maps.nrel.gov/node/10/

2.2.2 Determining the Solar Field's Performance under Design Conditions

A CSP power plant's performance can be susceptible to environmental conditions. Therefore, a certain set of environmental conditions, which is called reference design conditions, is specified. The solar plant's performance under such conditions is designated as reference design performance.

Three variables - ambient temperature, direct normal irradiance (DNI) and wind speed are important to determine a CSP plant's electricity production. The ambient temperature and wind speed have great influence on the heat losses of the collectors of the solar field and the storage tanks of the storage system. The annual average temperature and wind speed of the site location are reasonable to estimate the design ambient temperature and wind speed. The DNI has significant impact on the solar field's design performance. Typically, the DNI ranges from 750 to 1000 W/m^2, depending on its specific location. The documentation of the SAM model suggests the DNI value to be set as the design DNI that has a cumulative annual frequency of about 95% [49].

By simulating the field model under design conditions, the mass flow rate of heated HTF is obtained. Then the rated thermal energy production of solar field is:

$$\dot{Q}_{SF\_dgn\_ref} = \dot{m}_{HTF\_dgn}\left[h(T_{SF\_dgn,out}) - h(T_{SF\_dgn,in})\right] \quad (1)$$

2.2.3 Determining the Solar Field and Power Block's Sizes

Three optional methods are provided in the preprocessing routine to determine the size of the solar field and the power block; the solar multiple (SM) method, the solar field area method, and the individual setup method.

2.2.3.1 The SM method

For the SM method, the ratio of the solar field thermal energy output to power block thermal capacity under design conditions is used:

$$SM = \frac{\dot{Q}_{SF\_dgn}}{\dot{Q}_{PB\_dgn}} \tag{2}$$

The design thermal input to the power block $\dot{Q}_{PB\_dgn}$ can be evaluated according to rated electricity generation and rated conversion efficiency at the design conditions:

$$\dot{Q}_{PB\_dgn} = \frac{E_{PB\_dgn}}{\eta_{PB\_dgn}} \tag{3}$$

Therefore, the collected thermal energy of a solar field under design condition is:

$$\dot{Q}_{SF\_dgn} = \dot{Q}_{PB\_dgn} \cdot SM = \frac{E_{PB\_dgn}}{\eta_{PB\_dgn}} \cdot SM \tag{4}$$

$\dot{Q}_{SF\_dgn\_ref}$ is the collected thermal energy calculated from the solar field's numerical model under design conditions. Usually $\dot{Q}_{SF\_dgn}$ is different from $\dot{Q}_{SF\_dgn\_ref}$, and it is not easy to adjust the plant configuration to exactly match $\dot{Q}_{SF\_dgn\_ref}$ and $\dot{Q}_{SF\_dgn}$. Hence, a

scale factor f_{SF_scale} is used to coordinate $\dot{Q}_{SF\_dgn}$ and $\dot{Q}_{SF\_dgn\_ref}$. By multiplied with f_{SF_scale}, the $\dot{Q}_{SF\_dgn\_ref}$ is converted to the $\dot{Q}_{SF\_dgn}$, which accords with the design requirement.

$$f_{SF\_scale} = \frac{\dot{Q}_{SF\_dgn}}{\dot{Q}_{SF\_dgn\_ref}} \tag{5}$$

2.2.3.2 The Solar Field Area Method

For the solar field area method, the power block's gross output is calculated based on the solar field's rated thermal energy production, the SM factor, and the power block efficiency.

$$E_{PB\_dgn} = \eta_{PB\_dgn} \frac{\dot{Q}_{SF\_dgn\_ref}}{SM} \tag{6}$$

2.2.3.3 The Individual Setup Method

For the individual setup method, the solar field and the power block's sizes are set separately. The SM factor is calculated to compare the sizes of these two systems:

$$SM = \frac{\dot{Q}_{SF\_dgn\_ref}}{\dot{Q}_{PB\_dgn}} = \frac{\dot{Q}_{SF\_dgn\_ref} \cdot \eta_{PB}}{E_{PB\_dgn}} \tag{7}$$

2.2.4 Determining the Capacity and Volume of Storage System

A storage system's capacity is determined by the parameter "Maximum Storage Hours". It indicates the power block's operation hours when its thermal energy input is solely obtained from the storage system, and is operated under design conditions.

$$E_{STG\_dgn} = t_{STG\_dgm} \cdot \dot{Q}_{PB\_dgn} \tag{8}$$

Available TES mass is defined as the portion of TES that could be used for thermal energy storage. It is different from the total TES mass since the portion near the bottom could not be pumped out which makes it unable to participate in the heat exchange procedure, in that case its thermal energy cannot be utilized for storage or extraction. This portion of TES mass is called stagnant mass, and its height is named stagnant height. The available TES height is the difference between the TES height and stagnant height:

$$h_{TES\_avail} = h_{TES} - h_{\text{stag}} \tag{9}$$

The mass and volume of available TES are:

$$m_{TES} = \frac{E_{STG\_avail}}{h_{TES@hot\_dgn} - h_{TES@cold\_dgn}} \text{ for two-tank system} \tag{10}$$

$$m_{filled} = \frac{E_{STG\_avail}}{h_{filled@hot\_dgn} - h_{filled@cold\_dgn}} \text{ for thermocline system} \tag{11}$$

$$\begin{cases} V_{TES\_hot} = \dfrac{m_{TES}}{\rho_{TES@hot\_dgn}} \\ V_{TES\_cold} = \dfrac{m_{TES}}{\rho_{TES@cold\_dgn}} \end{cases} \text{ for two-tank system} \quad (12)$$

$$V_{filled} = \frac{m_{filled}}{\min\left(\rho_{filled@hot\_dgn}, \rho_{filled@cold\_dgn}\right)\left(1 - f_{void}\right)} \quad \text{for thermocline system} \quad (13)$$

f_{void} is the void fraction, which is defined as the ratio of the volume of void space to the total bulk volume.

2.2.5 Storage Tank's Size and Insulation

The storage tank's sizing and insulation models serve to calculate the geometric size and insulation configurations of storage tanks.

Spherical and cylinder shapes are the most commonly used geometries for a storage tank. A spherical tank has the least surface to volume ratio, which makes it possible to minimize the materials usage and surface area. However, it is only used for limited applications since it is hard to construct and complicated to arrange. A cylinder tank is frequently used for above ground applications because of its prevalent proof of construction feasibility. Table 2 lists the surface to volume ratio for several different geometries.

Table 2: The surface area to volume ratio of different tank geometry

Type	Surface Area	Volume	Surface Area/Volume
Sphere	$4\pi r^2$	$\frac{4}{3}\pi r^3$	$\frac{3}{r}$
Cylinder	$2\pi r^2 + 2\pi rh$	$\pi r^2 h$	$\frac{2r+2h}{rh}$
Cube	$6a^2$	a^3	$\frac{6}{r}$

The cylinder shape storage tank, which is the most commonly used commercial storage system, is implemented in this model.

2.2.5.1 Tank's Height and Radius Limitation

Mechanical stress and thermal strain are the main factors that need to be considered in storage tank design. Since a storage tank usually has a large diameter and relatively small wall thickness, its side surface could be regarded as a plate in the calculation. Therefore, its hoop stress and axial direction mechanical stress are characterized as:

$$\sigma_{radial} = \frac{P \cdot r}{t_{shell}} \tag{14}$$

$$\sigma_{axial} = \frac{P \cdot r}{2t_{shell}} \tag{15}$$

Thermal strain is the dimension change in response to the temperature variation. If the dimension is fixed, then the thermal strain would convert to thermal stress. This stress

occurs in both radial and axial directions. The thermal strain, Δx , and thermal stress, $\sigma_{thermal}$, are calculated as:

$$\Delta x = \alpha \Delta T L \tag{16}$$

$$\sigma_{thermal} = \alpha \Delta T E \tag{17}$$

Hence, the maximum stresses in the radial and axial directions are:

$$\begin{cases} \sigma_{radial} = \dfrac{P \cdot r}{t} + \alpha \Delta T E \\ \sigma_{axial} = \dfrac{P \cdot r}{2t} + \alpha \Delta T E \end{cases} \tag{18}$$

The static head of the TES fluid is calculated as:

$$P = \sigma g h \text{ and } P_{\max} = \sigma g h_{TES} \tag{19}$$

The maximum pressure from TES occurs at the bottom of the tank in radial directions. Thus, the maximum stress occurs at the bottom as well.

Assume the storage tank is constructed with the 304L type steel, whose parameters are shown in Table 3:

Table 3: 304L steel parameters

Parameters	Value
E	179 GPa (300 – 400 ˚C)
α	17.3 μm/m×K (300 – 400 ˚C)
σ	420 MPa (300 – 400 ˚C)

So, the first relation that is derived from the equation 18 for height, radius and thickness is:

$$\frac{\sigma}{f_{safe}} > \frac{P \cdot r}{t} + \alpha \Delta T E \tag{20}$$

Where f_{safe} is the safe factor, its value is 1.5. If the TES density is 2000 kg/m^3, and the temperature variation, ΔT, is $50\ K$, then equation 20 becomes:

$$\frac{h_{TES} r}{t} \leq 6400 \tag{21}$$

2.2.5.2 Height and Radius Ratio

Another relation between the height and radius of a storage tank is determined by minimizing construction material use. Less material usage indicates reduced material cost in industrial applications, which is preferable.

According to Table 2, if the tank size is small, the minimum surface area to volume ratio could be satisfied when $h=2r$, assuming a uniform thickness of storage tank is used.

For a large storage tank, the tank's surface thickness varies with its height. The thickness at the bottom could be much thicker, even several times compared with the top one.

If the tank thickness changes linearly with the tank height, then the material needed to construct a tank is:

$$V_{steel} = 2\pi r\left(rt_2 + ht_1\right) \tag{22}$$

Where t_1 is the average side thickness;

t_2 is the top and bottom thicknesses.

For a constant volume tank, the minimum material usage occurs when:

$$h = \frac{2t_2 r}{t_1} \tag{23}$$

It assumes $h \approx h_{TES}$, considering the top wall thickness and the freeboard height are both negligible. Combining with the mechanical limitation from equation 21, the maximum TES height is:

$$h_{TES} = \sqrt{12800t_2} \tag{24}$$

If the top and bottom steel thicknesses are both 8 *mm*, and the maximum wall thickness is 38 mm, which includes 36 *mm* of available wall thickness and 2 *mm* of reservation for corrosion[50]. therefore,

$$h_{TES} = 10.12\ (m) \tag{25}$$

$$r = 632.4t \tag{26}$$

$h_{TES} = 10.12\ m$ is used as the threshold which separates the small and large tank sizing models. Assume the freeboard height and stagnant heights are 0.3048 m and 0.6096 m constant. Then the relation between h_{TES}, h_{TES_avil} and h are shown in Figure 11.

$$\begin{cases} h_{TES} = 0.8607r + 0.021 & \text{if } r \le 11.38 \\ h_{TES} = 9.82 & \text{if } r > 11.38 \end{cases} \tag{27}$$

$$\begin{cases} h_{TES\_avil} = 0.8607r - 0.5886 & \text{if } r \le 11.38 \\ h_{TES\_avil} = 9.21 & \text{if } r > 11.38 \end{cases} \tag{28}$$

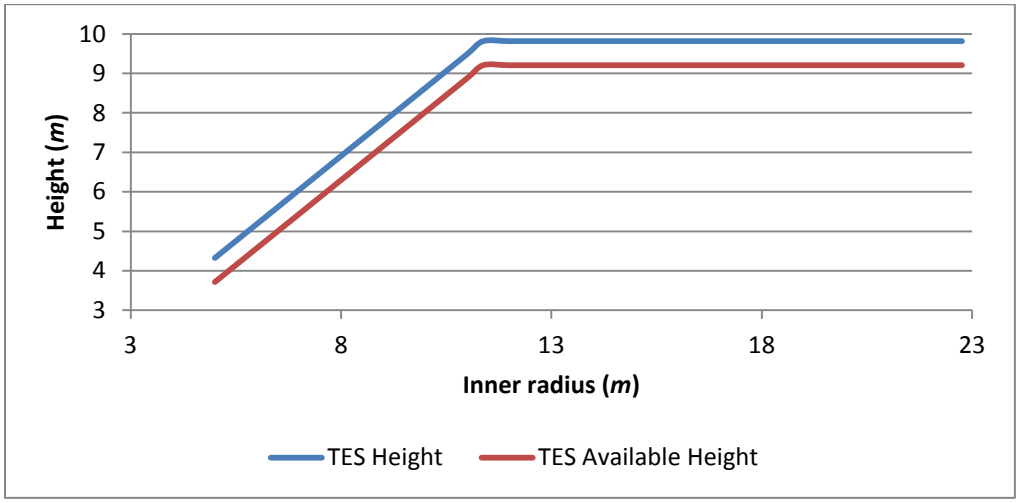

Figure 11: Total and available TES heights vary with inner radius

The tank height is the sum of the full TES height, freeboard height, top and bottom steel thicknesses, insulation layer thickness, top dome height, and foundation height, as shown in Figure 12.

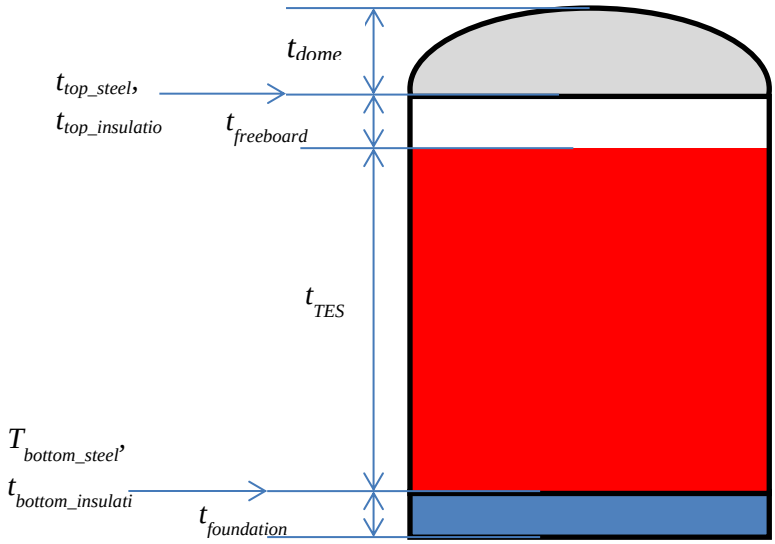

Figure 12: Components of the storage tank height

$$h_{tank} = h_{TES} + h_{freeboard} + h_{dome} + t_{steel,top} + t_{steel,btm} + t_{ins,top} + h_{foundation} \quad (29)$$

The dome height is scaled with its radius. The foundation height varies with its design storage temperature. The detail of foundation is discussed in Chapter 3.

The average outer radius is the sum of the inner tank radius, the average steel thickness and the insulation thickness, it is calculated as:

$$r_{\text{tank}} = r_i + t_{steel} + t_{ins} \tag{30}$$

The outside covering material's thickness is neglected since it is thin and is ignorable compared with the tank radius. The minimum and maximum acceptable side steel thicknesses are 8 *mm* and 38 *mm*. the average steel thickness is:

$$t_{steel}=0.5\times(0.008+t_{steel,btm}) \tag{31}$$

The insulation layer thickness is linearly correlated with tanks' design operation temperature. It is 0.375 *m* when the temperature is 666 *K*.

Figure 13 shows the model's predicted tank sizes compared with the actual sizes of storage tanks, which are used in operating CSP plants. Considering the tank's size may be affected by other factors such as the TES type, the operating temperature and the construction materials, the difference between the actual and predicted dimensions is acceptable. It is regarded that the tank sizing model is able to generate desired storage tank geometry.

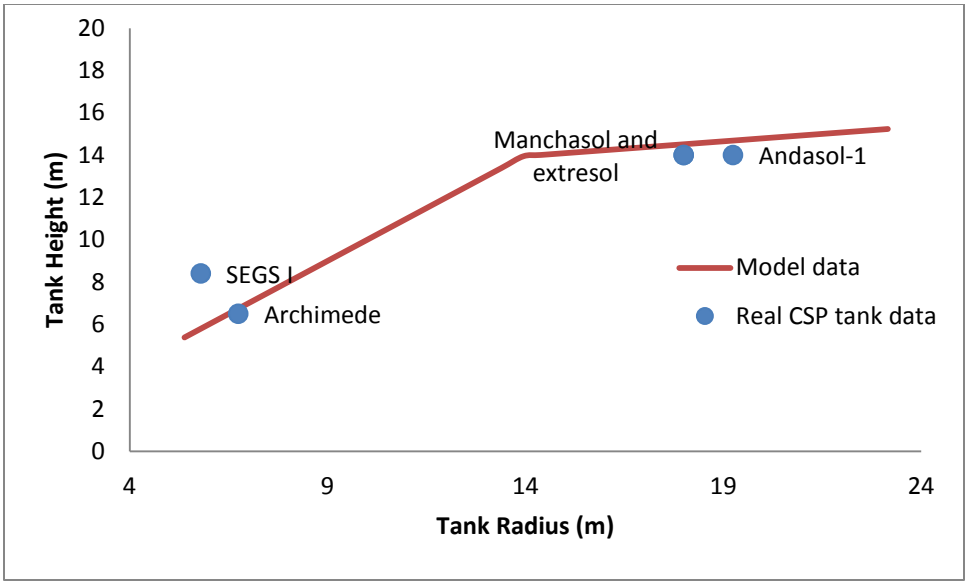

Figure 13: Comparison between simulated storage tank sizes and actual storage tank sizes

2.2.5.3 Insulation Thickness

The heat loss of a storage tank depends on factors such as the insulation material and its thickness, tank size, operating temperature, and its surrounding environment. Usually, the insulation configuration is determined in accordance to specified tank requirements and local environment. The tank profile of the Andasol-1 CSP plant and its local environment are chosen as an example for the following reasons:

1. This tank geometry is widely used in Spain's CSP plants. And currently Spain has been the world's leader in CSP area.

2. Storage tanks are becoming larger and larger to be consistent with the trend of increasing field size, and extending off-sun operational hours. The Andasol-1's storage tank is the representative of large vertical tanks systems.

The tank's top heat loss is small due to the air gap above TES, and the bottom heat loss is steady because of the thick foundation and stable ground temperature. This analysis focuses on the side insulation. It predicts the insulation thickness that has the lowest lifetime cost. The cost of insulation is estimated by a life cycle approach, which has incorporated the installation cost and saving on heat loss during operation. The heat loss cost indicates the cash flow reduction resulting from the diminished electricity production as a result of heat loss. Table 4 shows the key parameters used in the insulation model.

Table 4: Key parameters for the storage tank heat loss model

Parameter	Value
Tank Inner Diameter	18 *m*
Tank Steel Thickness -Surrounding	0.023 *m*
Tank Steel Thickness –Top	0.008 *m*
Tank Steel Thickness –Bottom	0.008 *m*
Insulation – Surrounding	0.395 *m*
Insulation – Top	0.3748 *m*
Insulation Type	Mineral Wool
Foundation Height	1.18 *m*
Tank Height	14 *m*

Table 4: Continued

TES Temperature	666 *K*
Environment Temperature	288 *K*
Soil Temperature	278 *K*
Wind Speed	6.7 *m/s*
Tank Status	Half Full
Plant Lifetime	30 years
Interest rate	7%
Insulation Material Cost	\$0.5 mm/m^2
Thermal to electricity efficiency	36%

The heat loss from the bottom and top directions are shown in Table 5.

Table 5: Storage tank heat losses in top and bottom directions

Heat loss direction	Heat loss rate (W/m^2)
Tank Top	2.5
Tank Bottom	41.8

The heat loss from the side varies with the insulation thickness, which is shown in Table 6 and Figure 14.

Table 6: Storage tank heat losses and costs with different insulation thicknesses

Insulation Thickness (m)	Heat Loss (W/m^2)	Insulation installment cost ($\$/m^2$)	Thermal Energy loss ($kWht/year/m^2$)	Heat Loss cost ($\$/year/m^2$)	Lifetime Heat Loss cost ($\$/m^2$)	Lifetime Cost ($\$/m^2$)
0	20490	0	179492.4	6461.7	85796.7	85796.7
0.01	1730	5	15154.8	545.6	7243.9	7248.9
0.05	370.6	25	3246.5	116.9	1551.8	1576.8
0.1	186.8	50	1636.4	58.9	782.2	832.2
0.15	124.7	75	1092.4	39.3	522.1	597.1
0.2	93.55	100	819.5	29.5	391.7	491.7
0.25	74.81	125	655.3	23.6	313.2	438.2
0.3	62.29	150	545.7	19.6	260.8	410.8
0.35	53.34	175	467.3	16.8	223.3	398.3
0.4	46.63	200	408.5	14.7	295.3	395.3
0.45	41.4	225	362.7	13.1	173.4	398.3
0.5	37.22	250	326.0	11.7	155.8	405.8

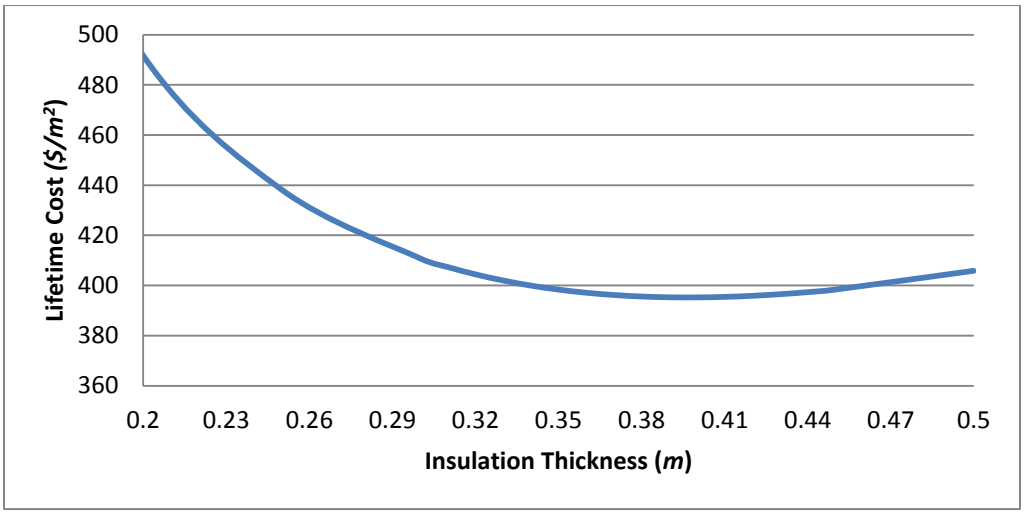

Figure 14: Lifecycle insulation cost varies with insulation thickness

Results from Table 6 and Figure 14 indicate that with the increasing of insulation thickness, the heat loss rate reduces while the installation cost escalates. The minimum lifetime cost occurs when the insulation thickness ranges from 0.35 *m* to 0.45 *m*. And these results agree with B.Kelly and D. Kearney's research[51].

Figure 15 shows that the tank insulation cost varies with insulation thickness and TES operating temperature. Figure 16 is derived from Figure 15, which shows the thicknesses when the lowest cost occurs, the regression equation is:

$$t_{ins} = 0.0005T+0.0532 \tag{32}$$

This relation is used to determine the surrounding insulation thickness in the storage model.

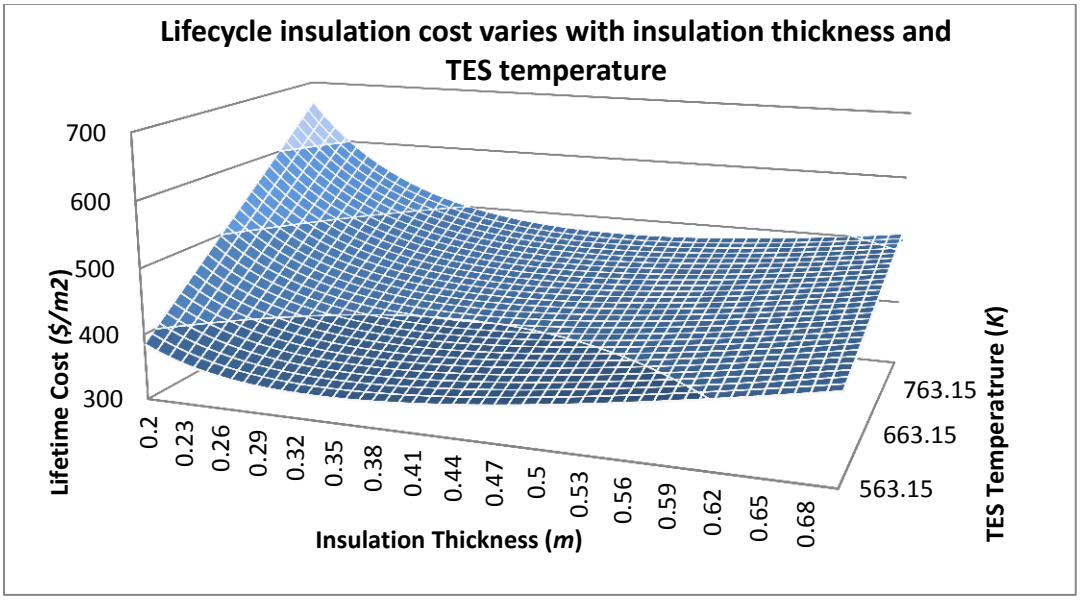

Figure 15: Lifecycle insulation cost varies with insulation thickness and TES temperature

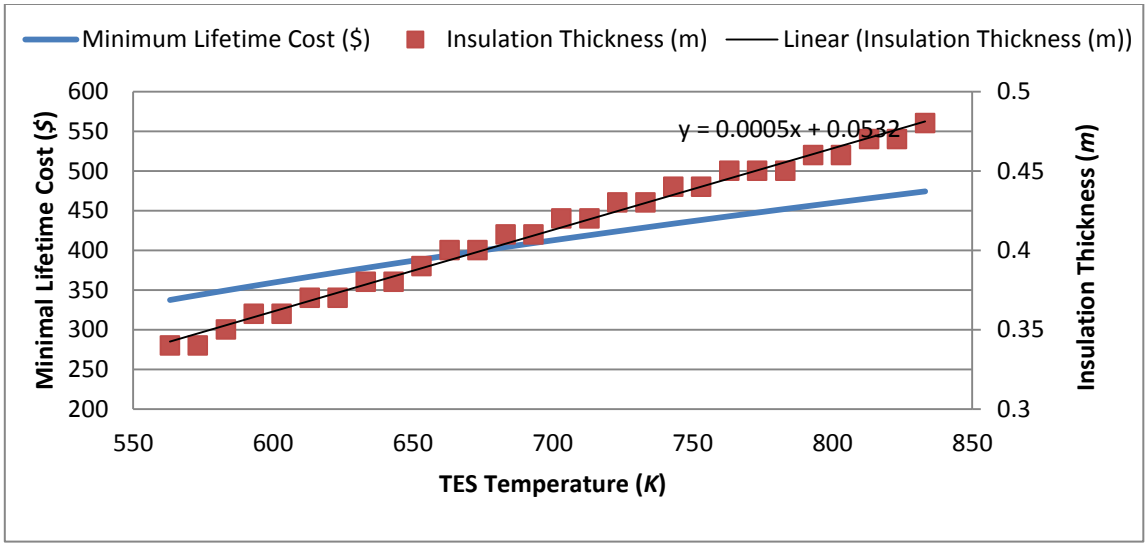

Figure 16: Lifecycle insulation cost and insulation thickness vary with TES temperature

This result confirms the key finding of B.Kelly and D. Kearney's research - the insulation thickness is linearly correlated to the storage system's design temperature. It increases from the minimum thickness of 300 *mm* at 290 ℃ to 500 *mm* at 565 ℃ [51].

2.2.6 Determine the Initial Status

An initial status that indicates the operating properties at the starting period needs to be defined to perform the calculation routine. To set an appropriate initial status is important. Otherwise the simulation would fail since the iteration might not converge as planned.

2.2.6.1 The Initial Status of the Solar Field

At the time $t = 0$, the initial variables are assigned from the inlet HTF temperature and the ambient temperature:

$$T_{absorb\_i\_guess} = T_{HTF} - 2 \tag{33}$$

$$T_{absorb\_o\_guess} = T_{HTF} - 5 \tag{34}$$

$$T_{envelope\_i\_guess} = T_{absorb\_o\_guess} - 0.8 \times (T_{absorb\_o\_guess} - T_{env}) \tag{35}$$

$$T_{envelope\_o\_guess} = T_{envelope\_i\_guess} - 2 \tag{36}$$

$$T_{HTF\_out\_guess} = T_{HTF\_in} - 30 \tag{37}$$

$$T_{pipe\_i\_guess} = T_{HTF} - 2 \tag{38}$$

$$T_{pipe\_o\_guess} = T_{insulation\_i\_guess} = T_{HTF} - 5 \tag{39}$$

$$T_{insulation\_o\_guess} = T_{env} + 4 \tag{40}$$

2.2.6.2 The Initial Status of the Storage System

A thermocline type storage system is full all the time, therefore the following discussion is based on the two-tank storage system, for which the TES mass distribution should satisfy the following requirements:

1. Any storage tank is capable of extracting and storing required amount of thermal energy;
2. The total TES mass should be minimized;

Thus, the total TES mass is:

$$m_{TES\_total} = \sum_{1}^{n} m_{TES\_stag,n} + m_{TES\_avail} \quad n \text{ is tank number} \tag{41}$$

Where

$m_{TES\_stag,i}$ is the stagnant TES mass of tank *i*;

m_{TES_avail} is the available TES mass;

The calculation routine usually starts at the midnight of January 1, thus it is reasonable to speculate that the storage system would be depleted at that time. Accordingly, the cold tank would be full and hot tank could be empty:

$$h_{TES\_hot,i} = h_{\text{stag,i}} \tag{42}$$

$$h_{TES\_cold,i} = h_{\max\_TES,i} \tag{43}$$

The TES masses in the cold and hot tanks are:

$$m_{hot\_TES,i} = \rho_{TES@high\_dgn} \pi r_{hot}^2 h_{stag} \tag{44}$$

$$m_{cold\_TES,i} = \rho_{TES@cold\_dgn} \pi r_{cold}^2 h_{\max\_TES} \tag{45}$$

The design temperatures are assigned to the two-tank system's initial temperatures, while low design temperature is assigned to the initial temperature of thermocline system, which indicates its empty status.

$$T_{TES\_hot,i} = T_{TES\_hot\_dgn} \tag{46}$$

$$T_{TES\_cold,i} = T_{TES\_cold\_dgn} \quad (47)$$

$$T_{thml,i} = T_{thml\_cold\_dgn} \quad (48)$$

2.3 Calculation Routine

Calculation routine serves to predict hourly performance for a specific period of time. In every time step, each system (the solar field, storage and power block) coordinates with the specific operation strategy and its performance is simulated independently.

2.3.1 Solar Field Model

The function of a solar field is collecting energy from sunlight and sending the collected energy which is represented as heated HTF, to the distribution pipeline. The dispense pipes distribute cooled HTF to collection loops which consist of several solar collector assemblies (SCA). HCEs are located in the focal lines of SCAs. HTF circulates through HCEs to receive thermal energy which is converted from the concentrated solar radiation. After being heated, the HTF is pumped to the associated distribution pipeline. A SCA and a HCE schemes are shown in Figure 17 and Figure 18. Figure 19 is the layout of the Andasol-1 CSP plant.

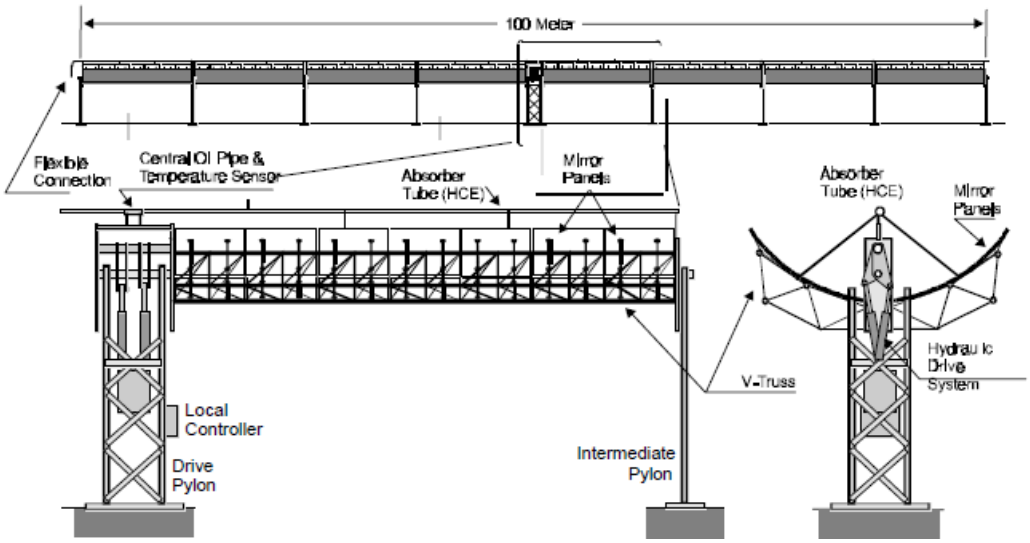

Figure 17: Diagram of the LS-3 solar collector assembly [52]

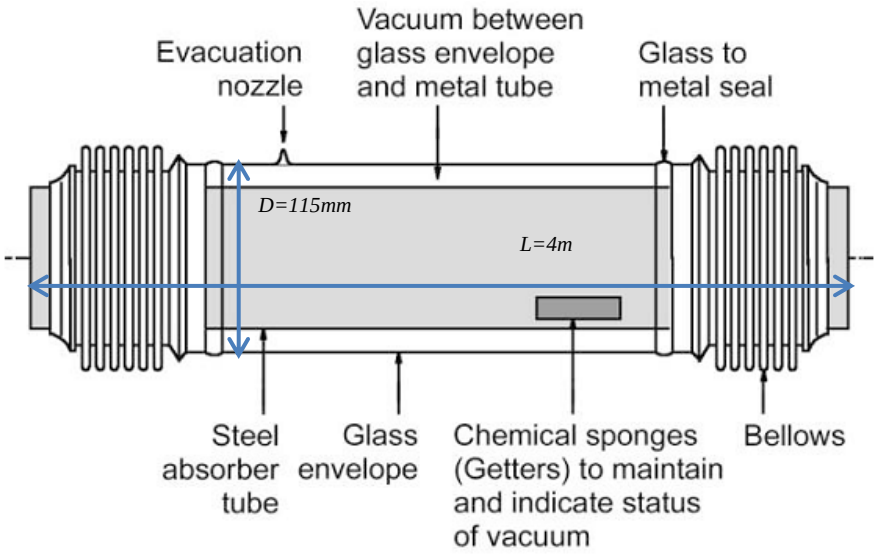

Figure 18: Diagram of a typical evacuated HCE [53]

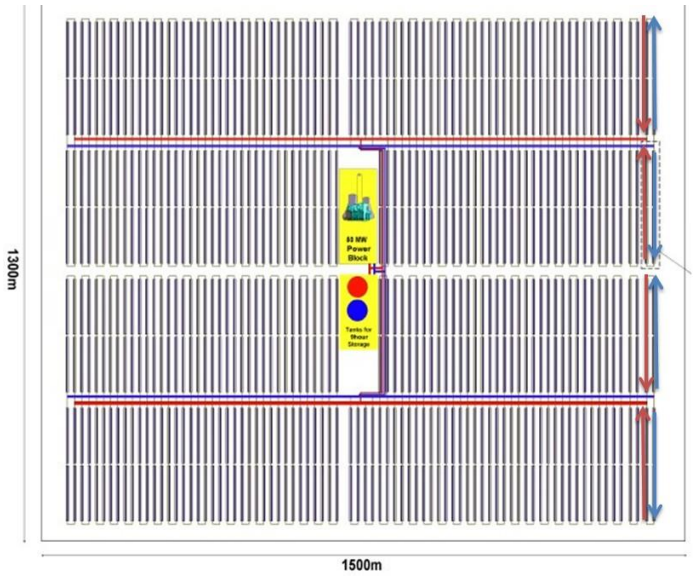

Figure 19: The solar field layout of the Andasol-1 project, the red and blue arrows indicate the directions of HTF flows [54]

During the energy collection process, a portion of the solar irradiation energy is absorbed by HTF and then transferred out, and the rest dissipates to the environment. Dissipation occurs in every energy transfer and conversion procedure, as shown in Figure 20. These procedures are:

1. Solar radiation hits on and then reflects from troughs;
2. Reflected radiation hits on the surfaces of absorbers;
3. HTF absorbs thermal energy;
4. Transfer Heated HTF to the distribution pipeline;

Each procedure is analyzed respectively in the following content.

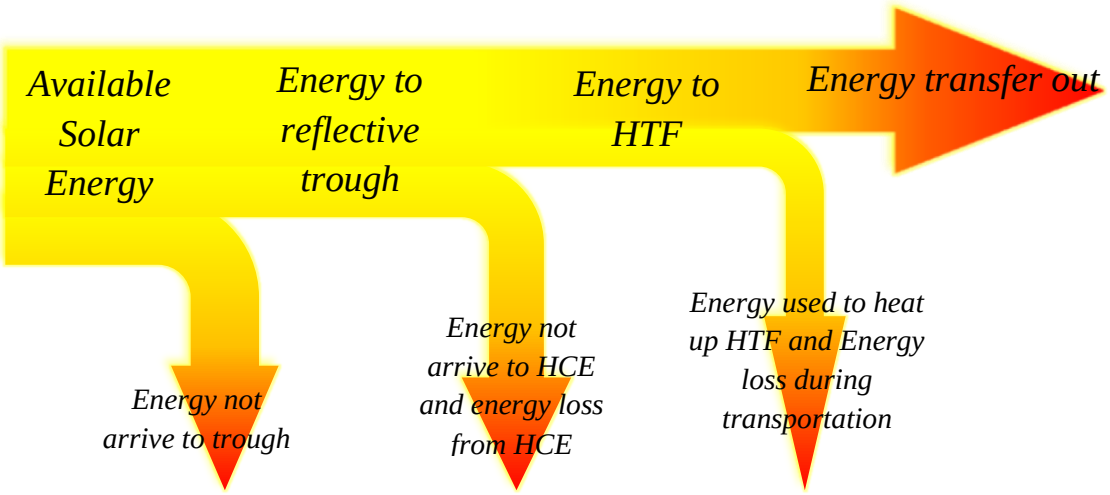

Figure 20: Diagram of the energy flows in a solar field

2.3.1.1 Reflecting Solar Energy by Troughs

Some radiation energy is dissipated because of troughs' reflection. The lost may be caused by imperfect reflectivity, collectors' end loss, row shadow, and collector's absorption. The reflected solar energy is derated by the factor of $f_{reflect\_general}$ from available solar energy, as shown in the following equation:

$$\dot{q}_{refl\_general} = \dot{q}_{avail} \cdot f_{refl\_general} \tag{49}$$

And the factor $f_{reflect\_general}$ is calculated as:

$$f_{refl\_general} = f_{\cos\_effect} \cdot f_{trough\_opt\_err} \cdot f_{row\_shadow} \cdot f_{1AM} \cdot f_{end\_loss} \cdot f_{deploy\&stow} \tag{50}$$

2.3.1.1.1 Cosine Loss Effect

A trough rotates about the lengthwise axis to track the sunlight. Its rotation is controlled in such a way that minimizes the incidence angle. The incidence angle is the angle between the aperture normal of the trough and the direction of solar radiation. Once the incidence angle is not zero, the effect collective area of the trough reduces from S_A to S_B, as shown in Figure 21.

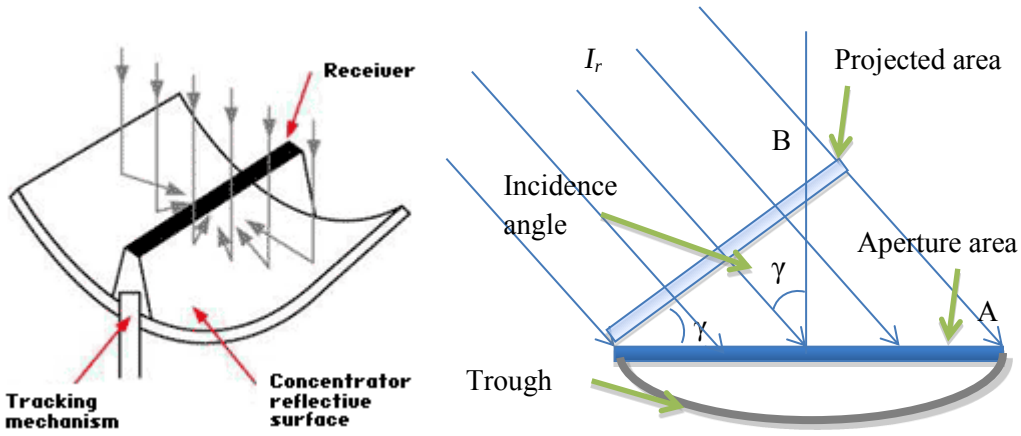

Figure 21: Illustration of the cosine loss effect

The effective solar radiation to a trough is

$$\dot{q}_{incident} = I_{DNI} \cdot S_B = \cos\gamma I_{DNI} \cdot S_A \tag{51}$$

Thus, the effective solar radiation is derated by the factor of *cosγ* because of the incidence angle.

$$f_{\cos\_effect} = \cos\gamma \tag{52}$$

2.3.1.1.2 Optical Effect Factor

The optical effect factor accounts for the optical loss caused by tracking error and twist, geometric accuracy, mirror reflectivity and cleanness, and others. It is estimated as:

$$f_{Trough\_opt\_err} = f_{track\_twist} \cdot f_{geo\_accu} \cdot f_{mirr\_refl} \cdot f_{mirr\_clean} \cdot f_{other} \tag{53}$$

The definitions of these factors are shown in Table 7.

Table 7: Definitions of each trough optical factor [49]

Item	Definition
f_{track_twist}	Tracking error and twist factor. Inability to perfectly rotate to tracking angle; twisting of the collector along rotation axis direction
f_{geo_accu}	Geometric accuracy factor. Poor alignment when install the trough; Poor position of the absorber tube; warping or discontinuities along the reflective surface
f_{mirr_refl}	Mirror reflectivity factor. Consider energy been absorbed by trough rather than reflects to absorber.
f_{mirr_clean}	Mirror cleanness factor. Dirt on the trough surface that prevents irradiation from reflecting to the receiver.
f_{other}	Any other factors that not includes in above categories.

2.3.1.1.3 Row Shadow Factor

The solar altitude is low in the morning or dawn. At that time, those troughs further into the interior of the solar field may be partial or fully shadowed by the troughs closer to the edge of the solar field. This is effect is illustrated in Figure 22.

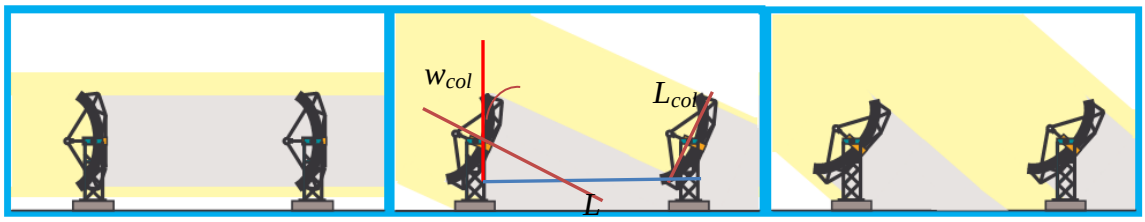

Figure 22: Illustration of row shading in a multi-row collectors array [55]

Row shadows reduce the incident solar radiation to troughs, thus diminishing the collected energy. This decrease is represented as the row shadow factor, which is defined as the ratio of the aperture area that is able to receive irradiation to the whole aperture area.

$$f_{row\_shadow} = \frac{S_{eff}}{S} = \frac{\cos w_{col} L}{L_{col}} \tag{54}$$

Where:

S_{eff} is the trough's effective aperture area;

S is the trough's whole aperture area;

L is the distance between two rows of collector;

L_{col} is the trough's aperture;

w_{col} is the incidence angle between the tough and sunlight;

2.3.1.1.4 Incidence Angle Modifier (IAM)

The IAM refers to other losses related to the varying solar direction. These losses may be caused by glass envelope transmittance, selective surface absorption, collector aperture foreshortening and others. An empirical formula is used to calculate the IAM factor, as shown in equation 55.

$$f_{IAM} = a_0 + a_1 \frac{\theta_{col}}{\cos\theta_{col}} + a_2 \frac{\theta_{col}^2}{\cos\theta_{col}} \tag{55}$$

2.3.1.1.5 End Loss Factor

When the sunlight is not normal to the collectors' axial directions, some of the reflected sunlight may escape from its absorber pipe. This portion of reflected sunlight may disperse to the environment or hit on the neighboring collectors' absorber pipes, as shown in Figure 23.

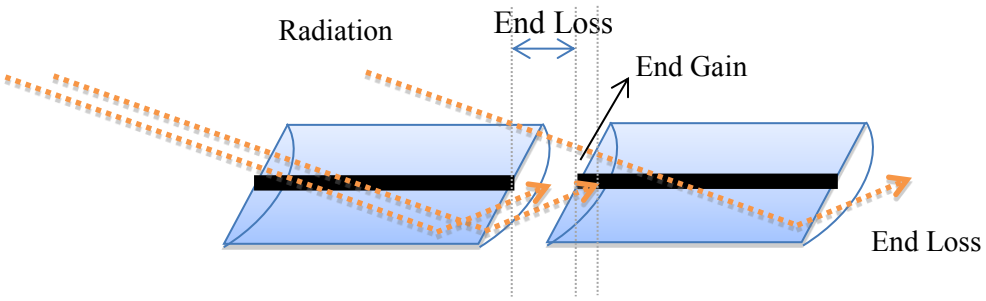

Figure 23: Illustration of the end loss

The end loss factor f_{end_loss} is defined as the ratio of the reflected radiation which incidents to absorbers to all the reflected radiation from troughs. It is determined by the collector's length, the incidence angle and the focal length:

$$f_{end\_loss} = 1 - \frac{R_{focal\_length} \cdot \tan(\theta_{col})}{L_{col\_length}} + \frac{N_{col\_per\_row} - 1}{N_{col\_per\_row}} \cdot \frac{R_{focal\_length} \cdot \tan(\theta_{col}) - D_{col\_row}}{L_{col\_length}} \quad (56)$$

Where

R_{focal_length} is the average focal length;

L_{col_length} is the collector's length;

D_{col_row} is the distance between each collector within a single row;

$N_{col\_per\_row}$ is the number of collector per row.

2.3.1.1.6 Deploy and Stow Time Factor

In real operation, the troughs are not capable of rotating along the entire course from sunrise to sunset because they cannot work on the extreme angles. These threshold

angles are defined as stow and deploy angles. Since trough's deploy and stow angles are essential solar altitude angles, therefore theirs stow and deploy times could be calculated as:

$$t = t_{solar\_noon} + \frac{sign(\tan(\pi - \omega))}{15} \cos^{-1}\left(\frac{fg + \sqrt{f^2 - g^2 + 1}}{f^2 + 1} \right) \tag{57}$$

$$f = \frac{\cos\varphi}{\tan\omega} \text{ and } g = -\frac{\tan\delta \sin\varphi}{\tan w} \tag{58}$$

While:

t is the deploy/stow time and ω is the deploy/stow angle in the deploy/stow situation.

The deploying and stowing factor is defined as the working time fraction for that simulation time step, they are:

$$\text{In the deploy period, } F_{deploy\&stow} = \frac{t_{end} - t_{deploy}}{t_{end} - t_{start}} \tag{59}$$

$$\text{In the stow period, } F_{deploy\&stow} = \frac{t_{deploy} - t_{start}}{t_{end} - t_{start}} \tag{60}$$

Under normal operation status, $F_{deploy\&stow}$ is one in daytime, and zero at night.

2.3.1.2 Converted Solar Radiation to the Surface of Absorber

Partial of the reflected solar radiation may dissipate before it is absorbed by the absorbers of collectors. The incident solar energy to absorbers is:

$$\dot{q}_{absb\_general} = \dot{q}_{refl\_general} \cdot f_{col\_opt\_err} = \dot{q}_{avail} \cdot f_{refl\_general} \cdot f_{col\_opt\_err} \quad (61)$$

$F_{col\_opt\_err}$ characterizes the energy loss during this procedure. Several factors are considered, as shown in equation 62:

$$f_{col\_opt\_err} = f_{dust}\, f_{bellow}\, f_{transmissivity}\, f_{absorb}\, f_{other} \quad (62)$$

The definitions of those factors are shown in Table 8.

Table 8: Definitions of each collector optical factor [49]

Item	Definition
f_{dust}	Dust in the absorber's annulus vacuum that reduces the solar thermal collection.
f_{bellow}	Bellow part in the tube that is not able to absorb solar thermal radiation.
$f_{transmissity}$	Envelope glass is not fully transparent and may reflect or absorb some of the solar thermal energy.
f_{absorb}	The absorber surface is not capable to absorb all the solar thermal energy
f_{other}	All other factors that reduce absorption that not includes in above categories

2.3.1.3 HTF Absorbed and Carried Energy

Concentrated solar radiation converts to thermal energy when it hits on absorbers. The heated absorbers may dissipate the absorbed thermal energy to the circuiting HTF which runs inside the collectors, or to the environment. A numerical model was developed to simulate the energy flows of this procedure.

2.3.1.3.1 HCE Energy Model

This model estimates the temperature change of HTF when it flows through the collection pipe, as shown in Figure 24.

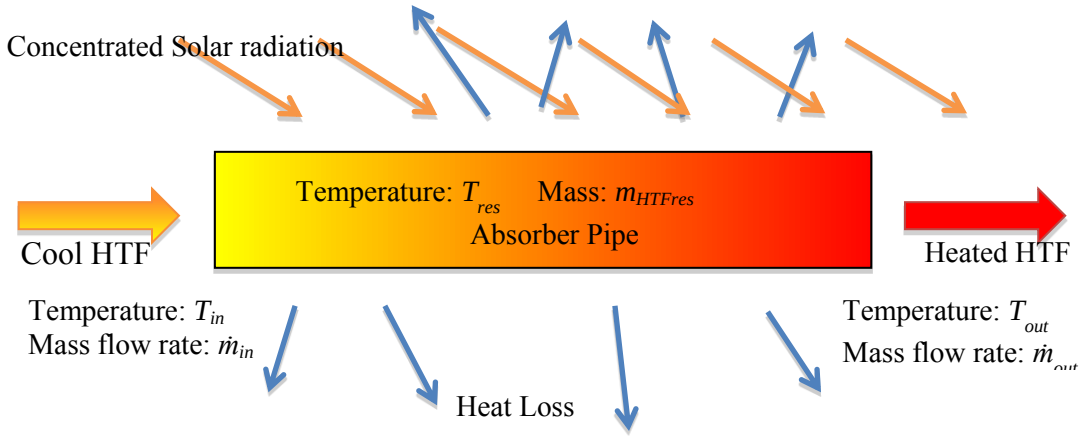

Figure 24: Diagram of the energy flows of a collector

The mass balance of HTF in a collector is:

$$\dot{m}_{in} - \dot{m}_{out} = \frac{dm_{res}}{dt} = \frac{d(\rho_{TES} V_{collector})}{dt} \tag{63}$$

Considering the residence HTF mass is much smaller than the flowing mass in each time step and the inlet and outlet temperatures are almost stable during the energy collection period, the residence HTF mass is taken as constant, which value can be determined

assuming density is evaluated at design temperature in simulation. Therefore, the inlet and outlet HTF mass flow rates are the same.

$$\frac{dm_{res}}{dt} = 0\,,\ \dot{m}_{in} = \dot{m}_{out} = \dot{m} \tag{64}$$

The energy balance is:

$$\dot{q}_{in} + \dot{q}_{absb\_general} S_{aperture} - \dot{q}_{HL} - \dot{q}_{out} = \frac{dU}{dt} \tag{65}$$

The Appendix B shows the detailed heat loss calculation. The outlet HTF temperature is derived according to its enthalpy,

$$h_{out} = \frac{\dot{m} h_{in} + \dot{q}_{absb\_general} S_{apeture} - \dot{q}_{HL} - m_{res}\left(h_{res\_t+\Delta t} - h_{res\_t}\right)}{\dot{m}} \tag{66}$$

While

h_{res_t} is the enthalpy of residence HTF at the beginning of simulation period;

$h_{res\_t+\Delta t}$ is the enthalpy of residence HTF at the end of simulation period:

The residence HTF temperature is evaluated as the average of inlet and outlet temperatures:

$$h_{res\_t+\Delta t} = \frac{T_{in} + T_{out}}{2} \tag{67}$$

The enthalpy of HTF is the function of its temperature. Reversely, the temperature could be obtained from its enthalpy.

$$h = f(T) \rightarrow T = f^{-1}(h) \tag{68}$$

2.3.1.3.2 HTF Transfer Pipe Energy Model

HTF transfer pipes connect HCE loops to the storage system or the power block. Similar to the HCE energy model, its energy balance diagram is shown in Figure 25.

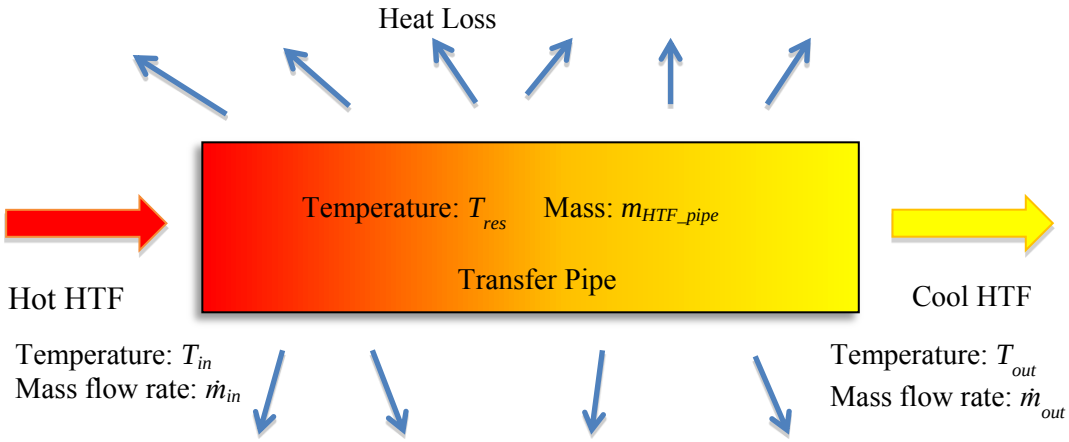

Figure 25: Diagram of the energy flows of a HTF transfer pipe

The HTF enthalpy leaving the transfer pipe is:

$$h_{out} = \frac{\dot{m}h_{in} - \dot{q}_{HL} - m_{res}\left(h_{res\_t+\Delta t} - h_{res\_t}\right)}{\dot{m}} \tag{69}$$

The heat loss estimation method is shown in the Appendix B. The HTF temperature used in the heat loss calculation is the average of the inlet and outlet HTF temperatures:

$$T_{HTF} = \frac{T_{in} + T_{out}}{2} \tag{70}$$

The HTF temperature leaving the pipe can be derived from its enthalpy:

$$T_{out} = f^{-1}(h_{out}) \tag{71}$$

2.3.1.4 Thermal Energy Deliver Model

The solar field consists of hundreds of loops of HCEs and several set of transfer pipes. In simulation, it is assumed the performance of each loop of HCEs is the same, so are each set of transfer pipes. Therefore, the field's mass flow rate could be obtained by only simulating one loop of HCEs and one set of transfer pipes. The black frames in Figure 26 show the simulation components when the loop is constituted of four HCEs. Figure 27 shows several common layouts of solar fields.

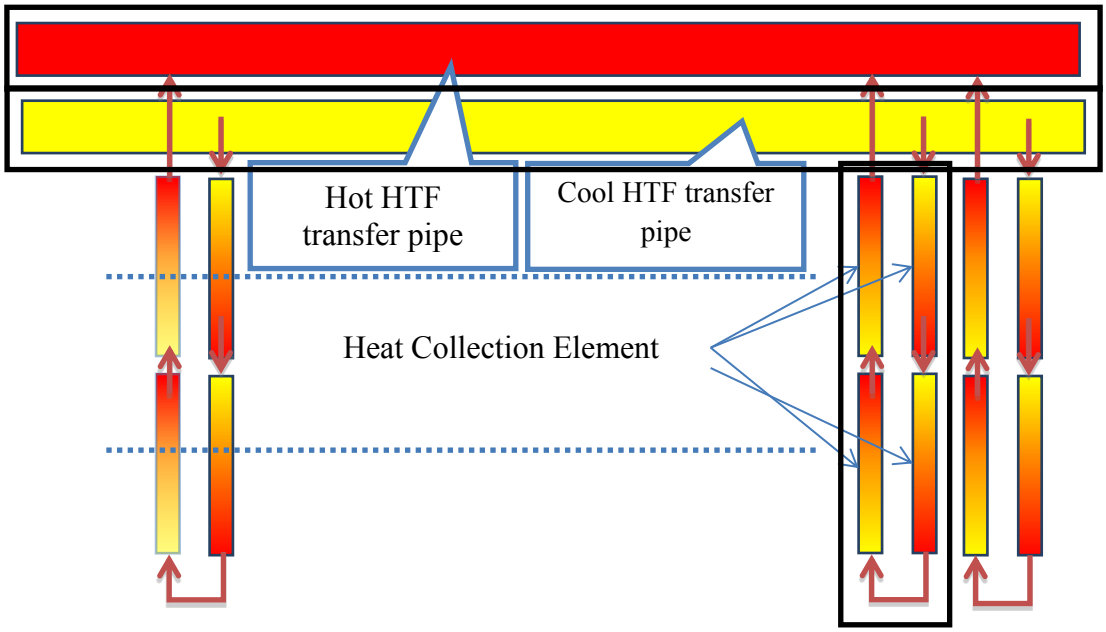

Figure 26: Demonstration of simulated components with loop constituted of four HCEs

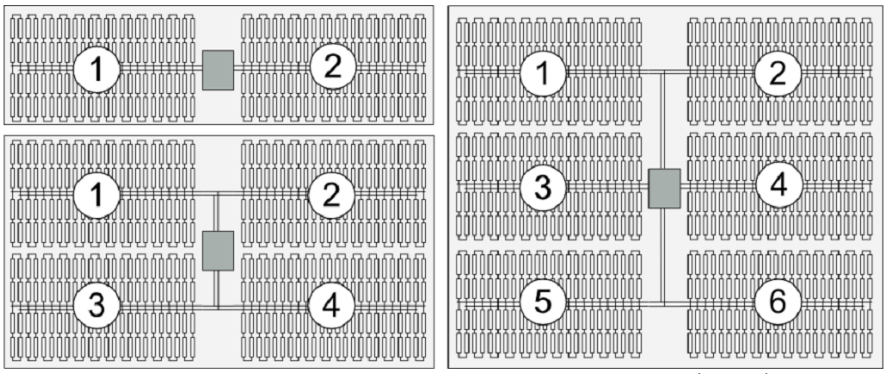

Figure 27: Different layouts of solar fields[9]

[9] Picture from System Advisor Model (SAM)'s help manual, 2013, Version 2013.1.15, National Renewable Energy Laboratory (NREL), Golden, CO.

The mass flows rates of single transfer pipe and general solar field are:

$$\dot{m}_{transfer\_pipe} = \dot{m}_{HCE} N_{loops\_per\_group} \tag{72}$$

$$\dot{m}_{SF} = \dot{m}_{transfer\_pipe} N_{group} \tag{73}$$

Because of the instability of the solar radiation, three operation modes are considered in the model, as shown in Figure 28.

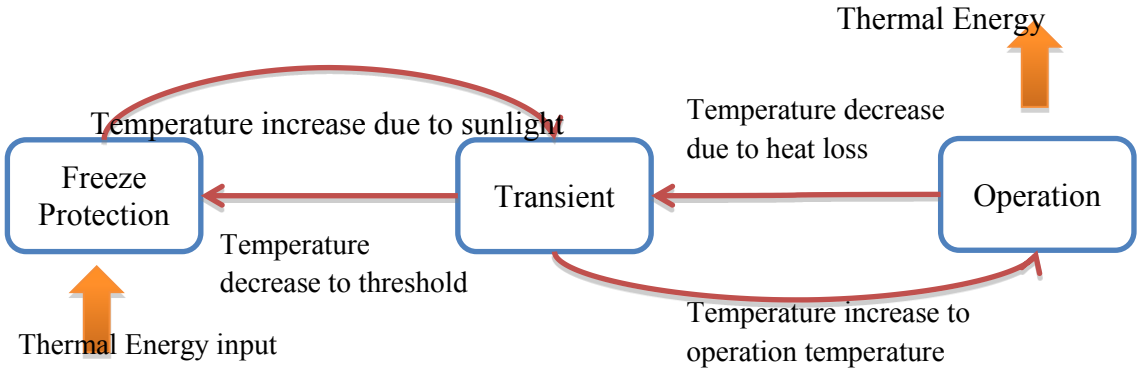

Figure 28: Flow chart of solar field operation modes

2.3.1.4.1 Operation Mode

The operation mode is the situation that a solar field steadily collects solar energy and outputs heated HTF. It is the only status that a solar field can exchange energy with the other systems. The HTF mass fluid rate is continuously adjusted to control the outlet temperature. The outputting energy is:

$$E_{SF} = \dot{m}_{HTF}\left(h_{HTF\_out} - h_{HTF\_in@dgn}\right) \quad (74)$$

2.3.1.4.2 Transient Mode

The Transient mode is defined as the period when HTF temperature has obvious fluctuations. It is the intermediary of the operation and the freeze protection modes. In transient mode, the HTF only circulates inside the solar field. Due to the limited reservoir of the HTF quantity in pipelines, its temperature increases or decreases quickly. The simulation time step is reduced to five minutes in order to better predict its temperature change. Its flow chart is shown in Figure 29.

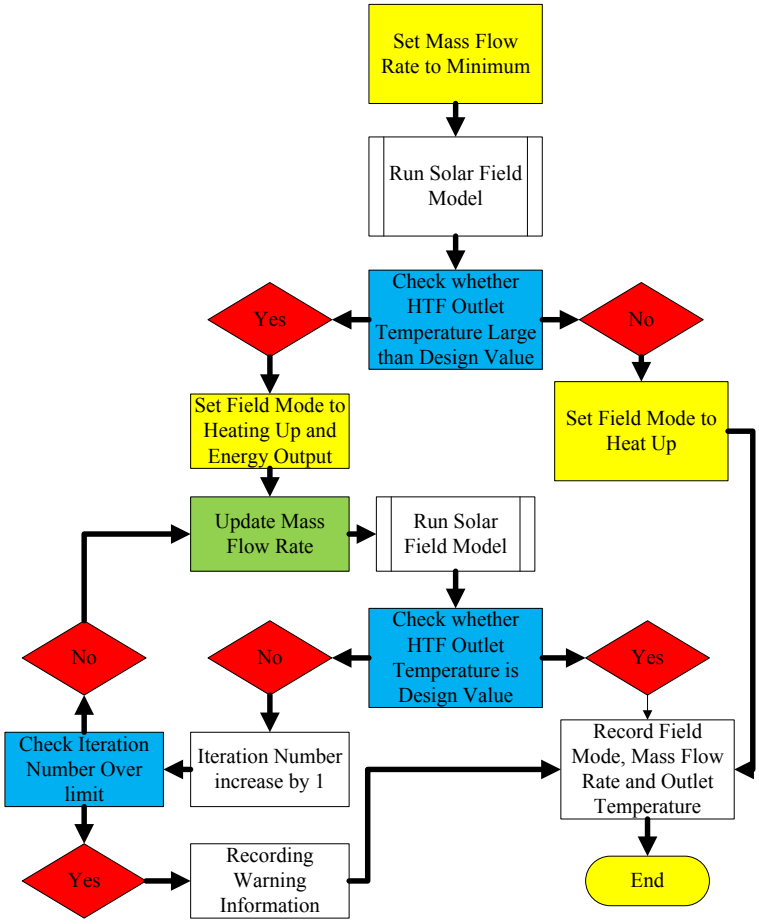

Figure 29: Flow chart of the transient status

2.3.1.4.3 Freeze Protection Mode

This mode describes the situation that the solar field is cooled down and its auxiliary heater is powered on to prevent HTF from further cooling and solidifying. The cooled HTF in the outlet port of solar field is heated by the auxiliary heater and then returned to the inlet port. The energy consumed by the auxiliary heater for freeze protection is:

$$\dot{q}_{field\_freeze\_pretection} = \dot{m}_{HTF\_\min}\left(h_{HTF\_freeze} - h_{HTF\_out}\right) \quad (75)$$

2.3.2 Thermal Energy Storage Model

The storage system serves to store or extract thermal energy. The adopting of storage system brings several unique advantages to solar thermal power compared with other alternative energy types, they are:

1. Improve power generation quality by smoothing solar field's fluctuating output and providing stable thermal energy to power block;
2. Support flexible dispatch schedule. The stored energy can be used to generate electricity when needed regardless of the weather conditions, which means:
    - It is able to shift the production period, such as switching from low revenue period to high revenue period;
    - Electricity generation is predictable according to the reservoir of the storage system, at least for a short period of time;
    - The electricity production can follow the grid's requirements;
3. Extend power generation time. It even has the potential to work as a baseload power plant if the storage system is large enough;
4. The storage is financially feasible. Since its installation cost and maintenance cost are both reasonably low compared to other energy storage methods.
5. The storage has a high performance. It has a high output to input energy ratio, and its performance does not decrease over time.

Two kinds of storage systems are available – the two-tank and thermocline systems. The two-tank system uses separate tanks to store high and low-temperature TES. During charging phase, the low-temperature TES in the cold tank is pumped out to heat exchangers, heated, and then stored in the hot tank. In the discharge phase, the procedure is reversed, the TES flows from the hot tanks to the cold tanks.

A two-tank system can be further divided into indirect and direct types from its heat exchange layout. The direct type uses the same materials for TES and HTF, thus the storage and the solar field systems can be connected directly. It exchanges thermal energy in one direct step. The power block system only draws thermal energy from the storage system. The main drawback of the direct type configuration is the high cost of the HTF/TES, because it needs to fulfill the requirements of both solar field and storage systems. This type of layout is usually used in early parabolic trough power plants. The indirect type uses different materials for HTF and TES, and one set of heat exchangers are used to exchange thermal energy between them. Though the heat exchangers require extra cost, the choices of TES and HTF materials are more flexible. They only need to fulfill individual needs of the solar field and storage system, therefore some inexpensive materials could be used, and finally the total storage system cost is lower than the direct type. These two layouts are shown in Figure 30:

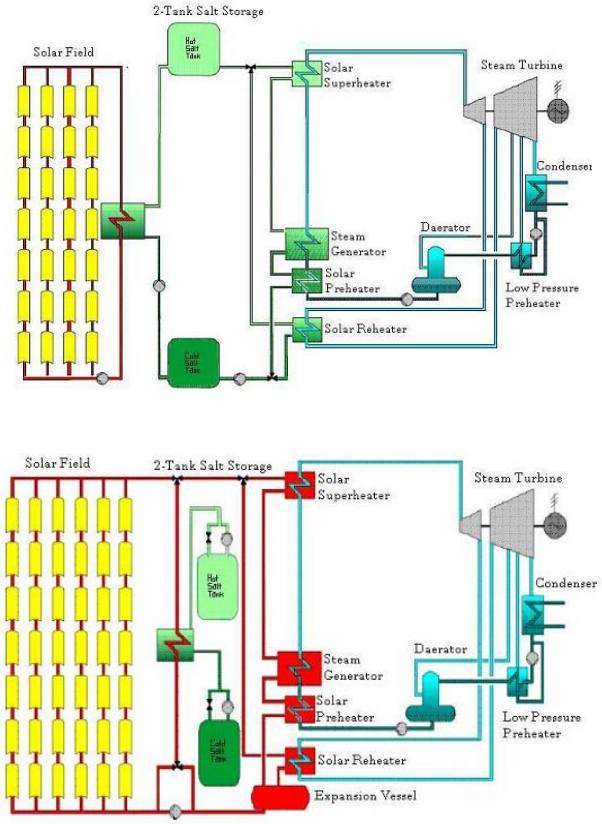

Figure 30: Diagrams of the direct (up) and indirect (down) storage systems [56]

Thermocline storage system stores hot and cold TES in one tank. The hot fluid is stored in the top while the cold stays at the bottom as designed. The hot and cold fluids are connected with a temperature gradient, which is called thermocline. During operation, the hot fluid always charges or discharges at the top while the cold fluid is pumped out or returned to the bottom.

Low cost solid materials, such as quartzite rocks and sands, can be used as the thermal storage materials of a thermocline system, to further lower the material cost. Also, the construction cost and heat loss of a thermocline storage system is supposed to be lower than the comparable two-tank system because of the reduced tank size and surface area. Figure 31 shows the diagram of thermocline storage system.

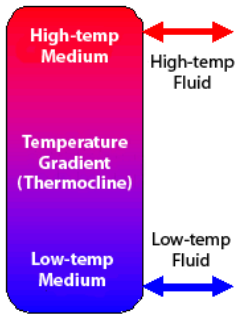

Figure 31: Diagram of a thermocline storage system[10]

2.3.2.1 Calculation Principle

The storage system model serves to predict the mass of stored TES and its temperature. The mass and energy balances of TES are:

$$\frac{dm_{TES\_tank}}{dt} = \int \left(\dot{m}_{in} - \dot{m}_{out} \right) dt \tag{76}$$

[10] Picture from U.S. Department of Energy, retrived on August 2013, address: http://energy.gov/eere/energybasics/articles/thermal-storage-systems-concentrating-solar-power

$$\frac{dH_{TES\_tank}}{dt} = \int\int h_{TES}\left(T_{in}\right)d\dot{m}_{in}dt - \int\int h_{TES}\left(T_{out}\right)d\dot{m}_{out}dt - \int \dot{q}_{HL} - \dot{q}_{heat\_in}dt \quad (77)$$

After being discretized, they become

$$m_{TES\_tank@t+1} = m_{TES\_tank@t} + \left(\dot{m}_{in} - \dot{m}_{out}\right)\Delta t \quad (78)$$

$$H_{TES\_tank@t+1} - H_{TES\_tank@t} = h_{TES}\left(T_{in}\right)d\dot{m}_{in}\Delta t - h_{TES}\left(T_{out}\right)d\dot{m}_{out}\Delta t - \dot{q}_{HL}\Delta t \quad (79)$$

For a two-tank system, it assumed all TES mass in each tank has same temperatures, its TES temperature is:

$$h(T_{TES@t+1}) = \frac{h_{TES}\left(T_{in}\right)d\dot{m}_{in}\Delta t - h_{TES}\left(T_{out}\right)d\dot{m}_{out}\Delta t - \dot{q}_{HL}\Delta t + m_{TES\_tank@t}h(T_{TES@t})}{m_{TES\_tank@t+1}} \quad (80)$$

$$T_{TES@t+1} = f^{-1}\left(h(T_{TES@t+1})\right) \quad (81)$$

Therefore, the available thermal energy is:

$$E_{tank\_avail} = m_{TES\_tank}\left\lfloor h\left(T_{TES}\right) - h\left(T_{TES\_low\_temp\_dgn}\right)\right\rfloor \quad (82)$$

For the thermocline system, it assumes its TES is only used to exchange thermal energy between HTF and the filled materials. The filled materials are fixed in storage tanks during operation. The energy balance of a thermocline system is:

$$\left[h\left(T_{filled\_hot\_dgn}\right) - h\left(T_{filled\_cold\_dgn}\right)\right]\Delta m_{filled\_hot} = \left\{\left[h_{TES}\left(T_{in}\right) - h_{TES}\left(T_{out}\right)\right]d\dot{m}_{out} - \dot{q}_{HL}\right\}\Delta t \quad (83)$$

The filled materials mass which endures temperature change is

$$\Delta m_{filled\_hot} = -\Delta m_{filled\_cold} = \frac{\left\{\left[h_{TES}\left(T_{in}\right) - h_{TES}\left(T_{out}\right)\right] d\dot{m}_{out} - \dot{q}_{HL}\right\}\Delta t}{h\left(T_{filled\_hot\_dgn}\right) - h\left(T_{filled\_cold\_dgn}\right)} \tag{84}$$

Then the masses of the hot and cold filled materials become:

$$m_{filled\_hot@t+1} = m_{filled\_hot@t} + \Delta m_{filled\_hot} \tag{85}$$

$$m_{filled\_cold@t+1} = m_{filled\_cold@t} + \Delta m_{filled\_cold} \tag{86}$$

The control system prevents the storage system from overcharging or overdrawing for a two-tank system; it also prohibits over heating or cooling for a thermocline system. However, there is still possibility that heated filled materials are depleted, but the heat loss to environment still continues. In this situation, all filled materials' temperature decreases simultaneously and there is no thermocline exists anymore. The filled materials enthalpy is calculated as:

$$h\left(T_{filled\_@t+1}\right) = h\left(T_{filled\_@t}\right) - \frac{\dot{q}_{HL}\Delta t}{m_{filled}} \tag{87}$$

The heat loss estimation is described in Appendix B.

2.3.2.2 Tank Auxiliary Heater

A storage system may be equipped with auxiliary heaters. It is used to keep the TES from solidifying. In this model, auxiliary heater which is powered by electricity is installed at the bottom of the tank. The electricity to thermal conversion efficiency is set to 100% in the model. Its power denotes the peak thermal energy generation rate that is capable to transfer to TES. Once the TES temperature falls below the set value, auxiliary

heaters are powered on until either the maximum heating power or the threshold temperature is achieved.

The power consumption for the auxiliary heater is:

$$\text{If } T_{TES} > T_{aux\_dgn},\ E_{tank\_aux}=0; \tag{88}$$

$$\text{If } T_{TES} <= T_{aux\_dgn},\ E_{tank\_aux}=\min(P_{aux\_max},\ m_{TES}(T_{aux\_dgn}-T_{TES})/\Delta t); \tag{89}$$

2.3.2.3 Storage System Status

Storage system updates its statuses in each calculation period. These statuses are the input of operation strategy module. They include:

2.3.2.3.1 Available Thermal Energy

The available thermal energy is the stored thermal energy that can be extracted. For a two-tank system, it is:

$$Q_{STG\_avil} = \left(m_{STG} - m_{res}\right)\left(h_{TES\_current} - h_{TES\_back}\right) \tag{90}$$

For a thermocline system, it is:

$$Q_{STG\_avil} = m_{filled\_high}\left(h_{filled\_high} - h_{filled\_low\_dgn}\right) \tag{91}$$

2.3.2.3.2 Acceptable Thermal Energy

The acceptable thermal energy is the thermal energy that could be accepted and stored in the storage system. For a two-tank system, it is:

$$Q_{STG\_accept} = \left(m_{STG\_dgn} - m_{STG}\right)\left(h_{TES\_charge\_dgn} - h_{TES\_back\_dgn}\right) \tag{92}$$

For a thermocline system, it is:

$$Q_{storage\_accept} = m_{filled\_low}\left(h_{filled\_high\_dgn} - h_{filled\_low}\right) \tag{93}$$

2.3.3 Power Block Model

A Power block converts thermal energy into electricity. It is usually equipped with conventional steam Rankine cycle turbines and electric generators for utility scale standalone CSP plant.

Power blocks of CSP plants have comparable performance and operating characteristics because their operating temperatures are similar, which is limited by the HTF's high temperature stability. The power block model serves to simulate its performance and operating characteristics by scaling the target CSP plant to the reference plant, and estimate the performance from the reference plant's operating characteristics[57].

The scaling factor is calculated as:

$$f_{scale} = \frac{E_{Rating\_dgn}}{E_{Rating\_ref}} \tag{94}$$

Also, the thermal energy to reference power block model is scaled:

$$Q_{ThE2PB\_ref} = \frac{Q_{ThE2PB}}{f_{scale}} \tag{95}$$

The thermal energy input of power block under design condition is determined by rated efficiency and power block's rated generation power, which is:

$$Q_{PB\_dgn} = \frac{E_{Rate\_ref}}{\eta_{Gross\_dgn}} \tag{96}$$

2.3.3.1 Turbine Starting Energy Consumption

When turbine starts, a portion of received thermal energy is used for starting and heating up. It is regarded that this portion of thermal energy is not converted into electricity. The starting energy is estimated as a fraction of design thermal energy input in the model, as:

$$\begin{cases} Q_{PB\_start} = Q_{PB\_dgn} \cdot F_{PB\_start} & \text{Starting condition} \\ Q_{PB\_start} = 0 & \text{Other condition} \end{cases} \tag{97}$$

2.3.3.2 Conversion Efficiency Corrections

A power block's conversion efficiency varies with environmental condition and its operation. In this model, the two most important factors - the workload of power block and the cooling temperature are considered.

$$\eta_{gross} = \eta_{gross\_dgn}\eta_{PB\_ld}\eta_{PB\_temp} \tag{98}$$

A fourth-order polynomial equation is used to indicate the variation caused by workload, as shown

$$\eta_{PB\_load} = f_{TE0} + f_{TE1}f_{ld} + + f_{TE2}f_{ld}^2 + f_{TE3}f_{ld}^3 + f_{TE4}f_{ld}^4 \tag{99}$$

Where

$$f_{load} = \frac{Q_{ThE2PB} - Q_{PB\_start}}{Q_{PB\_dgn}} \tag{100}$$

And Q_{PB_Start} is the energy used to start the power block.

Figure 32 shows the partial load factor of an 80MW power block which is used in the SEGS CSP plant, and Figure 33 is the relative efficiency of the partial load efficiency to the rated efficiency of the same turbine. It shows the efficiency decreases with the decline of workload.

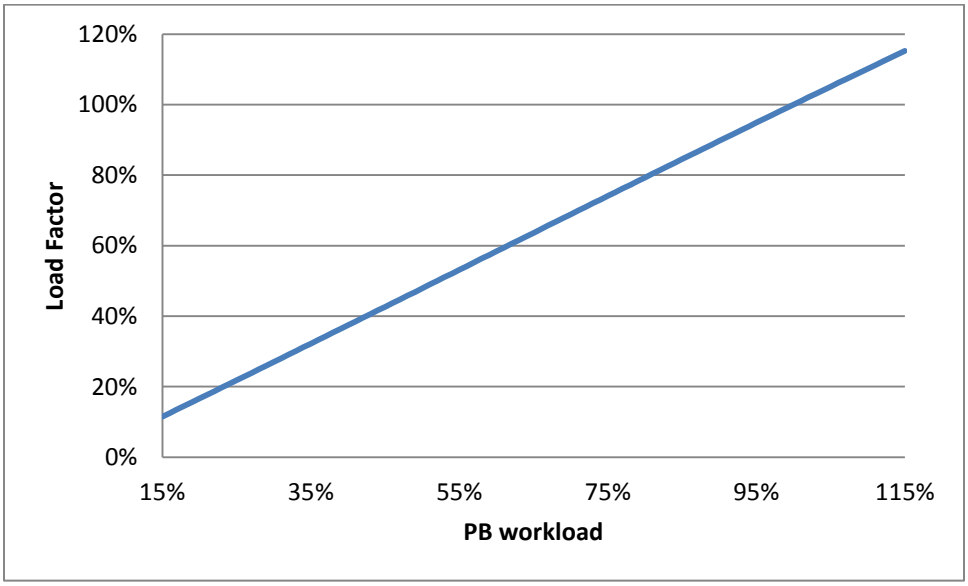

Figure 32: The variation of the partial load correction factor depending on workload of the SEGS 80 MW power block

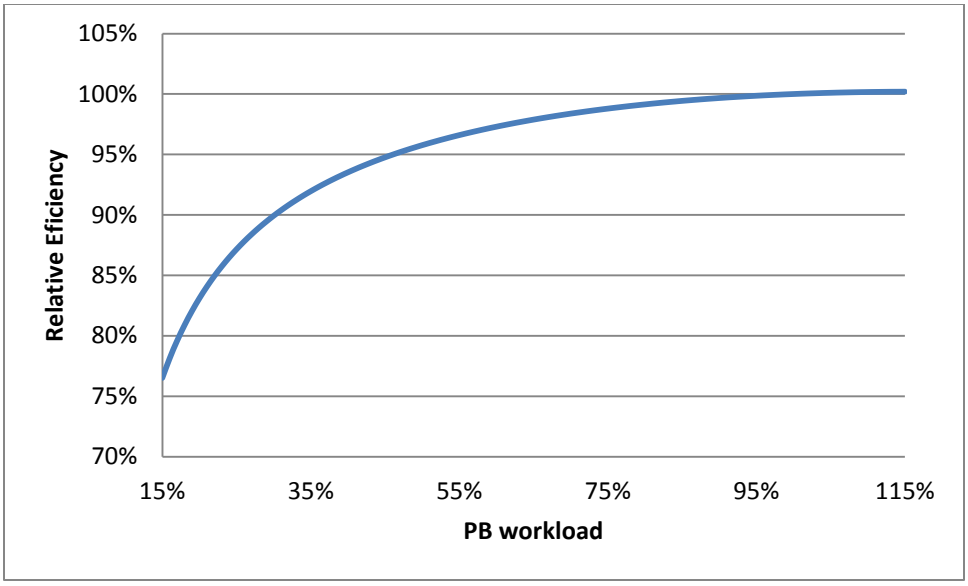

Figure 33: The variation of relative efficiency (partial worklad efficiency to design load efficiency) depending on the workload

In addition, Bartlett introduced an equation to predict the relation between the conversion efficiency and the steam flow rate. For instance, the conversion efficiency of the SEGS VI power block is [58, 59]:

$$\eta_{turbine} = \left(0.809 + 0.409\, f_{ld} - 0.218\, f_{ld}^2\right)\eta_{turbine\_dgn} \tag{101}$$

These two methods agree well with each other when the workload is larger than 30%, but mismatch under small load conditions. The first method is used since it is derived from real operation data.

The temperature correction factor has incorporated the performance variation caused by the cooling temperature of waste steam. It is estimated using cooling correction factors and the cooling temperature, as shown:

$$\eta_{PB\_temp} = f_{TC0} + f_{TC1}T + + f_{TC2}T^2 + f_{TC3}T^3 + f_{TC4}T^4 \quad (102)$$

Depending on the type of cooling tower, the temperature may refer to the ambient temperature when dry-cooling type is adopted or wet bulb temperature if wet-cooling is used.

2.3.3.3 Gross Electricity Generation

The operating capacity of power blocks are limited by their minimum and maximum design loads. Their effective thermal energy receiving rates are restrained by:

$$\dot{Q}_{PB\_gross\_min} = \dot{Q}_{PB\_dgn} \cdot F_{PB\_min} + \dot{Q}_{PB\_start} \quad (103)$$

$$\dot{Q}_{PB\_gross\_max} = \dot{Q}_{PB\_dgn} \cdot F_{PB\_max} + \dot{Q}_{PB\_start} \quad (104)$$

Thus, the minimum and maximum electricity generation rates are:

$$E_{PB\_\min} = Q_{PB\_dgn} \cdot \eta_{Gross\_dgn}\eta_{PB\_ld\_\min}\eta_{PB\_temp} \quad (105)$$

$$E_{PB\_\max} = Q_{PB\_dgn} \cdot \eta_{Gross\_dgn}\eta_{PB\_ld\_\max}\eta_{PB\_temp} \quad (106)$$

The minimum and maximum thermal energy limitations divide the power block load into three sections: the idle section, the regular operation section, and thermal energy waste section.

When the received thermal energy is lower than the minimum requirement, power block stays idle, and all the received thermal energy is dumped.

$$E_{PB\_gross} = 0 \tag{107}$$

$$Q_{PB\_dump} = Q_{ThE2PB} \tag{108}$$

When the received thermal energy ranges between the minimum and maximum requirements, the power block converts all the received thermal energy to electricity.

$$E_{PB\_gross} = Q_{PB\_dgn} \cdot \eta_{gross\_dgn} \eta_{PB\_load} \eta_{PB\_temp} \tag{109}$$

$$Q_{PB\_dump} = 0 \tag{110}$$

If the thermal energy input is more than the maximum requirement, the power block works on the maximum load, and the unconverted portion of the thermal energy is wasted. The generated electricity and dumped thermal energy are:

$$E_{PB\_gross} = Q_{PB\_dgn} \cdot \eta_{gross\_dgn} \eta_{PB\_ld\_\max} \eta_{PB\_temp} \tag{111}$$

$$Q_{PB\_dump} = Q_{ThE2PB} - Q_{PB\_dgn} \cdot F_{PB\_dgn\_\max} \tag{112}$$

Figure 34 shows the flow chart of the power block model:

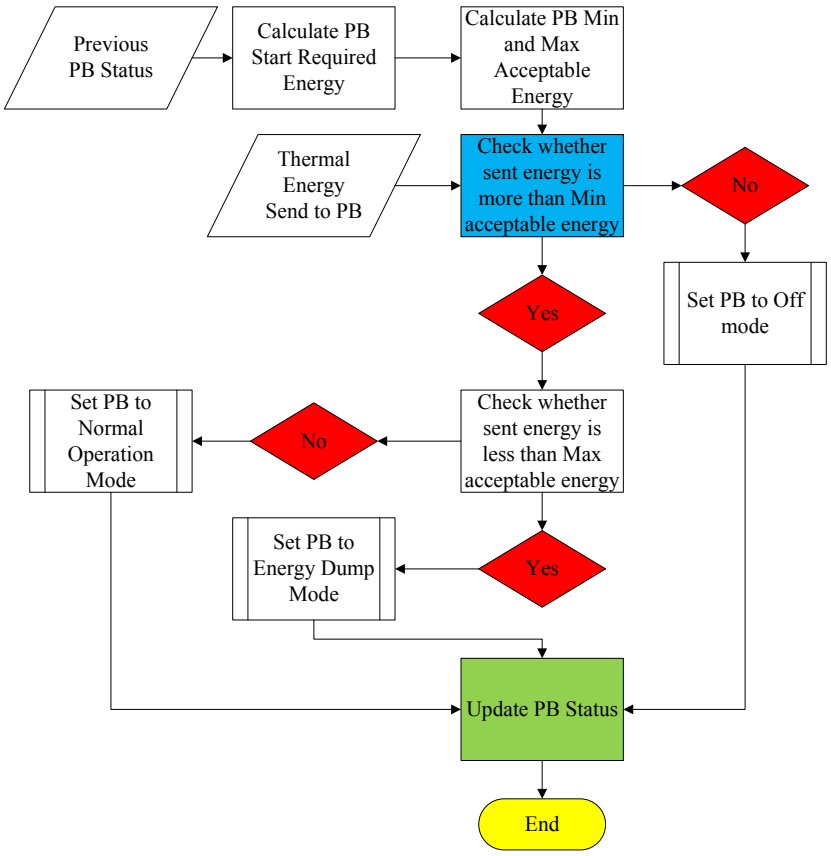

Figure 34: Flow chart of the power block calculation procedure

2.3.3.4 Net Electricity Generation

The net electricity generation is the gross electricity generation minus the electricity consumptions of a CSP plant during its operation period.

$$E_{PB\_net} = E_{PB\_gross} - \sum_{Each\_system} E_{parasitic} \tag{113}$$

2.3.4 Adjunct Electricity Consumption Model

A CSP plant needs energy to keep its devices working during operating, or keep them in appropriate status when the plant is idle. These devices include pumps, fans, sensors, auxiliary heaters, lights and so on. Previous research indicates that the total consumption may range from 10% to 20% of the produced electricity. This electricity consumption is regarded as adjunct electricity consumption.

Due to the uncertainties of specific devices, a general coefficient-based method is used to estimate the electricity consumptions. Each system's electricity consumption is estimated separately, and the total electricity consumption is the sum of them [49].

$$E_{Adj\_consumption} = E_{SF} + E_{PB} + E_{STG} \tag{114}$$

Electricity is used to drive sensors, motors and pumps in solar fields. Sensors and motors track the sunlight direction and adjust the positions of SCAs. Theirs electricity consumptions are:

$$E_{SF\_driver} = \begin{cases} N_{SCA} \cdot E_{SCA} & \text{with sunlight} \\ 0 & \text{without sunlight} \end{cases} \tag{115}$$

HTF main pumps keep HTF flowing between the solar field, the storage system and the power block. Its power consumption is estimated with the HTF flow rate and pump's load coefficients when solar field is operating.

$$\begin{cases} E_{SF\_pump} = E_{pump\_dgn}\left[F_{SF0} + F_{SF1}\left(\dfrac{E_{SF\_ThE}}{E_{SF\_ThE\_dgn}}\right) + F_{SF1}\left(\dfrac{E_{SF\_ThE}}{E_{SF\_ThE\_dgn}}\right)^2\right] & \text{with sunlight} \\ E_{SF\_pump} = 0 & \text{without sunlight} \end{cases} \quad (116)$$

During non-operation period, an antifreeze pump operates to drive HTF flowing in the solar field with constant power. It helps to prevent HTF from solidifying and clogging. Its electrical requirement is constant and proportional to the solar field size.

$$\begin{cases} E_{SF\_auxpump} = F_{SF\_auxpump} \cdot A_{SF\_area} & \text{without sunlight} \\ E_{SF\_auxpump} = 0 & \text{with sunlight} \end{cases} \quad (117)$$

A solar field's adjunct electricity is the sum of electricity consumptions from drivers, main pumps and antifreeze pumps.

$$E_{field} = E_{SF\_driver} + E_{SF\_pump} + E_{SF\_auxpump} \quad (118)$$

A storage system consumes electricity to pump or heat the stored TES. The electrical pump drives TES circling between storage tanks and heat exchangers to receive or extract thermal energy. Its electrical consumption is:

$$\begin{cases} E_{ST\_pump} = E_{pump\_dgn}\left[F_{ST0} + F_{ST1}\left(\dfrac{E_{ST\_ThE}}{E_{PB\_ThE\_dgn}}\right) + F_{ST2}\left(\dfrac{E_{ST\_ThE}}{E_{PB\_ThE\_dgn}}\right)^2\right] & \\ E_{ST\_pump} = 0 & \text{without thermal energy exchange} \end{cases} \quad (119)$$

The auxiliary heater heats TES if needed. Its energy consumption is stated in the thermal energy storage model section. The storage system's electricity consumptions are:

$$E_{STG} = E_{STG\_pump} + E_{STG\_aux} \quad (120)$$

Maintenance staff and support facilities are necessary for plants' operation. They account for lighting, building loads and devices, and other loads that are required to maintain plant operation. It is loaded 24 hours per day and seven days per week. Its electricity consumption is linearly correlated to the power block size:

$$E_{PB\_fixed} = f_{PB\_fixed} \cdot P_{PB\_size} \tag{121}$$

Balance of plant's load accounts for all electricity consumption in power block system, it is:

$$\begin{cases} E_{PB\_bal} = E_{PB\_size}\left[f_{PB0} + f_{PB1}\left(\dfrac{E_{PB\_eproduce}}{E_{PB\_eproduce\_dgn}} \right) + f_{PB2}\left(\dfrac{E_{PB\_eproduce}}{E_{PB\_eproduce\_dgn}} \right)^2 \right] \\ E_{ST\_pump} = 0 \qquad \text{if no electricity production} \end{cases} \tag{122}$$

The PB's electricity consumption is the sum of the fix and the balance electricity consumptions.

$$E_{PB} = E_{PB\_fixed} + E_{PB\_bal} \tag{123}$$

2.3.5 Heat Exchanger Model

One or more heat exchangers are used in parabolic trough systems. They may be used as the intermediary between solar field and storage system for the indirect type system, and between HTF and cooled steam in power block. Its size is determined by the design duty and temperature drops.

The count-flow type heat exchanger is used because it has higher cold side outlet temperature compared with parallel-flow type heat exchanger. The sketch of temperature distribution in heat exchanger is shown in Figure 35.

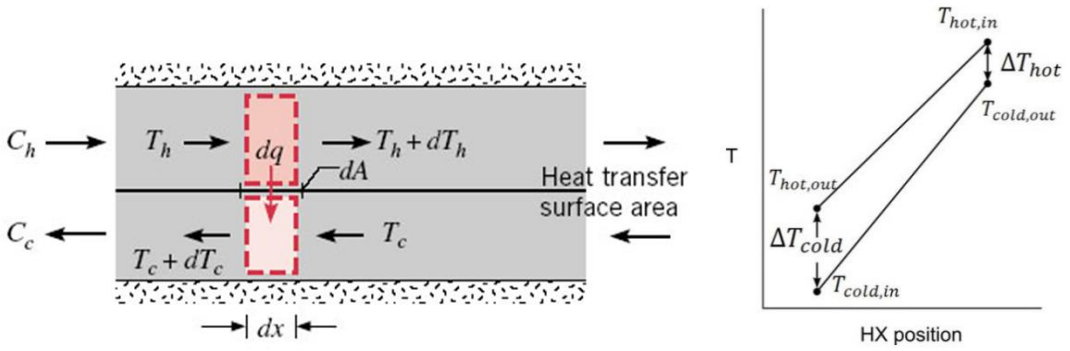

Figure 35: Diagram of temperatures in a count-flow heat exchanger vary with the position [60]

Because a solar field's thermal energy production is not always stable, heat exchangers in a CSP plant frequently endure off-design working situations, and therefore the operating parameters may not conform to the design values. The effectiveness – NTU method is able to predict the heat exchange rate and the outlet temperature. However, its result is strongly correlated with the heat exchanger layout, heat transfer coefficient and contact area. These values are usually not available. Therefore, another method was devised to predict heat exchangers' performance. This method assumes the outlet

temperature is equivalent to the design value, and the heat loss rate is one percent of the exchanged thermal energy. The heat exchange rate of the heat and cool fluids are:

$$\dot{Q}_{Exchange\_hot\_side} = \dot{m}_{hot\_fluid}(h_{h,i} - h_{h,o\_dgn}) \tag{124}$$

$$\dot{Q}_{Exchange\_cold\_side} = \dot{Q}_{Exchange\_heat\_side} - \dot{Q}_{HL} \tag{125}$$

The heat loss during heat exchange and energy received by cool fluid are:

$$\dot{Q}_{HL} = \dot{Q}_{Exchange\_hot\_side} \cdot 1\% \tag{126}$$

$$\dot{Q}_{Exchange\_cool\_side} = \dot{Q}_{Exchange\_heat\_side} \cdot 99\% \tag{127}$$

Thus, the mass flow rate of the cool fluid is:

$$\dot{m}_{cool\_fluid} = \frac{\dot{Q}_{Exchange\_cool\_side}}{h_{c,o\_dgn} - h_{c,i}} \tag{128}$$

2.3.6 Mixer Model

After heated HTF transfers its thermal energy to a storage system or a power block, the depleted HTF will be collected, and then returned to the solar field. The cold HTF temperature in solar field is same as the temperature of depleted HTF. The depleted HTF comes from the storage system or the power block, or both, is combined with the heated HTF from the as shown in Figure 36.

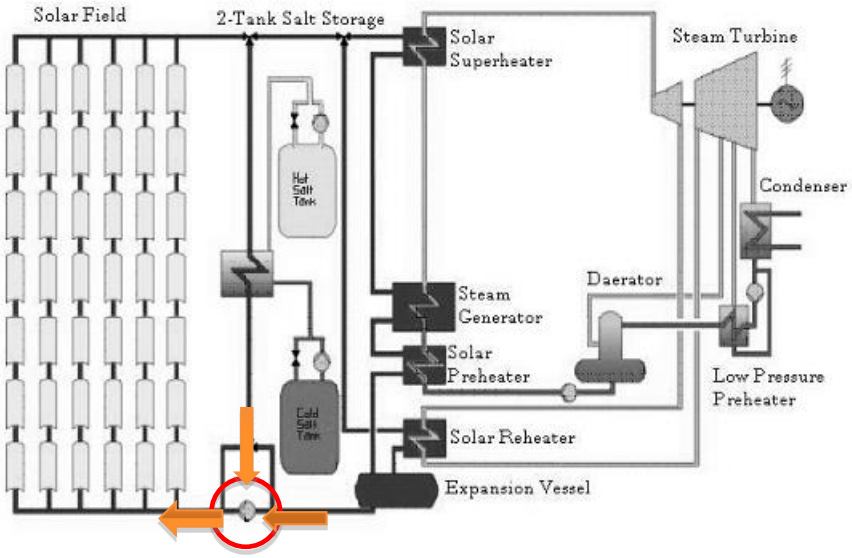

Figure 36: Diagram of the mixer in a CSP plant

The depleted HTF temperature is calculated as:

For indirect system:

$$h\left(T_{depleted\_HTF}\right)=\frac{m_{HTF\_STG}h\left(T_{HTF\_from\_exchanger}\right)+m_{HTF\_PB}h\left(T_{HTF\_from\_PB}\right)}{m_{HTF\_STG}+m_{HTF\_PB}} \quad (129)$$

For direct and two-tank system:

$$h\left(T_{depleted\_HTF}\right)=\frac{m_{HTF\_STG}h\left(T_{cold\_tank}\right)+m_{HTF\_PB}h\left(T_{HTF\_from\_PB}\right)}{m_{HTF\_STG}+m_{HTF\_PB}} \quad (130)$$

2.3.7 General Operation Strategy Model

Once the solar power plant is equipped with a storage system, its electricity generation would be flexible both in timing and loads. Therefore, a set of rules are necessary to determine the plant's operation and coordinate with each system. Two types of strategies are discussed in this chapter: the greedy strategy and longtime operation strategy.

2.3.7.1 Greedy Strategy

The greedy strategy emphasizes on maximizing electricity production. Its goals are listed according to priority as following:

1. Keeping the power block operating when there is enough thermal energy. The thermal energy could come from the solar field, the thermal storage system or both;
2. The work load of power block is set in the way that minimizing wasted thermal energy;
3. The power block is set to design load;

These requirements are also shown in Figure 37.

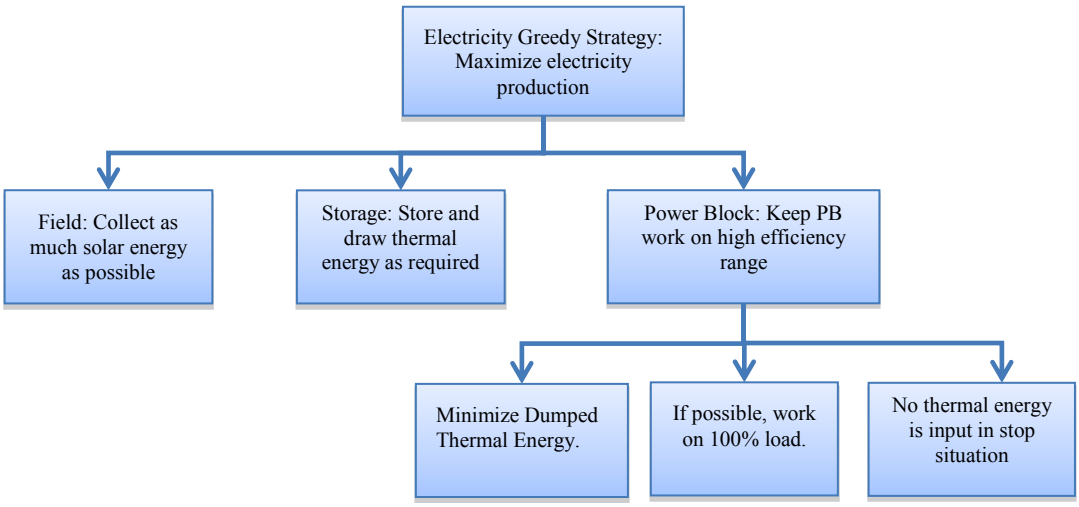

Figure 37: Demonstrate of the requirements of the electricity greedy strategy

Q_{2PB_avil} is defined as the thermal energy available to the power block, and it is calculated as:

$$Q_{2PB\_avil} = Q_{SF} \cdot \eta_{SF2PB} + Q_{STG} \cdot \eta_{STG2PB} \quad (131)$$

The value of thermal energy determines whether to keep power block working or not. If it is enough to supply minimal load of the power block, then the power block is set to operation status. Otherwise, the power block is in idle status. The storage system stores or extracts the balance thermal energy from the solar field and the power block if possible. Figure 38 shows detailed flow chart of this strategy.

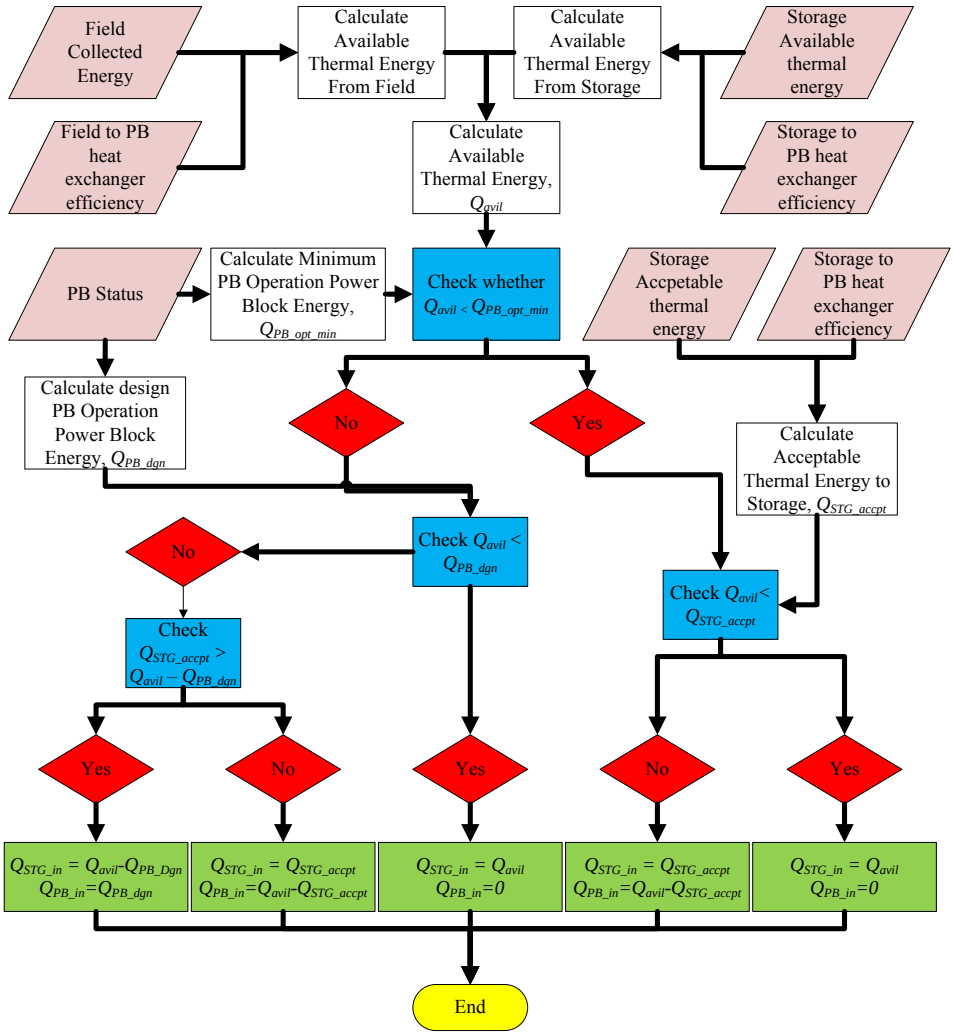

Figure 38: Flow chart of the electricity greedy strategy

2.3.7.2 Longtime Operation Strategy

The design of this strategy concentrates on maximizing power block's operating time and minimizing the idle period. With this strategy, minimal electricity from grid is consumed. The flow chart is shown in Figure 39.

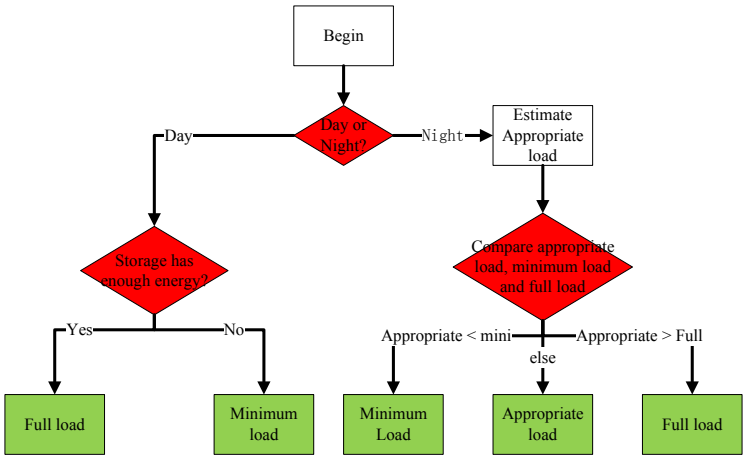

Figure 39: Flow chart of the longtime operation strategy

The following assumptions are used to calculate the desired work load:

1. The minimum workload of power block is 20%;
2. The 'enough energy' indicates the storage capacity that can support three hours operation;
3. Two hours is needed to heat up the solar field.

Therefore, the appropriate load is calculated as:

$$F_{appropriate} = \frac{available\_storage\_capacity(hour)}{next\_sunset\_time - current\_time + 2} \tag{132}$$

2.4 Post Processing Routine

The post processing routine works on processing the data which is generated by the calculation routine. Its functions are: summarize performance data and generate formatted reports.

2.4.1 Monthly, Yearly and Net Electricity Generation

The hourly net electricity production is the difference between the hourly gross production and adjunct consumption:

$$E_{PB\_net\_hour} = E_{PB\_net\_hour} - E_{Adj\_consumption} \tag{133}$$

Monthly and yearly gross and net electricity production are calculated by summing up each hour's gross or net electricity production:

$$E_{gross\_month\_n} = \sum_{\text{month n begin}}^{\text{month n end}} E_{PB\_gross\_hour} \tag{134}$$

$$E_{net\_month\_n} = \sum_{\text{month n begin}}^{\text{month n end}} E_{PB\_net\_hour} \tag{135}$$

$$E_{gross\_year\_1} = \sum_{1}^{12} E_{gross\_month\_n} \tag{136}$$

$$E_{net\_year\_1} = \sum_{1}^{12} E_{net\_month\_n} \tag{137}$$

In addition, the annual adjunct consumption is the difference between the yearly gross and net electricity productions:

$$E_{Adj\_consumption\_year\_1} = E_{gross\_year\_1} - E_{net\_year\_1} \quad (138)$$

2.4.2 Electricity Production during Plant's Lifetime

With the aging of the plant, degradation and deterioration of components might cause the electricity production decreasing with time. A degradation factor is used to describe the factor of aging:

$$E_{parasitic\_year\_n} = E_{parasitic\_year\_1}\left(1 - F_{\deg radation}\right)^{n-1} \quad (139)$$

2.5 Summary

The numerical solar field model predicts the performance in both the steady state and the transient state. The storage model serves to estimate the storage tank's volume and detailed geometry then simulates the operation of the storage tanks. The power block model employs the empirical method to estimate both in-design and off-design performance. In addition, two set of control strategies which are used to coordinate the operation of each system are discussed.

The performance model predicts each system's performance for a certain period of time. It can be used as a determination tool to estimate the performance under different design/weather/control strategy conditions.

3. DEVELOPMENT OF THE FINANCIAL MODEL[*]

3.1 Introduction

Financial payback is critical to determine whether a project is feasible. A financial model is used to estimate a project's lifetime economic performance based on its lifecycle cash flows and other financial metrics. The financial model was developed with the assumption that the simulated CSP plant was operated under commercial power purchase agreement (PPA) mode because typical CSP plants were constructed for utility operation. The acquired LCOE (Levelized Cost of Energy) from the model is the lowest price which meets all the financial and payback requirements.

3.2 Operation Cash Flows

The installed cost, electricity sale revenue, operation and maintenance cost (O&M cost), salvage cost, taxes, loan and incentives are components of the major cash flows of a CSP plant, as shown in Figure 40.

[*] Part of the research in this chapter is reprinted with permission from "Trough Type Concentrating Solar Power Plant Cost Assessment With Component Scaling" by Luo, Jun, Michael Schuller, and Thomas Lalk, 2012, *ASME 2012 6th International Conference on Energy Sustainability collocated with the ASME 2012 10th International Conference on Fuel Cell Science, Engineering and Technology*. Copyright 2012 by American Society of Mechanical Engineers

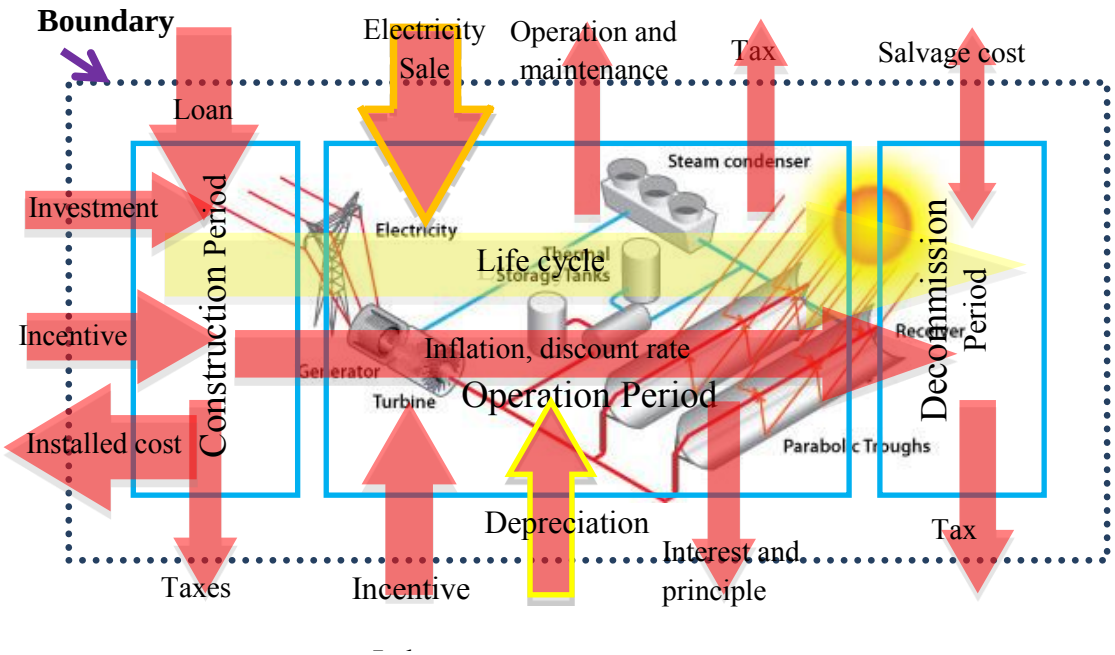

Figure 40: Diagram of cash flows during the lifecycle of a CSP plant

3.2.1 Electricity Sale Revenue

Electricity sale revenue is the major income of a CSP plant. The annual revenue $R_{elec\_sale,i}$ is calculated from the electricity sale price, $c_{elec,i}$ which is determined from the PPA, and the electricity production, $P_{elec,i}$ as shown in the following equation:

$$R_{elec\_sale,i} = P_{elec,i} c_{elec,i} \tag{140}$$

3.2.2 Installed Cost

The total investment before electricity production is called the installed cost. The installed cost is comprised of the direct cost and indirect cost. The direct cost is the cost associated with the specific components or systems (solar field, storage system and power block); the indirect cost is the remaining costs which cannot be classified into any specific category.

3.2.3 Direct Cost

This cost is estimated respectively for the solar field, thermal storage, and power block systems.

$$C_{direct} = C_{SF} + C_{STG} + C_{PB} \tag{141}$$

3.2.3.1 Solar Field Cost

Before 2013, the operating CSP plants are no larger than 80 MW around the world [61], accurate cost data for a solar field of varied sizes, especially for large scale ones is not available. However, the costs data can still be predicted by other indirect methods, such as the estimates based on materials and labor costs or using exponent scaling methods; whereby, the cost of the solar field is determined by multiplying a cost associated with a reference plant by the ratio of the area of the proposed plant to the reference plant area (scaling factor) raised to some exponent.

Several sources provide estimates based on various exponents for the cost of solar fields. The FSI model, which is developed by the mirror supplier for the Luz plant, uses an

exponent factor of 0.7 in its cost model [29]. In the SAM program, a linear cost model is used. Its exponent factor is one [43]. The European Commission recommends the value of exponent factor to be 0.83[62]. From regress calculation of field sizes for different sized power plants, an exponent factor of 0.8 is obtained [63].By using the estimates from several sources [64], for a regression analysis resulted in an average value of 0.8 for the exponent factor.

The scaling method with an exponent factor of 0.8 was used since it is a reasonable value from the scaling done in several sources. The cost of solar field is estimated as the cost of the site improvement, solar field devices and HTF sub-system, as shown in the following equation.

$$C_{SF} = C_{Site\_Improvement} + C_{SF\_devices} + C_{HTF\_System} \tag{142}$$

A hypothetical 100 MWe CSP plant in southwest Arizona is used as the reference power plant since its detailed cost data is available and up to date [43]. Then costs associated with the various sub-systems, of a proposed plant, of any size, can be calculated from the following equations, where the costs from the reference plant are scaled with the scale factor raised to the 0.8 power:

$$C_{\text{Site\_Improvement}} = \$28/m^2 \times \left(\frac{A_{Project\_Size}}{854000m^2} \right)^{0.8} \tag{143}$$

$$C_{SF\_devices} = \$295/m^2 \times \left(\frac{A_{Project\_Size}}{854000m^2} \right)^{0.8} \tag{144}$$

$$C_{HTF\_System} = \$90/m^2 \times \left(\frac{A_{Project\_Size}}{854000 m^2} \right)^{0.8} \quad (145)$$

3.2.3.2 Storage System Cost

The SAM model uses a linear model to estimate the storage system cost with \$90/kWt, and its documentation provides a scaling method with scaling exponent factors range from 0.5 to 1 for different components.

Rather than using a linear model, storage system cost could be estimated based on the detailed material and labor costs. This method is used in the model reported herein, since it may provide more accurate result.

The storage tank shell's cost is estimated based on the material and unit cost. The unit price for carbon steel is \$4.4/kg, including material, fabrication, and shipping. The tank shell's weight, m_{tank_shell}, and cost, c_{tank_shell}, are calculated as:

$$m_{tank\_shell} = \rho_{steel} \left[2\pi r_{tank} h_{tank} t_{surf} + \pi r_{tank}^2 \left(t_{btm} + t_{top} \right) \right] \quad (146)$$

$$c_{tank\_shell} = c_{steel\_unit} m_{tank\_shell} \quad (147)$$

Calcium silicate blocks are used for the walls and roof insulation, and a corrugated aluminum jacket covers the insulation for weather protection. The insulation cost, c_{tank_ins} varies linearly with its thickness, increasing from \$160/m^2 at a thickness of 300 *mm* to \$235/m^2 at 500 *mm* [51].

$$C_{\tan k\_ins} = (160 + \frac{x-300}{200} \cdot 75)[\int_0^H 2\pi(r + \frac{(t_{\text{shell\_btm}} - t_{\text{shell\_top}})h}{H} + t_{\text{shell\_top}})dh + f_{roof}\pi r_{\text{tank}}^2] \quad (148)$$

The tank foundation consists of several layers, from bottom to top, there are: concrete foundation, thermal foundation, foamglass insulation, insulating firebricks, and a steel slip plate, as illustrated in Figure 41. The foundation costs are the sum of costs of these layers [51].

$$C_{\text{Foundation}} = C_{\text{Concrete}} + C_{\text{Ins\_concrete}} + C_{\text{Foam\_glass\_ins}} + C_{\text{Ins\_firebrick}} + C_{\text{Per\_ring\_wall}} + C_{\text{Steel\_slip}} + C_{\text{Cooling\_pipe}} \quad (149)$$

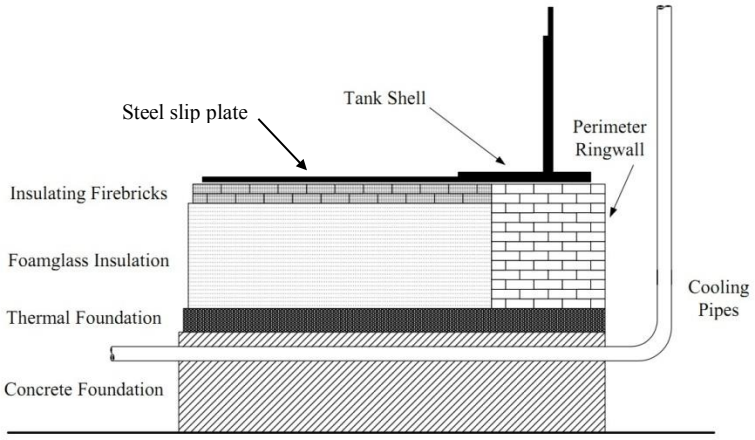

Figure 41: Diagram of the thermal storage tank foundation [51]

A concrete slab has a fixed thickness of 610 *mm*. For each cubic meter of concrete, 73 *kg* of reinforce steel is used to improve the mechanical strength. The prices and installation hours for the concrete and reinforce steel are \$85/m^3, \$0.80/kg and 1.3hr/m^3, 0.022hr/kg respectively. Therefore, the cost of concrete can be calculated via equation 150.

$$c_{concrete} = \pi r_o^2 t_{concete}[c_{unit\_concret} + h_{unit\_concrete} c_{lbr} + w_{steel}(c_{unit\_steel} + h_{unit\_concrete} c_{lbr})] \quad (150)$$

The thickness of insulating concrete slab, $t_{ins\_concrete}$, is increasing linearly with the tank's operating temperature. Its unit cost and installation time are \$100/m^3 and 1.3 *hr/m*^{3}.

$$t_{Ins\_concrete} = 0.23 \frac{T_{tank\_dgn} - 563.15}{275} \quad (151)$$

$$c_{ins\_concrete} = \pi r_o^2 t_{ins\_concete}(c_{unit\_ins\_concrete} + h_{unit\_concrete} c_{lbr}) \quad (152)$$

The thickness of the foam glass insulation, $t_{\text{foam\_glass}}$, is inversely proportional to the operating temperature, T_{tank_dgn}. Its unit cost, $c_{\text{foam\_glass\_ut}}$, including labor is \$356/m^3. The equations for the thickness and cost are given below.

$$t_{\text{foam\_glass}} = 0.4 - 0.1 \frac{T_{tank\_dgn} - 563.15}{275} \quad (153)$$

$$c_{\text{foam\_glass\_ins}} = \pi r_o^2 t_{\text{foam\_glass}} c_{\text{foam\_glass\_ut}} \quad (154)$$

The thickness of insulating firebrick, t_{ins_brick}, increases linearly with the design temperature of the storage system. The cost of brick is \$1 each, and the size of each brick is 230×115 ×75 *mm*^{3}. Installation hour is rated as 0.1 *hour/brick*.

$$t_{ins\_brick} = 0.165 \frac{T_{tank\_dgn} - 563.15}{275} \quad (155)$$

$$c_{\text{ins\_brick}} = \frac{\pi r_o^2 t_{\text{ins\_brick}}}{v_{brick}} \left(c_{\text{firebrick\_ut}} + h_{unit\_brick} c_{lbr} \right) \quad (156)$$

The height of the perimeter ring wall is the sum of the thicknesses of foam glass and insulating firebrick. In the radial direction, the thickness of bricks is one meter. Its labor hour is 0.33 *hr/brick*. The cost of the perimeter ring wall is:

$$c_{\text{per\_ring\_wall}} = \frac{\pi(2r_o+1)(t_{\text{ins\_brick}}+t_{foam\_glass})}{v_{brick}}\left(c_{\text{unit\_brick}}+h_{brick\_ut}c_{lbr}\right) \tag{157}$$

The steel slip plate has a fixed thickness of 6 *mm*. its price is \$1.3/kg and needs 0.22hr/kg for installation. The cost of the steel plate is:

$$c_{\text{steel\_slip}} = \pi r_o^2 t_{\text{steel\_slip}}\rho_{steel}\left(c_{\text{firebrick\_ut}}+h_{brick\_ut}c_{lbr}\right) \tag{158}$$

The schedule 20 carbon type steel pipes are used for foundation cooling pipes. Its length is $8r_o$, its cost is estimated as \$2.2/kg and its installation hour is 1.15 *hour/m*. The cost of the cooling pipes is:

$$c_{\text{Cooling\_pipe}} = 8r_o(f_{pipe\_length\_weight}c_{pipe\_ut}+h_{cooling\_pipe\_ut}c_{lbr}) \tag{159}$$

Storage media contributes to a large portion of the storage system cost. For example, the nitrate salt, which is the commonly used material for the two-tank system, its cost, including material price, transportation, labor and handling at site is \$0.5/kg. The costs of quartzite rock and silica sand, which are used as the filled materials in the thermocline system, are \$0.08/kg and \$0.03/kg [65].

$$C_{TES} = m_{storage\_nitrate}c_{nitrate\_ut} \text{ For two-tank system} \tag{160}$$

$$C_{TES} = m_{st\_quartite}c_{quartite\_ut}+m_{st\_sand}c_{sand\_ut}+m_{st\_quartite}c_{quartite\_ut} \text{ For thermocline system} \tag{161}$$

The cost for the oil to salt heat exchanger is linearly correlated with the contact surface area $S_{exchanger}$. Its cost is \$146/m^2. Installation labor hour is 0.44 *hr/m*^{2}. The contact area and cost, $C_{exchanger}$, are:

$$S_{exchanger} = \frac{max(SM-1,1)\cdot Q_{PB\_ThE\_dgn}}{\Delta T_{exchanger\_avg} k_{exchange\_contact}} \tag{162}$$

$$C_{exchanger} = S_{exchanger}(c_{exchanger\_ut} + h_{exchanger\_ut} c_{lbr}) \tag{163}$$

The cost of nitrate salt pumps used in storage systems is obtained from the budget of the Solar Two and Solar Tres projects. The unit costs are derived by regression analysis, and are shown in following equations [51].

$$C_{\text{pump}} = C_{\text{pump,hot}} + C_{\text{pump,cold}} \tag{164}$$

$$C_{\text{Pump,hot}} = N_{\text{Pump,hot}} P_{\text{motor\_power,hot}} 14720 \cdot P_{\text{motor\_power,hot}}^{(-0.4488)} \tag{165}$$

$$C_{\text{Pump,cold}} = N_{\text{Pump,cold}} P_{\text{motor\_power, cold}} 5512 \cdot P_{\text{motor\_power,cold}}^{(-0.1845)} \tag{166}$$

The remaining cost which includes the piping, electricity heat traces and thermal insulation are estimated as 10% of the other components costs in the storage system.

3.2.3.3 Power Block Cost

The State-of-the-Art Power Plant (SOAPP, product of Electric Power Research Institute) software's prediction is used in the power block cost estimation [45].

The cost of power block and balance of plant are rated separately. A power block includes steam turbines, generators, and its auxiliaries – feed water devices and

condensate systems. The balance of plant includes general balance of plant equipment, water condenser and cooling tower system, water treatment system, fire protection system, piping, the compressed air system, the closed cooling water system, plant control devices, other electrical equipment, and cranes and hoists [45]. Their respective costs are:

$$C_{power\_block} = \frac{1275.8}{1000} \times P_{plant}^{-0.3145} \tag{167}$$

$$C_{\text{Balance}} = \frac{461.33}{1000} \times P_{plant}^{-0.1896} \tag{168}$$

$$C_{PB} = C_{power\_block} + C_{bal} \tag{169}$$

3.2.4 Indirect Cost

Costs that could not be tied to a specific subsystem account for the indirect cost. It includes design and construction costs, land acquisition cost and sales tax.

$$C_{\text{Indirect}} = C_{\text{Direct}} \cdot (P_{\text{dgn\_construction}} + P_{\text{land\_acq}} + P_{\text{sale\_tax}}) \tag{170}$$

3.2.5 O&M Cost

The O&M cost contributes to a majority of the costs during a plant's operation period, since there is few or none fuel cost, the O&M cost only takes up a small portion in a CSP plant. The O&M cost includes: operational labor, service contracts, utilities, materials, and miscellaneous items.

Operational personnel operate solar power plants. The personnel include administrators, operators, and plant maintenance personnel. Service contracts include cost specifications for computers, office equipment, grounds and facility cleaning, mirror washing, and water treatment. These costs are almost stable once the size of the power plant is determined. Therefore, an exponent factor of 0.2 is assigned to estimate these costs for different power plants.

The utilities, materials and maintenance costs account for the resources consumed during operation. The resources include natural gas, water, and auxiliary power. They have a linear relationship with the electricity production.

The Arizona CSP plant is used as the reference plant. The sum of labor and service costs is \$69/(kWe·year), the utility cost is \$2.5/(MWe·h), and the material and maintenance costs are \$34.5/kWe-year. The O&M cost is summarized as:

$$C_{\text{lbr\_service}} = \left(\$69000 / MWe - year\right) P_{\text{plant}} \times \left(\frac{P_{\text{plant}}}{110\ MWe} \right)^{0.2} \tag{171}$$

$$C_{\text{Material\_Maintenance}} = \left(\$34500 / MWe\right) \times P_{\text{plant}} \tag{172}$$

$$C_{\text{Utility}} = \$2.5 / MWh \cdot E_{\text{annual\_gen}} \tag{173}$$

3.2.6 Salvage Value and Depreciation

Salvage value is the remaining value of an asset after been used. For a CSP plant, it is the value after it has been fully depreciated. Depreciation is the loss of value of physical properties with passage of time and usage. It is an accounting concept that establishes an

annual deduction of before tax income. Therefore, the passing time and usage of properties can be reflected in a firm's financial statement.

Depreciation is a virtual cash flow that reflects the yearly value loss of an asset during its life. It affects the after tax cash flows by changing the taxable income, but having no impact on the before tax cash flows. A firm can only begin to depreciate a property after it has been in service for use and producing income. Depreciation ends when the cost of placing an asset has been fully recovered or sold, whichever occurs first.

The depreciation value is the difference between the installed cost and the salvage cost. The depreciation value of each year is:

$$C_{depr,n} = F_{depr,n}(C_{installed\_cost} - C_{salv}) \tag{174}$$

It is assumed the construction period begins at year zero and ends at year one. Thus, the electricity production and depreciation starts in year one.

Different depreciation methods have been adopted in history. Modified Accelerated Cost Recovery System (MACRS) is based on previous Accelerated Cost Recovery System (ACRS) in service for the depreciation of tangible property placed in service after year 1986 in U.S.[66]. And there are other methods, such as straight-line and declining balance methods, are also used in some cases.

3.2.6.1 MACRS Depreciation Method

Solar energy property is eligible for a MACRS cost recovery period of five years in the U.S. Different depreciation recovery rate may be used in calculation based on the service time of the asset. These rates are shown in Table 9.

Table 9: MACRS 5-year type depreciation recover rate

Year	Depreciation begins at				
	1st -MidQuarter	2nd -MidQuarter	3rd -MidQuarter	4th -MidQuarter	Half Year
1	0.35	0.25	0.15	0.05	0.2
2	0.26	0.3	0.34	0.38	0.32
3	0.156	0.18	0.204	0.228	0.192
4	0.1101	0.1137	0.1224	0.1368	0.1152
5	0.1101	0.1137	0.113	0.1094	0.1152
6	0.0138	0.0426	0.0706	0.0958	0.0576

3.2.6.2 Straight Line Depreciation Method

The straight line depreciation method is the simplest and most often used method. Its depreciation is charged uniformly over its depreciation period. The depreciation in year *n* is calculated as:

$$C_{depr,n} = \frac{C_{installed\_cost} - C_{salv}}{T_{depreciation}} \tag{175}$$

3.3 Cost Associated with Taxes

Tax is an enforced pecuniary burden laid upon a taxpayer to support the government. As a legal entity, it may need to pay several kinds of taxes. In the financial aspect, they are all treated as expenses.

3.3.1 Income Tax

Income tax is levied by federal and states governments. For company income tax, it is based on the profits earned and allowable deductions. These allowable deductions include depreciations, tax credits, and tax exempted incentives. Several different income tax systems exist, such as progressive, proportional, or regressive taxes. For example, In the United States, the corporate federal income tax rates are progress with taxable income, and when a corporation has a taxable income greater than $18,333,333 in a tax year, federal taxes are calculated at 35% flat rate.

In the model, tax is treated like an expense, and tax allowable deductions are handled as savings. Also, because solar power companies are generally in large scale, the flat rate income tax is used, and the income tax is calculated as:

$$C_{income\_tax} = R_{taxable\_income} f_{income\_tax} = (R_{rvu} - C_{cost} - \sum C_{tax\_saving}) f_{income\_tax} \qquad (176)$$

3.3.2 Sales Tax

Sales taxes are evaluated based on purchasing or leasing of goods or services, and independent of its incomes or profits. It is calculated as applicable tax rate, f_{income_tax},

sales price, $C_{installed\_cost}$, and the applicable factor, $f_{income\_tax\_applicable}$. Tax rate varies by categories and locations, usually ranging from 1% to 10%, and it is collected at the time of purchasing only.

$$C_{sale\_tax} = f_{income\_tax} f_{income\_tax\_applicable} C_{installed\_cost} \tag{177}$$

3.4 Debt and Equity Fund

Generally, a solar project owner would not choose to fund the project with only its own capital. There are several reasons. First, the solar project is usually large and its cost is huge. Second, funding it with multiple sources may reduce project risks. Third, funding it with other sources reduces economic pressure to the owner. Last, its capital return rate may be improved when funding it with other sources.

Besides the equity fund, the other funding resources may come from loans by banks, or obtain from the sale of bonds or debentures. The costs to use external funding are paying interests, and the interest rates should be attractive to lenders. The attractiveness depends upon the offered interest rates and the project risks.

The interest paid for the borrowed money is tax deductible. It resulted in a tax saving which should be considered in the financial analysis.

In the economic model, the borrowed money amount, borrowed period and interest rate are fixed. It assumes that the owner pays the debt (principal and interest) evenly every year until all owed money is cleared. The annual payment, p_{debt_pmt}, is:

$$F_{debt} = f_{debt} F_{installed} \tag{178}$$

$$F_{equity} = F_{installed} - F_{debt} \tag{179}$$

$$p_{debt\_pmt} = \frac{F_{debt}(1+q)^n (1-q)}{1-q^n} \tag{180}$$

Where:

f_{debt} is the debt percent;

$F_{installed}$ is the total installation cost;

q is interest rate;

n is the total payback period;

F_{debt} is the total debt amount;

In year i (i is any year in payback period), the interest, $F_{\mathrm{int}erest,i}$, and paid principal $F_{debt,i}$ are:

$$F_{\mathrm{int}erest,i} = F_{debt,i-1} \cdot q \tag{181}$$

$$F_{debt,i} = p_{pmt} - F_{\mathrm{int}erest,i} \tag{182}$$

3.5 Incentive

The application of solar energy is still at an early development stage. Its electricity generation cost is much higher than the market electricity price. Therefore, incentives are important to lower the cost and motivate the development of solar energy, and finally

accomplish the stated future development goal. The incentives serve the following purposes:

1. Secure energy supply: ensure domestic energy supply, reduce import dependency;
2. Reduce pollution, improve environment condition, and help to fulfill international obligations;
3. Stimulate economy, promote local and energy related economic sectors' development;

Incentives can be classified according to its application methods. In the financial model, incentives could be established with investment, capacity or production. Also, incentives may come from different sources. Some common sources are governments (states or federal) and utility companies.

The Investment Based Incentives (IBI) is evaluated as a fraction of the installation cost, and occurs only once per project.

$$p_{IBI} = f_{IBI} F_{installed} \tag{183}$$

The Capacity Based Incentives (CBI) is the subsidy which is calculated according to the capacity. It is a one-time incentive and occurs at the beginning of the project.

$$p_{CBI} = f_{CBI} P_{capacity} \tag{184}$$

The Performance Based Incentive (PBI) is the incentive which is estimated based on the electricity production. It is a multi-time incentive and has an assigned effective period.

In the financial model, it assumes the PBI occurs at the end of each year during its effective period. The PBI for year *i* is:

$$p_{PBI,i} = f_{PBI,i} P_{gen,i} \tag{185}$$

3.6 Performance Metrics

3.6.1 Electricity Sale Price

The electricity sale price is specified in the power purchase agreement (PPA). The PPA is a long time contract between an electricity generator (provider) and a power purchaser (buyer, utility or power trader). The PPA defines all the commercial terms for the sale of electricity between these two parties.

Usually, prices for goods and services increase with time due to inflation. Figure 42 shows the annual average electricity price in the U.S. between year 2002 and 2012 [67].

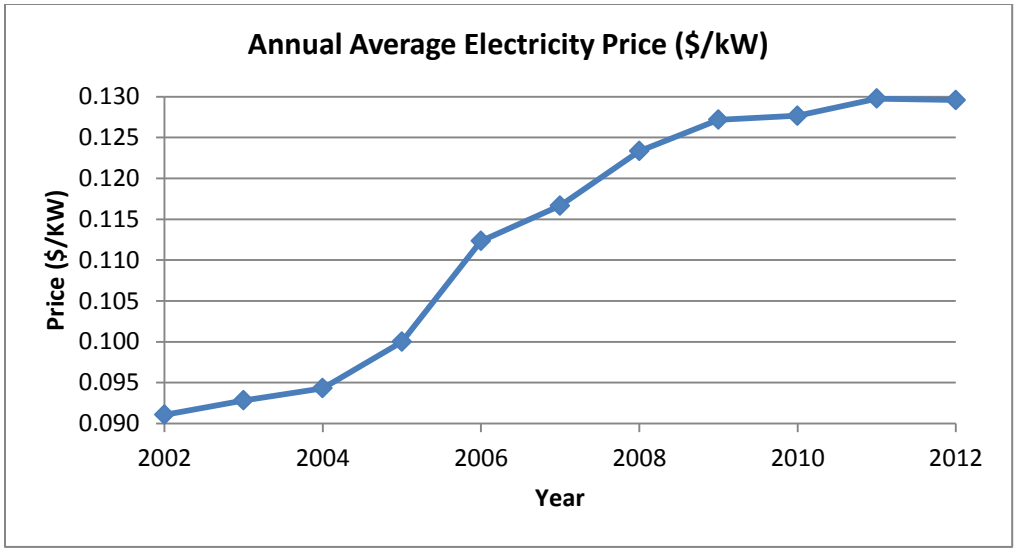

Figure 42: Annual average electricity price in U.S between year 2002 and 2012

The electricity sale price usually escalates over time. It assumes that the escalation rate is fixed in the financial analysis. The electricity price in year *i* is:

$$p_{elec,i} = p_{elec,0}\left(1+i_{PPA\_esc}\right)^{i-1} \tag{186}$$

3.6.2 Capacity Factor

The capacity factor indicates how often an electric generator operates. It is the ratio of the actual output over one year period, P_{elec}, to its nameplate capacity, $p_{capacity\_dgn}$, over every hour of the year, as shown in equation 187. For a baseload power plant, it has an average annual capacity factor of 0.7 or higher. For a solar power plant, its capacity factor is lower since its operation is intermittent.

$$f_{capacity} = \frac{P_{elec}}{p_{capacity\_dgn} \cdot 8760} \tag{187}$$

3.6.3 Debt Service Coverage Ratio (DSCR)

The DSCR is the ratio of yearly cash revenue, $C_{gross\_income,i}$, to total debt payment, including interest, $C_{interest,i}$, principal, $C_{principle,i}$, and leasing payment. It is used to measure a firm's ability to produce enough revenue to cover its debt payment. From the lender's perspective, it may represent the system's ability to resist default risks. High DSCR makes it easier for the owner to obtain a loan. Commercial banks or other lenders may require a minimum DSCR to prevent load default. For a solar power plant, the DSCR is calculated as:

$$DSCR_i = \frac{C_{gross\_income,i}}{C_{debt,i}} = \frac{p_{sale\_price,i} P_{elec\_generation,i}}{C_{principle,i} + C_{interest,i}} \tag{188}$$

3.6.4 Levelized Cost of Energy (LCOE)

LCOE is the price at which electricity must be sold to break even over the system's assumptive economic lifetime. It is the net present value in terms of the generated electricity price. It could be used for the comparsion of various generation options. The LCOE could be either nominal LCOE or real LCOE, depends on the discount factor used[66]. The LCOE is calculated as:

$$LCOE = \frac{\sum_{0}^{n} \frac{C_{ATCF,i}}{(1+f_{dsct})^{i}}}{\sum_{1}^{n} \frac{P_{elec\_gen,i}}{(1+f_{dsct})^{i}}} \quad (189)$$

Where

n is the lifetime of solar power plant;

$C_{ATCF,i}$ is the after tax cash flow in year i;

$P_{electricity\_generation,i}$ is the electricity generation in year i;

f_{dsct} is the discount rate;

3.7 Inflation

Inflation is defined as an increase in the general price paid for goods and services. It leads to a purchasing power reduction of each money unit. The common measurements of price change in economy are the Consumer Price Index (CPI), and the Producer Price Index (PPI). The CPI is a composite price index that measures average change in personal and family aspects, such as food, housing, medical care, transportation, apparel and other individual and family related services. The PPI measures the selling prices for items and services for production use based on the Standard Industrial Classification (SIC). From their definitions, the PPI data is more suitable for engineering economic analysis. Figure 43 shows the PPI (finished goods) and the CPI (all items, cities average) in U.S from year 2002 to year 2012 [67].

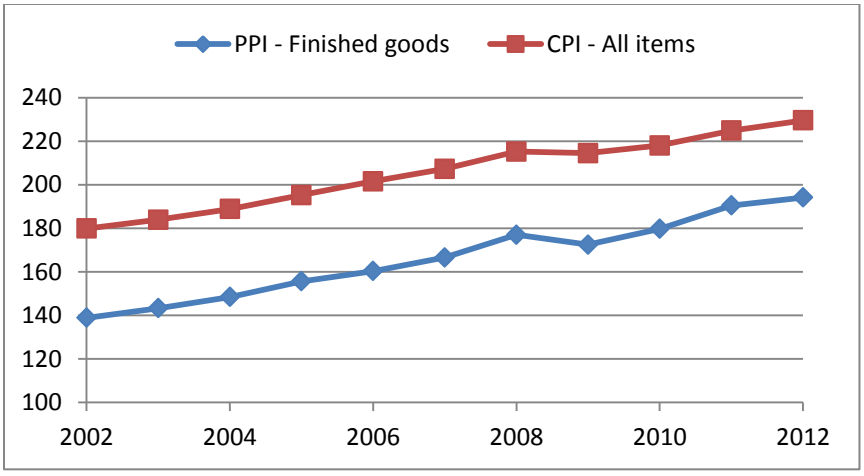

Figure 43: Finished goods PPI and All items average cities CPI in U.S between year 2002 and 2012

The lifetime of a CSP plant could be more than twenty years. The inflation can be serious for these long periods. The model uses a fix inflation rate, *i*, to coordinate the present, *P*, and future values, *F*. Their relation is

$$P = \frac{F}{(1+i)^n} \tag{190}$$

Where:

n is the year difference between the present and future value;

3.8 Lifecycle Cash Flows

Cash flows are the money movement of a project during a specified period. For a CSP plant, the specified period refers to its lifetime. The cash flows over the lifecycle of the

plant can be used for calculating other parameters, which may provide information about the project's condition and value.

In the financial model, after tax cash flows are calculated from the construction to the salvage of a CSP plant. It assumes that year 0 is the construction period and no electricity would be generated; year 1 to year *n* is the normal operation period, and the CSP plant is decommissioned in the end of year *n*.

3.8.1 Cash Flow in Year 0

The cash flow in year 0 is comprised of the installed cost and investment, the difference is the equity which is also the cash flow for this year.

$$C_{year,0} = F_{equity} \tag{191}$$

3.8.2 Cash Flow in Year 1 to Year n-1

In year 1, cash flow is the combination of the revenue from the sale of the generated electricity, the debt payment, the federal and state taxes and incentives.

$$C_{year,i} = C_{rvu} + C_{debt\_pmt} + C_{tax\_fed} + C_{tax\_state} + C_{IBI} + C_{CBI} + C_{PBI} \tag{192}$$

3.8.3 Cash Flow in Year n

In year n, besides the cash flow occurred in year n-1, the salvage cost or revenue occurs at the end of year n as well.

$$C_{year,n} = C_{rvu} + C_{debt\_pmt} + C_{tax\_fed} + C_{tax\_state} + C_{PBI} + C_{salv} \tag{193}$$

3.9 First Year Sale Price Calculation

3.9.1 IRR (Internal Rate of Return) Method

The IRR method is used to calculate a project's financial payback. In a typical IRR method, it solves the interest rate that equivalent worth of revenues to the equivalent worth of costs, the resultant interest rate is the IRR, which is commonly used to evaluate the desirability of an investment. The higher a project's IRR is, the more desirable it is to proceed with the project. Among all the projects with the same investment, the project with the highest IRR would be considered to have the best payback and usually will be taken first.

In the financial model, the IRR is given, and the first year electricity sale price is unknown and determined directly based on the IRR calculation method.

$$PW = \sum_{0}^{n} \frac{C_{CF,i}}{(1+i_{irr})^{i}} = 0 \Rightarrow \sum_{0}^{n} \frac{p_{sale,0}(1+i_{esc})^{i} P_{elec\_gen,i} + C_{CF\_rest,i}}{(1+i_{irr})^{i}} \tag{194}$$

Therefore,

$$p_{sale,1} = \frac{\sum_{0}^{n} \frac{C_{CF\_rest,i}}{(1+i_{irr})^{i}}}{\sum_{0}^{n} \frac{(1+i_{esc})^{i} P_{elec\_gen,i}}{(1+i_{irr})^{i}}} \tag{195}$$

Where

$C_{CF\_rest,i}$ is the yearly cash flow except electricity sale revenue in year i;

i_{irr} is the specified IRR;

i_{esc} is the electricity sale price escalating rate;

$P_{electricity\_gen,i}$ is the electricity generation amount in year i;

The calculated electricity sale price satisfies the investment payback requirement. However, the electricity sale price may need to satisfy other requirements such as minimum yearly cash flows or minimum DSCR. Figure 44 shows the calculation flow chart:

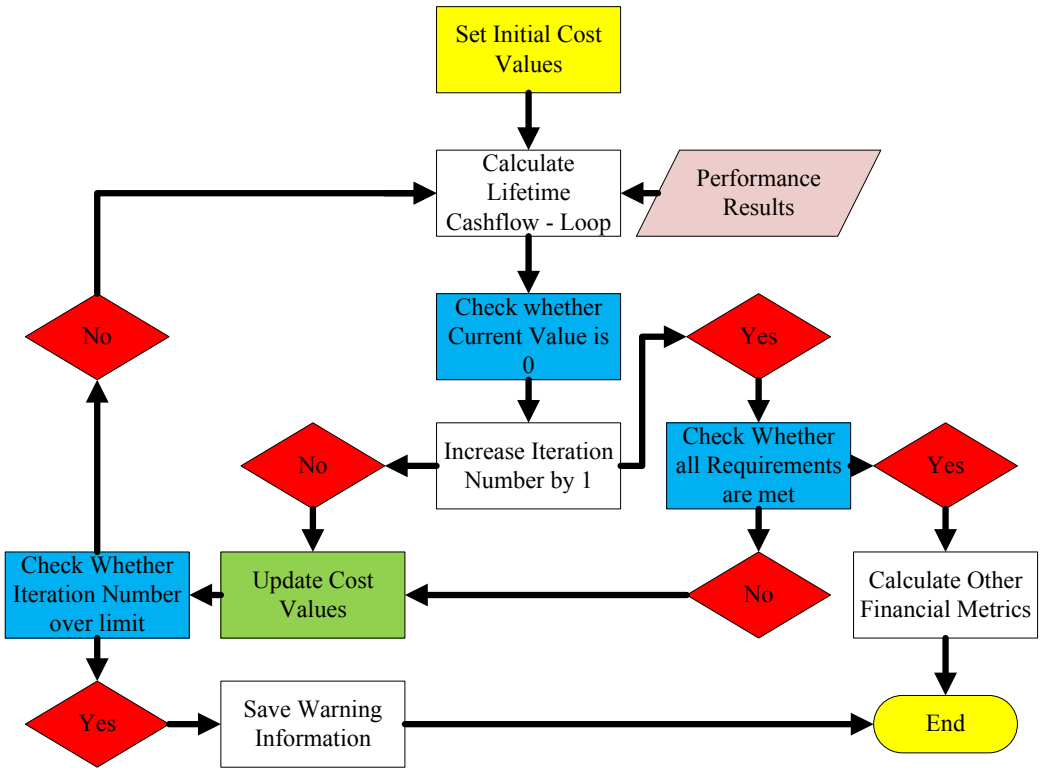

Figure 44: Flow chart of the financial model

3.10 Summary

Cost of a CSP plant is vital for its survival and prosperity. Not only the electricity production, but also the financial parameters and incentives are critical to determine its LCOE. The financial model, which is based on the results of the performance model, estimates the installation, operation, and decommissioning costs, reports annual lifecycle cash flows and the LCOE. It is able to work as a tool to estimate the electricity cost of a specific plant, or used to compare costs between different configurations.

4. DEVELOPMENT OF THE NET ENERGY AND RISK MODELS

4.1 Net Energy Model

4.1.1 Introduction

The financial analysis predicts a CSP plant's lifetime payback in economic aspect. Its results show whether a plant is profitable, but could not prove whether it is energy feasible, especially for renewable energy, which cost is usually lowered due to incentives and subsides. Thus, if a renewable power is only evaluated by its economic payback, the decision may be seriously distorted, for example, a power plant with good profit, but not having positive net energy may be approved.

The energy payback is evaluated with the net energy analysis (NEA), as shown in Figure 45. It identifies energy flows that are consumed and produced by a system. These energy flows include direct energy flows - energy consumed and produced from inception to salvage, and indirect energy flows – energy flows associated with materials and human labor, including material mining, manufacturing, transportation and installation, operation and maintenance, disposal, and recycle. The net energy of a system is calculated as:

$$E_{net} = \sum E_{produced} - \sum E_{consumed} \tag{196}$$

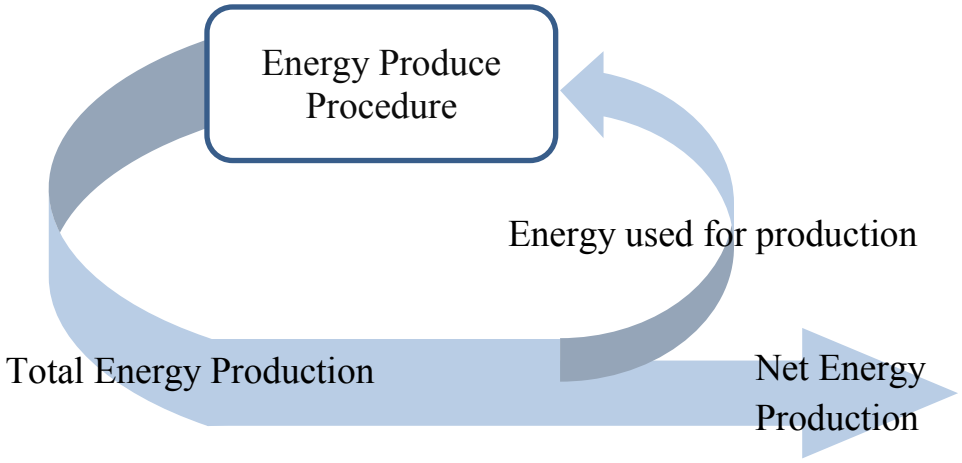

Figure 45: Demonstration of Net Energy

The net energy is a key parameter to evaluate the attribution of a plant, it could be used to determine whether a power plant is an energy source, carrier, or sink. If the lifetime energy recovered from the plant is more than the energy consumed, the plant is an energy source. If it is equal, it is an energy carrier, which converts one form of energy into another without gain or loss of energy. Otherwise it is regarded as an energy sink. Energy harvest systems should not be energy sinks, since their operation consumes more external energy than their production. Therefore the total energy production is reduced. Figure 46 shows a typical power plant's net energy performance during its lifecycle.

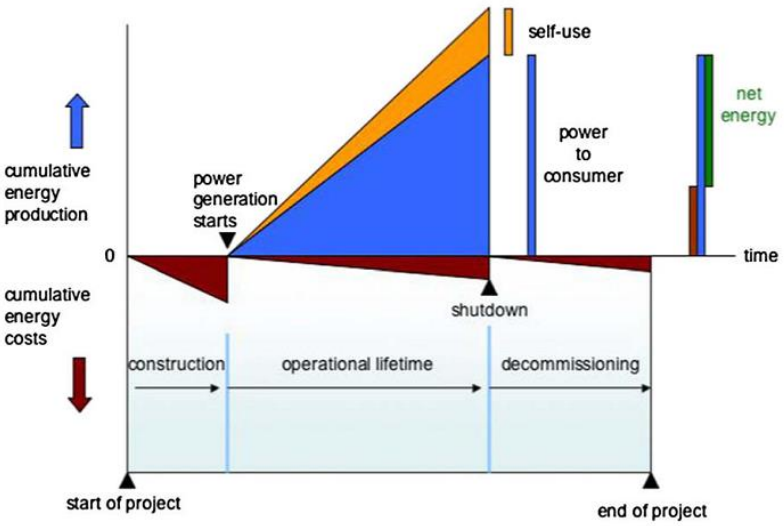

Figure 46: A typical power plant's energy outputs and energy costs [68]

However, one important factor about the NEA is that energy contained in fuels (coal, natural gas, wind, solar and else) is not included as an input because the NEA is defined to estimate the energy cost or investment to support a specific process [69]. If energy sources are included, the analysis result would be negative constantly, and the analysis would change to describe a physical energy conversion efficiency of the process instead.

However, to implement a fairly accurate analysis may be quite difficult and complicated, even impracticable, because:

First, it is impossible to find all indirect energy flows. Take human labor as an example, as shown in Figure 47: A person who works in a power plant needs to consume physical power. The consumed energy is represented as the energy coming with food. There is

additional energy required for preparing the food, such as the energy consumed in food transportation, planting, fertilization and irrigation, which all need to be considered. In addition, anything associated with people's living, for instance, the housing, transportation, entertainment or medical care, all result in significant energy flows. Therefore the list can be infinite, which makes it unrealistic to analyze.

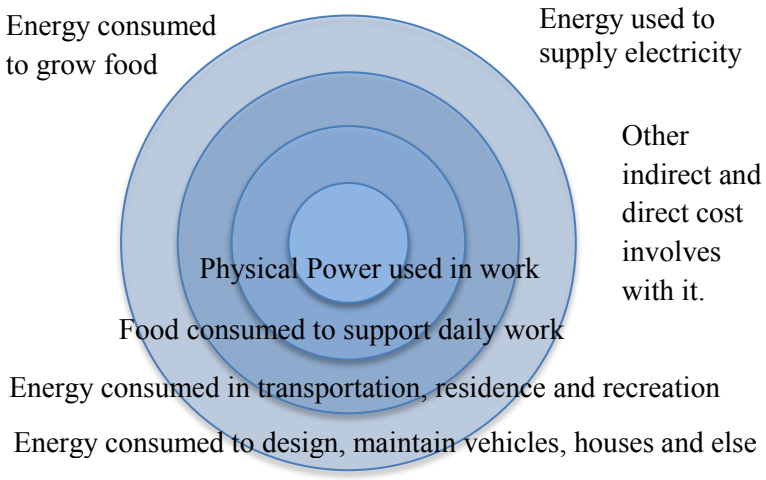

Figure 47: Demonstration of energy flows caused by human labor

Second, the accurate energy flow involved with each activity is not available, because the consumed energy is not easy to measure, and the consumed energy associated with each activity/procedure/product is not absolutely the same. Numerous factors, such as

location, weather, environment, economic level may affect the energy flow. So it is hard to obtain specified energy flows data for a specified CSP plant.

Therefore, only major energy flows are estimated. These energy flows data are obtained from different sources. The result is used to evaluate the energy payback performance of CSP plants.

4.1.2 Evaluation Parameters

Besides lifetime net energy, there are some other parameters which also could be used to evaluate the system's status and characteristics.

4.1.2.1 Energy Return on Investment (EROI)

The EROI is defined as the ratio of the lifetime cumulative energy production to the energy flows invested in a system.

$$F_{EROI} = \frac{\text{Energy return to society}}{\text{Energy required to get that energy}} = \frac{\sum_{lifetime} E_{production}}{\sum_{lifetime} E_{consumption}} \tag{197}$$

A qualified CSP plant should have an EROI larger than one. Large EROI represents higher energy recovery rate, which is more preferable.

4.1.2.2 Energy Payback Time (EPT)

The EPT is defined as the time, usually in years, that takes the system to produce the amount of energy equal to the lifetime cumulative consumption energy. If the annual energy production is fixed, the EPT, t_{EPT}, can be calculated as:

$$t_{EPT} = \frac{\sum_{lifetime} E_{consumption}}{E_{production,annual}} \tag{198}$$

However, CSP plants are supposed to have a decreasing electricity production during their lifetime due to aging and degradation. In this case, the EPT should be calculated according to:

$$\sum_{year,0}^{year,t_{EPT}} E_{production,annual} = \sum_{lifetime} E_{consumption} \tag{199}$$

4.1.3 Method to Estimate Required Energy

Several different methods are used to estimate the required energy, they are:

1. Direct method, which accounts for all materials and energy flows within the system boundary. The energy flows include direct energy flows and indirect flows such as materials, human labor or machinery.

   One data source is the Global Emission Model for Integrated Systems (GEMIS). It is a free database which provides net energy consumption information on materials, processes and transportations.
2. Another method is to evaluate the energy flows based on the financial costs by using energy intensity indicators which are derived for each sector of a country's economy. The energy intensity indicator is defined as the energy flows coming with monetary unit, as shown in equation 200.

$$F_{energy\_intensity} = \frac{E_{energy\_req\_by\_section,i}}{C_{monetary\_req\_by\_section,i}} \quad (200)$$

One advantage of this method is that the cost data has already been calculated in the financial model. Therefore if the corresponding energy intensity indicators are available, the required energy can be calculated. However, one disadvantage is that the result may be not very accurate since the energy intensity indicator has counted various energy sources besides solar energy. That indicates sole reliance on a general energy intensity indicator data may result in significant data distortion when the research is only focused on solar energy.

The Green Design initiative in Carnegie Mellon University provides guidance on the relative impacts of different types of products, materials, services, or industries with respect to resources and emissions throughout the supply chains [70, 71].

4.2 Risk Model

4.2.1 Introduction

The objective of risk engineering is to understand what events can happen to a designed system, how likely these events might happen, what consequences could occur when they happen, and how confident in making these predictions.

Risk not only refers to an undesirable consequence, but also the probability of the consequence. A system may involve many undesirable events. If the magnitude of the probability of each event is low, the overall risk would be still small. However, if the

consequence may cause extremely high loss, the risk may still be considered high even though the frequency of that hazard is low. A general expression for risk can be expressed as:

$$Risk[\frac{consequence}{time}] = Frequency\left\lfloor \frac{event}{time} \right\rfloor \times Magnitude\left\lfloor \frac{consequence}{event} \right\rfloor \quad (201)$$

Probabilistic Risk Assessment (PRA) is a method used to manage risk and improve reliability. It can produce quantitative risk estimate for complex systems, and further evaluate different alternatives, identify dominant risk contributors, and reduce the frequency of failure. The basic task flow of risk assessment is shown in Figure 48. Risk may come from different sources: program risks, production risks, technical risks, and engineering risks. Fault tree analysis and event tree analysis are commonly used methods to estimate the probability.

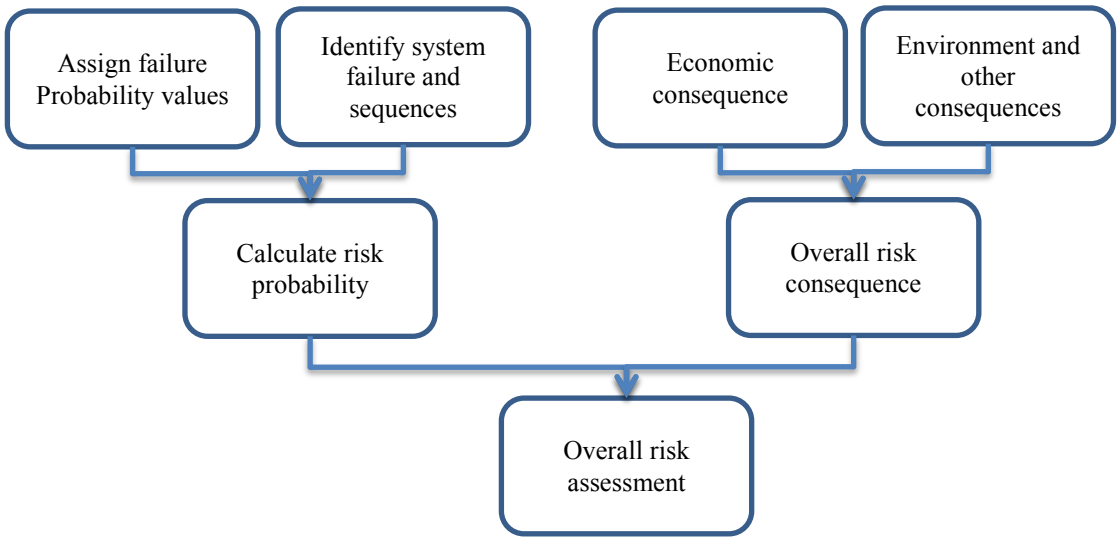

Figure 48: Basic task flow of risk assessment

4.2.2 Fault Tree Analysis (FTA)

FTA is an inductive logic method which begins with a specified undesirable failure event. Then its sub events are constructed according to its logical relationship which is used to determine the specified event's probability. Events in the relationship are connected with basic logical functions - the AND or OR gates, as shown in Figure 49.

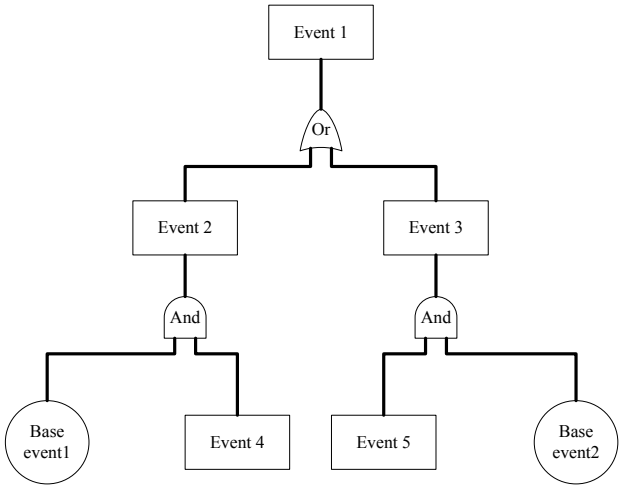

Figure 49: Demonstration of a fault tree

As shown in Figure 50, equations 202 and 203, the AND gate represents the situation that all the sub events must occur to yield the event A to occur. The OR gate denotes that any occurrence of the sub event would lead to the occurrence of the event A.

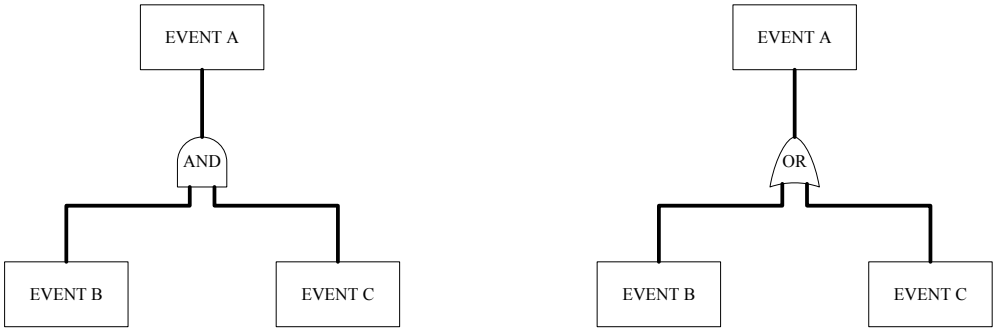

Figure 50: Demonstration of AND and OR gates

$$\text{If } A = B \text{ AND } C,\ P_{fail}(A) = P_{fail}(B) \times P_{fail}(C) \tag{202}$$

$$\text{If } A = B \text{ OR } C,\ P_{fail}(A) = 1 - (1 - P_{fail}(B)) \times (1 - P_{fail}(C)) \tag{203}$$

For redundancy system, if each unit is identical, its reliability is:

$$R(t) = \sum_{k=m}^{n} \frac{n!}{k!(n-k)!} \left(e^{-\lambda t}\right)^{k} \cdot \left(1 - e^{-\lambda t}\right)^{n-k} \tag{204}$$

If each basic event is able to be assigned a frequency or probability, the failure probability of top event can be determined.

4.2.3 Event Tree Analysis (ETA)

ETA is similar to the FTA except that it uses forward logic method to conduct all possible subsequent events from an initial event. It is a logical evaluation process, conducted with Boolean logic method to analyze how components' failure and success states affect the failure frequency and consequence, as shown in Figure 51.

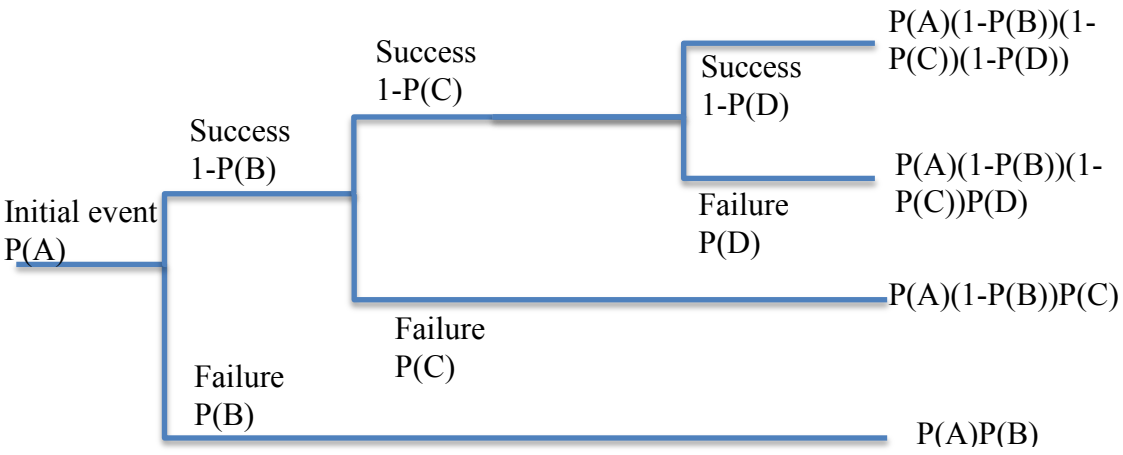

Figure 51: Demonstration of an event tree

4.2.4 Reliability Data

The reliability Information Analysis Center (RIAC) is a leading worldwide source for reliability data. Its products (electric parts reliability data and nonelectric parts reliability data) contain extensive quantitative and qualitative data on components and assemblies. Its data is collected from numerous industry and government tests and field sources with continuous updates [72].

4.2.5 Monte Carlo Method

Monte Carlo method relies on repeated random sampling to compute numerical results. It runs a simulation many times to make the results approach the true value. It is widely used in probability risk assessment due to its ability to solve coupled degree freedom problems, or problems that infeasible to apply a deterministic algorithm.

4.2.6 Risk Consequence

Consequence is defined as the real or potential conditions following one or multiple specified undesired events. The consequence may be disastrous, such as the Chernobyl nuclear disaster and the Space Shuttle Columbia disaster, bringing enormous casualties and property losses; or as slight as short time performance degradation.

Though the PRA has been proved to be a valuable tool for risk management, and is widely used in the nuclear and aerospace industry, few applications are found in the solar power industry. This may be caused by the solar power industry has much less environmental hazard and welfare loss. The substance involved has almost none acute threaten to human and ecosystems. Of greatest concern is the performance deterioration,

including the electricity production decreases and the cost rises up. For this reason, more emphasis was placed on risk associated with performance and cost rising rather than on catastrophic events.

In general, the discussed PRA concentrates on the normal operation of a CSP plant with undesired events, and estimates its economic loss caused by the performance degradation. All other losses, such as life loss and economic loss are excluded in this analysis.

4.3 Summary

In this chapter, the net energy analysis and PRA are described. The net energy analysis predicts a system's sustainability and feasibility from the energy conservation perspective. The PRA is a method to systematically quantify risk, and capable to subsequently identify the vulnerable components or procedures.

5. VALIDATION OF MODELS

5.1 Introduction

The model is validated by comparing the simulation results with the experimental data. The comparing objects are: the heat loss and temperature of heat collection element (HCE), the electricity production, the installed cost, and the cost of the the Andasol-1 CSP plant. The net energy analysis of the Andasol-1 CSP plant is conducted in this chapter as well.

5.2 Validation of HCE Model

The NREL has conducted tests on the PTR70 parabolic trough receiver's heat loss performance from 100˚C to 500 $˚C$ with 50 $˚C$ increments. Its experimental uncertainties of temperature and heat loss are ±1 $˚C$ and ±10 W/m [40].

Table 10 shows the key parameters of the PTR70 type receiver. Figure 52 to Figure 55 depict the comparison of the test and simulation results.

Table 10: Parameters used in the heat loss model

Item	Parameters
Model	PTR70 Receiver
Conductivity of glass	1.1 $W/m^2˚C$
Conductivity of Absorber	k = 14.8 + 0.0153*T_{abs} $W/m^2˚C$

Table 10 Continued

Emissivity of glass	0.89
Inner Radius of absorber	0.033 *m*
Outer Radius of absorber	0.035 *m*
Inner Radius of glass envelope	0.033 *m*
Outer Radius of glass envelope	0.035 *m*
Fluid mass rate	≈8 *m/s*
Ambient Temperature	depends on the test environment
Pressure in vacuum	0.001 *torr*

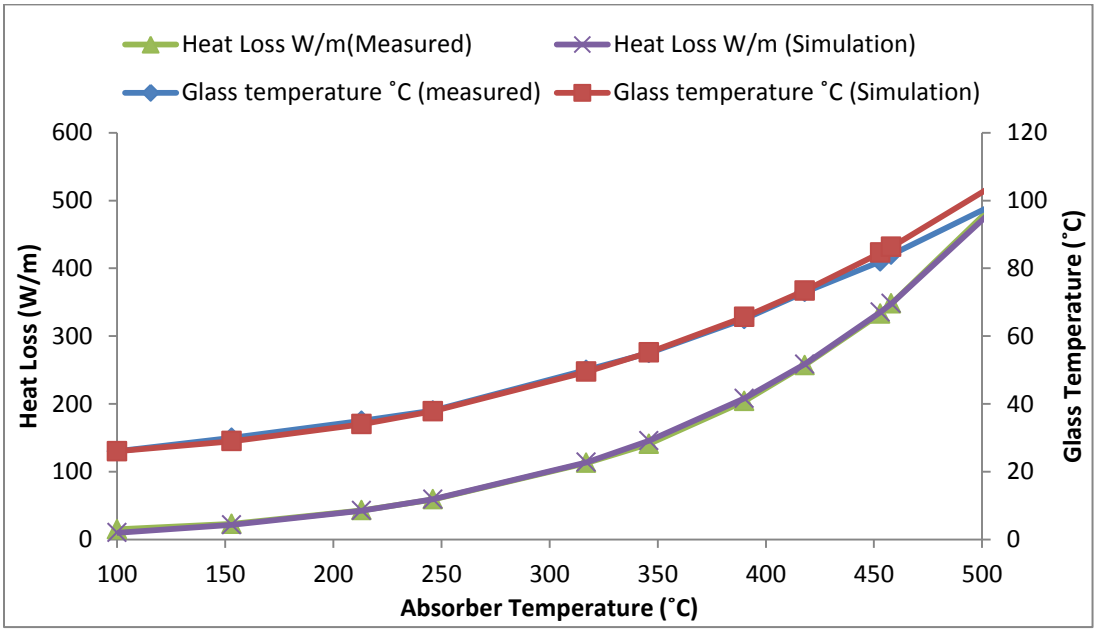

Figure 52: Comparison between the measured and the simulated heat losses and glass temperatures of HCE under different temperature – test 1

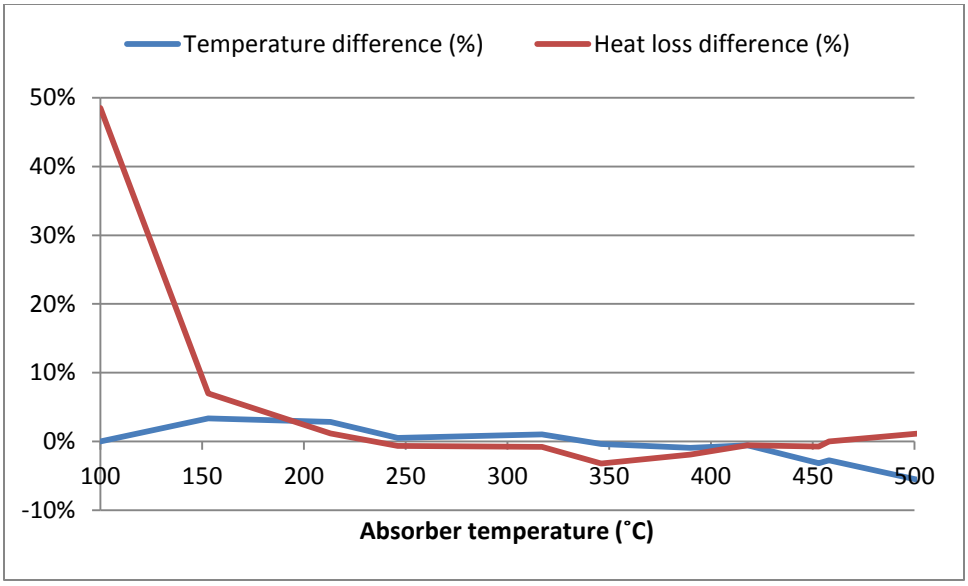

Figure 53: Difference between the measured and the simulated heat losses and glass temperatures – test 1

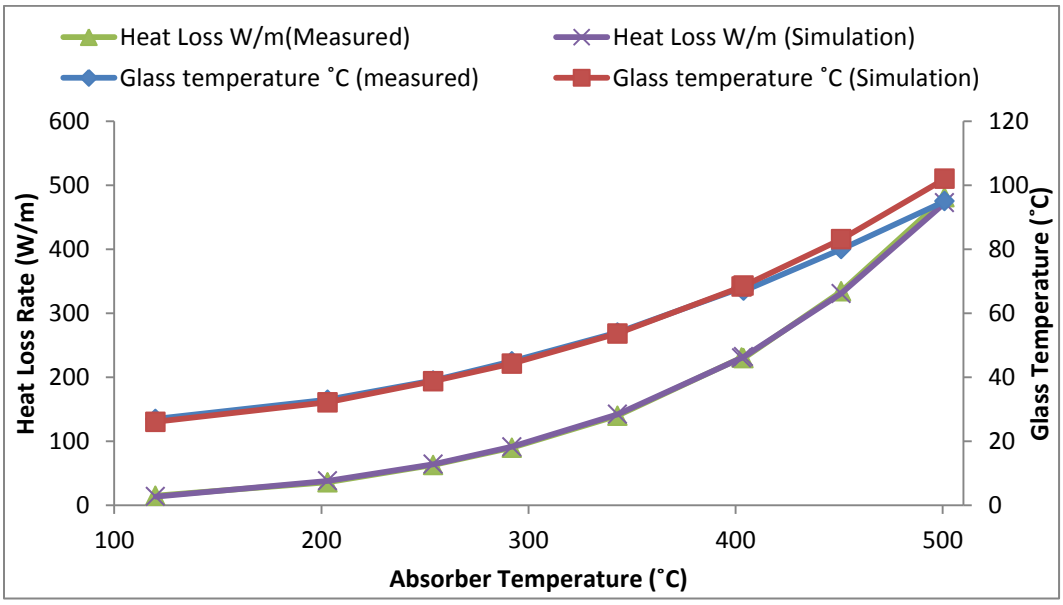

Figure 54: Comparison between the measured and the simulated heat losses and glass temperatures of HCE under different temperature – test 2

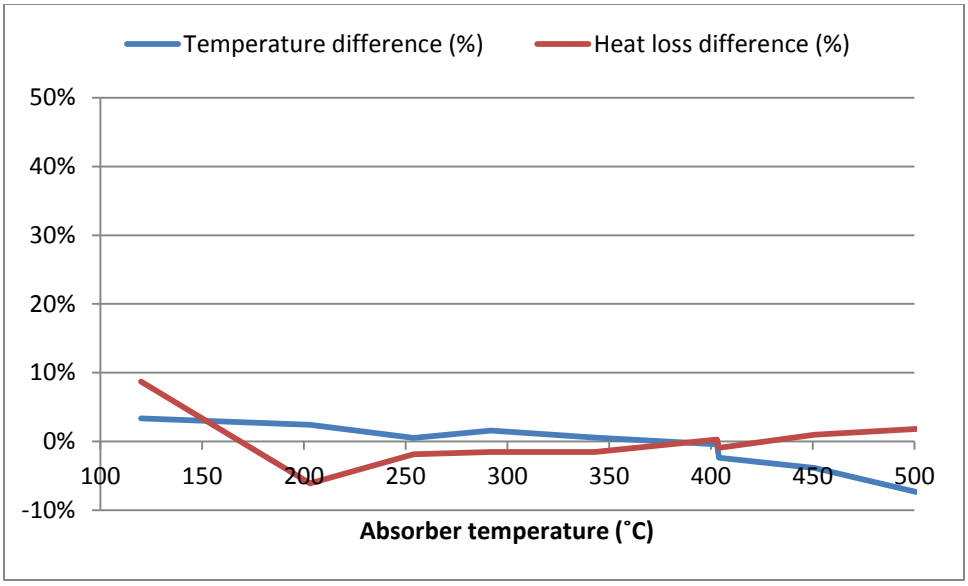

Figure 55: Difference between the measured and the simulated heat losses and glass temperatures – test 2

The comparison of the heat loss indicates that the simulation results are well agreed with the measured data when the absorber temperature ranges between 200 and 500 ˚*C*. The glass temperature is accurate for temperature from 100 to 450 ˚*C*. Considering the working temperature of receiver ranges from 250 to 400 ˚*C*, it is regarded that the simulation model is able to predict the operation performance of HCE.

5.3 Validation of Performance and Financial Model

5.3.1 Concentrating Solar Plant's Configuration

Till today, there are tens of CSP plants either have been built, or in construction or planning stages. The first commercial concentrating solar power plants were developed in the 1980s in California, United States, and they are still the largest (354 MW) trough

type concentrating solar power plants in the world. The Andasol-1 solar power station is European's first commercial parabolic trough solar thermal power plant which went online in March 2009. One significant difference between the SEGS and the Andasol-1 is that the latter one equipped with a larger thermal energy storage system, which is the development trend for the CSP industry, most recently constructed or planning CSP plants are equipped with larger than seven hours capacity storage system.

The coordinates of the Andasol-1 CSP plant are 37˚13' *N* and 3˚04' *W*, located on the Guadix plateau in the Granada province of Spain, as illustrated in Figure 56. To construct a CSP plant in this location has several advantages: There is no residence, and it is free from shading; has abundant of sunlight; close to motor way; with solid ground; and proximity to water resource. These conditions make it a decent place to construct a solar power plant.

Figure 56: Location of the Andasol-1 power plant

The configuration and performance of the Andasol-1 power plant are used as the benchmark. All other improvements are all based on and compared with it.

Table 11 shows the key parameters used in the simulation. They are obtained from open sources such as articles, news, official, academic and the operation companies' websites. However, since the ACS-Cobra Energy does not release performance data for the plant, the information is not complete, these assumption values of parameters are marked with '*'.

Table 11: Key parameters used for simulation [73]

	Items	Simulation
Climate	DNI	Granada, Spain, 1989
	Wind Speed	
	Humidity (%)	
	Dry Temperature	
	Atmosphere Pressure	
Field	Collector	EuroTrough ET150
	Receiver	Solel UVAC3
	Design Inlet Temperature (*k*)	566
	Design Outlet Temperature (*k*)	666
	HTF Type	Therminol VP-1
	Parallel Loop Number	156
	SCAs per Loop	4
Storage	Full Load Hours	7.7
	TES materials	Nitrate Salt
	Storage Type	Two-Tank System
	Hot Tank Number	1
	Cold Tank Number	1
	Effective TES mass (*ton*)	2.42E+04
	Hot Tank Radius / Height (*m*)	21.36 / 14.99*
	Cold Tank Radius / Height (*m*)	20.94 / 14.75*
Power Block	Turbine Type	Siemens SST-700
	Start Up Energy (*%*)	20*
	Start Time (*hour*)	1*
	Design Net Output (*MW*)	49.9
	Cooling Tower Type	Wet Cool
	Deplete HTF Temperature (*k*)	566*
	Max Turbine Load	110.2%*
	Min Turbine Load	15%*
	Design Efficiency	38.1%

Table 11 Continued

System	Operation Strategy	Greedy*
	Annual Degradation	1%*
Cost	Site Improvement ($/m^2)	31*
	Solar Field ($/m^2)	327*
	HTF System ($/m^2)	99*
	Storage ($/kWt)	52*
	Power Plant ($/kWe)	459*
	Balance of plant ($/kWe)	270*
	Fixed Cost - Labor ($ first year)	2.95E+06*
	Fixed Cost - Materials ($/MWe first year)	34500*
	Variable Cost ($/MWh)	2.5*
Finance	Minimum Required IRR	15%*
	PPA Escalation Rate	1.20%*
	Loan Rate	8.25%*
	Loan-to-Cost Ratio	80%*
	Loan term (*year*)	20*
	Loan payback	End of year, evenly*
	Real Discount Rate	8.20%*
	Insurance Rate	0.50%*
	Inflation Rate	2.50%*
	State Tax	7.00%*
	Federal Tax	3.50%*
	Federal Depreciation	MACRS(MidQuarter) *
	State Depreciation	MACRS(MidQuarter) *
	Analysis Period (life of plant, year)	30*

5.3.2 Simulation Results

Two simulations are performed, the first one uses the original DNI data, as shown in Figure 57; the second one uses the adjusted DNI data, whose yearly DNI intensity is prorated to match the reported annual DNI intensity. Both simulations are performed under the greedy operation strategy. The simulation results are shown in Table 12. With the original DNI data, the gross and net annual electricity generations are 174 GWh/year and 151 GWh/year, which have 3% and 4% difference from the reported ones. If the adjusted DNI is used, the gross and net electricity generations increase to 178GWh/year and 154 GWh/year, and the difference with reported ones reduce to 1% and 2%. The capacity factors of the simulated results and disclosed data are very close because the capacity factor is directly derived from the electricity production.

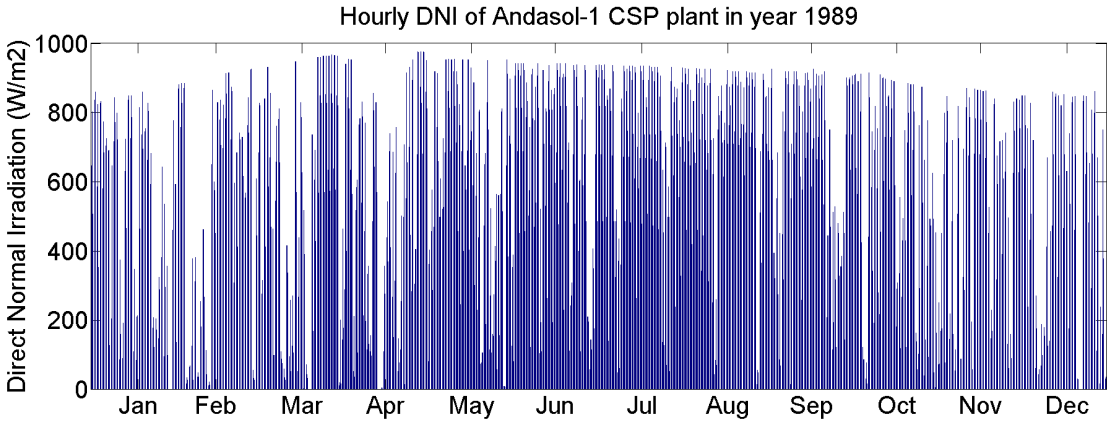

Figure 57: Hourly DNI data in year 1989

The cost analysis results agree with International Renewable Energy Agency (IRENA)'s report [74]. The difference of the installed cost between the predicted and reported values is 10%, which may be caused by the Euro to U.S dollar exchange rate, money depreciation, and other uncertainties. For the LCOE, the difference is caused by several important but unknown factors including design plant lifetime, interesting rate, loan-to-cost ratio, required IRR, and depreciation method.

Table 12: Andasol-1 simulation results and disclosed data

Parameter	Real	Simulation	Simulation Adjusted
Annual DNI (*kWh/m2/year*)	2136	2033	2104.155
Solar Field Size (m^2)	510120	518469.12	518469.12
Total Solar Energy (*kwh/year*)	1.09E+09	1.05E+09	1.09E+09
Gross Annual Electricity Generation (*MWh/yr*)	179,103	175,942	179,759
Net Annual Electricity Generation (*MWh/yr*)	158,000	152,726	155,888
Capacity Factor	0.41	0.40	0.41
Installed Cost *($/kwh*)	7615	8395	8395
LCOE *($/kwh*)	0.343	0.275	0.269

Figure 58 illustrates how the energy flows from sunlight to electricity in the Andasol-1 CSP plant. The results indicates that majority of the solar energy is dissipated during the energy collection and thermal-to-electricity conversion procedures.

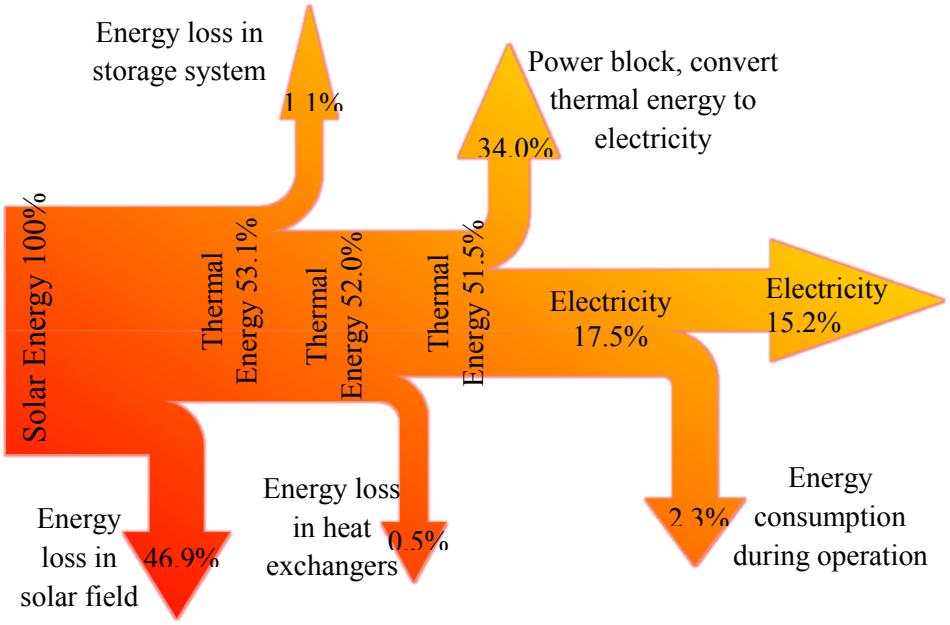

Figure 58: directions of the energy flows of the simulated CSP plant

Figure 59 illustrates the monthly energy flows of the simulated results. It shows that the solar energy is varied with seasons. The peak DNI occurs in the summer, and is almost twice as the lowest which takes place in the winter. The collected solar energy is generally proportional to the collected energy, and the collective ratio is mainly affected by the sunlight directions – in the winter, the solar altitude is smaller than the altitude in the summer, therefore the projected area of troughs is smaller. The thermal energy delivered to the power block is linear to the collected solar energy. The difference of field collected and power block received thermal energies is the heat loss which occurs in the storage, transportation, and heat exchange procedures. In addition, the gross

energy generation has a noticeable cut during the summer period. That is because the received thermal energy goes beyond the power block's capability, and is wasted during that period. The summer season has the strongest solar intensity and the longest daytime, so it has the most wasted energy.

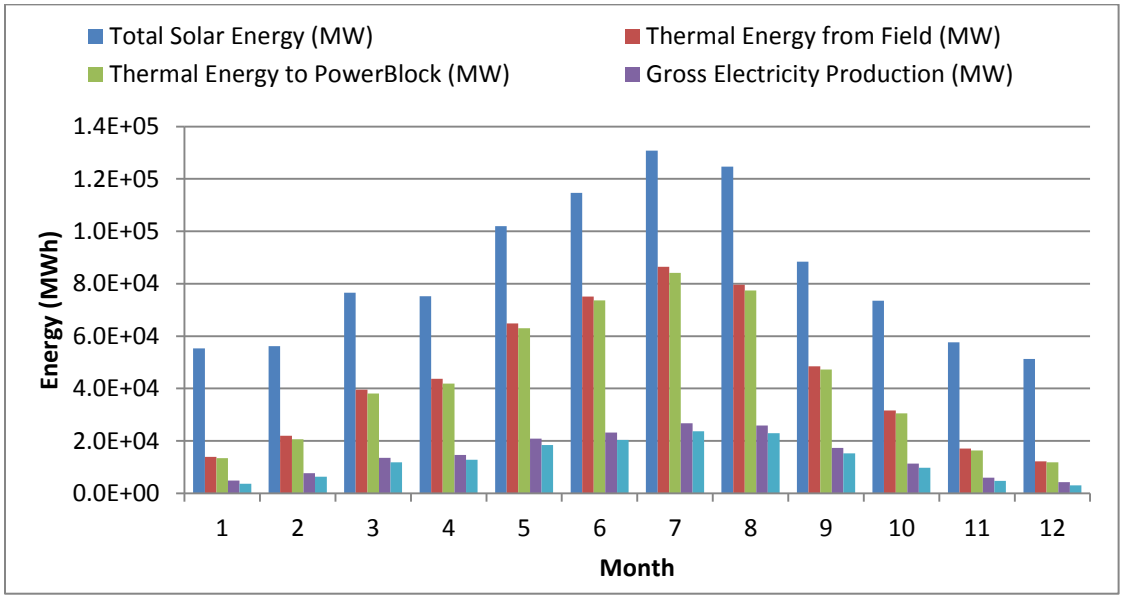

Figure 59: Monthly energy flows of the simulated plant

Figure 60 to Figure 63 show the hourly performance of typical sunny days in winter (Figure 60), summer (Figure 61), fall and spring (Figure 62) seasons, and typical cloudy day (Figure 63). There are some meaningful finds:

First, the hourly figures clearly show the function of the storage system – balances extra or deficit thermal energy. In most of the time, power block operates under design load, regardless of the fluctuating of solar intensity.

Second, the collected thermal energy is much higher in summer than winter season because the day times and solar altitude angles are varied with seasons. The daytime is long in summer and short in winter, while the solar altitude is high in summer and low in winter. The variation leads to possible thermal energy waste in summer and devices idle in winter.

Third, Figure 61 shows that the storage system along could support the operating of the power block for more than seven hours as designed. It extends the operation period from 19:00 PM to 2:00 AM next day. In addition, it shows the power block operates with its maximum capacity (110% of rated capacity) when there is exceed thermal energy available to the power block. It helps to convert maximal thermal energy to electricity and minimize the energy waste as request.

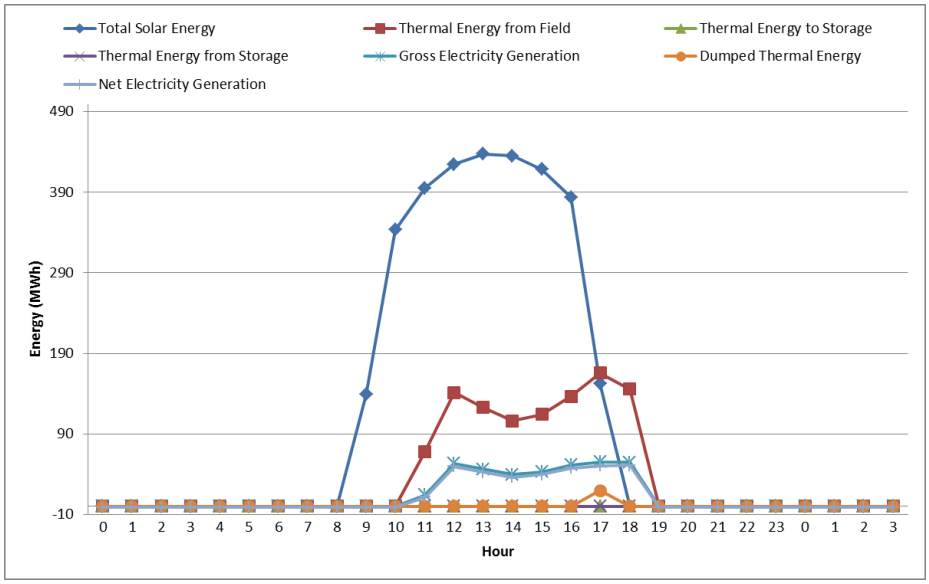

Figure 60: Daily energy flows of the simulated plant in Jan 15, 1989

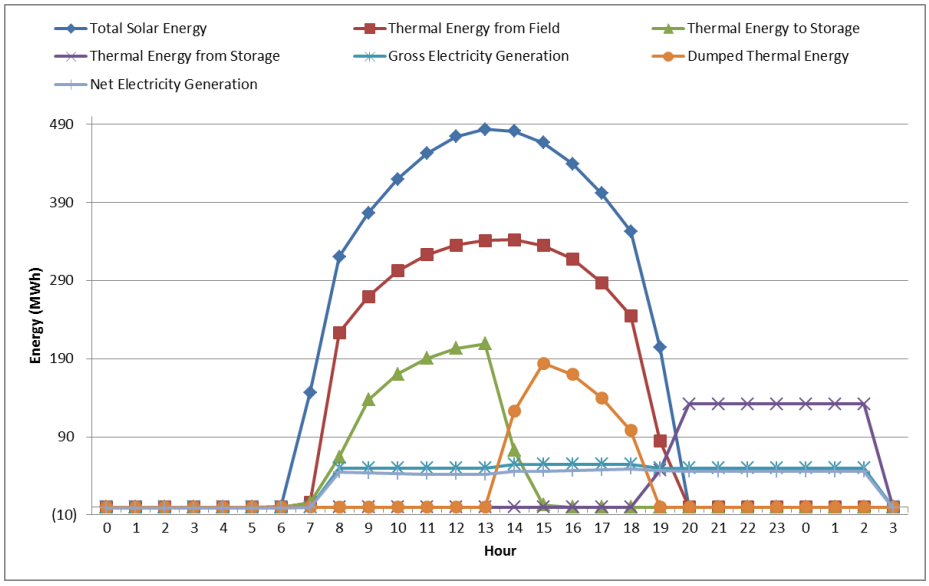

Figure 61: Daily energy flows of the simulated plant in June 23, 1989

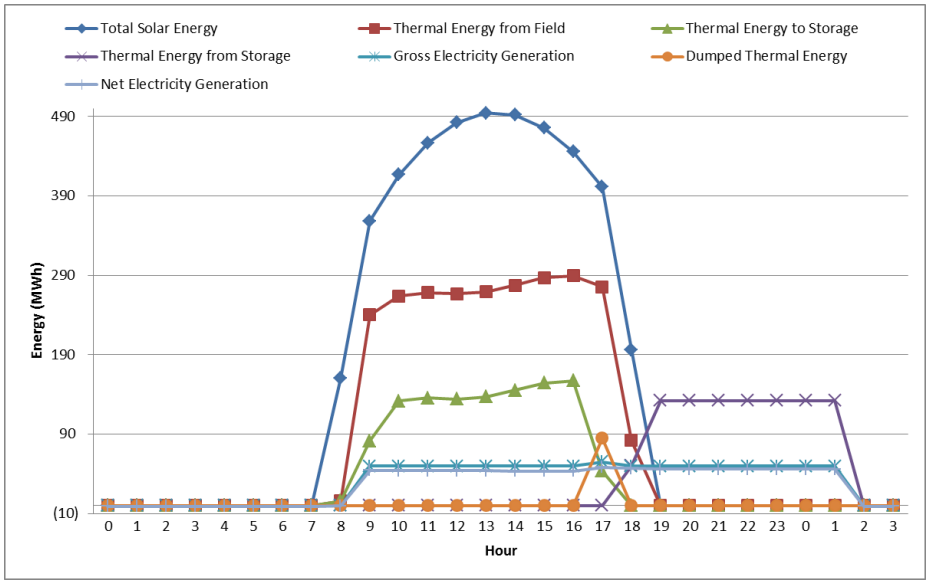

Figure 62: Daily energy flows of the simulated plant in March 23, 1989

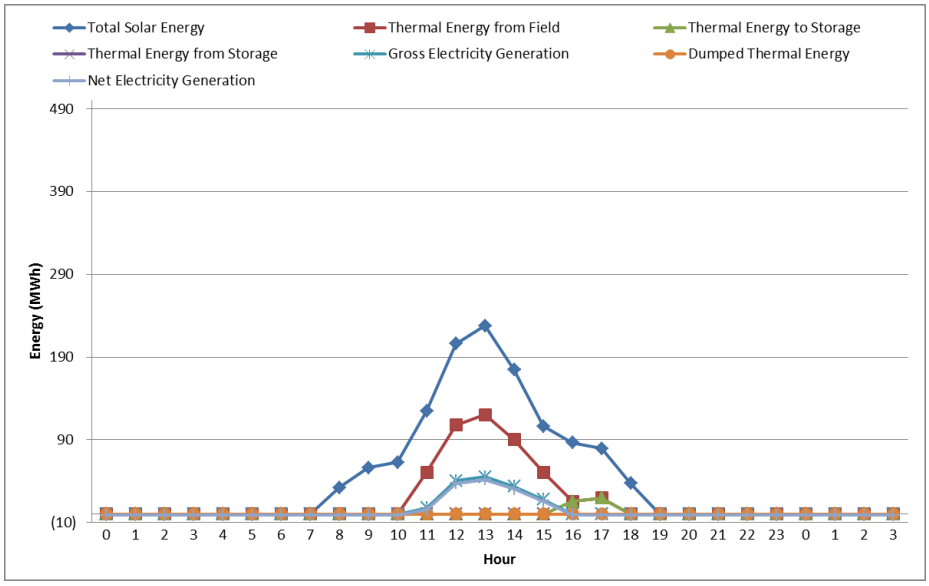

Figure 63: Daily energy flows of the simulated plant in April 1, 1989

Typical summer and winter loads of the grid are shown in Figure 64. By comparing the daily energy flows (Figure 60 to Figure 63) with Figure 64, it indicates that a CSP plant's electricity production period could fully cover the peak load period and most of the intermediate load period of the grid. In addition, considering a CSP plant could adjust its output, it could meet the variation requirement of the grid.

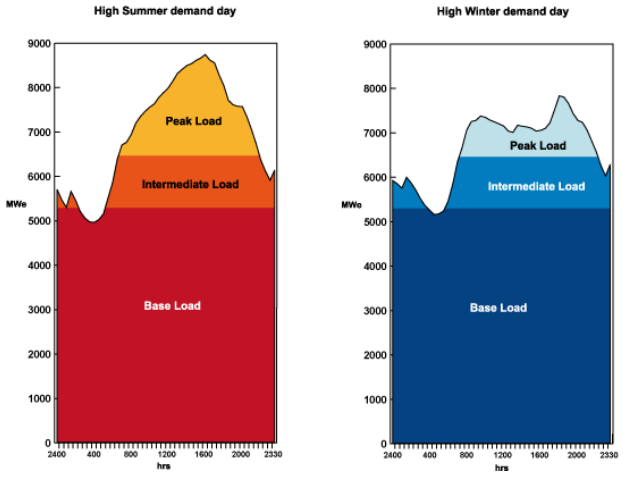

Figure 64: Load curves for typical electricity grid[11]

Figure 65 shows the lifetime cash flows from the simulation results. In year zero, the initial investment brings a large negative cash flow. During year one to year five, the cash flows decrease rapidly, which are caused by the decrease of the investment depreciation, and this revenue vanishes after year six according to its five years

[11] Image retrived on June 2013, from website: http://www.world-nuclear.org/info/Energy-and-Environment/Renewable-Energy-and-Electricity/

depreciation schedule. Then, the cash flows keep declining because the taxable income has been increasing as a result of the decreasing tax deductible loan interests. After year 20, there is a sudden increase due to the ending of the loan. The cash flows are steady in the last ten years of its lifetime, due to the multiple effects of decreasing electricity generation and increasing electricity sale price.

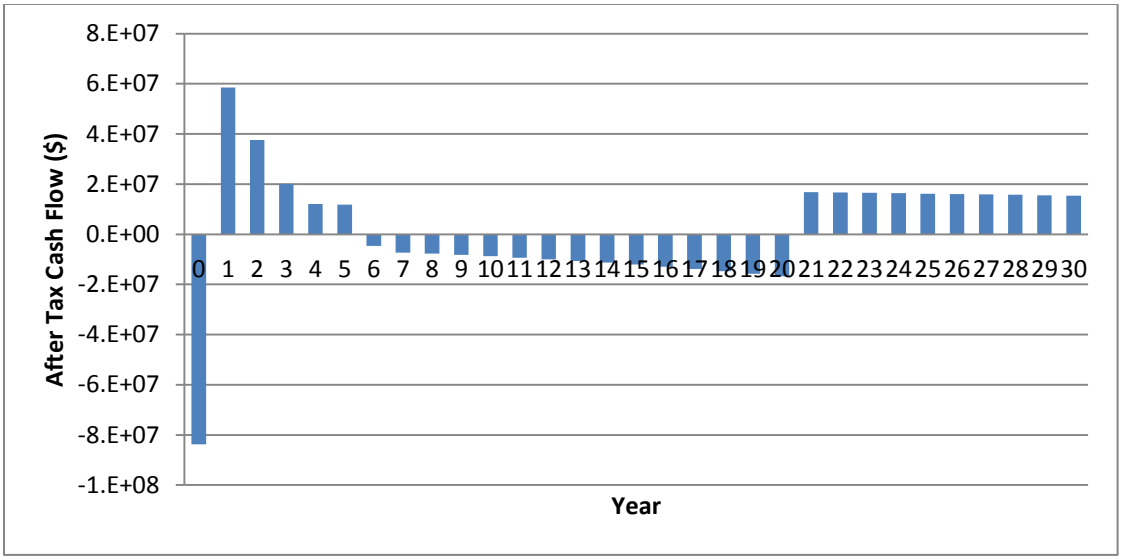

Figure 65: Simulated lifetime yearly cash flows

5.4 Net Energy Analysis

The following net energy analysis is based on Andasol-1 power plant.

Figure 66 depicts the considered phases of a CSP plant and related energy flows. Figure 67 indicates its logical framework and calculation methods.

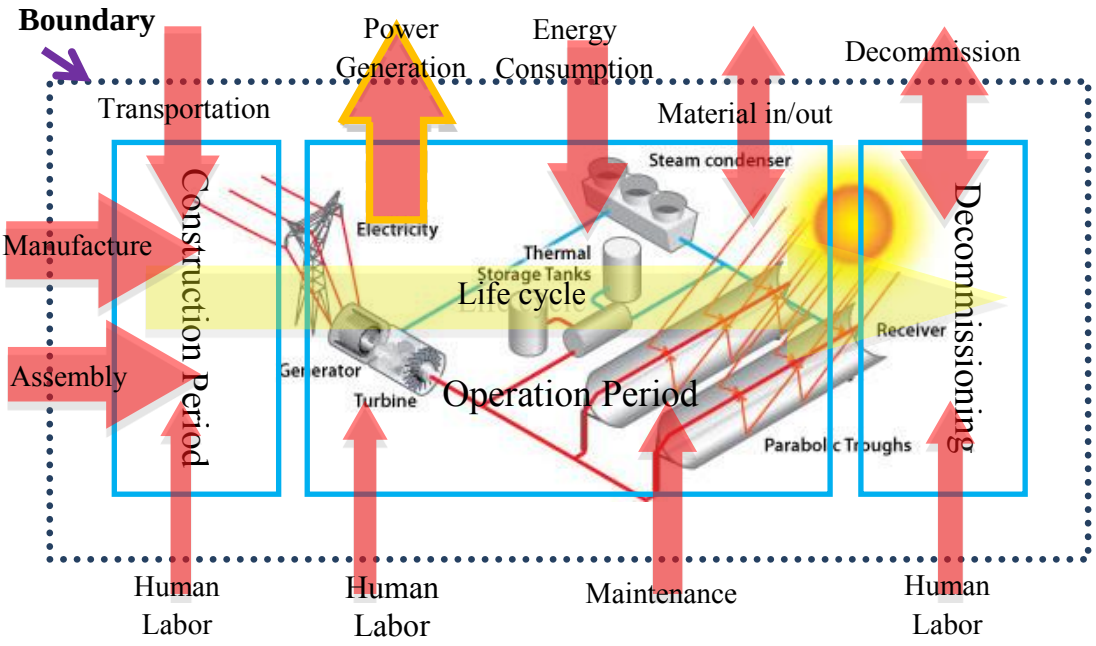

Figure 66: Diagram of the energy flows of a CSP plant

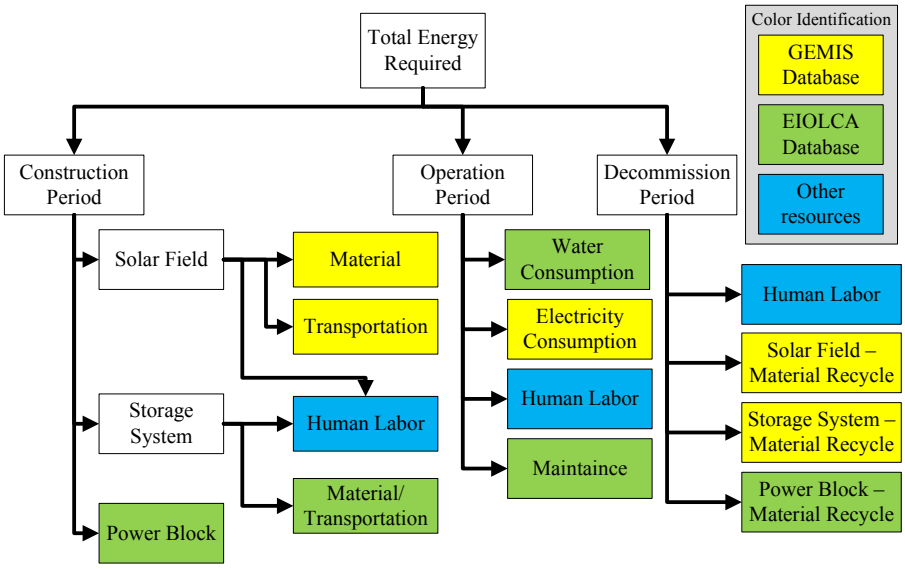

Figure 67: Framework of energy flows of a CSP plant

5.4.1 Energy Recovered by Electricity Generation

The electricity generated during the lifecycle of a CSP plant is regarded as the 'recovered energy' in the net energy analysis. The electricity power sent to grid is:

$$\begin{cases} E_{Pb2grid,t} = 0 & \text{when } E_{PB\_net\_hour} <= 0 \\ E_{Pb2grid,t} = E_{PB\_net\_hour} & \text{when } E_{PB\_net\_hour} > 0 \end{cases} \tag{205}$$

The first year plant output is:

$$E_{PB2grid,annual} = \sum_{i=1}^{8760} E_{Pb2grid,i} \tag{206}$$

For the Andasol-1 CSP plant, the annual electricity productions with greedy and longtime strategies are 5.71×10^5 and 4.85×10^5 *GJ/ year*.

5.4.2 Energy Flows caused by Installment, O&M and Decommission

All energy flows, mass flows, processes and human activities involved in installment, O&M and decommission must be accounted. These energy flows are estimated and appeared as energy inputs or outputs in the energy analysis sheet.

The required energy of a CSP plant is calculated separately according to its lifecycle phases, these phases are:

- Plant construction phase: includes components manufacturing, transportation and installment;
- Plant operation phase: includes operation and maintenance;

- Plant decommissioning phase: includes material recycling and refurbishment;

The energy requirement is the sum of the energy consumed in these three phases.

$$E_{Consumption} = E_{Install} + E_{OM} + E_{Decommission} \tag{207}$$

5.4.3 Human Labor

It is necessary to include energy flows of human labor to the NEA. Though human labor may only contribute to a small share of all the net energy costs, it supports human life and is the most important component in the power generation process.

Different methods have been used before to evaluate the embodied energy in human labor. One idea is to estimate it based on the work load, and then convert to the calories needed for each day or hour. The first method is to evaluate the physiological energy required to perform the specific work. And the physiological energy could be quantified with the energy input from feeding. Then the energy required by human labor is the mean energy consumed by workers. For an adult male, based on his size and activity strength, the energy consumption ranges from 2000 to 3000 calories per day [75]. In addition, considering different jobs have varied activity intensities, it would be more accurate to evaluate the energy consumption according to the work types. With heavy/medium/light workloads, a worker weights 80 *kg* has an energy consumptions of 495/390/190 calories per hour. Moreover, it is reasonable to assume that a worker does not perform same intensity duties during its daily working. Therefore the eight hours daily work could be further classified into different intensity, as shown in Table 13.

Table 13: Energy expenditure for different type of workers [46]

Type	$Hour_{HI}$	$Hour_{MI}$	$Hour_{LI}$	*cal/day*	*Wh/hw*
Engineers, administration	0	0	8	1520	221
Maintenance	1	5	2	2825	411
Construction worker	5	2	1	3445	501

Where:

$Hour_{HI}$ is hour of high intensity work;

$Hour_{MI}$ is hour of medium intensity work;

$Hour_{LI}$ is hour of high intensity work;

hw is hours of work (typically 8 hours per day).

The second method includes the infrastructure energy associated with human labor in addition to the energy associated with food. That infrastructure associated energy is the energy used in housing, transportation, health care, entertainment and else. Its human labor associated energy can be much more significant than only considering the physiological energy required.

It would be difficult and complicated to estimate the energy consumption of each activity. The energy used per worker-hours is evaluated based on the total primary energy supply (TPES), the industrial primary energy supply (IPES) and the population [76].

$$EPWH = \frac{TPES - IPES}{population \times hours / year} \quad (208)$$

For the U.S., the primary energy usage per work-hour per person is 30 MJ.

The estimation results from these two methods are different. The results from the second method could be 50 times more than the first one. Considering the first method failing to include the great amount of indirect energy embodied or used in the infrastructure, nor does it consider the indirect energy consumption during food production and digestion, thus the result from the second method is considered to be a closer estimate to the real value.

5.4.4 Lifetime Energy Consumption

The energy consumed in the construction phase is calculated separately for different components. The transportation distance is based on assumption. Their detailed calculations are shown in Table 14.

Table 14: Construction phase energy consumption

Category	Item	Unit cost (GJ/ton)	Weight (ton)	Unit (GJ)
Solar Field - Material	Glass (receiver)	11.89	207.31	2.46E+03
	Glass (trough)	11.89	7038.20	8.37E+04
	High alloyed steels	72.65	361.65	2.63E+04
	Carbon Steel	24.91	17109.48	4.26E+05

Table 14 Continued

Category	Item	Unit cost (TJ/ton·km)	Distance (km)	Weight (ton)	Unit (GJ)
Solar Field - Transportation	Truck	1.09E-06	500	24716.63	1.35E+04
	Train	2.99E-07	1000	24716.63	7.39E+03
	Ship	1.59E-07	5000	24716.63	1.96E+04
Category	Item	Unit cost (MJ/hour /person)	Personnel Number	Hours	Unit (GJ)
Power Plant	Human labor (field and storage)	30	400 -500	2years	2.73E+04
Category	Item	Unit (TJ/million$)	Million $	Inflation	Unit (GJ)
Storage System - Material	TES material / transportation	17.7	16.78	0.78125	2.32E+05
	Tank materials	12.6	9.79	0.78125	9.64E+04
	Pumps	7.97	1.74	0.78125	1.08E+04
	Heat exchangers	11	19.30	0.78125	1.66E+05
Category	Item	Unit (TJ/million$)	Million $	Inflation	Unit (GJ)
Power block	manufacturing	5.89	2.29E+01	0.78125	1.05E+05
	Power boiler and heat exchanger manufacturing	11	1.35E+01	0.78125	1.16E+05

The energy consumptions during operation and decommission phases are shown in Table 15 and Table 16.

Table 15: Operation and maintenance phase energy consumption

Category	unit cost (TJ/TJ)	Annual Consumption (MWh)	Transmission Loss	Unit (GJ)
Electricity Consumption	2.5809811	5376/2303[12]	5%	5.26E4/2.25E4[12]
Category	Unit cost (L/kWh)	First year electricity production (MWh)	Water cost	Unit (GJ)
Water Consumption	5	176512.55	0	0.00E+00
Category	Unit cost (MJ/hour/person)	Personnel Number	Hours	Unit (GJ)
Human Labor	30	50	1920	2.88E+03
Category	Unit cost TJ/million $	Million $	Inflation	Unit (GJ)
Maintenance	2.44	2.1045	0.78125	4.01E+03

Table 16: Decommission phase energy consumption

Category	Unit cost (MJ/hour/person)		Personnel Number	Period	Unit (GJ)
Human Labor	30		400-500	2 years	1.37E+04
Category	Item	Unit cost (GJ/ton)	Weight (ton)	Recycle rate	Unit (GJ)
Recycle - Material	Glass (receiver)	-11.888	207.31	0.4	-9.86E+02
	Glass (trough)	-11.888	7038.20	0.4	-3.35E+04
	High alloyed steels	-72.651	361.65	0.7	-1.84E+04
	Carbon Steel	-24.91	17109.48	0.7	-2.98E+05

[12] Two strategies, first is the value for the greedy strategy, second is for the longtime strategy.

Table 16 Continued

Category	Item	Unit cost (TJ/million $)	Million dollar	Recycle rate	Inflation	Unit (GJ)
recycle - Storage	TES material / Transportation	-17.7	16.7772	0.4	0.78125	-9.28E+04
	Tank material	-12.6	9.79326	0.5	0.78125	-4.82E+04
	Pumps	-7.97	1.74045	0.4	0.78125	-4.33E+03
	Heat exchangers	-11	19.2987	0.6	0.78125	-9.95E+04
Category	Item	Unit cost (TJ/million $)	Million $	Recycle rate	Inflation	Unit (GJ)
Recycle - power block	Manufacture	-5.89	2.29E+01	0.2	0.78125	-2.11E+04
	Power boiler and heat exchanger manufacturing	-11	1.35E+01	0.2	0.78125	-2.32E+04

5.4.5 Net Energy Analysis Results

Table 17 shows the net energy analysis results using the greedy and longtime operation strategies respectively. The results from the greedy strategy have a larger lifetime net energy, but a lower EROI and longer payback time compared with the results from the longtime operation strategy. With the greedy strategy, the power block has more time to work on rated power. Therefore it has more time to keep the power block operating on high conversion rate. In addition, it intends to convert thermal energy to electricity rather than to store it, so less energy is wasted. The comparison of annual and net energy productions are shown in Figure 68.

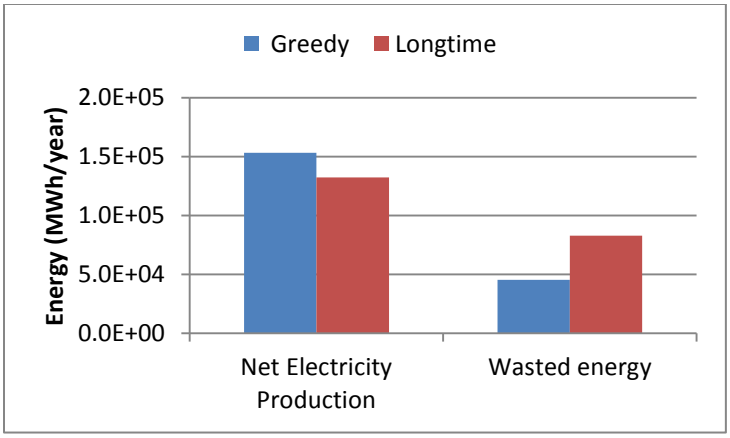

Figure 68: Simulated net electricity productions and wasted energies with the greedy and longtime strategies

However, the storage system depletes quickly in the night time with the greedy strategy. It has longer idle time and more starts and stops times, as shown in Figure 69 and Figure 70. During the idle period, it needs to have electricity support from the grid, in which process the consumed electricity would be converted to a large amount of primary energy. This electricity consumption worsens the net energy analysis results.

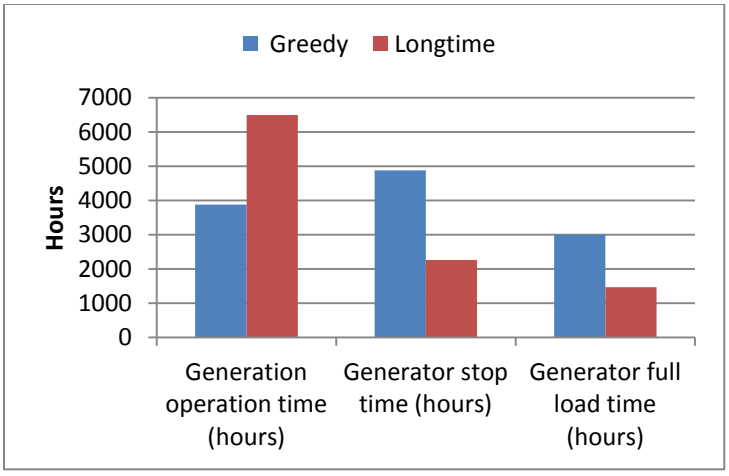

Figure 69: Operation statistics with the greedy and longtime strategies

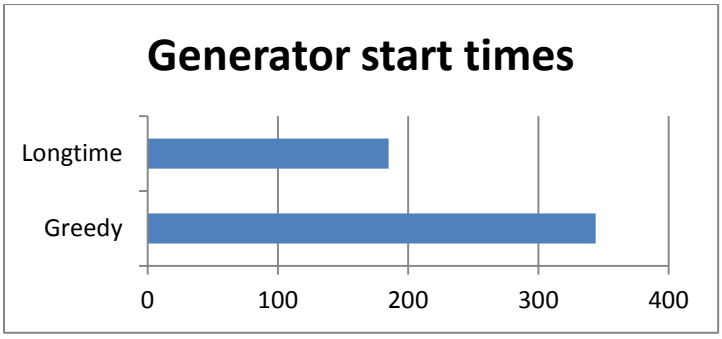

Figure 70: Generator start times of the longtime and greedy strategies

The statistics of power block's loads are shown in Figure 72. The greedy strategy has almost doubled the stops and starts times, and more than doubled full load times compared with the longtime operation strategy. In contrast, the longtime strategy has

longer operation hours under partial loads, which loads draw less thermal energy, so the operation hours could be extended.

Table 17: Results compare between two strategies

Strategy	Construction (GJ)	O&M (GJ)	Decommission (GJ)	Net energy (GJ)	EROI	EPT (years)	LCOE ($/kwh)
Greedy	1.33E+06	1.78E+06	-6.27E+05	1.46E+07	6.87	4.36	0.275
Longtime	1.33E+06	8.82E+05	-6.27E+05	1.29E+07	9.15	3.28	0.317

Figure 71 illustrates that the net energy payback varies with times, based on equation 209:

$$E_{net,year\ i} = -\sum_{lifetime} E_{consumption} + \sum_{year=0}^{i} E_{recovered,i} \quad (209)$$

Figure 71: Accumulated net energy of the two strategies

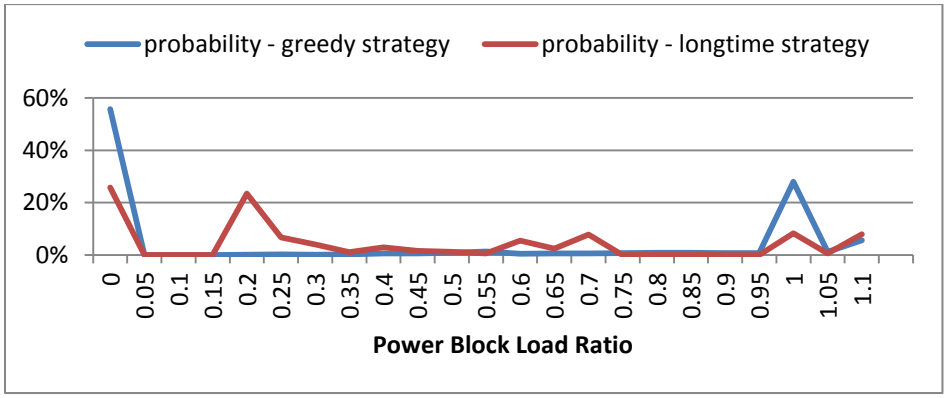

Figure 72: Statistics of the power block's load

Though the longtime strategy has a short payback period and a large EROI, it has a small net energy over its lifecycle, and a high LCOE. It shows the conflict between the

consideration from the economy and net energy perspectives. The conflict is mainly caused by the different ways to treat the consumed energy –it is converted to primary energy in the net energy analysis, while it is not in the economic analysis. The consumed electricity becomes significant after being converted to primary energy that in general, the CSP plant has a less electricity consumption would have a better net energy performance.

For a CSP plant, if economic payback is in high priority, it should adopt the greedy operation strategy. If the net energy is important, it should have long time operation therefore minimizing the electricity consumption. The optimization preference will determine which operation strategy to adopt. Since right now the economy payback is more important, in the following case analysis, the greedy strategy is used.

5.5 Summary

This chapter presents predictions which aim to validate the performance and financial models by comparing the results against test data and disclosed operation data from the Andasol-1 CSP plant. The comparison reveals that the majority of the predictions are in good agreement with actual test and operation results, in particular for the engineering performance aspects. It can be regarded that the models are reliable and able to predict the performance and payback of a CSP plant.

The net energy results indicate that the Andasol-1 CSP plant is an energy source, which is able to bring net energy. By comparing its performance under different control strategies, it shows the conflict between the energy payback and financial payback.

6. APPLICATION OF THE POWER PLANT SIMULATION MODEL*

6.1 Introduction

This chapter depicts several optimization cases and their analysis results. The simulation results of the Andasol-1 CSP plant which is shown in Section 5.3 are used as the baseline. These cases are:

- Engineering configurations
    - Change of storage system's size
    - Change the specific heat of the TES
    - Change the relative sizes of the solar field, storage system and power block
    - Increase the scale of CSP plant
    - Adopt the thermocline storage system
- Financial parameters
    - Change the loan-to-cost ratio
    - Change the discount rate
    - Change the incentive
    - Change the lifespan
- Risk analysis

* Part of the research in this chapter is reprinted with permission from "Trough Type Concentrating Solar Power Plant Cost Assessment With Component Scaling" by Luo, Jun, Michael Schuller, and Thomas Lalk, 2012, *ASME 2012 6th International Conference on Energy Sustainability collocated with the ASME 2012 10th International Conference on Fuel Cell Science, Engineering and Technology*. Copyright 2012 by American Society of Mechanical Engineers

- Risk analysis
- Risk of weather fluctuation
- Risk of broken heat collection element
- Risk of loss HTF circulation in the solar field

These cases are discussed in the rest of this chapter.

6.2 Influence of Engineering Configurations

6.2.1 Change of Storage System's Size

To better understand the function of storage system, a CSP plant without storage system is simulated. The plant has the same configurations with the Andasol-1 except the storage system. Figure 73 to Figure 76 show the daily energy flows at the same period as Figure 60 to Figure 63.

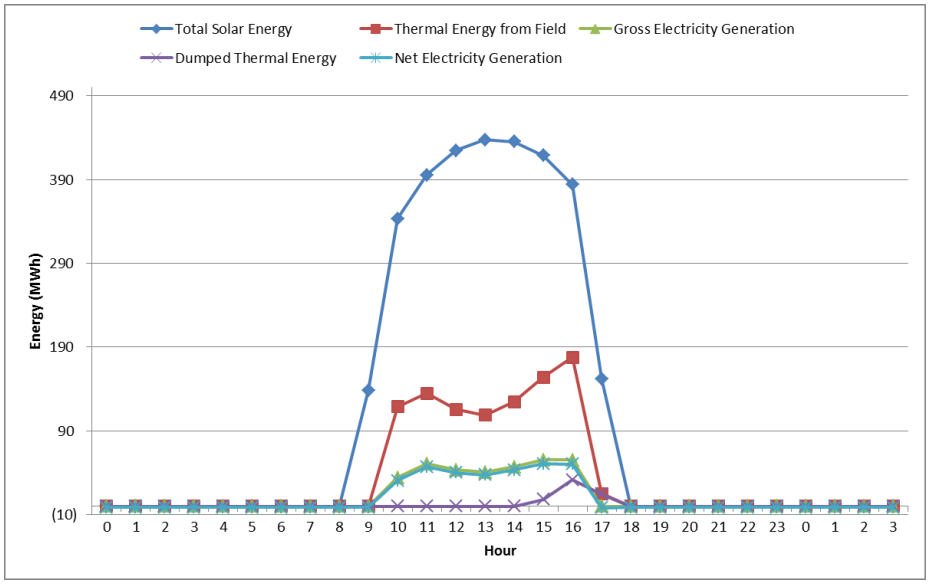

Figure 73: Daily energy flows of simulated plant without storage in Jan 15, 1989

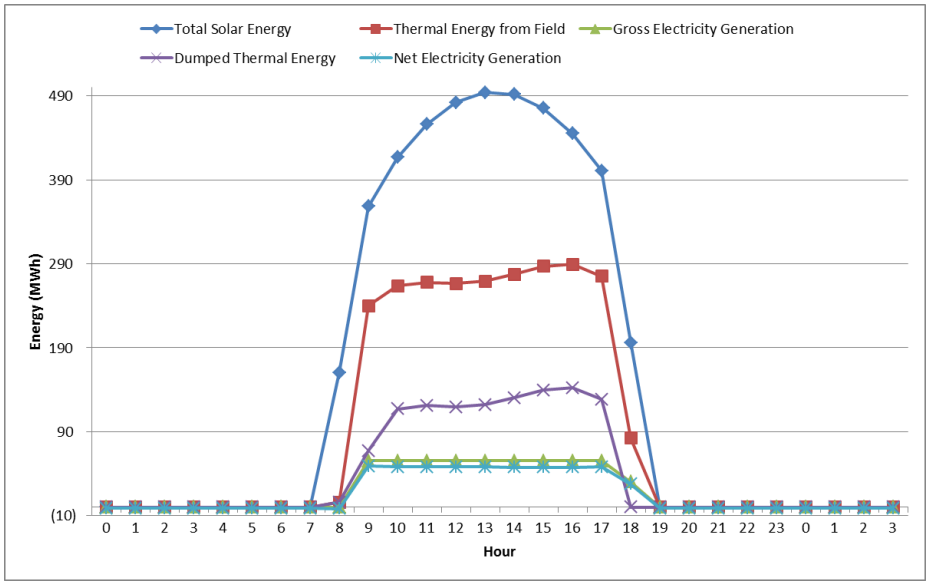

Figure 74: Daily energy flows of simulated plant without storage in Mar 23, 1989

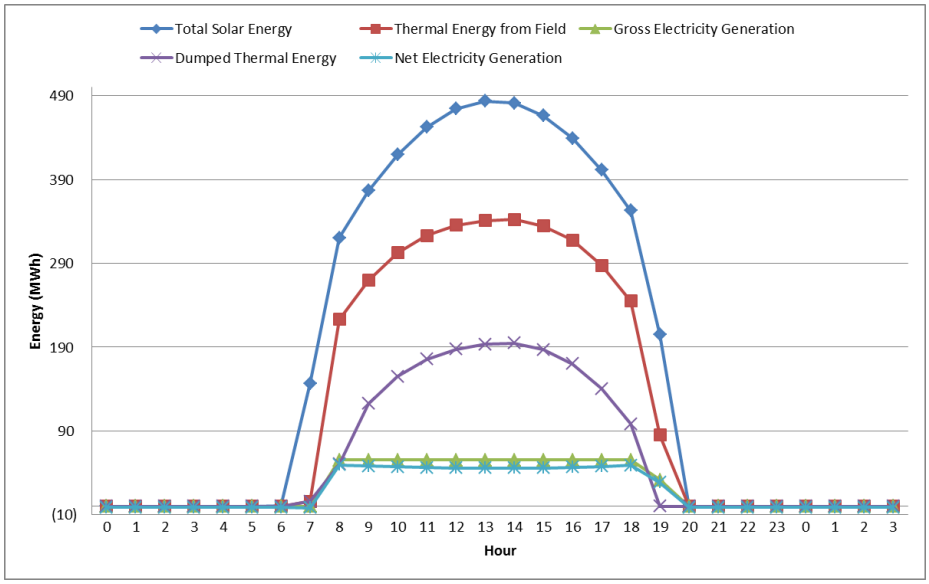

Figure 75: Daily energy flows of simulated plant without storage in Jun 23, 1989

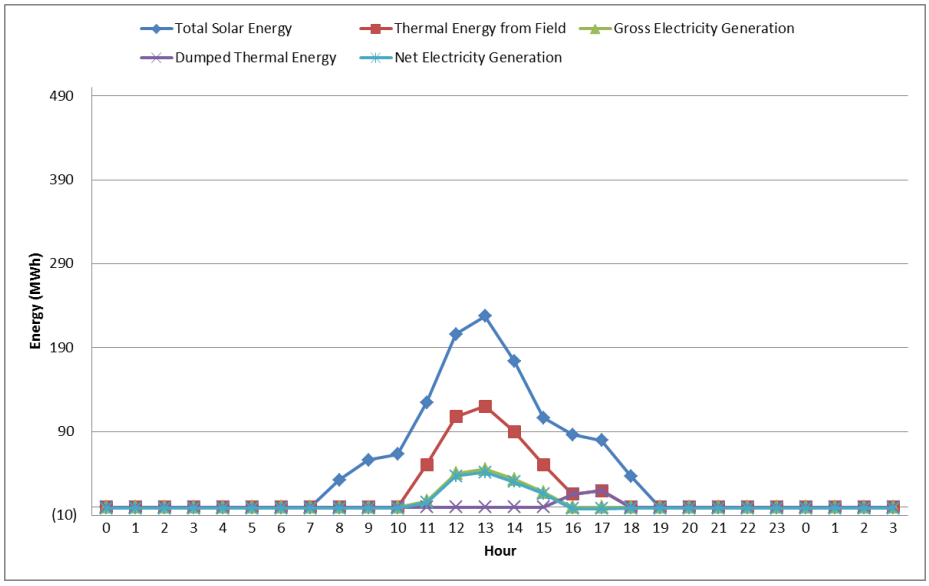

Figure 76: Daily energy flows of simulated plant without storage in Apr 1, 1989

The simulated result clearly shows the drawbacks if the storage system is not adopted:

1. The solar energy is not fully utilized:
2. The output is only available in the daytime, and fluctuating. The solar intensity and the weather condition have great influence on the electricity production, which explains why the electricity production is fluctuating.

However, choosing the right size for the storage system is also important. A small one may be able to smooth the electricity production, but it may easily be filled or depleted, in that case it would not balance the thermal energy any more. If an oversized one is chosen, it requires substantial investments to build, and demands excess heat loss during operation due to its large surface area.

Figure 77 shows the simulation results of the electricity production, the dumped energy and the LCOE when the storage sizes range from one to fifteen hours. The results indicate that when the storage capacity is less than twelve hours, the increasing of the electricity production and declining of the wasted energy with the increase of storage capacity are obvious. These increased electricity leads to a lower LCOE.

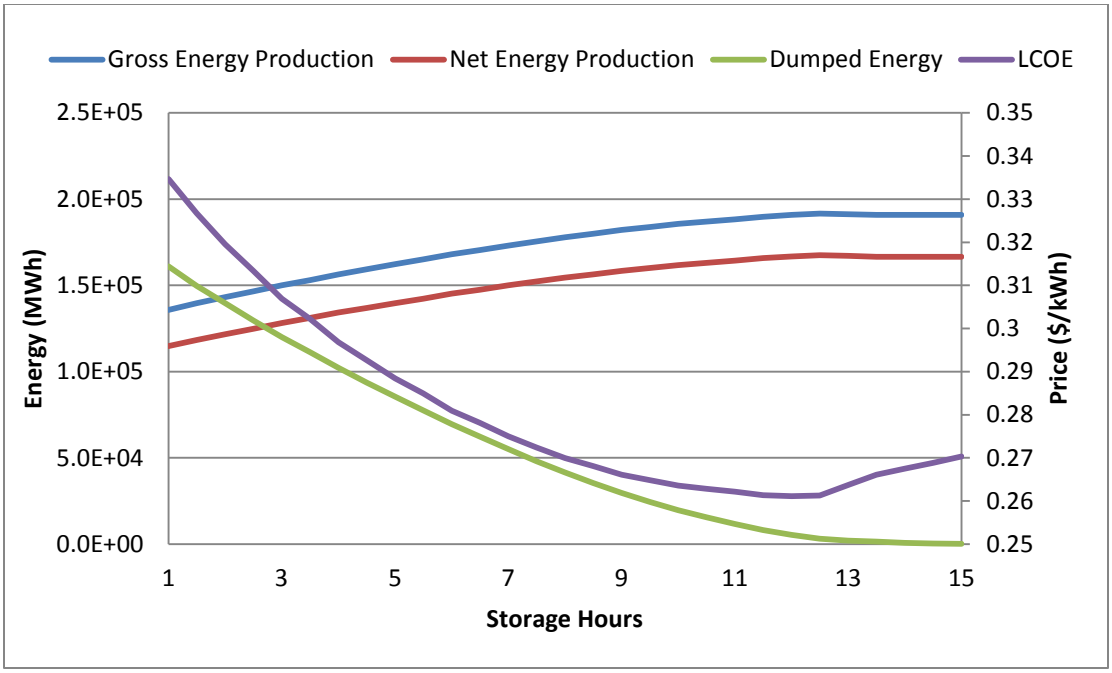

Figure 77: Gross/Net energy productions, dumped energy and LCOE vary with the storage size

The storage capacity could help increase converted thermal energy up until reaching a threshold value, upon which would have no impact on electricity production. At the same time, the cost for the extra capacity and the increased heat loss during operation would compromise the performance, which is represented as an increased LCOE, as shown in capacity beyond 12.5 hours storage in Figure 77.

Figure 78 shows the cold and hot tanks' size varying with the storage capacities. There is a decrease occurring at thirteen hours capacity, which means one pair of tanks is not enough to store the required TES, an additional pair is needed, thus each pair of the hot

and cold tank's size is reduced. They also cause a sudden increase of the surface area, which leads to an abrupt increase of heat loss, as shown in Figure 79.

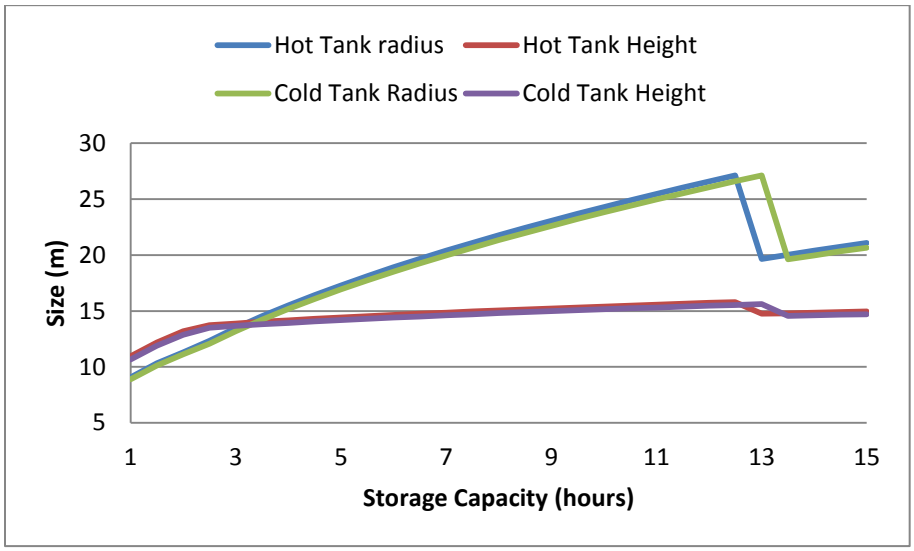

Figure 78: The variation of tank geometric size depending on storage capacity

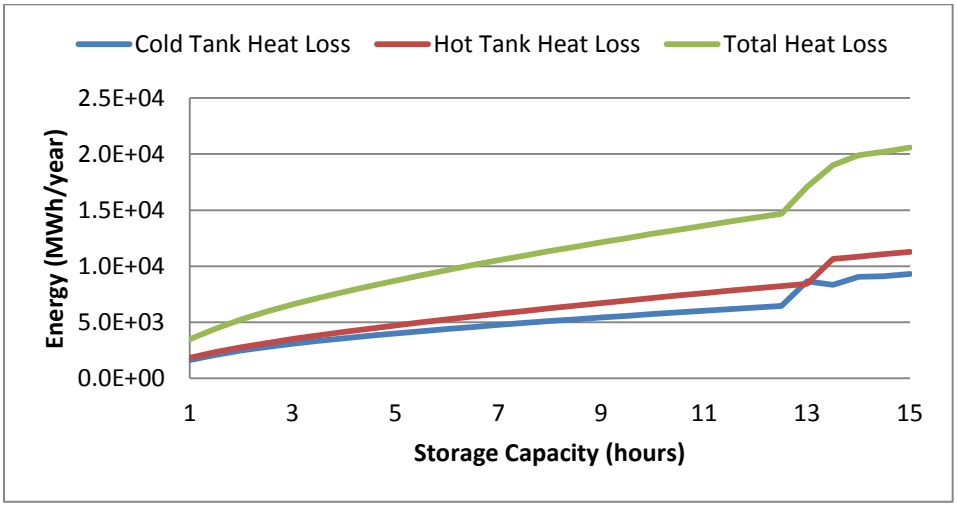

Figure 79: The variation of tank annual heat loss depending on storage size

6.2.2 Increase the TES' Specific Heat

The previous research indicates that the electricity production increases with the increasing storage capacity when the storage capacity is less than thirteen hours. Current operating CSP plants generally have less than eight hours storage capacity, some of the collected solar energy would be dumped due to the limited capability of the storage and power block systems. In order to recover this potential, some research was conducted to improve the specific heat of TES by adding additives, such as aluminum nanoparticles. With such improvement, the capacity of existing storage system would be increased.

The following simulation assumes that the additive could increase the specific heat of TES by 0% to 50% with 5% step; and the TES cost could be raised by 50% at most. The simulation results of LCOE are shown in Figure 80.

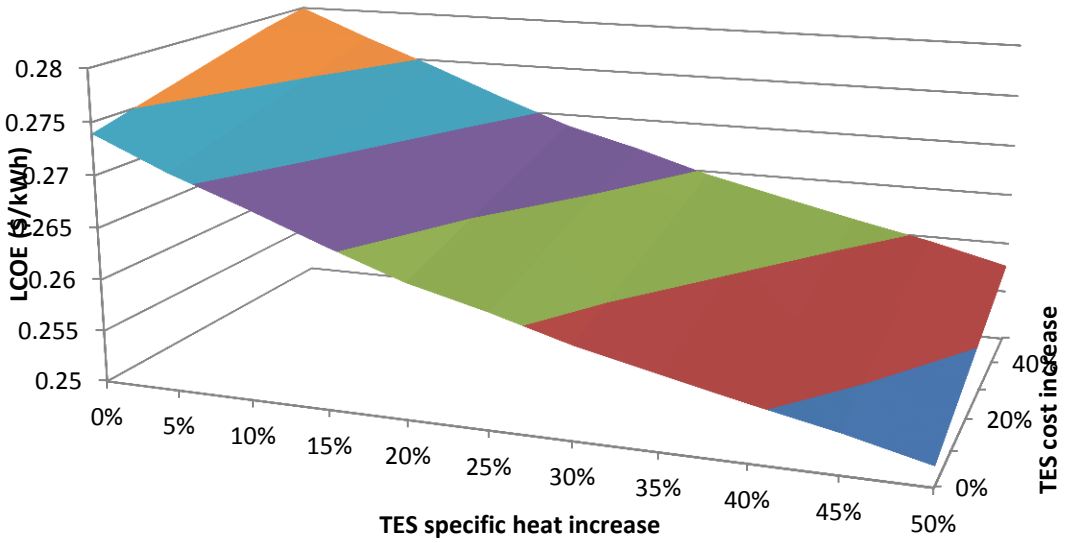

Figure 80: The variation of LCOE depending on TES specific heat and TES cost

The results indicate that the increased specific heat has a significant effect on reducing the LCOE. If the specific heat increases by 50% and cost of additive is zero, the LCOE would be decreased by 8%. Even with 50% material cost increasing, it would still reduce the LCOE by 6%. The result is consistent with the conclusion of increasing storage tank since both methods increase the storage capacity at last, but through a different approach. Moreover, by using improved specific capacity method, it does not need to change the existing storage tank, which means the storage's surface area is the same. So, the heat loss from the storage tanks is almost constant, while the enlarged storage tank has linearly increased heat loss with its capacity. The comparisons are shown in Figure 81. Other advantages include: the required pumping power could be reduced due to the

decrease of TES flow rate. And it is easier to add additives to existing storage systems than to enlarge them.

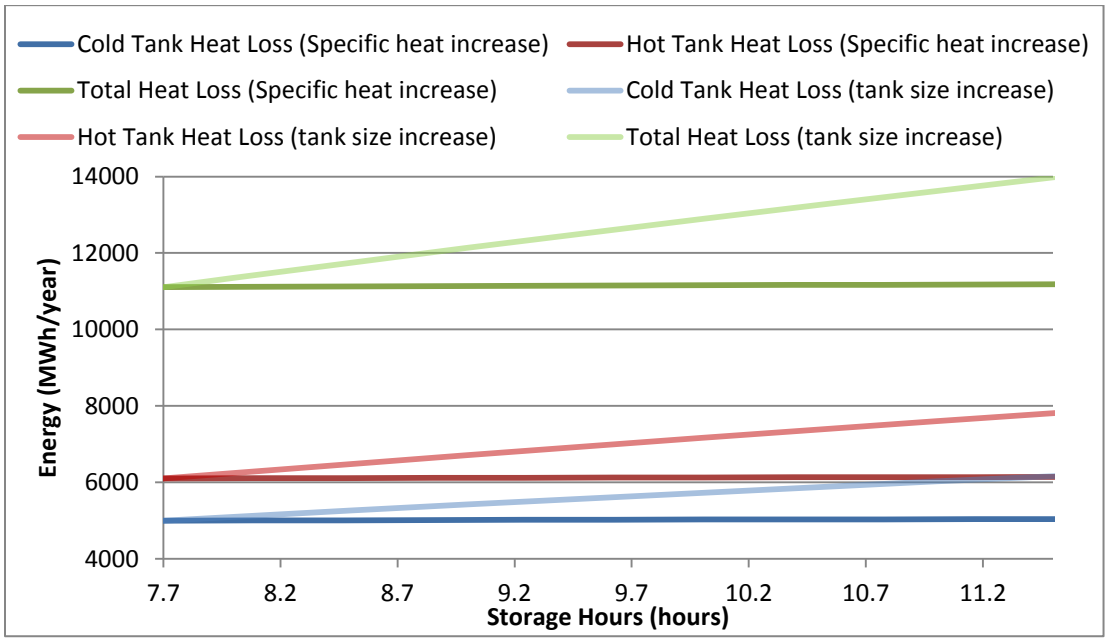

Figure 81: Heat losses from the storage system with increased TES specific heat or enlarged storage tank

6.2.3 Change of Relative Size of Solar Field, Storage System and Power Block

The relationship between the electricity cost and the scale of each system was investigated. These scales are: the area of the solar field, the capacity of storage capacity, and the rated power of the power block. Since these sizes are related, the solar field size is set as fixed and exactly the same as the one used in the Andasol-1 power plant. The

power block and storage's sizes are adjusted by the parameters - solar multiple (SM) and full load hours.

During simulation, the SM is set to range from one to three, with the interval of 0.1. The minimum solar multiple indicates that the solar field should supply enough thermal energy to power block under design condition, and the maximum value refers to the non-stop operation condition.

The full load hours range from one to fifteen. The minimum storage (one hour capacity) was set in order to smooth out the fluctuation of the collected solar energy, and prevent frequently stopping and starting of the power block. The maximum value was set to store enough thermal energy for non-stop operation (the interval between two successive daytimes is usually less than 15 hours).

The simulation results are shown in Figure 82. The net electricity production increases and then decreases with either the storage capacity or the solar multiple.

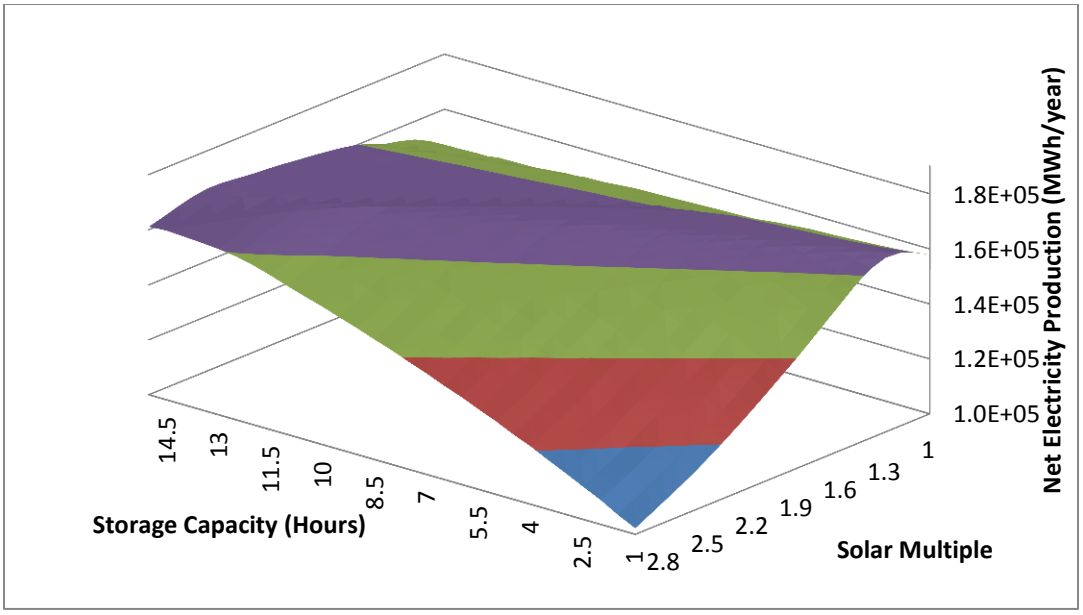

Figure 82: The variation of net electricity production depending on SM and storage capacity

Figure 83 shows the dumped energy varies with the storage capacity and the solar multiple. The best configuration should occur in the area that the dumped energy is close to zero. In such condition, the system is almost fully utilized. Also, the figure indicates that improper design may cause large amount of energy waste. For example, when the solar multiple is large and the storage capacity is small, the collected solar energy is wasted since it exceeds the capacity of the storage and power block systems. Another example is, if the storage capacity is large and the solar multiple is small, the solar field produces equal or slightly more energy than the power block's need, the storage tank would barely be utilized. And with the most inappropriate configurations, such as when

SM is one and storage capacity is fifteen hours, the storage system may malfunction after some operation period, and cause energy dumps, as shown in Figure 83.

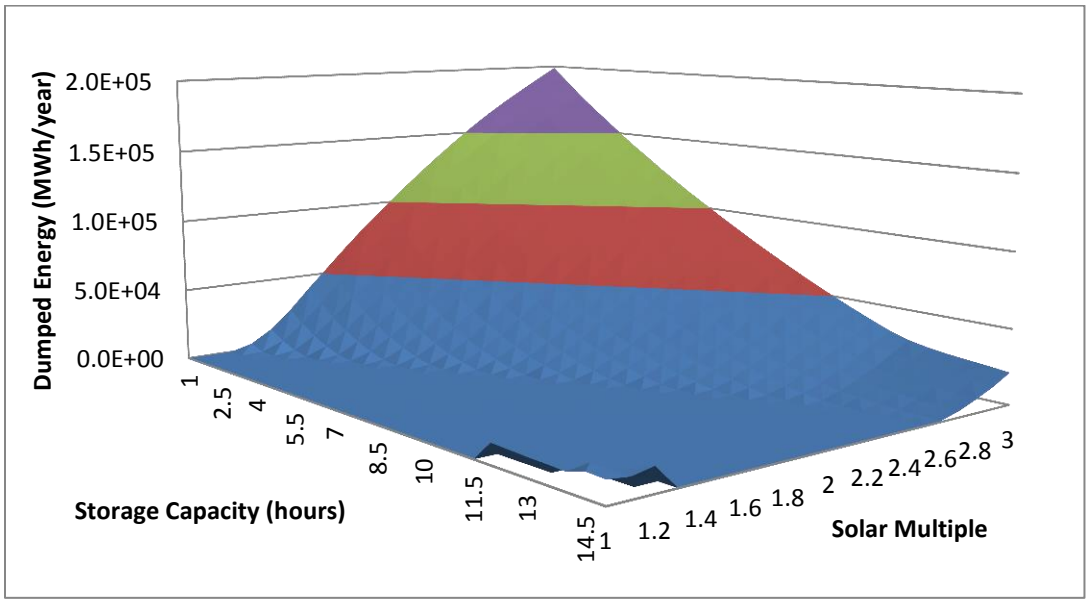

Figure 83: The variation of dumped energy depending on SM and storage capacity

Figure 84 and Figure 85 show the hourly simulation results when SM = 1 and storage capacity = 15. It shows why the dumped energy exists: The hot tank is slowly charged at the beginning, but due to the large heat loss and the slow charging rate, its temperature is low, so the stored energy could not be used. Once the hot tank is full, the storage system tends to malfunction - it could not accept or reject TES. In that case the extra collected thermal energy from the solar field has to be wasted.

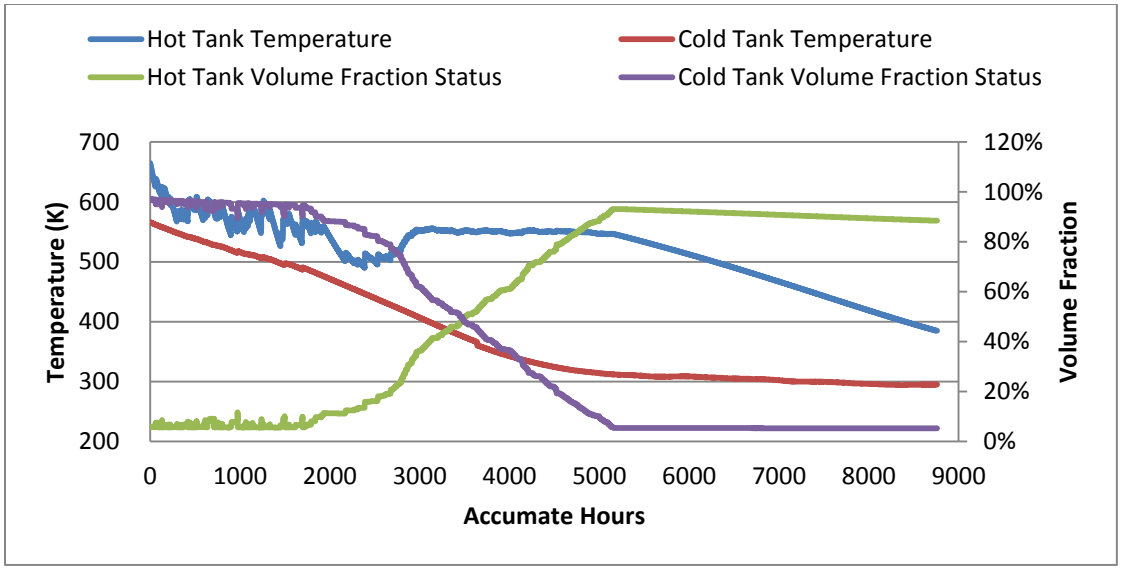

Figure 84: Hourly hot/cold tanks' temperatures and volume fractions when SM = 1 and storage capacity Hours = 15

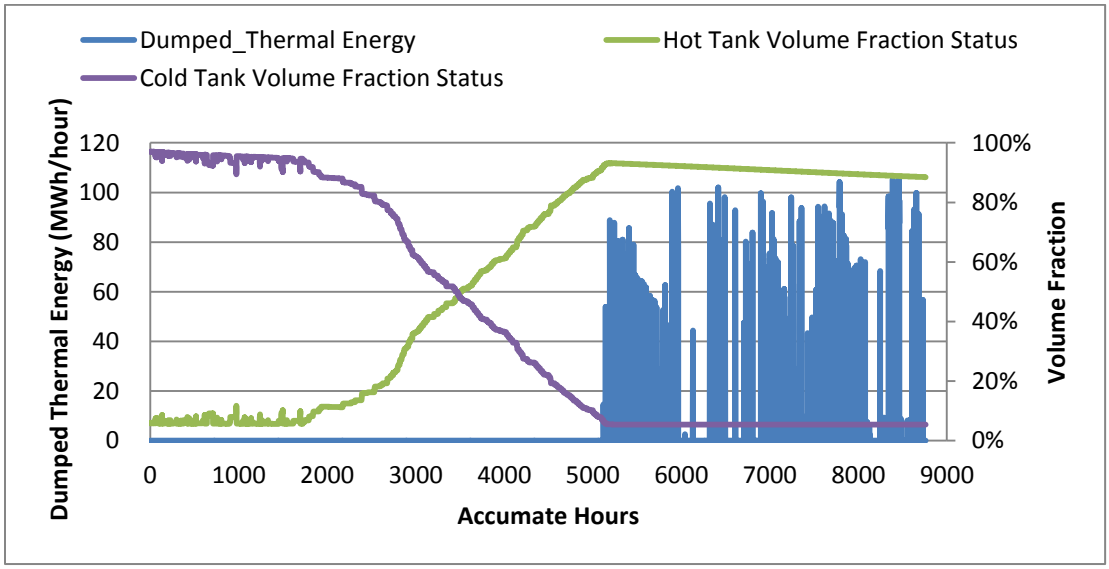

Figure 85: Hourly hot/cold tanks' volume fractions and dumped energy when SM = 1 and storage capacity Hours = 15

Figure 86 shows the LCOE varies with different configurations. The lowest LCOE occurs with the most feasible configurations from the financial payback perspective.

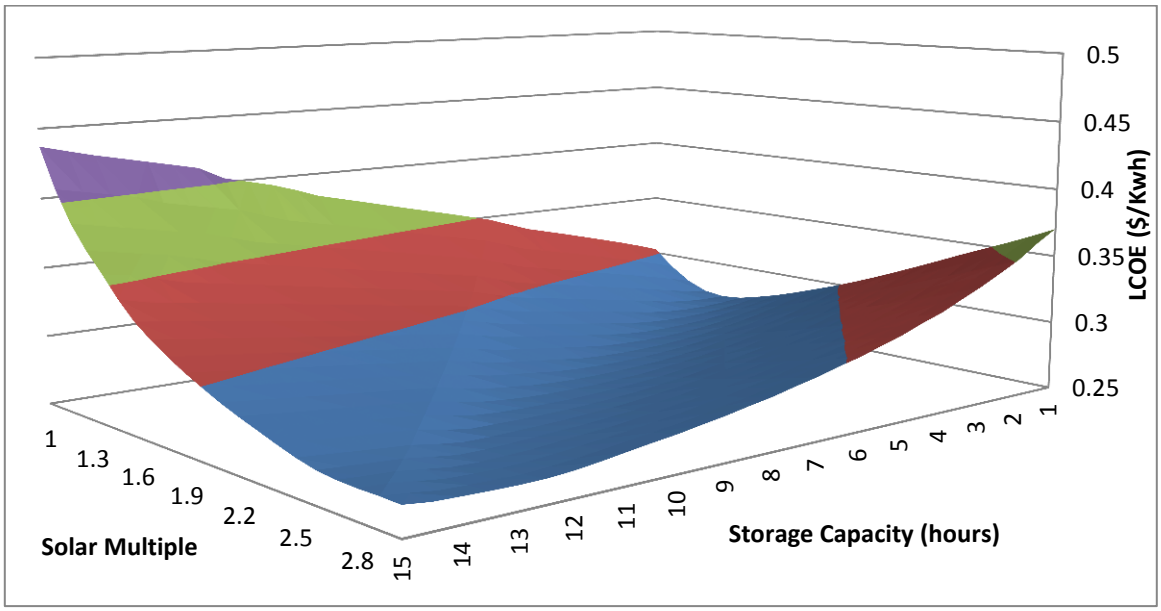

Figure 86: The variation of LCOE depending on SM and storage capacity

Figure 87 shows the storage capacity when the maximum net electricity production or the lowest LCOE occurs. Both results have similar pattern: the storage capacity increases with the solar multiple. The configuration of Andasol-1 is located in the minimum LCOE line, which indicates its design is able to achieve the lowest cost.

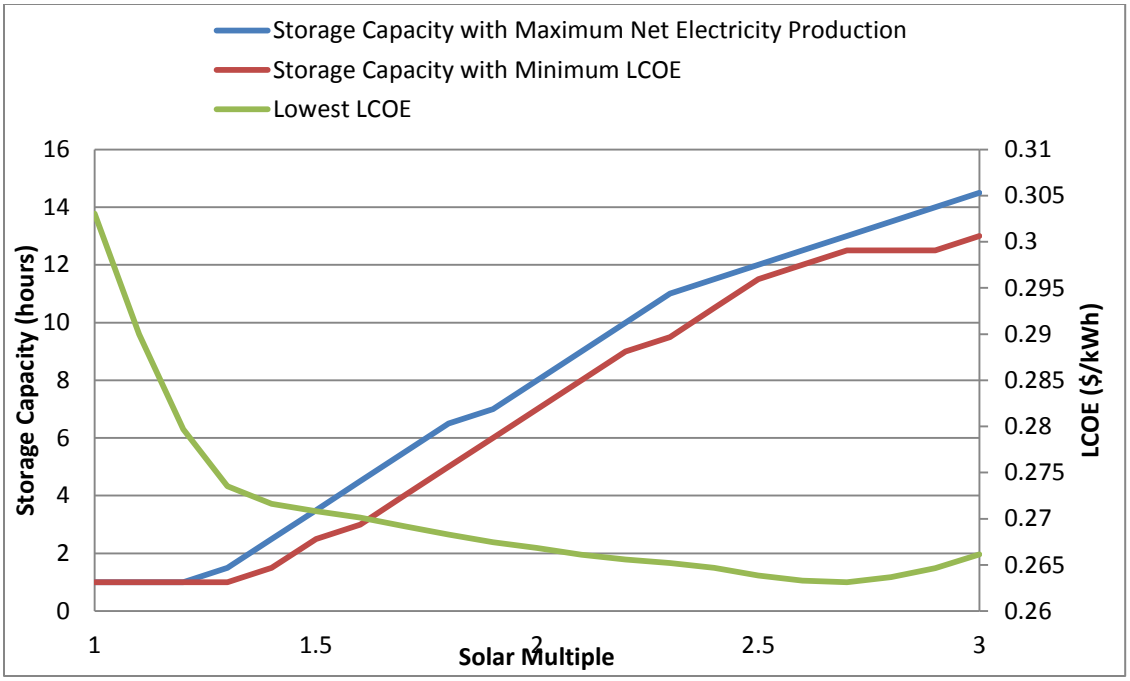

Figure 87: The storage capacity and LCOE when the lowest LCOE and the highest net electricity production occur

6.2.4 Increase the Scale of plant

Typical fossil power plants have hundreds or thousands of megawatts capacity. However, the solar power plants' capacities are no more than 50 *MW*. The small scale may be an important reason for solar powers' high electricity cost.

Figure 88 shows how the subsystems' costs vary with the plant sizes. The cost can be reduced by 50% of its original values when the plant size increases from 50 *MWe* to 400 *MWe*. The increase of plant size would result in the largest cost reduction in the power block system among all subsystems, because the original scale is small, so the scale

effect is obvious. The reduction of relative cost of the storage system is indistinct, since the cost of the TES is linearly correlated with the scale.

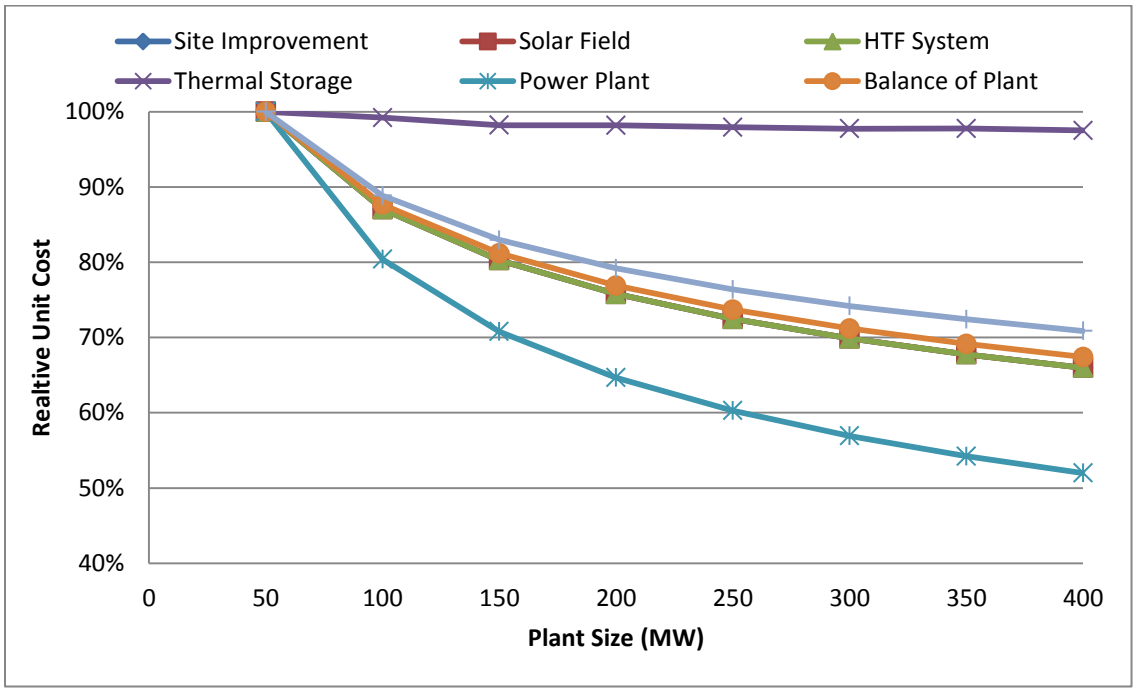

Figure 88: Comparison of relative components cost with different plant sizes

As expected, the annual electricity generation increases linearly with the scale, as shown in Figure 89. The scaling up is similar with the effect of having multiple plants operating at the same time, it is reasonable to justify that the electricity production is linearly correlated with its scale.

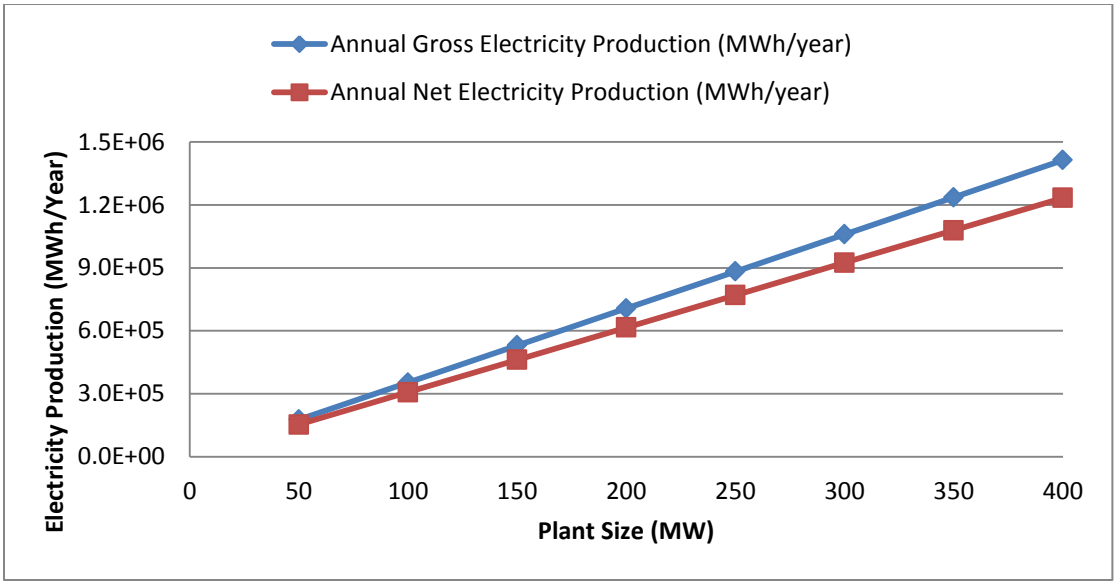

Figure 89: The variation of gross and net electricity production depending on plant size

Figure 90 shows how the installed cost and the LCOE vary with the plant scale. The decreasing rates of the installed cost and LCOE slow down with each scale increment. That indicates the increasing size is approaching the economic threshold and the scale effect has less effect on the cost reduction. When the power plant size reaches 400 MW, the curve becomes flat. With that plant size, the installed cost would be reduced by 29.1% and the LCOE would be reduced by 32.9% compared with the original 50 MWe size.

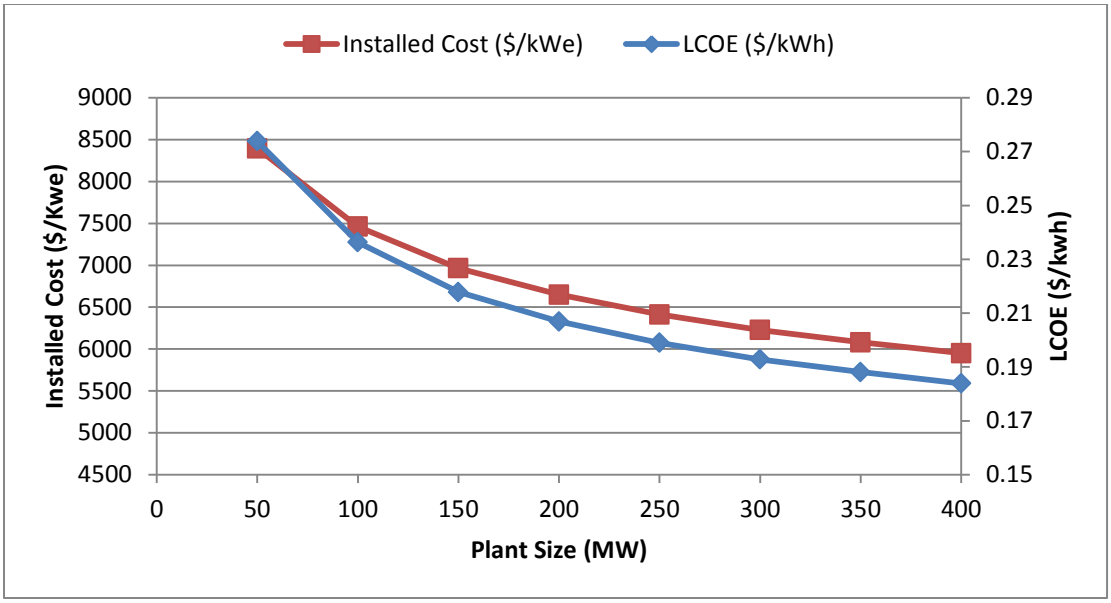

Figure 90: The variation of installed cost and LCOE with different plant sizes

6.2.5 Adopt the Thermocline Storage System

One promising way to reduce the cost of the storage system is by using the thermocline type storage system instead of the two-tank type storage system. Because the thermocline storage system is able to store the hot TES on top of the cold TES in the same tank, which potentially eliminates the necessary of using additional tanks to achieve the same storage capacity.

During the charging phase, hot TES is charged into the tank from the top, while the cold TES at the bottom is pumped out for energy absorbing at the same time. When energy is being discharged, this procedure is reversed. The thermocline storage system reduces the costs in two ways: first, the tank installation cost is reduced. Second, it could use a

secondary energy storage medium to store the thermal energy, and the medium could be much cheaper than the TES used in a two-tank system. Table 18 shows the tank diameters and storage medium cost. It indicates the thermocline system only needs one tank to store the design amount of thermal energy, and the construction cost is lower than the two-tank system. In addition, the storage medium cost is 28% lower than the cost of the two-tank system.

Table 18: Comparison of the storage systems

	Height (m)	Radius (m)	Number	Storage Medium Cost ($)
Hot Tank	14.99	21.36	1	6.61E+07
Cold Tank	14.75	20.94	1	
Thermocline	14.84	26.93	1	4.76E+07

Another benefit of adopting the thermocline system is that its heat loss is reduced by around 30%, because its surface area is smaller than the two-tank system. The reduced heat loss boosts the annual gross and net electricity productions by around 0.3% and 1%, as shown in Figure 91.

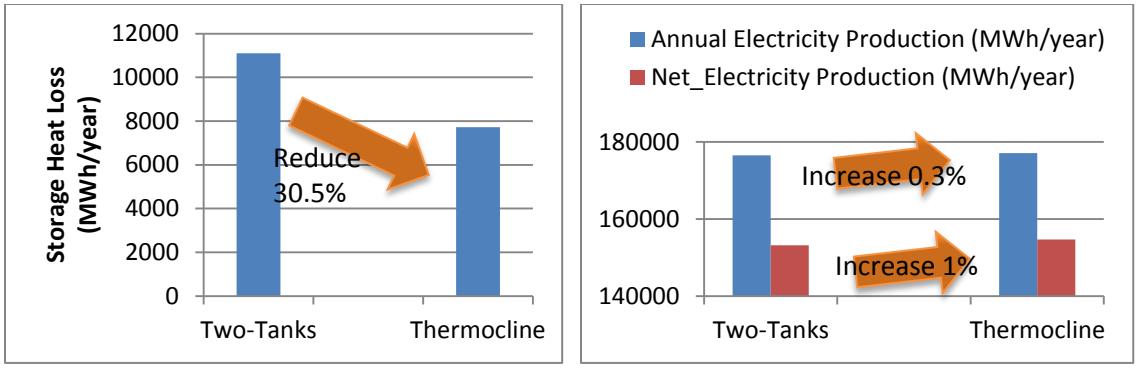

Figure 91: Comparison of storage system heat loss and electricity production between the two-tank and the thermocline storage systems

From the financial aspect, the installed cost is reduced by 4.2%, from $8400/kw to $8040/kw when the two-tank type storage system is replaced with the thermocline one. The LCOE is lowered by 4.5%, or $0.01/kWh, as shown in Figure 92.

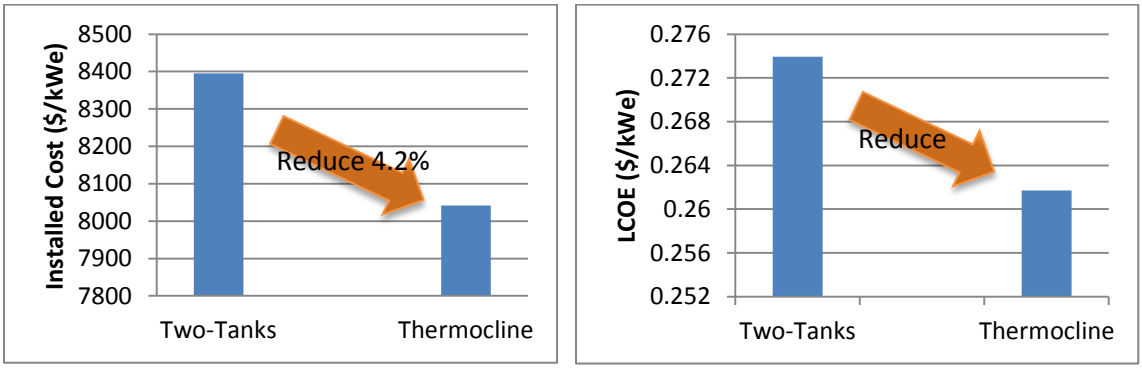

Figure 92: Comparison of the installed cost and the LCOE between the two-tank and the thermocline type systems

6.3 Influence of Financial Parameters

6.3.1 Loan-to-cost Ratio

Loan is leveraged to guarantee financial feasibility of a CSP project. In the following content, three kinds of loan configurations were analyzed:

1. Low loan rate, 4% is used;
2. Middle loan rate, 7% is used;
3. High load rate, 10% is used;

And the loan term varies from 10 to 30 years, the loan-to-cost ratio changes from 0 to 100%. The simulation results of LCOE are shown in Figure 93.

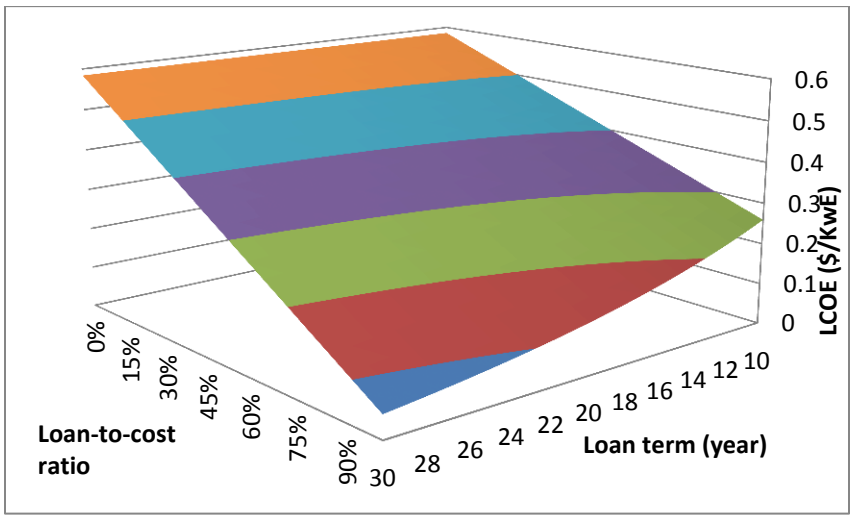

Figure 93: The variation of LCOE depending on loan term and loan-to-cost ratio (rate 4%, 7% and 10% from top to bottom)

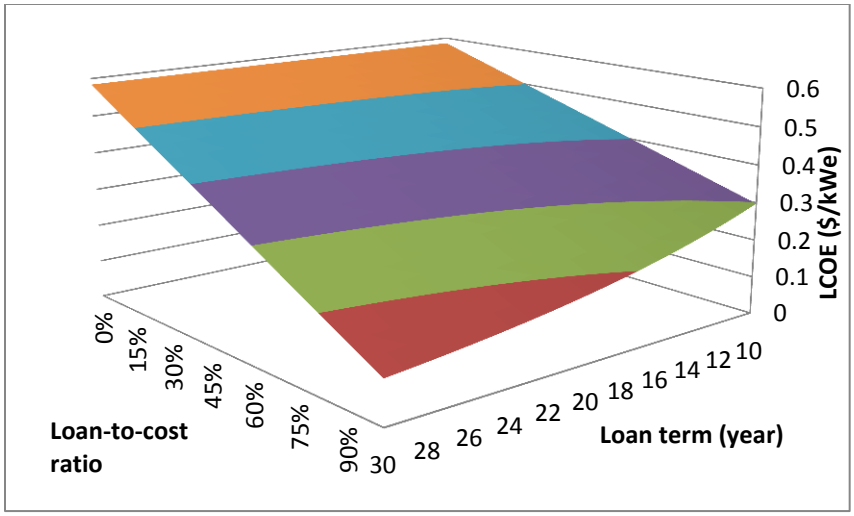

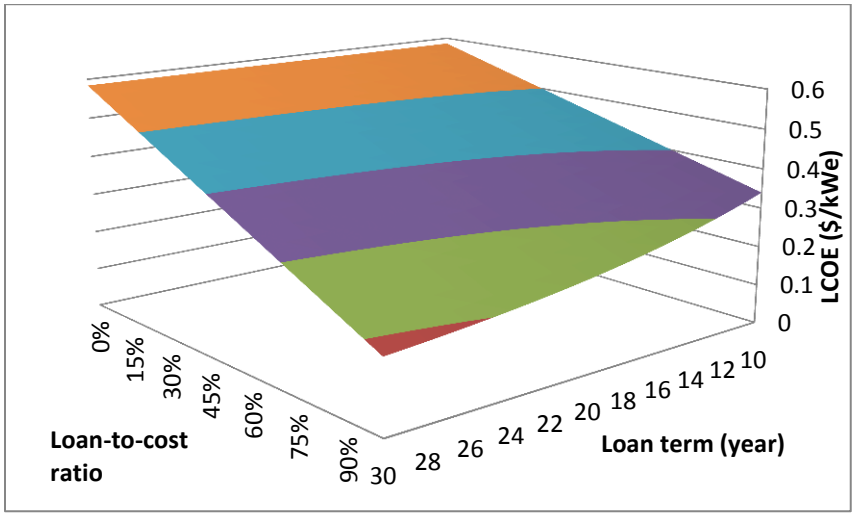

Figure 93 Continued

The results indicate that the loan configuration has a great effect on altering the LCOE. With all three loan rates, LCOE decreases with the loan-to-cost ratio and loan term. This

phenomenon is significant when the loan rate is low. For example, with a 4% loan rate, 30 years amortization term and 100% loan-to-cost ratio, the LCOE could be reduced to \$0.055/kWe, which is less than 10% of the one without any loan (\$0.584/kWe). Though the extreme condition is not realistic, it still shows the potential cost can be reduced by adopting loans.

Figure 94 shows the plot that the LCOE varies with the loan term when the loan-to-cost ratio is 80% fixed. The figure indicates that longer loan term or lower interest rate leads to low LCOE.

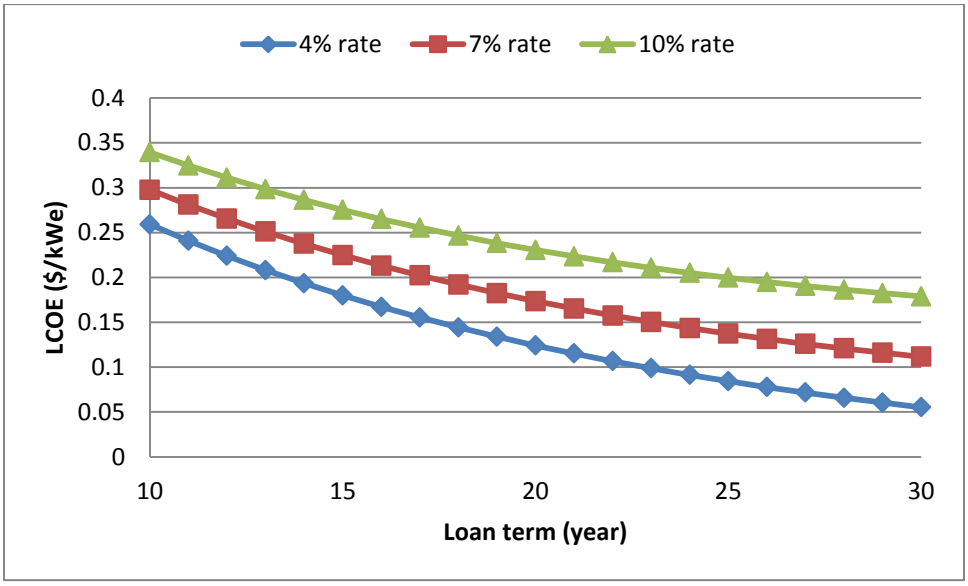

Figure 94: Minimum LCOE with different loan terms

Figure 95 shows another set of financial configurations of the same CSP plant. It has a 20 years loan term and 80% loan-to-cost ratio. The annual payment increases from 2.5×10^7 to 3.9×10^7 when the loan rate increases from 4% to 10%. Due to the high payment, a higher LCOE is required to cover this additional interest cost, it escalates from \$0.22/kWe to \$0.30/kWe.

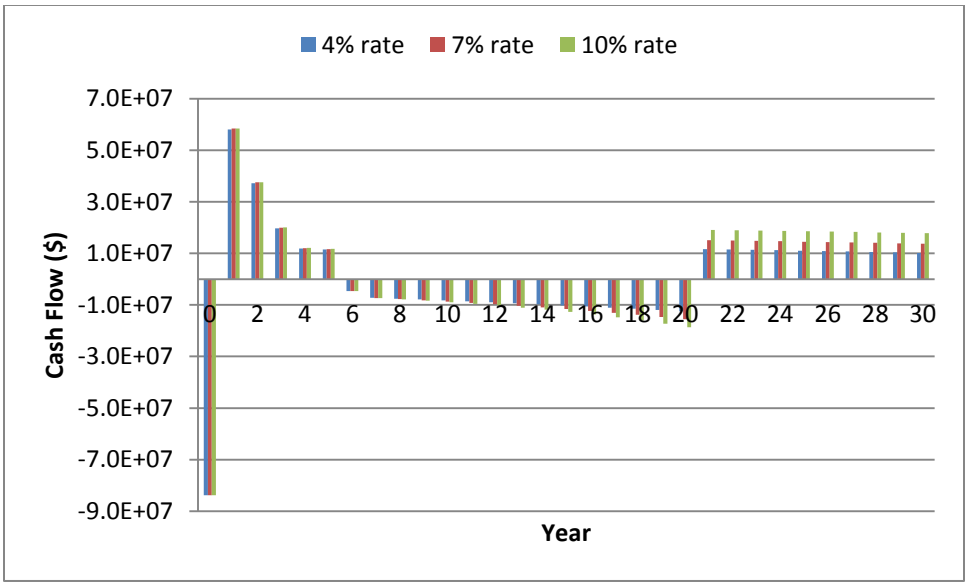

Figure 95: Cash flow comparison among 4%, 7% and 10% loan rates

6.3.2 Discount Rate

Discount rate is an economic parameter used to estimate the time value of the LCOE. It converts all future cash flows to present values using a given required rate of return. It is used to estimate the risk inherent in an investment and the time value of money.

There are two kinds of discount rates, real and nominal discount rate, the difference is: nominal discount includes the inflation while the real discount does not. In the following simulation, the real discount rate is adjusted from 4% to 12% to see how it influences the LCOE, as show in Figure 96.

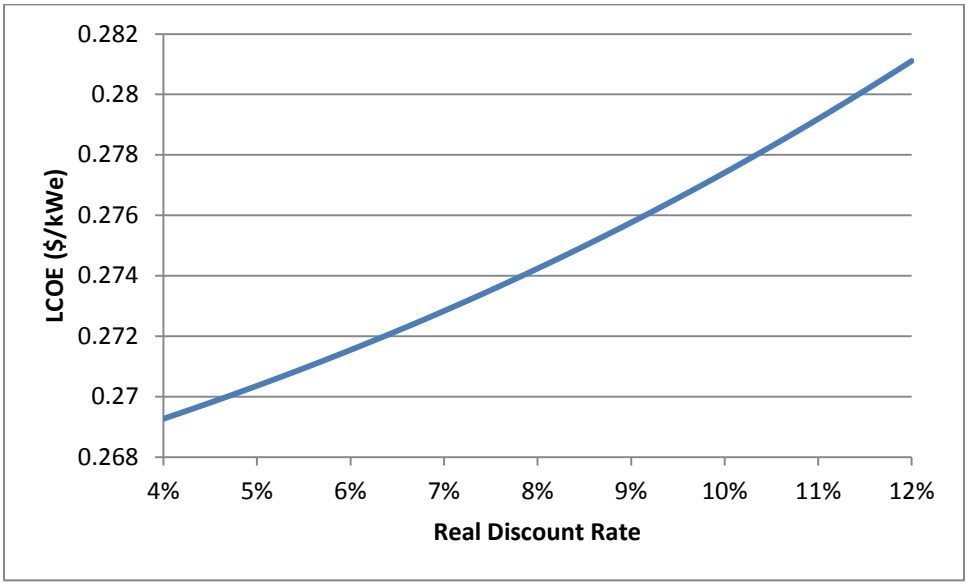

Figure 96: The variation of LCOE depending on real discount rates

The result indicates the LCOE increases with real discount rate. When the discount rate escalates from 4% to 12%, the LCOE rises by 5%. The reason is such: when a project has a higher risk level, its cost would be increased to offset the potential risk.

6.3.3 Incentive

Spain has more than one thousand megawatts of installed CSP plants. It accommodates 55.4% of the world's CSP capacity, ranking the first among all countries. The United States has 38.3% of world's CSP capacity, ranks the second. The third one, Iran only contributes to five percent of total CSP capacity in 2010 [77].

There are several reasons why this disparity exists: The first and one of the largest reasons is the environment. Spain and the Unites States have well suited environment for the development of CSP technology.

However, other countries may have the same good environment conditions. So another big reason why Spain and the U.S. dominate CSP market is the strong regulatory support.

Spain and the U.S use two different methods to support the development of CSP industry.

The Feed-in Tariffs (FiT) is adopted by Spain and is considered as the most successful example for spurring the CSP industry development. In 1998, the Royal Decree on the Special Regime (RD 2819/1998) provided two options for renewable energy: (1) a fixed total price or (2) a fixed premium on top of the market electricity price. In 2004, the amended RD 436/2004 allowed renewable energy producers to sell electricity to distributors or market directly. In 2007, the modified RD 661/2007 decoupled renewable energy support from average electricity tariff (AET), and tied it to the CPI [78]. It also instituted a cap-and-floor system for the premium on top of the electricity market price [79].

However, in early 2013, may be due to the economic crisis in Spain, the Spanish government approved a new law which was to modify the RD 661/2007 regulation, aiming at reducing the electricity sector cost. The new regulation could cause a 30% reduction of revenue for CSP plants.

The U.S. government prefers to support the renewable energy industry with the Renewable Purchase Standard (RPS). It is usually combined with an assortment of incentives, such as properties and sales tax reduction, investment and production tax credits, federal loan guarantees, clean energy bond and fast properties depreciation. Some of the incentives and subsidies may benefit the solar industry are [80]:

1. Investment Tax Credit for companies investing in solar project (IRC Section 48);
2. Five Year Modified Accelerated Cost Recover (IRC Section 168(e)(3)(B));
3. Tax Credit for Clean Renewable Energy Bonds (IRC section 54);

Since the Andasol-1 is a Spanish CSP plant, so the feed-in tariffs according to RD 661/2007 are adopted as the incentive. The detailed content is:

A fixed FiT rate of EUR 26.9375 cents/kWh is guaranteed for 25 years, and adjusted annually according to the changing CPI minus one percent. After 25 years, the FiT drops to a constant of 21.5 cent/kWh [79].

The following modifications have been applied in this model:

1. The depreciation method is changed to the straight line method;
2. In the first 25 years of operation, incentive is set to $0.34/kWe and escalates by 1.5% annually. This incentive is a taxable income;
3. In the operation years beyond 25, incentive is set as $0.27/kWe constant, and is regarded as a taxable income;

The simulation result indicates that the LCOE can be reduced to $0.044/kWe after the above incentives are applied. This cost is competitive with fossil energy and makes it profitable to operate. It may explain why Spain has a boom development of the CSP industry after year 2007.

Figure 97 shows the annual cash flows and incentives during its lifespan. The after tax cash flows has experienced several variations: in year one, the change is caused by the sale tax deduction; in year 20, the change is caused by the ending of the depreciation, and the variation after year 25 is due to the variation of incentives.

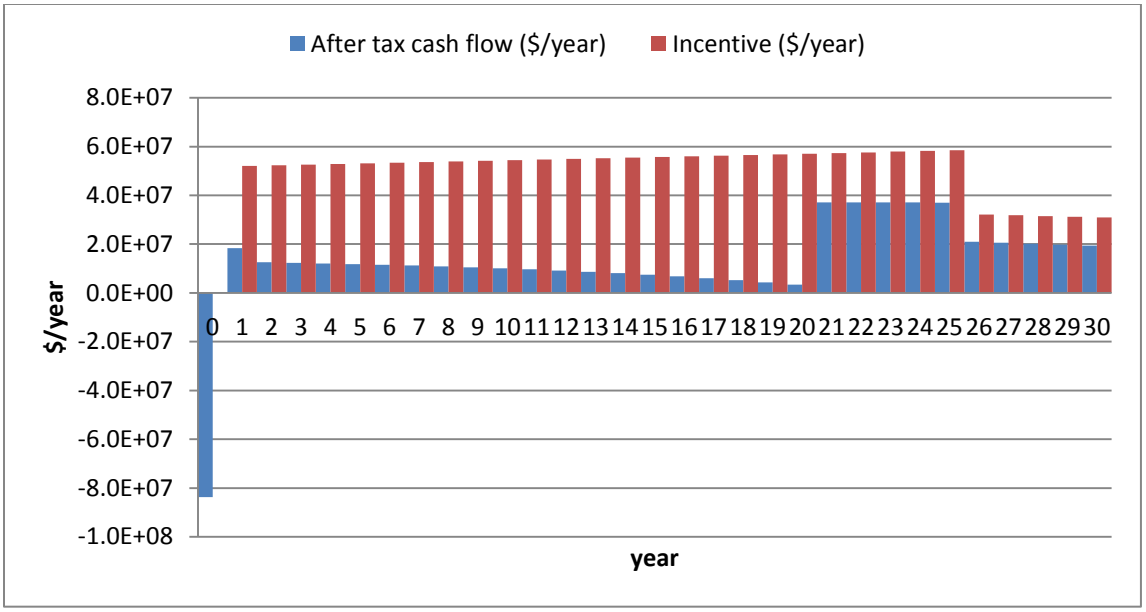

Figure 97: Yearly after tax cash flows and incentives during the CSP plant's lifespan

From Figure 97, it clearly shows that the incentives are critical for the reduction of the LCOE. The cash flows caused by incentives are dominant. It can be concluded that the incentive is the most important factor that makes the CSP plant feasible and profitable.

6.3.4 Lifespan

To determine the lifespan of a CSP plant is complicated. Generally it may involve several factors such as whether its performance or reliability is compromised to an unacceptable level; whether it is not financially feasible anymore; Or whether its external environment have gone through drastic changes – such as lack of resource to maintain the operation, pollution or changing public opinion. Those potential risks

would not be an issue for a CSP plant due to its replaceable components, infinite energy life, and relatively positive public opinions. So maybe the economic payback is the only concern for its lifespan. During simulation, its lifespan is set from 20 to 50 years and the relation between the LCOE and lifespan is analyzed.

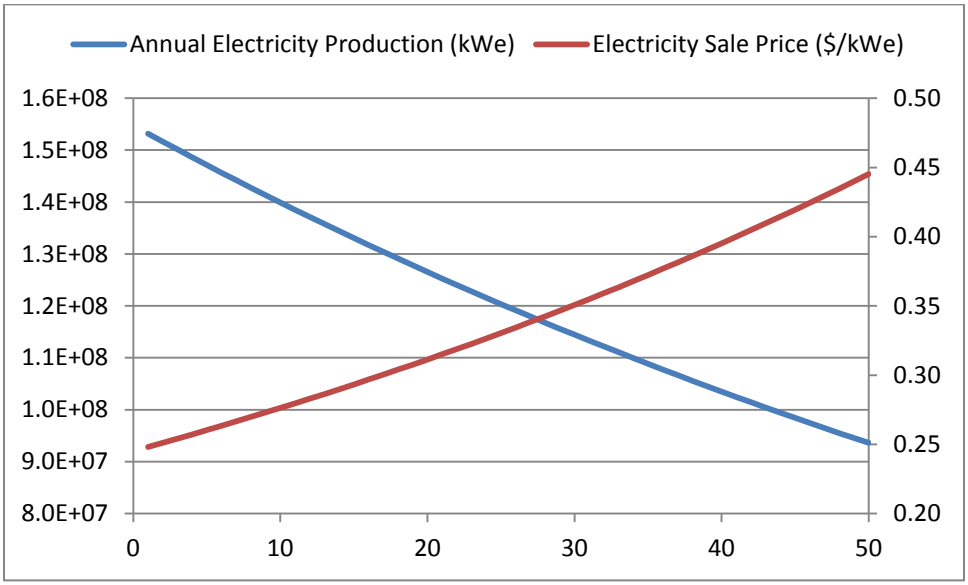

Figure 98: Electricity production and its sale price during CSP plant's lifespan

Figure 98 is the electricity production and price of the CSP plant during the designated operating period. The electricity production would be reduced by 40%, and the electricity sales price would increase by 80% after 50 years' operation. However, considering the inflation is 2.5% while electricity sales price only escalates by 1.2% annually, the value of sale price actually depreciates with times, as shown in Figure 99.

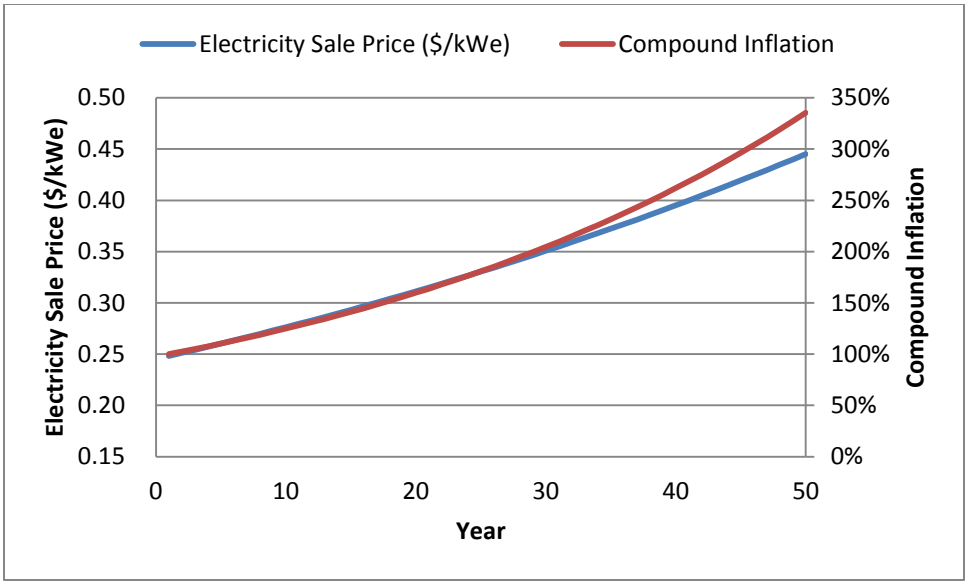

Figure 99: Electricity sale price and compound inflation vary with time

Figure 100 shows how the operation cost and income vary with time in a 50 years' operation period. With the performance deteriorating over time, the income would drop slowly, and the cost of operation increases due to the increase of salaries, intensive maintenance work and inflation. These two cash flows are equal in year 43, which is regarded as the maximum acceptable lifespan, operation after which time leads to negative cash flow and economic loss.

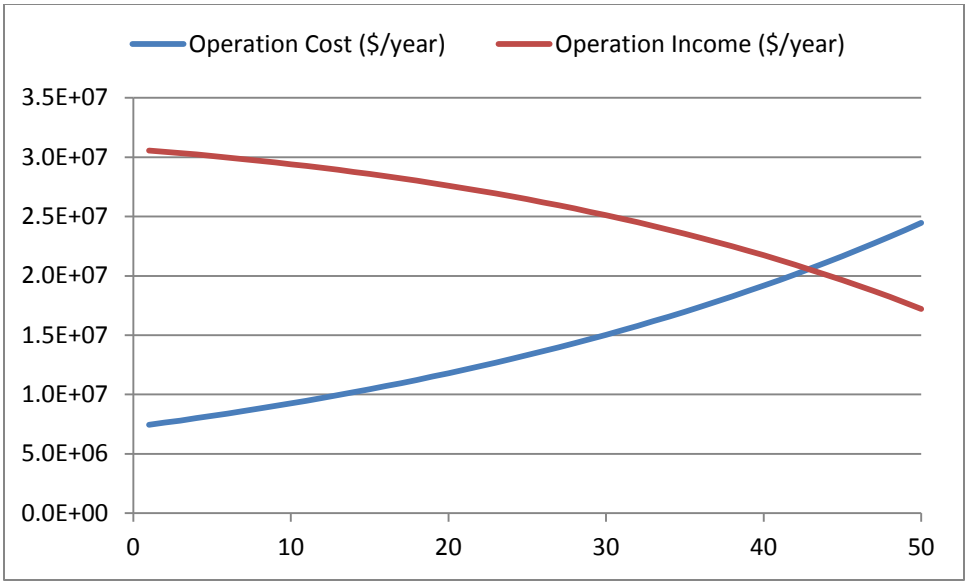

Figure 100: Operation cost and income during the CSP plant's lifespan

Figure 101 shows the LCOE changes with different lifespans. It reaches the lowest value when the lifespan is 30 years, which is the same as the expected lifespan of current CSP plants. Shorter or longer lifespans would accrue high LCOE. However, the variations of LCOE caused by different lengths of lifespan are not obvious. It may not be an important factor to affect the economic payback.

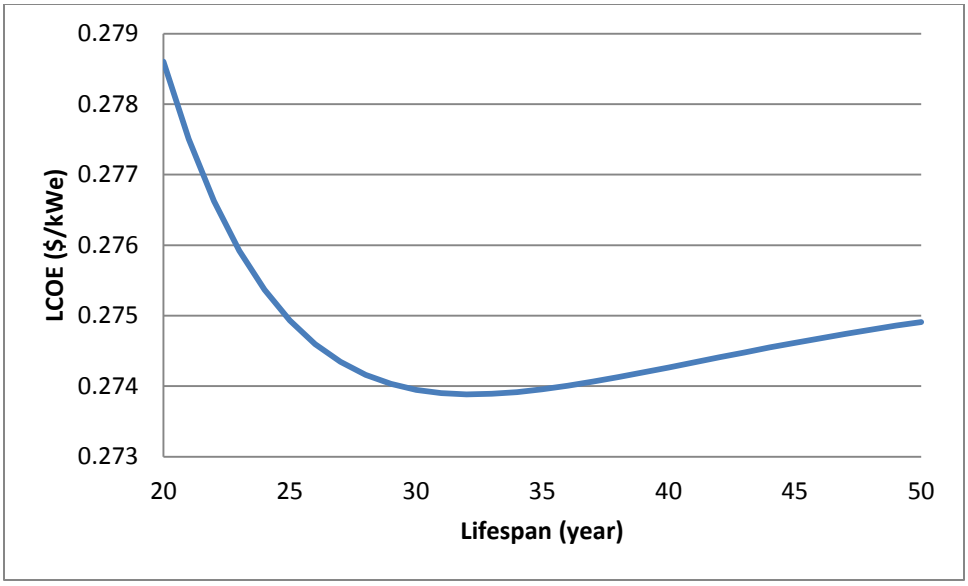

Figure 101: The variation of LCOE with different lifespan lengths

6.4 Risk Analysis

6.4.1 Weather Fluctuation Risk

The sunlight, as the fuel of CSP plants, is important to the plants' performance and financial viability. The variability of the sunlight supplement may be the greatest uncertainty in the plant's predicted performance. However, the DNI of a specified location varies with time and is affected by local weather, and it is hard to predict, especially for long time periods. For example, Figure 102 shows the annual averaged insolation data in Granada, Spain for more than twenty years (1984 – 2005), the mean value is 4.76 $KWh/m^2/day$, and the standard deviation is 0.15 $KWh/m^2/day$. The DNI should in the range between 4.46 and 5.06 $KWh/m^2/day$ with 95% confidence, if the DNI is normal distribution. Additional, both measurement and solar intensity modeling bring

uncertainty to the solar intensity historical data. The measurement uncertainty ranges from 3% to 10%, the modeling uncertainty of a stationary measurement is 5%[81], and the modeling uncertainty of a satellite measurement is more than 10% [82]. the uncertainties are not ignorable, and the performance and financial fluctuations caused by the variation of the DNI may even changes a profitable project to one that is losing money.

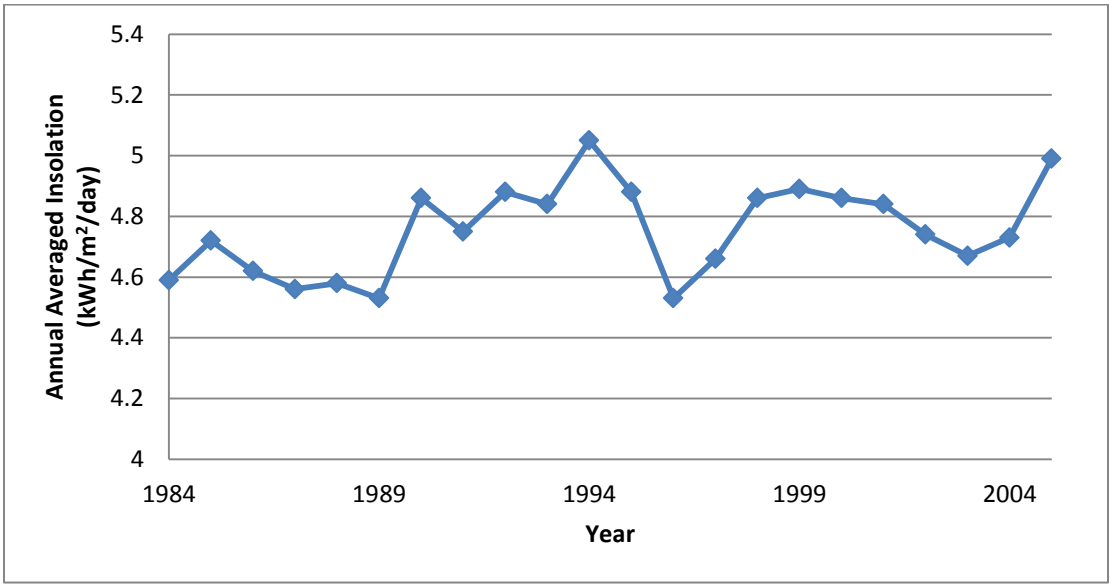

Figure 102: Annual averaged insolation on a Horizontal Surface in Granada, Spain between year 1984 and 2004

In the following sensitive analysis, the DNI value is adjusted from 90% to 110% of the original value with 1% step. The simulation results are shown in Figure 103 and Figure 104. The results indicate that the gross and net electricity productions have a slightly

decelerated increasing trend when the DNI varies from 90% to 110%, which is reasonable since the electricity production is limited by the power block's capacity, therefore the increased DNI may not be fully utilized.

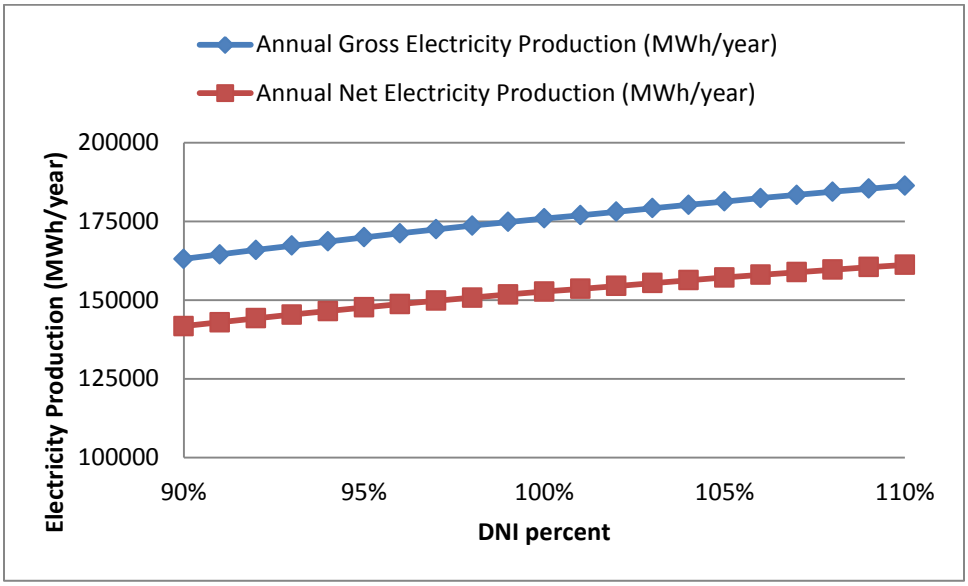

Figure 103: The variation of gross and net electricity production with different DNI

With ±10% DNI varies, the LCOE would change by ±8%, or $0.02 cents. The LCOE has similar changing pattern with electricity production except that it is in the opposite direction. Figure 105 shows the trends of three parameters.

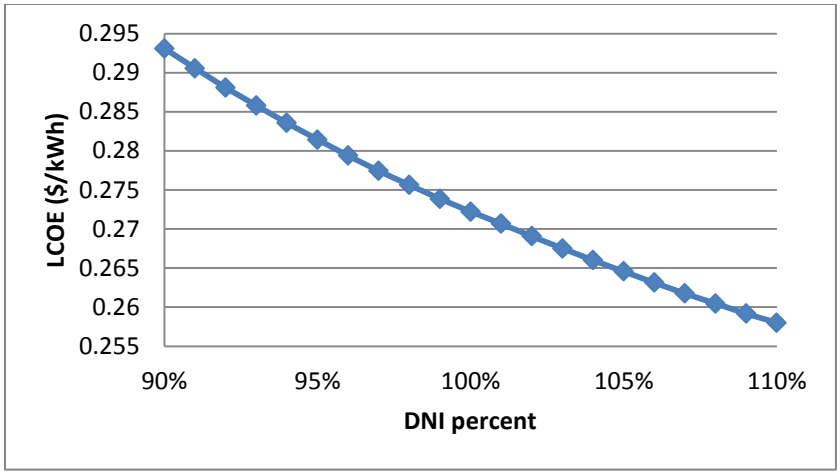

Figure 104: The variation of LCOE with different DNI

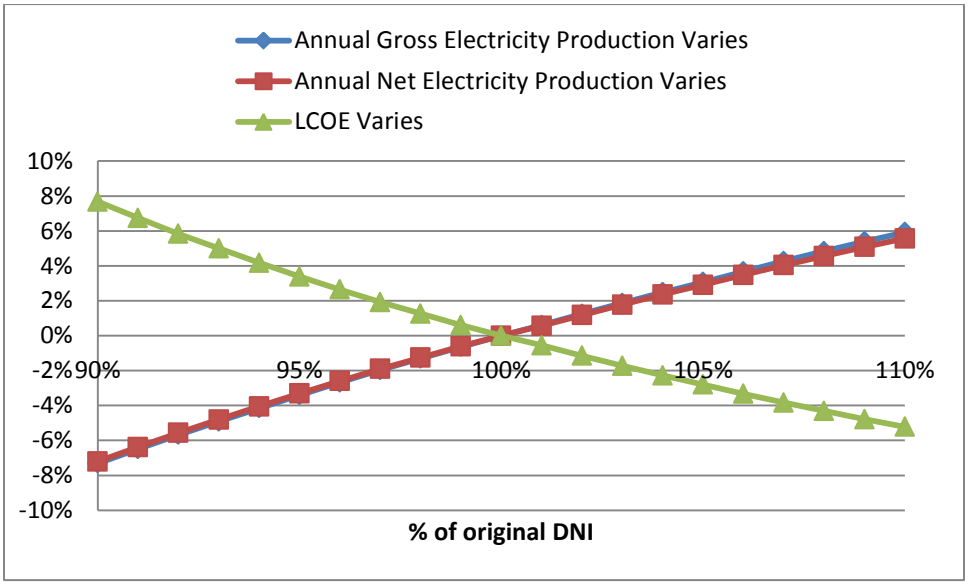

Figure 105: The variation of electricity production and LCOE with different DNI

6.4.2 Risk of broken heat collection element (HCE)

A solar field utilizes thousands of HCE to collect solar energy. During operation, collectors are exposed to tough outdoor environment, including frequently alternating heat and cold temperature, strong wind, and intensive dust. The tough environment causes high failure rates.

At SEGS VI-IX power plants, 30% to 40% of the HCEs failed during nine to eleven years of operation [83], and the NREL supposes it has a 0.02 annual replacement rate [45]. In the model, it assumed the collector has a failure rate of 0.02/year.

The Andasol-1 CSP plant uses 22464 HCEs, half of them is PTR70 from Schott while the rest is UVAC 2008 from Solel [84]. Assuming they have identical failure rates, the possibility of failure of *i* HCEs is*:*

$$P(i) = C_{22464}^{i}(0.02)^{i}(0.98)^{22464-i} \tag{210}$$

In real situation, the failure rate of each HCE would not be exactly 0.02. In this analysis it assumes the failure rate has a triangle distribution with a ±50% range, as shown in Figure 106.

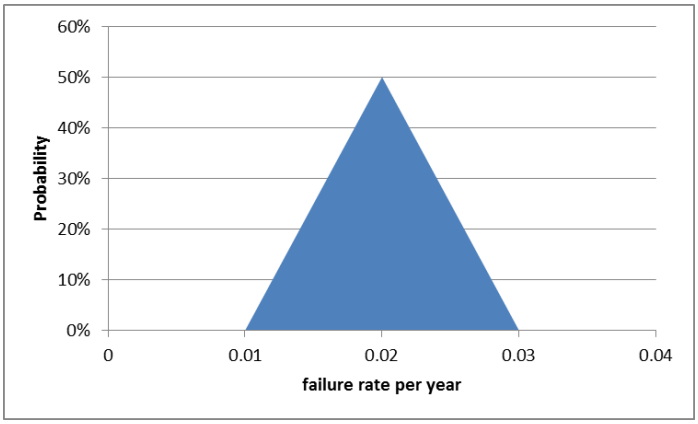

Figure 106: HCE failure rate distribution

The Monte Carlo method is used to predict the failure number of HCEs per year, the result with 100000 trials is shown in Figure 107. It indicates that the solar field would expect to have around 450 failure HCEs per year, and should have less than 607 failure HCE with 95% confidence.

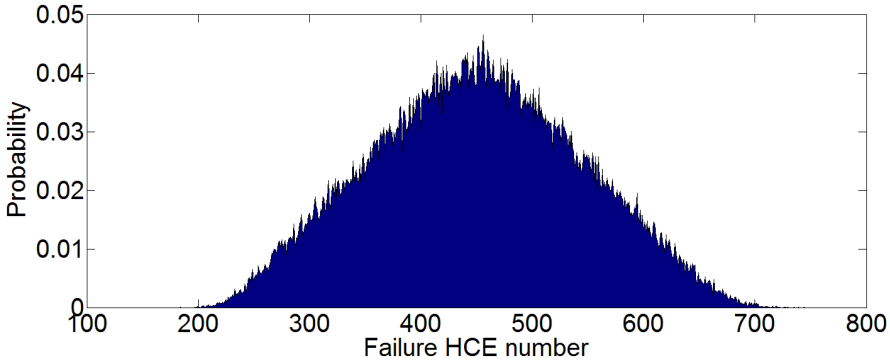

Figure 107: HCE failure probability

The HCE is supposed to have three kinds of failures. The heat losses of these three models under design conditions are shown in Figure 108.

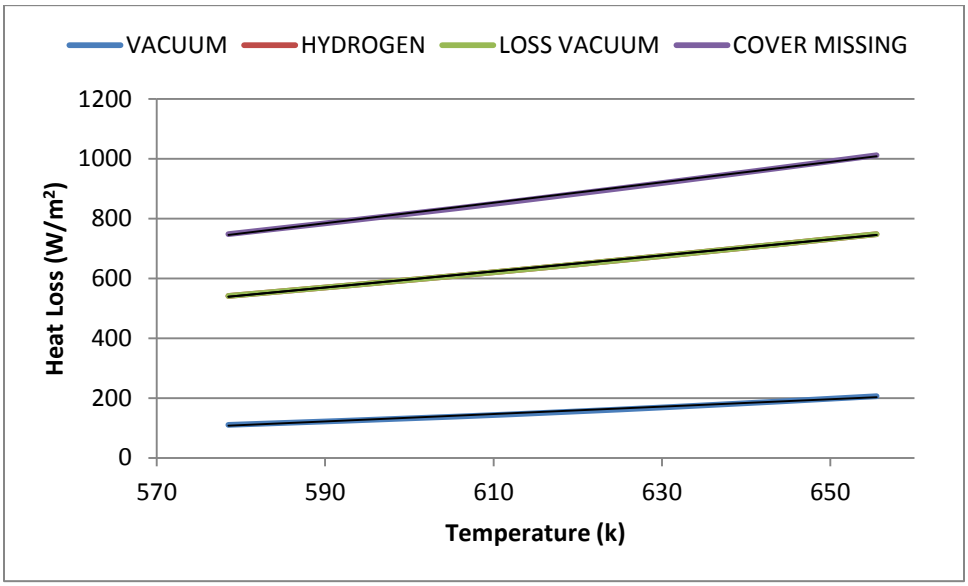

Figure 108: Collector heat losses with different failure conditions

Figure 109 depicts the HTF mass flow rates from the solar field with different HCE conditions. The result indicates that the failure of collectors would lead to higher heat losses and smaller HTF mass flow rates. The collected thermal energy could decrease by 10% to 20% if the HCEs failed.

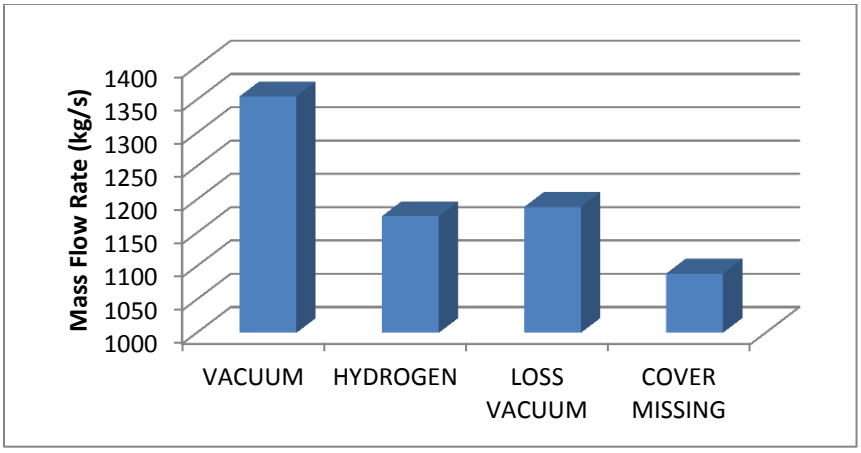

Figure 109: Solar field's mass flow rates with different collector conditions

Figure 110 shows the annual operation performance. It demonstrates that the net electricity production could be reduced by more than 30% due to the HCE failure.

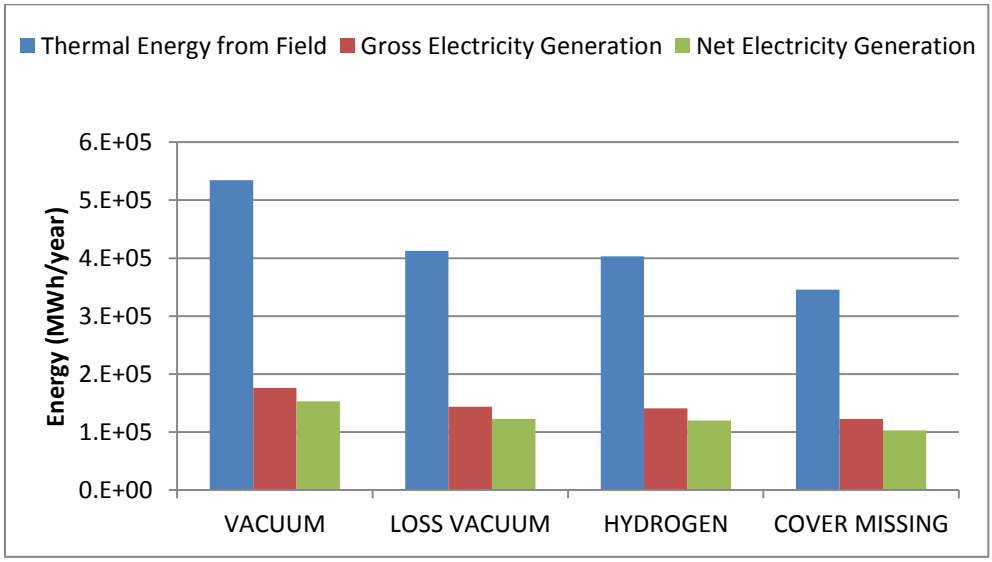

Figure 110: Collected thermal energy and electricity production under different collection conditions

Figure 111 characterizes the annual performance and LCOE with up to 5% of the failure HCEs ratio in the solar field. The net electricity production could be reduced by 2%, and raises the LCOE by 2% as well. The results indicate that if the collectors' failures are detected and replaced in time, the performance loss could be limited to an acceptable low range.

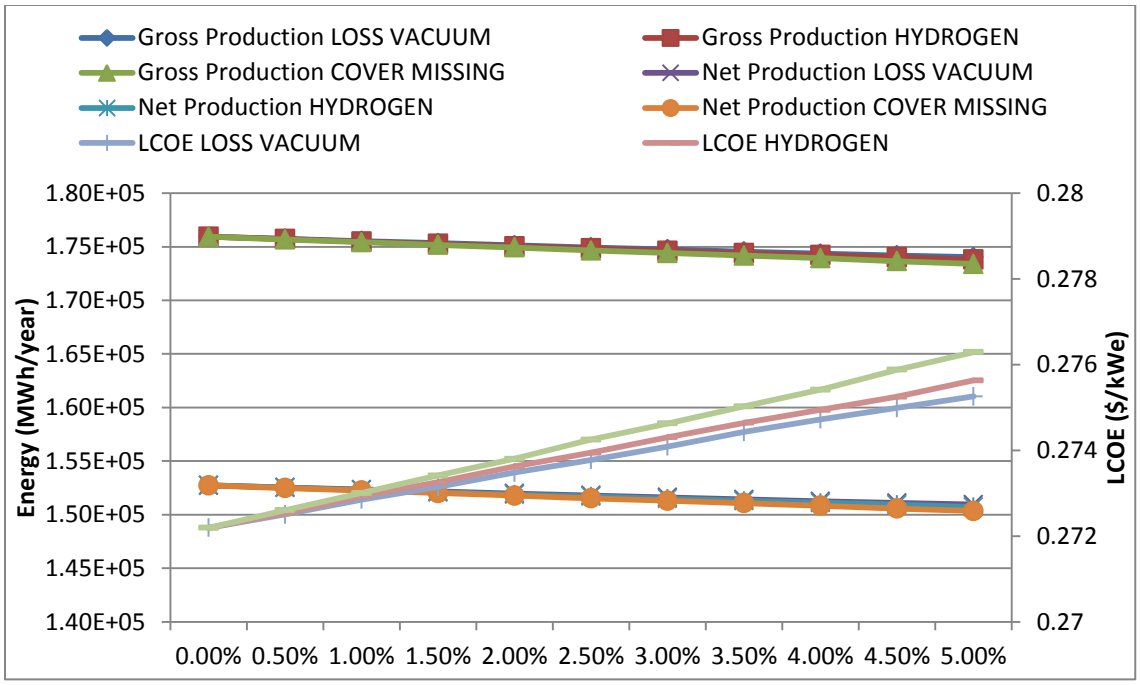

Figure 111: The variation of gross/net electricity production and LCOE with different HCE failure ratio

6.4.3 Risk of Loss HTF Circulation in the Solar Field

In a CSP plant, HTF circulates between different systems to absorb and reject thermal energy. In this scenario, it estimates the risk of partial or full loss the HTF circulation in the solar field. The risk may be caused by multiple reasons, such as failure of pumping, wrong commands, or failure of piping network. The approach to find the probabilistic risk of this scenario is by performing 5000 Monte Carlo trials for each evaluation condition. The fault tree was developed as shown in Figure 112. The fault tree describes the most vulnerable events instead of any event that may cause occurrence of the top event.

The components' mean failure rate is listed in Table 19. Most components' failure data were obtained from Nonelectric Parts Reliability Data (NRPD) Handbook, and are shown in the unshaded cell. The data that are not covered are estimated from experience, which are shown in the shaded cells. It assumes there are four HTF pumps available in solar field, and each pump could supply 30% of the field's design flow capacity. The extra 20% backup capacity is used for over design situation and backup. For pipe clogging condition, which is not supposed to happen during plant's operation, its frequency is estimated as once per lifetime (40 years). The grid and power block are supposed to have a regularly once per month and once per year maintenance schedules. And for the personnel, it has a 2% failure operation percent and it estimated to have five operations per day.

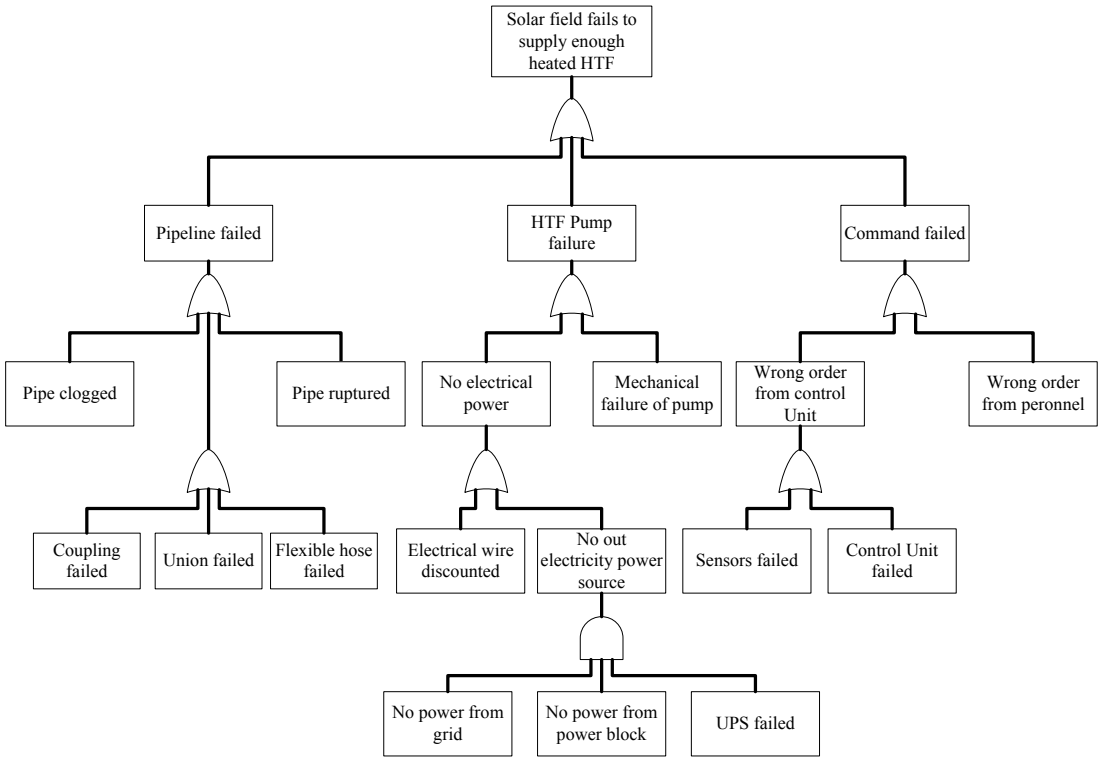

Figure 112: Fault tree diagram of losing HTF circulation

Table 19: Component failure data

Component Name	Number of components	Median fpmh
Pipe clogged	2	2.89
Pipe ruptured	500	0.15
Coupling	250	0.06
Union	250	0.02
Flexible hose	1248	1.36
Electrical wire discounted	50 m	0.21
No power from grid		1388.89
No power from power block		115.74
Uninterruptible power supply	1	7.37
Pump failed	4	3.29
Flow sensors failed	6	0.44

Table 19 Continued

Component Name	Number of components	Median fpmh
Control unit failed	1	3107.52
False commend	2	4166.67

A triangular distribution is used to describe each component's fpmh. Its range, distribution and most likely value are shown in Figure 113.

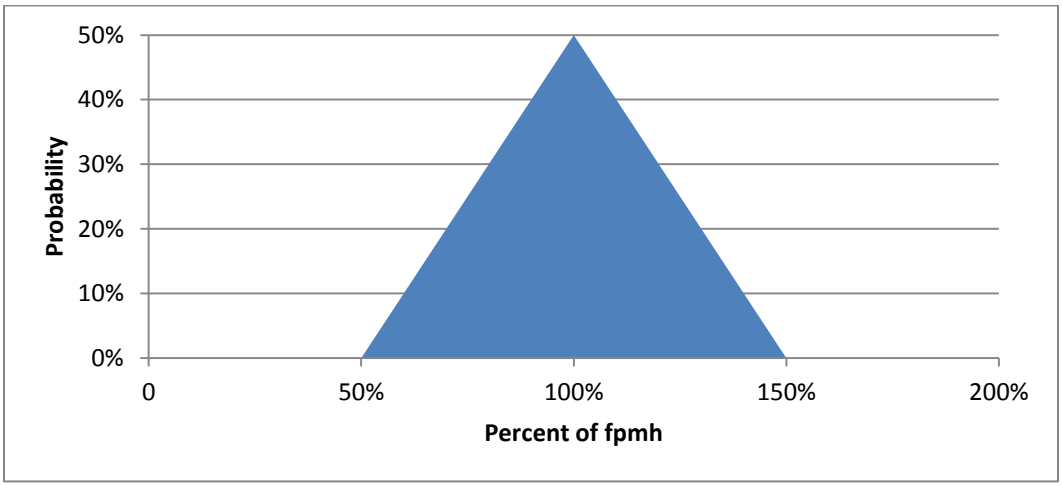

Figure 113: Probability distribution of mean fpmh

The upper and lower range of the reliability values and distribution are defined for each component, and the system reliability for each evaluation is the 'forecast value'. The effect of randomly chosen components reliability values on the total system reliability is

recorded and shown in Figure 114. This evaluation is done at different times to evaluate the trends.

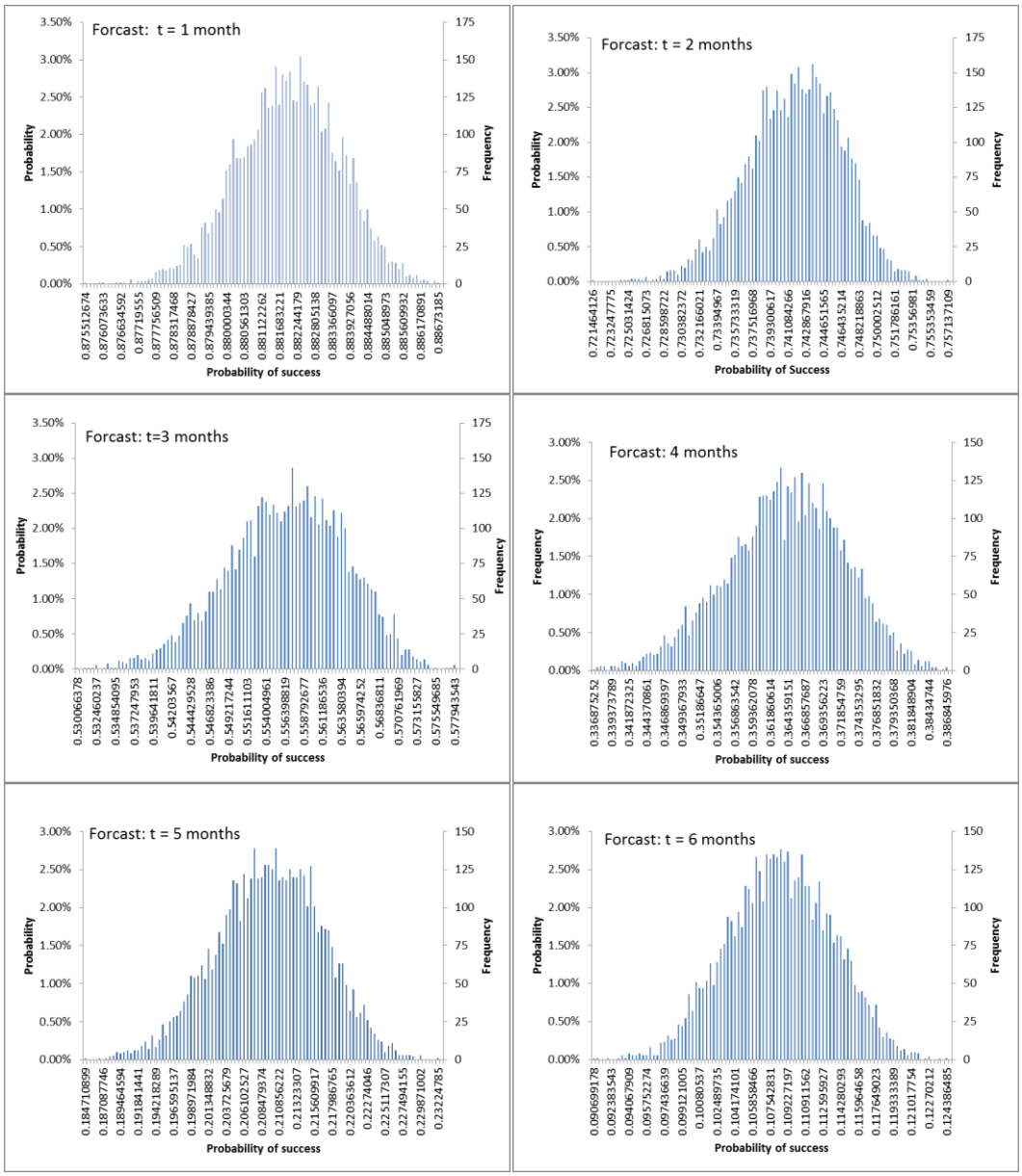

Figure 114: Distributions of reliabilities for t = 1 to 6 months

Figure 115 depicts the reliability of current configurations with 90% and 100% confidence bands when different operation times are used. This trend diagram takes the distribution of reliability (as shown in Figure 114) for each time and plots the information as vertical bands.

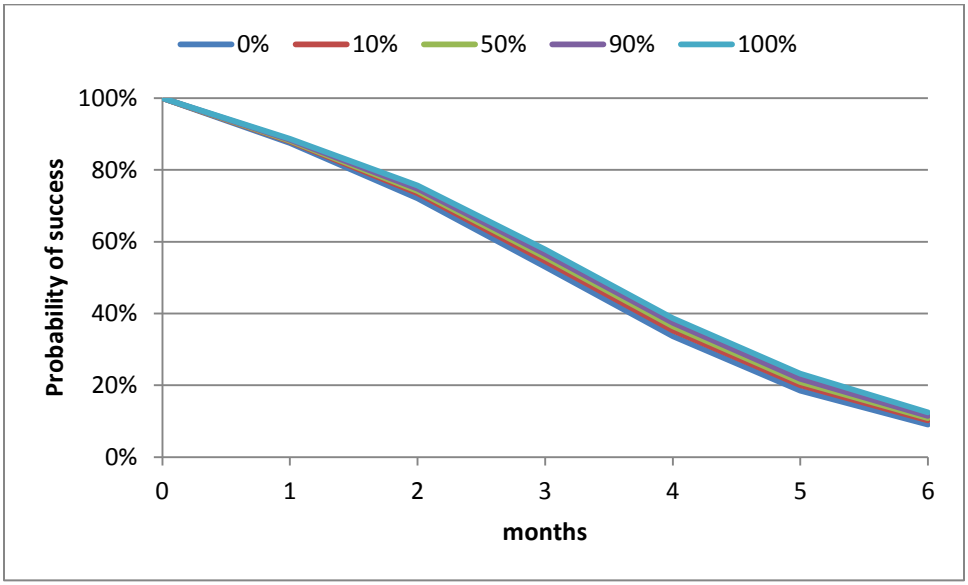

Figure 115: Variation of failing to supply HTF reliability with evaluated operation times

As seen from the trend, the solar field is almost certain to fail after five months' operation without maintenance. The system essentially becomes unstable after three months. The main problem is that the system has thousands of flex hoses, as shown in Figure 116. They are moving component, and have a high pressure drop due to the inner corrugations. Though it needs to have six or more failures of the flex hoses

simultaneously to trigger the main failure event; the flex hoses are still the main reason to initiate the top undesired event. And this conclusion agrees with the result from the Sandia National Lab's result [85]. Catastrophic failure of flex hoses would lead to high temperature HTF spills and fires.

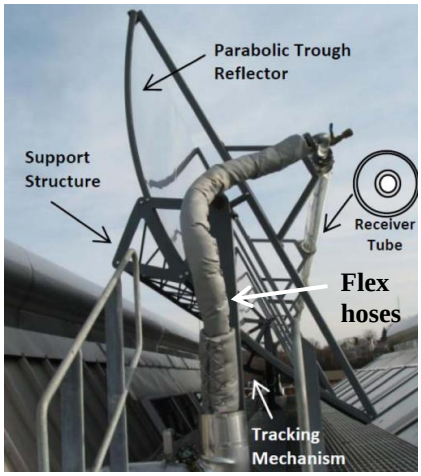

Figure 116: The flex hoses used in the solar field[13]

The collected thermal energy is varied depending on seasons. Figure 117 depicts how the failure of pumps affects the thermal energy output of the solar field based on the HTF mass flow rate: with 30% and 60% residual pumping capacity, the solar field's collection ability is limited most of the time. With 90% residual capacity, its capacity is restricted only during the summer periods.

[13] Picture retrieved from Qu, M, Yin, H., and Archer, D. H., 2010, "Experimental and model based performance analysis of a linear parabolic trough solar collector in a high temperature solar cooling and heating system." *Journal of Solar Energy Engineering* 132.2: 021004.

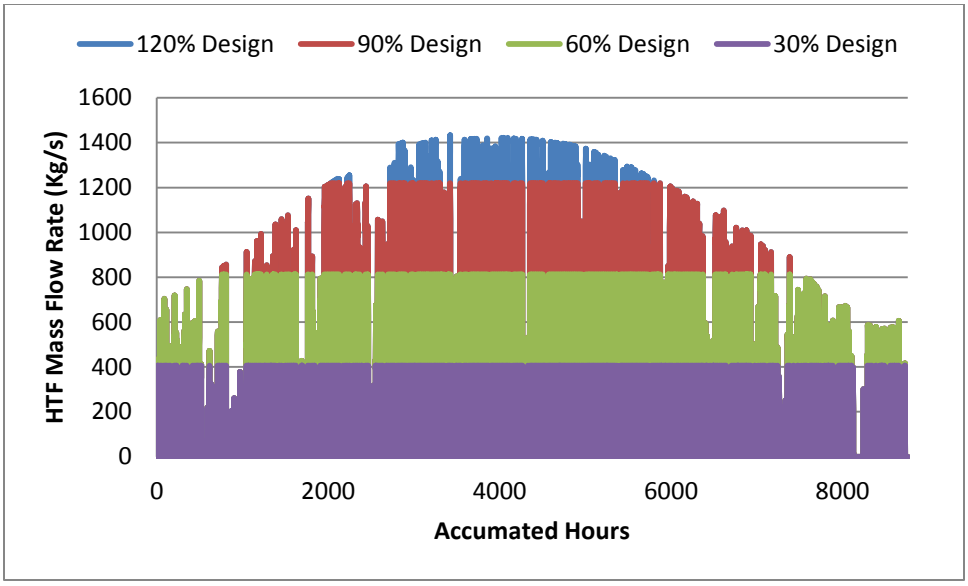

Figure 117: Solar field HTF mass flow rate with 30%, 60%, 90% and 120% pumping capacity

Figure 118 shows the summary of the energy flows. With 30% or 60% residual pumping capacity, it reduced the annual electricity production by 53% or 13%. When the capacity is 90%, the final electricity generation is almost the same as the 120% design condition. A reason to explain it is that the limited pump capacity only cuts the flow rates in summer, at which time the energy carried by the extra flow rates is beyond the power block's capacity. The excess energy would become wasted in the end.

In real operation, the chance of failures of two or more pumps at the same time is rare. The result indicates failure of one pump does not affect the performance much, especially not in summer periods.

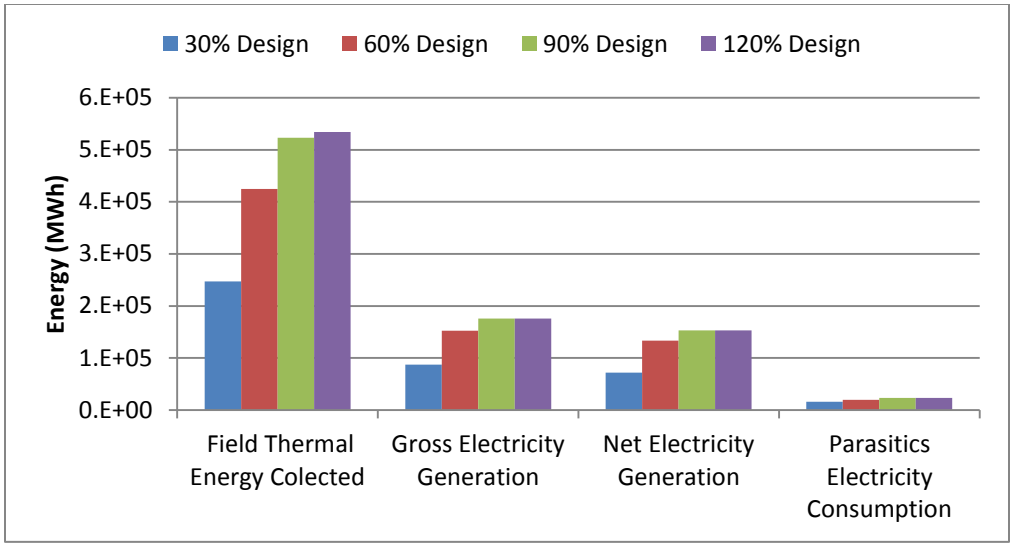

Figure 118: Energy flows with 30%, 60%, 90% and 120% pumping capacity

6.5 Summary

In this chapter, several cases were conducted and their influences on the performance were analyzed. The results indicate that the technology improvements could help lower the LCOE, but the cost is still not competitive with the fossil energy. They also show that the support from the government is important for the future development of CSP industry.

7. FINDINGS AND CONCLUSIONS

7.1 Findings

A comprehensive engineering model for the parabolic trough type CSP plants, including the solar field, storage system, power block, control strategies and other components has been developed and used for predicting the engineering performance. In addition, financial, risk and net energy models were developed. Compared with previous models, the newly developed models:

1. Provide a method to determine the dimension of storage tanks and their associated insulation layer thickness;
2. Process environmental data, which are more suitable for hourly simulation model;
3. Employ theoretical based models for the solar field and storage system, such that the simulation works under both in-design and off-design conditions, which can not be done with regression-based models;
4. Use small time steps under transient condition, which may provide a better simulation result for transient operation condition;
5. Use dynamic operation strategy, the operation is optimized according to the status at that time;
6. Use the exponent scaling method, and the detail material and labor cost method to predict the installed cost and operation and maintenance costs. This method could better evaluate the cost change when the scaling of CSP changes;

7. Include a net energy model, which could be used to evaluate the net energy performance of CSP plants;
8. Incorporate a probability risk model for the solar field;

These engineering and financial models were validated by comparing the operating data for the Andasol-1 power plant and predicted results. The comparison indicates that the actual and simulated data have excellent agreement (within 10%), which implies the models are capable of predicting the performance and payback with small uncertainties. Then they served as a tool to understand the plant's operation characteristics, the factors that can affect the plant's performance and payback, and the potential technical advancements and incentives that contribute to performance improvement and cost reduction.

Findings drawn from the engineering optimization include:

1. Under Andasol-1's environmental condition and configuration (except storage system), the electricity production was increased by about 30%, and the cost was reduced by about 20% when the storage capacity changed from zero to 12 hours. Enlargement of the existing storage (7.8 hours capacity) system resulted in a reduction of the LCOE by 6%.
2. Increasing the specific heat of thermal energy storage (TES) by 50% led to up to 10% cost reduction for the Andasol-1 plant.
3. Under Andasol-1's environmental condition, the lowest LCOEs occur when the solar multiple is in the range from 2.2 to 3 and the storage capacity is in the range

between 8 and 12 hours. The lowest LCOE is 5% lower than the LCOE of Andaosl-1 CSP plant.

4. The LCOE decreased by 32% and the installed cost decreased by 30% when the plant size increased from 50 MWe to 400 MWe. However, according to the trends, the potential for cost reduction by further scaling up is limited, because it is hard to implement thousand-MW size solar power plants for which too much area is needed.
5. The adopting of thermocline system lowered the installed cost and LCOE by 4% for the Andasol-1 CSP plant.

Findings drawn from the financial optimization include:

1. Two kinds of incentives (production based incentive, and guaranteed low rate loan and fast depreciation) were simulated. The lifetime electricity costs are reduced significantly with both types of incentives, the cost after incentives is low enough to compete with fossil energy.
2. The economic lifespan of the Andasol-1 CSP plant ranges between 30 and 35 years.
3. Decreasing the discount rate from 12% to 4% reduces the LCOE by 5%.

Findings drawn from the net energy analysis and risk analysis include:

1. The Andasol -1 CSP plant has positive net energy. Its energy payback period is about 5 years, and the energy return on investment (EROI) is below 10.

2. The electricity production and LCOE are linearly correlated with the variation of solar intensity when the variation of solar intensity is less than 5%.
3. The solar field uses thousands of flex hoses, which were found have the greatest risk of failure.
4. The failure of heat collection element causes degradation of operation performance. The degradation is acceptable if only a small fraction (<5%) of heat collection elements are broken.

7.2 Conclusions

The developed model provides a way to estimate transient, off-design operation performance, lifetime financial payback and net energy performance. The application of the model is not limited to the particular cases simulated. It could be used to investigate a vast number of combinations of design and operating conditions. Therefore, the performance, financial and net energy improvements resulting from potential configuration modifications, technical innovation, incentives and other modifications could be evaluated with this model.

Conclusions drawn from the engineering optimization include:

1. Either adopting or enlarging of a storage system, or increasing the specific heat of TES could help to increase the electricity production and reduce the LCOE.
2. The CSP plant with low LCOE should have a large solar field (solar multiple > 2), and a large storage capacity (storage hours > 7 hours).

3. Increasing the scale of CSP plant could help reduce the LCOE by lowering the unit installed cost.
4. The adopting of thermocline system could lower the installed cost of storage system, and thereby slightly lower the general installed cost and LCOE.

Conclusions drawn from the financial optimization include:

1. Incentives are important to the development of CSP industry. It should be one of the most critical factors to lower the LCOE of CSP technology currently.
2. Reducing the discount rate could reduce the LCOE, but the reduction is not obvious.

Conclusions drawn from the net energy analysis and risk analysis include:

1. CSP power plants should have positive net energy. Its energy payback period is approximate 5 years and the EROI would be less than 10.
2. Performming regular maintenance work in the solar field would be necessary to maintain the performance level.

8. RECOMMENDATIONS FOR FUTURE WORK

The recommendations include:

1. The gross and net electricity production has been simulated and validated with available plant disclosed data. However, the power block model (generator, turbine, and cooling tower) is modeled based on the regression models from fossil power plants' data, assuming they have similar working status. Future studies may require developing a theoretically based numerical power block model which may bring more accurate simulation results.
2. Two kinds of strategies, the greedy strategy and longtime operation strategy are developed and used. Considering the CSP plant may need to operate to meet the peak or intermediate loads of the grid, the grid's load requirement is important for the operation strategy. The future optimization of the control strategies may need to include the grid load in order to better fulfill the requirement of the grid.
3. The net energy analysis of the CSP plant is conducted. However, one problem of the NEA is that the quality of energy is not considered. So, the net exergy analysis, which considers both the quality and quantity of energy, could be conducted in future.
4. One concern about the CSP plant is that it needs to consume significant amount of water during operation. The consumed water may be used for mirror washing, potable supply and cooling. The water consumption during life cycle operation

could be 890 gal/MWh [86]. The future work could work on the impact of water consumption on the environment, performance and net energy payback.

5. The performance and cost of a CSP plant are simulated and analyzed. It is based on the results from the performance model which estimates the electricity production of the first year, and then uses a degradation factor to predict the productions for the rest of the lifespan. Future study may focus on developing more accurate performance decrease model, which may better estimate the lifetime performance variation, and produce more precise payback results.

REFERENCES

[1] United Nations Environment Programme, 2012, *Global Environment Outlook 5: Environment for the Future We Want*, United Nations Environment Program, Progress Press Ltd, Valletta, Malta, ISBN: 978-92-807-3177-4

[2] BP-Review-2013: Statistical Review of World Energy, Workbook (xlsx), London, 2013. Retrieved on August, 2013, http://www.bp.com/statisticalreview [Online]

[3] Butler, J., Montzka, S., 2013, "The NOAA Greenhouse Gas Index (AGGI), Updated summer 2013", NOAA Earth System Research Laboratory, Boulder, CO. Retrieved on November, 2013, http://www.esrl.noaa.gov/gmd/aggi/aggi.html [Online]

[4] Energy Information Administration, 2011, *Annual Energy Review 2011*, U.S. Government Printing Office, Report No: DOE/EIA-0384(2011). Retrieved on January, 2014, http://www.eia.gov/totalenergy/data/annual/pdf/aer.pdf [Online]

[5] Strategic, 2013, *World Energy Resources, 2013 Survey*, World Energy Council, Regency House, London W1B 5LT, ISBN: 978-0-946121-29-8

[6] Karl, T., and Trenberth, K., 2003, "Modern Global Climate Change", *Science*, 5 December 2003: Vol. 302 no. 5651 pp. 1719-1723, DOI: 10.1126/science.1090228

[7] National Research Council, 2010, *Advancing the Science of Climate Change*, Washington, DC, The National Academies Press, 2010. ISBN: 978-0-309-14588-6, pp. 4

[8] Briefing, 2013, *International Energy Outlook 2013*, U.S. Energy Information Administration, DOE/EIA-0484(2013)

[9] Breidthardt, A., 2011. "German government wants nuclear exit by 2022 at latest". *ReutersUK Edition, 30*

[10] Faris, S., 2011,"Italy Says No to Nuclear Power — and to Berlusconi", *Time*, June 14, 2011. Retrived on December, 2013, http://content.time.com/time/world/article/0,8599,2077622,00.html [Online]

[11] "Gauging the Pressure", 2011, *The Economist*, April 28, 2011, The Economist Newspaper Limited, London 2011

[12] Gee, D., Grandjean, P., Hansen, S. F., van denHove, S., MacGarvin, M., Martin, J., & Stanners, Jan 2013, *Late Lessons from Early Warnings: Science, Precaution, Innovation*, ISSN: 1725-9177, European Environment Agency Report, No 1/2013, p. 444

[13] Expert Group on Renewable Energy, *Increasing Global Renewable Energy market Share, Recent Trends and Perspectives*, 2005, Beijing International Renewable Energy Conference, Renewables 2005 Background report, United Nations, Department of Economic and Social Affairs

[14] Philibert, C, 2011, *Solar Energy Perspectives, Renewable Energy Technologies*, International Energy Agency, 75739 Paris Cedex 15, France, ISBN: 978-64-12457-8

[15] Klein, J., Rhyne, I., Bender, S., and Jones, M., 2009, Comparative *Costs of California Central Station Electricity Generation*, California Energy Commission, CEC-200-2009-017-SD

[16] REN21. 2012. Renewables 2012 Global *Status Report*, Paris: REN21 Secretariat

[17] "The Experts: What Renewable Energy Source Has the Most Promise?", 2013, *WSJ.com*, Dow Jones and Company, Inc, April 17, 2013

[18] Lopez, A., Roberts, B., Heimiller, D., Blair, N., and Porro, G., 2012. *US Renewable Energy Technical Potentials: A GIS-Based Analysis*. National Renewable Energy Laboratory (NREL), Golden, Colorado. Report No: NREL/TP-6A20-51946

[19] Hoogwijk, M., Graus, W., 2008, *Global Potential of Renewable Energy Sources: A Literature Assessment: Background Report*. Renewable Energy Policy Network for the 21st Century, Report No: PECSNL072975

[20] Aftim, A., Raffoul, Z., and Karahagopian, Y., 1984, "Solar Disinfection of Drinking Water and Oral Rehydratoin Solutions: Guidelines for Household Application in Developing Countries", *Solar Energy: World Distribution*. Published by UNICEF, Amman, Hashemite Kingdom of Jordan

[21] Lombardi, M., Parker, D., Vieira, R., and Fairey, P., 2004, "Geographic Variation in Potential of Rooftop Residential Photovoltaic Electric Power Production in the United States," *Proceedings of ACEEE 2004 Summer Study on Energy Efficiency in Buildings*, American Council for an Energy Efficient Economy, Washington, DC

[22] Forristall, R., 2003, *Heat Transfer Analysis and Modeling of a Parabolic Trough Solar Receiver Implemented in Engineering Equation Solver*. National

Renewable Energy Laboratory (NREL), Golden, Colorado. Report No: NREL/TP-550-34169

[23] Sawin, J. L., and Martinot, E., 2011, "Renewables Bounced Back in 2010, Finds REN21 Global Report", *Renewable Energy World, 29*.

[24] Finat, A. G., and Liberali, R., 2007, *Concentrating Solar Power: From Research to Implementation*. Luxembourg: European Communities. ISBN 978-92-79-05355-9

[25] Wagner, S. J., and Rubin, E. S., 2014, "Economic Implications of Thermal Energy Storage for Concentrated Solar Thermal Power", *Renewable Energy*, 61(1), 81−95,

[26] World Bank Global Enviornment Program, 2006, *Assessment of the World Bank Group/Gef Strategy for the Market Development of Concentrating Solar Thermal Power*, The International Bank for Reconstruction and Development, The World Bank, Washington, D.C, U.S.A

[27] Jones, J., 2000, *OUT Success Stories: Solar Trough Power Plants*. National Renewable Energy Laboratory (NREL), Golden, CO. Report No: NREL/FS-330-23671

[28] Brown, A., Müller, A., and Dobrotková, Z., November 2011, *Renewable Energy: Markets and Prospects by Technology*, Information Paper, International Energy Agency, Paris Cedex 15, France, Retrived on April, 2014. http://www.iea.org/publications/freepublications/publication/Renew_Tech.pdf [Online]

[29] Price, H., 2003, "A Parabolic Trough Solar Power Plant Simulation Model", ISES 2003: International Solar Energy Conference, Hawaii

[30] Nelson, R., and Cable, R., 1999, "The KJC Plant Performance Model – An Improved SEGS Plant Simulation," *Proceedings of the ASES 1999, Annual Conference*

[31] Pilkington Solar., 1996, *Status Report on Solar Thermal Power Plants*. Pilkington Solar International, Cologne, Germany

[32] Quaschning, V., Ortmanns, W., Kistner, R., and Geyer, M., 2001, "Greenius: A New Simulation Environment for Technical and Economical Analysis of Renewable Independent Power Projects", *Solar Engineering*, 413-418

[33] Ratzel, A. C., Hickox, C. E., and Gartling, D. K., 1979, "Techniques for Reducing Thermal Conduction and Natural Convection Heat Losses in Annular Receiver Geometries", *Journal of Heat Transfer,* 101(1), 108-113

[34] Thomas, A., Thomas, and S. A., 1994, "Design Data for the Computation of Thermal Loss in the Receiver of a Parabolic Trough Concentrator", *Energy Conversion and Management*, 35(7)7, 555–568

[35] Garcı ´a-Valladares, O., and Velázquez, N., 2009, "Numerical Simulation of Parabolic Trough Solar Collector: Improvement Using Counter flow Concentric Circular Heat Exchangers", *International Journal of Heat and Mass Transfer*, 52(3–4), 597–609

[36] Odeh, S. D., Behnia, M., and Morrison, G. L., 2003, "Performance Evaluation of Solar Thermal Electric Generation Systems", *Energy Conversion and Management*, 44/15, 2425-2443

[37] Odeh, S. D., Morrison, G. L., and Behnia, M., 1998, "Modelling of Parabolic Trough Direct Steam Generation Solar Collectors", *Solar Energy*; 62(6), 395–406

[38] Padilla, R. V., Demirkaya, G., Goswamic, D. Y., Stefanakos, E., and Rahman, M. M., 2011, "Heat transfer analysis of parabolic trough solar receiver", *Applied Energy*, 88, 5097–5110

[39] Herrmann, U., and Nava, P., 2008, "Performance of the SKAL-ET Collectors of the Andasol Power Plants", *Proceedings of 14th International SolarPACES Symposium on Solar Thermal Concentrating Technologies*, Las Vegas, EEUU

[40] Burkholder, F., and Kustscher, C., 2009, *Heat Loss Testing of Schott's 2008 PTR70 Parabolic Trough Receiver*, National Renewable Energy Laboratory (NREL), Golden, Colorado. Report No: NREL/TP-550-45633

[41] Herrmann, U., Kelly, B., and Price, H., 2003, "Two-tank molten salt storage for parabolic trough solar power plants", *Energy*, 29 (2004) 883-893

[42] Kopp, J. E., 2009, *Two-Tank Indirect Thermal Storage Designs for Solar Parabolic Trough Power Plants*, Master Thesis, University of Nevada, Las Vegas

[43] Turchi, C., 2010, *Parabolic Trough Reference Plant for Cost Modeling with the Solar Advisor Model (SAM)*, National Renewable Energy Laboratory (NREL), Golden, Colorado. Report No: NREL/TP-550-47605

[44] Kelly, B., and Kearney, D., 2002 – 2004, *Thermal Storage Commercial Plant Design Study for a 2-Tank Indirect Molten Salt System*, National Renewable Energy Laboratory (NREL): Golden, Colorado. Report No: NREL/SR-550-40166

[45] Sargent & Lundy LLC Consulting Group, 2003, *Assessment of Parabolic Trough and Power Tower Solar Technology Cost and Performance Forecasts*, National Renewable Energy Laboratory (NREL), Golden, Colorado. Report No: NREL/SR-550-34440

[46] Larrain Mujica, T. J., 2009, *Net Energy Analysis of Hybrid Concentrated Solar Thermal Power Plants in Chile: A Selection Methodology for Optimal Plant Location Based on Sustainability Attributes*, Master Thesis, Pontificia Universidad Catolica de Chile

[47] Dale, M., 2013, "A Comparative Analysis of Energy Costs of Photovoltaic, Solar Thermal, and Wind Electricity Generation Technologies", *Applied Sciences*,3,2,325-337

[48] Hall, C. A., Cleveland, C. J., and Kaufmann, R. K, 1986, "Energy And Resource Quality: The Ecology Of The Economic Process", Wiley Interscience, NY, ISBN-10: 0471087904, ISBN-13: 978-0471087908

[49] Solar Advisor Model Reference Manual for CSP Trough System, July 2009. SAM Version 3.0. Retrived on January, 2011, https://www.nrel.gov/analysis/sam/pdfs/sam_csp_reference_manual_3.0.pdf [Online]

[50] Standard, American Petroleum Institute, 1998. 650, Welded steel tanks for oil storage. Washington, DC: API.

[51] Kelly, B., and Kearney, D., 2006, *Thermal Storage Commercial Plant Design Study for a 2-tanks indirect Molten Salt System. Final Report. May 13, 2002 – December 31, 2004.* National Renewable Energy Laboratory (NREL), Golden, Colorado. Report No. NREL/SR-550-40166

[52] Nava, P., Aringhoff, R., Svoboda, P., and Kearney, D., 1996, *Status Report on Solar Thermal Power Plants*, Pilkington Solar International GmbH, Koeln, Germany. Report ISBN: 3-9804901-0-6.

[53] Price, H., L pf ert, E., Kearney, D., Zarza, E., Cohen, G., Mahoney, R., and Gee, R., 2002, "Advances in Parabolic Trough Solar Power Technology", *Journal of solar energy engineering*, 124(2), 109-125.

[54] Herrmann, U., Geyer, M., and Kistner, R., *The AndaSol Project - Workshop on Thermal Storage for Trough Power System*, 2002, FLABEG Solar International GmbH. Retrived on June, 2013, http://www.nrel.gov/csp/troughnet/pdfs/uh_anda_sol_ws030320.pdf [Online]

[55] Stuetzle, T. A., 2002, *Automatic Control of the 30 MWe SEGS VI Parabolic Trough Plant*, Master Thesis, University of Wisconsin-Madison

[56] Kopp, J. E., 2009, *Two-Tank Indirect Thermal Storage Designs for Solar Parabolic Trough Power Plants*, Doctoral dissertation, University Of Nevada, Las Vegas

[57] Wagner, M. J., and Gilman, P., 2011, *Technical Manual for the SAM physical Trough Model*, National Renewable Energy Laboratory (NREL), Golden, Colorado. Report No: NREL/TP-5500-51825

[58] Bartlett, R. L., 1958, *Steam Turbine Performance And Economics*, McGraw-Hill, New York, U.S

[59] Patnode, A.M., 2006, *Simulation and Performance Evaluation of Parabolic Trough Solar Power Plants*, Doctoral dissertation, University of Wisconsin

[60] Incropera, F. P., DeWitt, D. P., Bergman, T. L., and Lavine, A. S., 2007, *Fundamentals of Heat and Mass Transfer, 6th edition*, Hoboken, NJ, John Wiley & Sons, Inc, ISBN-10: 0471457280, ISBN-13: 978-0471457282

[61] Parabolic Trough Projects, National Renewable Energy Laboratory (NREL). Retrived on May, 2013, http://www.nrel.gov/csp/solarpaces/parabolic_trough.cfm [Online]

[62] Directorate-General for Research, European Commission, *Renewable Energy Technologies, Long Term Research in the 6th Framework Programme 2002-2006,* 2007, Luxembourg: Office for Official Publications of the European Communities, Belgium, ISSN 1018-5593, ISBN 92-79-02889-8

[63] Efficiency Energy, 1997, *Renewable Energy Technology Characterizations*, Energy Efficiency and Renewable Energy (EERE), US Department of Energy. Report No: TR-109496

[64] DeMeo, E. A., and Galdo, J. F., 1997, *Renewable Energy Technology Characterizations*, U.S. Department of Energy and EPRI (Electric Power Research Institute). Report No: TR-109496

[65] St. Laurent, S. J., Kolb, W. J., and Pacheco, J. E., 2000, *Thermocline Thermal Storage Test for Large-Scale Solar Thermal Power Plants*. Sandia National Labs, Albuquerque, NM. Report No: SAND2000-2059C

[66] Sullivan, W. G., Wicks, E. M., and Luxhoj, J. T., 2009, *Engineering Economy 14th edition*, N.J, Pearson Prentice Hall, ISBN-10: 0136142974, ISBN-13: 978-0136142973

[67] Data, *Consumer Price Index*, Bureau of Labor Statistics, U.S. Department of Labor. Retrived on December, 2013, http://www.bls.gov/data/ [Online]

[68] Kubiszewski, I., Cleveland, C. J., and Endres, P. K., 2010, "Meta-analysis of Net Energy Return for Wind Power Systems", *Renewable Energy*, 35(1), 218–225

[69] Herendeen, R. A., 2004, "Net Energy Analysis: Concepts and Methods", *Encyclopedia of Energy*, 4, 283–289

[70] The Interstate Technology & Regulatory Council Green and Sustainable Remediation Team, 2011, *Green and Sustainable Remediation: A Practical Framework*, Technical/Regulatory Guidance, Interstate Technology & Regulatory Council, Washington, DC

[71] Carnegie Mellon University Green Design Institute. 2008, Economic Input-Output Life Cycle Assessment (EIO-LCA), US 1997 Industry Benchmark model. Retrived on January, 2011, http://www.eiolca.net [Online]

[72] Data, *Nonelectronic Parts Reliability Data*, 2011, the Reliability Information Analysis Center. Rome, NY

[73] Millennium Solar, 2008, *The Parabolic Trough Power Plants Andasol 1 to 3*, Solar Millennium AG. Retrived on Feburary, 2014, http://large.stanford.edu/publications/coal/references/docs/Andasol1-3engl.pdf [Online]

[74] IRENA, 2012, *Renewable Energy Technologies: Cost Analysis Series*, International Renewable Energy Agency, Vol 1: Power Sector, Issue 2/5 Concentrating Solar Power, Bonn, Germany

[75] U.S. Department of Agriculture and U.S. Department of Health and Human Services, 2009, *Dietary Guidelines for Americans 2010, 7th Edition*, Washington, DC: U.S. Government Printing Office

[76] Zhang, T. W., and Dornfeld, D. A., 2007, "Energy Use per Worker-Hour: Evaluating the Contribution of Labor to Manufacturing Energy Use", *Advances*

in Life Cycle Engineering for Sustainable Manufacturing Businesses, pp 189-193, Springer London

[77] Ardani, K., and Margolis, R., 2011, *2010 Solar Technologies Market Report*, U.S Department of Energy, Energy Efficiency & Renewable Energy. Report No: DOE/GO-1012011-3318

[78] Decree, R., 2007, *Royal Decree*, 661, 2007.

[79] Kulichenko, N., and Wirth, J., 2011, *Regulatory and Financial Incentives for Scaling Up Concentrating Solar Power in Developing Countries*, Energy and mining sector board discussion paper, No. 24, The World Bank, Washington, D.C.

[80] Keith, G., Jackson, S., Napoleon, A., Comings, T., and Ramey, J. A., 2012, *The Hidden Costs of Electricity: Comparing the Hidden Costs of Power Generation Fuels*, Synapse Energy Economics, Inc. Cambridge, MA

[81] Stoffel, T., Renne, D., Myers, D., Wilcox, S., Sengupta, M., George, R., Turchi, R., 2010, *Concentrating Solar Power Best Practices Handbook for the Collection and Use of Solar Resource Data*. National Renewable Energy Laboratory (NREL), Golden, CO. Report No: NREL/TP-550-47465

[82] Cebecauer, T., Šúri, M., and Gueymard, C. A., 2011, "Uncertainty Sources in Satellite-Derived Direct Normal Irradiance: How Can Prediction Accuracy be Improved Globally?", *Proceedings of the SolarPACES Conference*, Granada, Spain, Vol. 23222

[83] Mahoney, R., 2000, "Trough Technology—Heat Collector Element (HCE) Solar Selective Absorbers" Trough Workshop, ASES 2000. Sandia National Laboratories, Albuquerque, NM and National Renewable Energy Laboratory (NREL), Golden, CO

[84] Richter, C., Blanco, J., Heller, P., Mehos, M., Meier, A., and et al, 2008, *Solar Power and Chemical Energy Systems*, SolarPACES Annual Report, International Energy Agency (IEA).

[85] Cohen, G. E., Kearney, D. W., and Kolb, G. J., 1999, *Final Report on the Operation and Maintenance Improvement Program for Concentrating Solar Power Plants*. Sandia National Laboratories, SAND 99-1290. Albuquerque, NM, and Livermore, CA

[86] Meldrum, J., Nettles-Anderson, S., Heath, G., and Macknick, J., 2013, "Life Cycle Water Use for Electricity Generation: A Review and Harmonization of Literature Estimates" , *Environmental Research Letters*, 8(1), 015031

[87] Camacho, E. F., Berenguel, M., Rubio, F. R., & Martínez, D., 2012, *Control of Solar Energy Systems,* Springer London, ISSN: 1430-9491, ISBN: 978-0-85729-916-1

[88] Iqbal, M., 1983, *An Introduction To Solar Radiation*, Elsevier, New York, ISBN: 0-12-373752-4

[89] Cooper, P. I., 1969, "The Absorption of Radiation in Solar Stills", *Solar Energy*, 12(3), 333 - 346.

[90] Honsberg, C, and Bowden, S., 2008, "PV Education.ORG". Retrived on Feburary, 2013. Retrived on August, 2013, http://www.pveducation.org/pvcdrom/properties-of-sunlight/azimuth-angle [Online]

[91] *Solar Advisor Model Reference Manual for CSP Trough Systems*, 2009, National Renewable Energy Laboratory, Draft July 15 2009 for SAM Version 3.0

[92] Duffie, J. A., Beckman, W. A., 2013, *Solar Engineering of Thermal Processes*, Hokoken, New Jersey, John Wiley & Sons, ISBN-10: 0470873663, ISBN-13: 978-0470873663

[93] Swinbank, W. C., 1963, "Longwave radiation from clear skies", *Quarterly Journal of the Royal Meteorological Society*, 89(381), 339-348.

[94] Stull, R., 2011, "Wet-Bulb Temperature from Relative Humidity and Air Temperature", *Journal of Applied Meteorology and Climatology*, 50.11

[95] Watt, A. D., 1978, "On the Nature and Distribution of Solar Radiation", U.S. Department of Energy, Report No: HCP/T2552-01.

[96] Forristall, R., 2003, *Heat Transfer Analysis and Modeling of a Parabolic Trough Solar Receiver Implemented in Engineering Equation Solver*, National Renewable Energy Laboratory (NREL), Golden, CO. Report No: NREL/TP-550-34169

[97] Harding, G. L., & Window, B., 1981, "Free Molecule Thermal Conduction in Concentric Turbular Solar Collectors", Solar Energy Materials, 4(3), 265-278

APPENDIX A

DERIVE THE NEEDED WEATHER DATA

A.1 Local Standard Time Meridian (LSTM)

The LSMT is a reference meridian used for a specified time zone. There are 24 LSTM evenly spread in the earth. When the LSTM has a longitude of zero, it coincides with the Prime Meridian, which represents the Greenwich Mean Time.

$$LSTM = \frac{360^o}{24} \cdot \Delta T_{GMT} = 15^o \cdot \Delta T_{GMT} \tag{211}$$

A.2 Local Time (LT) and Local Solar Time (LST)

The LT is the time for daily use, while the LST is the time when the sun is highest in the sky, it is twelve noon. LT and LST is generally different due to the eccentricity of earth's orbit (the earth moves on elliptical path) and factitious adjustment such as daylight saving and time zones.

However, the measured data is generally based on the LT while the solar related calculation prefers to work with the LST. The relationship between LT and LST is:

$$LST = LT + \frac{\lambda - LSTM}{15} + \frac{EoT}{60} \tag{212}$$

The EoT (Equation of Time in minute) is the small daily inordinance due to the Earth's elliptical path and axial tilt. Several empirical equations have brought out to calculate it, as shown in equation 213 and equation 215:

$$EoT = 9.87\sin(2B) - 7.53\cos(B) - 1.5\sin(B) \text{ [87]} \quad (213)$$

Where:

$$B = \frac{360}{365}(d - 81) \quad (214)$$

Or

$$EoT = 229.18(0.000075 + 0.001868\cos(B) - 0.032077\sin(B) - 0.014615\cos(2B) - 0.04089\sin(2B)) \text{ [88]} \quad (215)$$

Where:

$$B = \frac{360}{365}(d - 1) \quad (216)$$

The comparison of those two methods is illustrated in Figure 119.

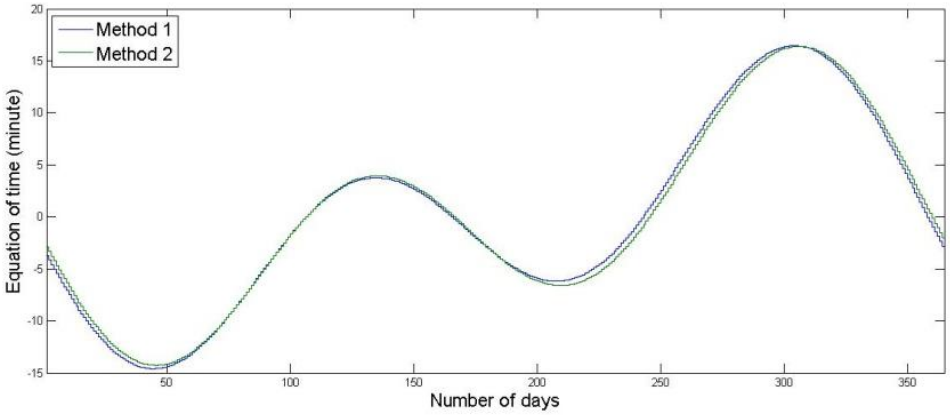

Figure 119: Equation of time varies with days of the year

A.3 Hour Angle (HRA)

The HRA is converted from the LST. It describes the sun movement in across the sky. The HRA is zero at solar noon (LST = 12), and negative before noon and positive afternoon.

$$\omega = 15^{o} \cdot (LST - 12) \tag{217}$$

A.4 Declination Angle

The declination angle is the angle between the equator and the line connected with the center of earth or sun. It changes due to Earth's self-rotation axis and Earth to Sun rotation axis is not coincidence. Else, the declination angle will always be zero degree. The tilt angle is 23.45^{o}, and the declination angle is always varies between negative and positive this amount. The pictorial representation of the declination angle is shown in Figure 120.

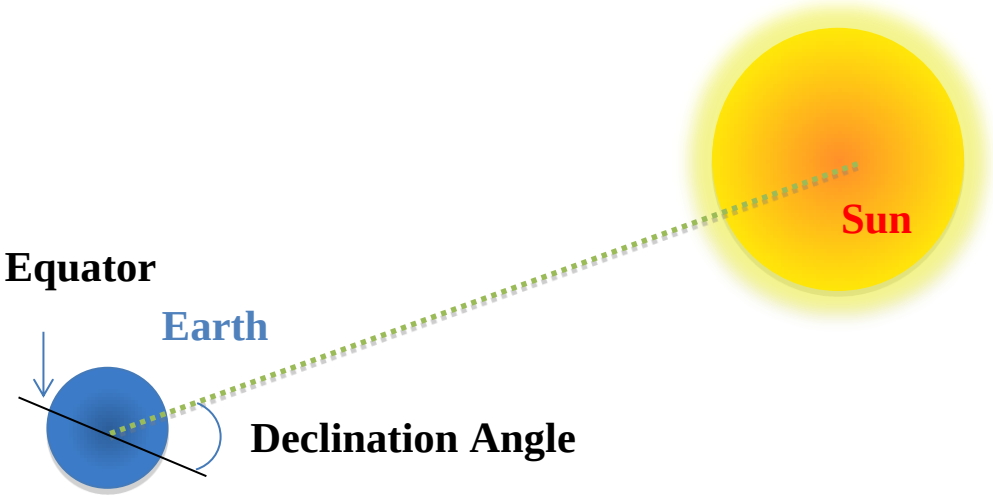

Figure 120: Demonstration of the declination angle

In March 22 and September 22 (Equinoxes), the declination is zero. In summer solstices day, it achieves its maximum value of 23.45^{o}. While in winter solstices day, it researches its minimum value of -23.45^{o}.

The following experience is developed by Cooper PI [89]:

$$\delta = 23.45^{o} \cdot \sin\left[\frac{360}{365}(d+284)\right] \tag{218}$$

Figure 121 is the plot of declination angle during a whole year according the experience equation.

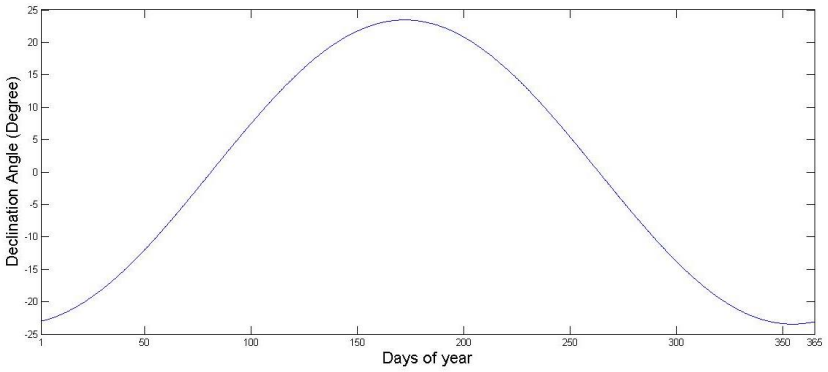

Figure 121: Declination angle varies with days of year

A.5 Altitude Angle and Zenith Angle

The solar altitude angle, also means the elevation angle, is the angle between the location's horizontal plane and the line connected with the center of sun and the location.

The altitude angle, θ, varies with time, geographical position, and the days of the year. The zenith angle is defined as the angle between the sun and the vertical plane, as demonstrated in Figure 122.

$$\theta = \sin^{-1}\left[\sin\delta\sin\varphi + \cos\delta\cos\varphi\cos\omega\right] \tag{219}$$

$$\text{Zenith Angle} = 90^{o} - \theta \tag{220}$$

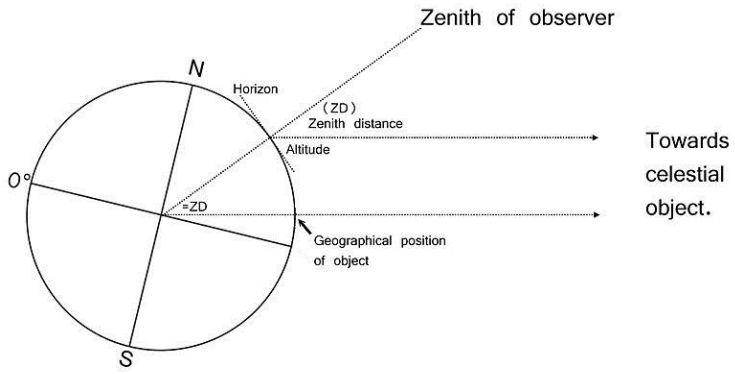

Figure 122: Altitude angle and zenith angle[14]

[14] Image retrieved on July 2014, from Wikipedia, address: http://commons.wikimedia.org/wiki/File:Diagram_showing_GP_distance_%3D_ZD.jpg

A.6 Sun Rise and Set Time

The sun rise time is the local time when the sun rises to the horizon, while the sun set time is the local time when the sun falls to the horizon. At both times, the Altitude Angle is 0.

$$0 = \sin^{-1}\left[\sin\delta\sin\varphi + \cos\delta\cos\varphi\cos\omega\right] \tag{221}$$

And the solutions of equation 221 are the sun rise and sun set times:

$$t_{sun\_rise} = 12 - \frac{1}{15^o}\cos^{-1}\left(-\tan\varphi\tan\delta\right) - \frac{4\left(\lambda - LSTM\right) + EoT}{60} \tag{222}$$

$$t_{sun\_set} = 12 + \frac{1}{15^o}\cos^{-1}\left(-\tan\varphi\tan\delta\right) - \frac{4\left(\lambda - LSTM\right) + EoT}{60} \tag{223}$$

A.7 Azimuth Angle

The azimuth angle is the angle between two vector, one vector is the northern direction projected to the horizon plane, the other vector is the line connected with the specified location and the center of sun projected to the horizon plane. At equinoxes, the sun rise at exact east (90^o) and set at exact west (270^o), regardless of the latitude. In general situation, its value varies with the latitude, days of the year and time. The pictorial representation of the azimuth angle is shown in Figure 123.

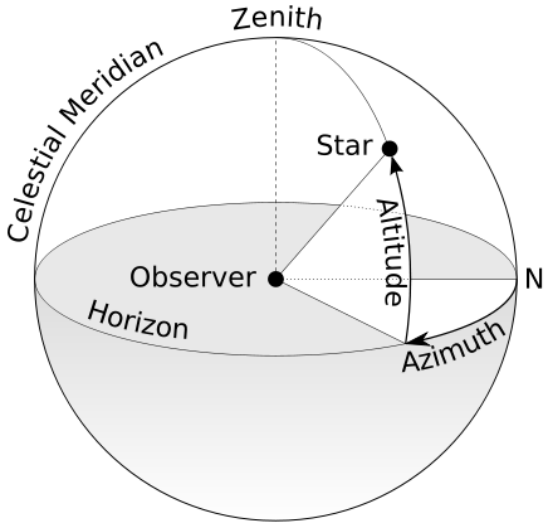

Figure 123: Illustration of the azimuth angle[15]

As shown in Figure 123, its value ranges from 0 to 360. The calculation method is shown as following:

$$\gamma = \cos^{-1}\left(\frac{\sin\delta\cos\varphi - \cos\delta\sin\varphi\cos\omega}{\cos\theta}\right) \text{ when } \omega < 0 \text{ [90]} \tag{224}$$

$$\gamma = 360^{o} - \cos^{-1}\left(\frac{\sin\delta\cos\varphi - \cos\delta\sin\varphi\cos\omega}{\cos\theta}\right) \text{ when } \omega \geq 0 \text{ [90]} \tag{225}$$

The latitude angle is positive for northern hemisphere locations and negative for southern hemisphere locations.

[15] Picture retrieved on June 2014, from Wikipedia website, address: http://commons.wikimedia.org/wiki/File:Azimuth-Altitude_schematic.svg

A.8 Incidence Angle on a Rotatable Surface

The incidence angle is the angle between the sun's rays on a surface and the line normal to the surface. In the model, the surface is the trough's aperture. It assumes all the troughs have the same tilt and azimuth angles, therefore they have same incidence angle.

Current collection trough is able to track sunlight in single direction, it is capable to rotate in the lengthwise axis, and this axis is typically in north-south or east-west direction. During operation, the troughs are rotated to face the sun rays' direction, the direction is controlled in the way that minimizes the incidence angle. This incidence angle, γ_{inc}, is calculated as:

$$\gamma_{inc} = \cos^{-1}\left|1-\cos\left(\theta-\theta_{col}\right)-\cos\left(\theta_{col}\right)\cos\left(\theta\right)\cdot\left[1-\cos\left(\gamma-\gamma_{col}\right)\right]\right| \text{[91]} \qquad (226)$$

Also, the track angle could be calculated as:

$$w_{col} = \tan^{-1}\left\{\frac{\cos\left(\theta\right)\sin\left(\gamma-\gamma_{col}\right)}{\sin\left(\theta-\theta_{col}\right)+\sin\left(\theta_{col}\right)\cos\left(\theta\right)\left[1-\cos\left(\gamma-\gamma_{col}\right)\right]}\right\} \text{[91]} \qquad (227)$$

A.9 Sky Temperature

Sky is considered as a blackbody when exchanges energy by radiation with HTF. The blackbody's temperature is defined as sky temperature. It varies with time, location and weather conditions. Several experimental correlations are available to calculate it with clear skies. Some of these correlations are:

$$T_{sky} = T_{amb}\left[0.711 + 0.0056T_{dp} + 0.00073T_{dp}^2 + 0.013\cos(15t)\right]^{0.25} \text{ [92]} \qquad (228)$$

$$T_{sky} = 0.0553T_{amb}^{1.5} \text{ [93]} \qquad (229)$$

$$T_{sky} = T_{amb} - 6 \qquad (230)$$

Where:

T_{sky} is the sky temperature in degree Kelvin;

T_{amb} is the ambient temperature in degree Kelvin;

T_{dp} is the dew point temperature in degrees Celsius;

t is the hour from midnight.

The first method is used in our simulation if the dew points data are available, or the second method is used.

A.10 Web Bulb Temperature

The web bulb temperature is calculated according to the ambient temperature, T_{amb}, and relative humidity, *RH*, as following:

$$T_{wet\_bulb} = T_{amb} \cdot atan(0.151977(RH \cdot 100 + 8.313659)^{0.5}) + atan(T_{amb} + RH \cdot 100) - atan(RH \cdot 100 - 1.676331) + 0.00391838 \cdot \left(RH \cdot 100\right)^{1.5} \cdot atan(0.023101 \cdot (RH \cdot 100)) - 4.686035$$

[94](231)

A.11 Available Solar Energy

Available of the solar thermal energy to the solar field at any time is defined as:

$$\dot{Q}_{avil} = \dot{q}_{avil} \cdot N_{SCA} \cdot S_{aperature} \tag{232}$$

$$\dot{q}_{avil} = DNI \tag{233}$$

Where

N_{SCA} is the number of SCA in solar field;

$S_{aperture}$ is the aperture area of each SCA;

This value represents the maximum solar energy flux rate that the solar field may obtain.

A.12 Direct Normal Irradiance (DNI)

DNI is the solar insolation measured on certain location. The normal means the measurement surface is perpendicular to the sunlight. It equals to the radiation entering the earth's atmosphere minus the diffused radiation which caused by air, vapor and dust in the atmosphere, as shown in Figure 124. Its value is affected by distance between earth and sun, time of day, weather condition and else.

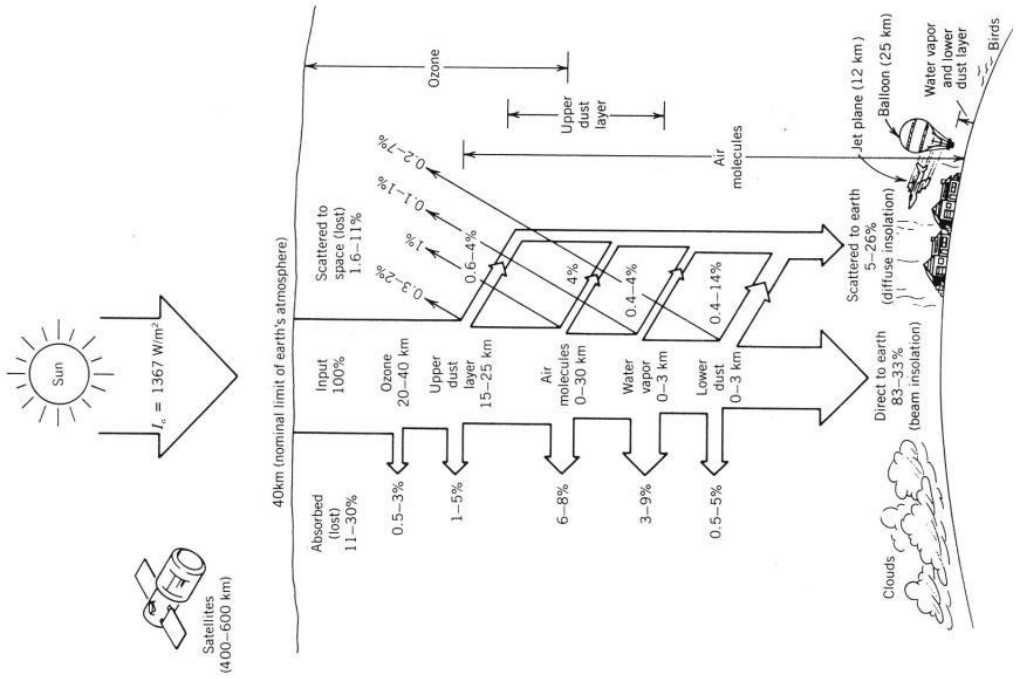

Figure 124: Typical clear sky absorption and scattering of incident sunlight [95]

A.13 Process of Raw DNI data

The raw data obtained is measured on each hour. It is capable to exactly describe the DNI in that moment, but not suitable to accurately characterize the DNI during a period of time, especially during sunset and sunrise period. Therefore some processing is needed to convert the discrete DNI data to period average DNI data.

Figure 125 describes the DNI data processing procedure. It assumed that the DNI varies linearly with time, and the average value of two end points is adopted in that period to represent the period averaged DNI.

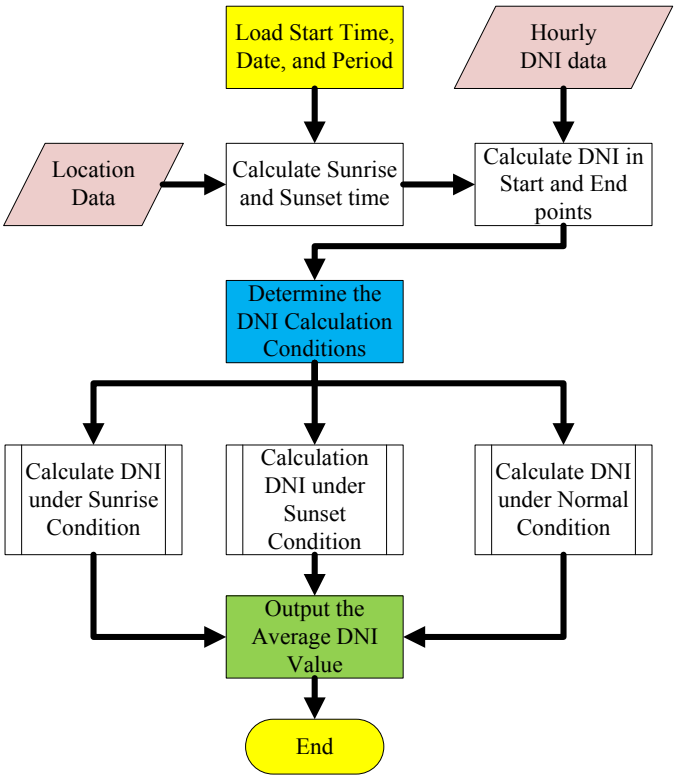

Figure 125: DNI data process flow chart

First, the start and end time is calculated:

$$t_{end} = t_{start} + \Delta t \tag{234}$$

The average DNI during that period is interpolated as (the time format is *hh:mm*, *hh* is the hour, *mm* is the minutes, *mm* may be a fraction therefore it also include seconds):

$$DNI = \frac{DNI_{@hour[hh+1]} - DNI_{@hour[hh]}}{60} \cdot mm + DNI_{@hour[hh]} \tag{235}$$

$DNI_{@hour[hh]}$ represents the measured DNI value at *hh* o'clock.

According to sunrise and sunset situation, four sub situations appear, as shown in Table 20.

Table 20: DNI calculation decision table

		Sunrise time in this period?	
		Y	N
Sunset time in this period?	Y	Condition 1	Condition 2
	N	Condition 3	Condition 4

Practically, situation 1 will never happen since the time step it use is one hour, the time difference between sunrise and sunset should always larger than time step. Therefore situation 1 is ignored. Situation 2, 3 and 4 represent sunset, sunrise and normal situation, as shown in Figure 125.

For normal situation, the period averages DNI is calculated based on start and end time DNI values:

$$DNI_{\text{Avg}} = \frac{DNI_{@\text{start}} + DNI_{@\text{end}}}{2} \tag{236}$$

For sunrise situation, we assume at sunset time, the DNI is zero and then increased to the end time. Therefore the average DNI is calculated as:

$$DNI_{\text{Avg}} = \frac{DNI_{@end} + DNI_{@deploy}}{2} \tag{237}$$

Where

$$DNI_{@deploy} = DNI_{@end} \frac{t_{deploy} - t_{sunrise}}{t_{end} - t_{sunrise}} \tag{238}$$

Similarly, for the sunset situation, the average DNI is calculated as:

$$DNI_{Avg} = \frac{DNI_{@start} + DNI_{@stow}}{2} \tag{239}$$

Where

$$DNI_{@stow} = DNI_{@start} \frac{t_{sunset} - t_{stow}}{t_{sunset} - t_{start}} \tag{240}$$

APPENDIX B

HEAT LOSS CALCULATION

B.1 Collector Heat Loss Model

One dimensional physical model was developed to simulate the energy flows of the HCE pipe. The temperature change and heat loss in the radial direction are considered, while the axial and circumferential heat transfer is neglected. The model is deducted from basic energy balance principle. Figure 126 shows the diagram of a typical collector.

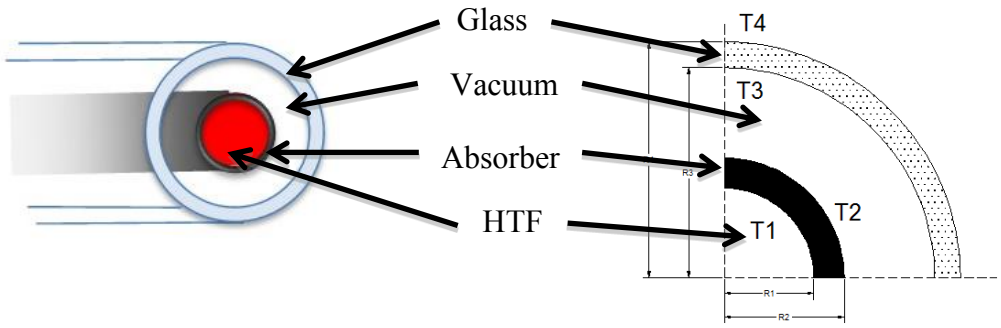

Figure 126: Diagram of a collector pipe

Four situations are considered in this model. They are:

1. Normal situation: the pipe is intact, and works as expected.

2. Loss vacuum situation: the glass cover of HCE is cracked and air fills in the annulus space.
3. Hydrogen situation: Hydrogen from the absorber seeps into the vacuum.
4. Cover missing situation: The whole glass cover is broken and missed, the absorber contacts with environment directly.

Figure 127 and Figure 128 show the diagrams of these situations and theirs heat resistance networks.

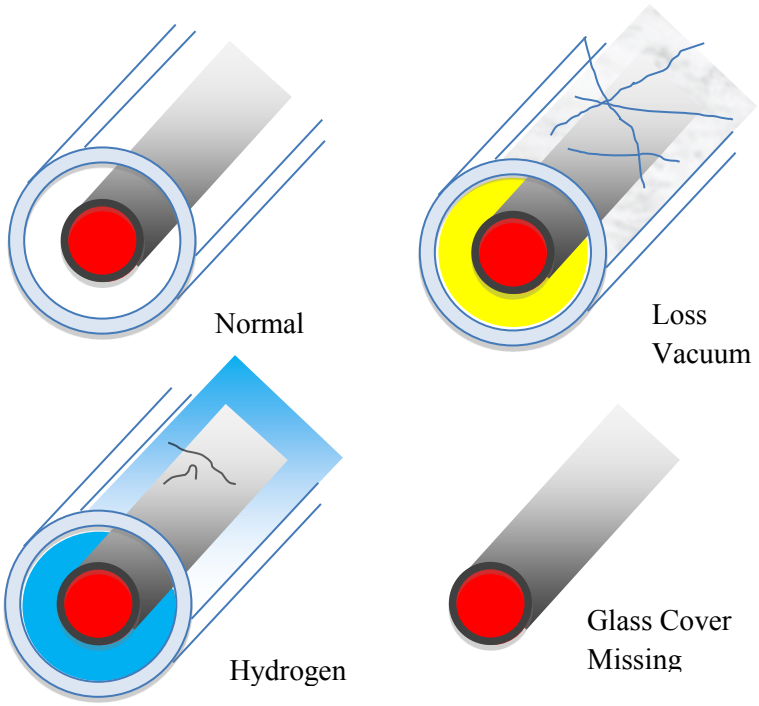

Figure 127: Diagram of HCE's failures

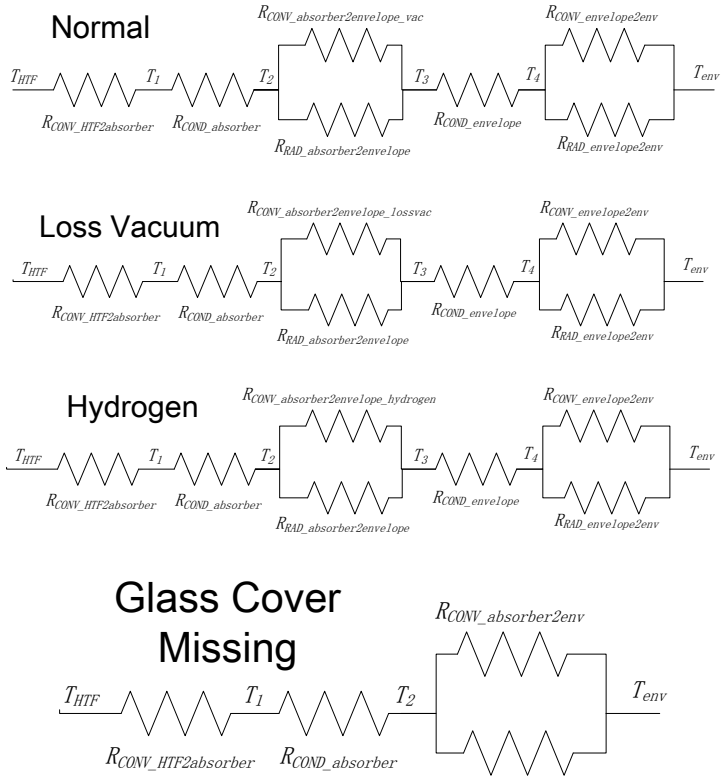

Figure 128: Heat collect pipe's heat resistance diagrams with normal, loss vacuum, hydrogen, and glass cover missing situations

B.1.1 Normal Situation

According to the energy conservation law, the energy flow of HCE is:

$$\dot{q}_{solar\_rad} = \dot{q}_{energy2HTF} + \dot{q}_{HL} \tag{241}$$

In the daytime, $\dot{q}_{solar\_rad}$ represents for the solar energy converges to the absorber coating. At night, it is zero. The change of HTF's thermal energy is the collector's heat loss.

Under the normal condition, the heat flows to the HTF and the environment are:

$$\dot{q}_{energy2HTF} = \dot{q}_{COND\_absb} = \dot{q}_{CONV\_HTF2absb} \tag{242}$$

$$\dot{q}_{HL} = \dot{q}_{CONV\_absb2enlp\_vac} + \dot{q}_{RAD\_absb2enlp} = \dot{q}_{COND\_enlp} = \dot{q}_{CONV\_enlp2env} + \dot{q}_{RAD\_envlp2env} \tag{243}$$

If temperature and heat resistance are used to represent the heat flows:

$$\dot{q}_{energy2HTF} = \frac{T_2 - T_{HTF}}{R_{CONV\_HTF2absb} + R_{COND\_absb}} \tag{244}$$

$$\dot{q}_{HL} = \frac{T_2 - T_{env}}{\left(R^{-1}_{CONV\_absb2enlp\_vac} + R^{-1}_{RAD\_absb2enlp}\right)^{-1} + R_{COND\_enlp} + \left(R^{-1}_{CONV\_enlp2env} + R^{-1}_{RAD\_enlp2env}\right)^{-1}} \tag{245}$$

In the same way, the loss vacuum, hydrogen and glass cover missing situations' heat flows are:

B.1.2 Loss Vacuum Situation

$$\dot{q}_{HL} = \frac{T_2 - T_{env}}{\left(R^{-1}_{CONV\_absb2enlp\_lossvac} + R^{-1}_{RAD\_absb2enlp}\right)^{-1} + R_{COND\_enlp} + \left(R^{-1}_{CONV\_enlp2env} + R^{-1}_{RAD\_enlp2env}\right)^{-1}} \tag{246}$$

B.1.3 Hydrogen Situation

$$\dot{q}_{HL} = \frac{T_2 - T_{env}}{\left(R^{-1}_{CONV\_absb2enlp\_hydrogen} + R^{-1}_{RAD\_absb2enlp}\right)^{-1} + R_{COND\_enlp} + \left(R^{-1}_{CONV\_enlp2env} + R^{-1}_{RAD\_enlp2env}\right)^{-1}} \tag{247}$$

B.1.4 Glass Cover Missing Situation

$$\dot{q}_{HL} = \frac{T_2 - T_{env}}{\left(R^{-1}_{CONV\_absb2env} + R^{-1}_{RAD\_absb2env}\right)^{-1}} \tag{248}$$

The following content discusses each heat resistance item. Table 21 describes all the parameters used during the heat resistance calculation.

Table 21: Description of parameters used in HCE model

Parameters	Description
T_{HTF_i}	HTF inlet temperature
T_{HTF_o}	HTF outlet temperature
T_{HTF}	Average HTF temperature
T_1	Absorber inside surface temperature
T_2	Absorber outside surface temperature
T_3	Envelope inside surface temperature
T_4	Envelope outside surface temperature
T_{sky}	Sky temperature
T_{vac}	Annulus vacuum temperature
R_1	Absorber inner radius
R_2	Absorber out radius
R_3	Envelope inner radius
R_4	Envelope out radius
L	Pipe Length
$\dot{m}$	HTF mass flow rate
$k_{absorber}$	thermal conductance of absorber
k_{air}	thermal conductance of air
$k_{envelope}$	thermal conductance of envelope glass
f	Fraction factor

Table 21 Continued

μ_{HTF}	HTF's dynamic viscosity
ε_1	Emissivity of the absorber coating surface
ε_2	Emissivity of the envelope inside surface
ε_4	Emissivity of the envelope outer surface
g	gravitational constant
β	volumetric thermal expansion coefficient
σ	Stefan-Boltzmann Constant
b	interaction coefficient
k_{std}	annulus gas' thermal conductance at standard temperature and pressure
λ	molecule's mean free path
a	accommodation coefficient
γ	ratio of specific heats (c_p / c_v)
δ	molecular diameter of annulus gas
P_a	annulus gas pressure

B.1.5 Heat Resistance Calculation

B.1.5.1 Convection Heat Transfer between Insider Surface of Absorber and HTF

The convection heat transfer rate is:

$$\dot{q}_{CONV\_HTF2absb} = \frac{T_{HTF} - T_1}{R_{CONV\_HTF2absb}} \tag{249}$$

The heat resistance is:

$$R_{CONV\_HTF2absb} = (\pi RLNuk_{absb})^{-1} \tag{250}$$

The calculation of *Nu* varied depends on whether the flow is laminar or turbulent:

$$\begin{cases} Nu = 4.36 \quad \text{if } \mathrm{Re} < 2300 \text{ Laminar} \\ Nu = \dfrac{(f/8)(\mathrm{Re}_D - 1000)\,\mathrm{Pr}}{1 + 12.7(f/8)^{0/5}\left(\mathrm{Pr}^{2/3} - 1\right)} \quad \text{Else Turbulent} \end{cases} \tag{251}$$

And f is defined as:

$$f = (0.790 In\,\mathrm{Re}_D - 1.64)^2 \tag{252}$$

It assumes HTF flow is steady, incompressible, and the collector is a tube with uniform cross-sectional area. The Reynolds number is defined as [60]:

$$\mathrm{Re} = \frac{4\dot{m}}{2\pi R_1 \mu_{HTF}} \tag{253}$$

B.1.5.2 Conduction Heat Transfer in Absorber

Conduction heat flow in the absorber and its heat resistance are:

$$\dot{q}_{COND\_O2I\_absb} = \frac{T_2 - T_1}{R_{COND\_absb}} \tag{254}$$

$$R_{COND\_absb} = \frac{In(R_2 / R_1)}{2\pi L k_{absb}} \tag{255}$$

Where:

k is the conduction of the absorber, its value is estimated at temperature $(T_1+T_2)/2$.

B.1.5.3 Radiation Heat Transfer between the Absorber and the Envelope

Radiation heat flow and heat resistance between out surface of absorber and envelope are:

$$\dot{q}_{RAD\_absb2enlp} = \frac{T_2 - T_3}{R_{RAD\_absb\_enlp}} \tag{256}$$

$$R_{RAD\_absb2enlp} = \frac{\frac{1}{\varepsilon_1} + \frac{1-\varepsilon_2}{\varepsilon_2}\left(\frac{R_2}{R_3}\right)^2}{2\sigma\pi R_2 L\left(T_2 + T_3\right)\left(T_2^2 + T_3^2\right)} \tag{257}$$

B.1.5.4 Convection Heat Transfer between Absorber and Envelope – Vacuum Situation

When the receiver is intact, the annulus space between absorber and envelope is vacuumed. Free-molecular is the dominate heat transfer mechanism. The heat flow and heat resistance between the absorber and envelope are:

$$\dot{q}_{CONV\_absb2enlp\_vac} = 2\pi R_2 Lh\left(T_2 - T_3\right) \tag{258}$$

$$R_{CONV\_absb2enlp\_vac} = \left(2\pi R_2 Lh\right)^{-1} \tag{259}$$

The heat transfer convection coefficients are [96]:

$$h = \frac{k_{std}}{R_3 / In\left(R_3 / R_2\right) + b\lambda\left(R_2 / R_3 + 1\right)} \tag{260}$$

$$b = \frac{(2-\alpha)(9\gamma-5)}{2\alpha(\gamma+1)} \tag{261}$$

$$\lambda = \frac{2.331\times10^{-20}T_{vac}}{P_a\delta^2} \tag{262}$$

During calculation, T_{vac} is estimated as $(T_2+T_3)/2$.

The correlation is valid for $Ra_{R3} < (R_3/(R_3-R_2))^4$, and a bit overestimation for high vacuum situation - when pressure ~<10^{-4} torr. Some typical parameters' values are listed in Table 22 [97].

Table 22: Heat transfer constants for the annulus gas [96]

Annulus Gas Type	k_{std} [W/m·K]	δ [cm]	γ	α
Air	0.02551	3.53E-08	1.39	1
Hydrogen	0.1769	2.40E-08	1.398	1.09
Argon	0.01777	3.80E-08	1.677	0.85

The heat resistance estimation for hydrogen condition is similar to the one for normal condition, except that properties of hydrogen are used instead of air.

B.1.5.5 Convection Heat Transfer between Absorber and Envelope – Loss Vacuum Situation

Under the loss vacuum condition, the convection heat transfer between an absorber and its corresponding envelope is dominated by natural convection. Raithby and Holland's natural convection correlation for the annular space between two long horizontal cylinders situation is used [96]. This correlation is validated for $Ra_3>(R_3/(R_3-R_2))^4$ situation.

$$\dot{q}_{CONV\_absb2enlp\_lossvac} = \frac{2.425 k_{air} L\left(T_2 - T_3\right)\left[\Pr Ra_2 / \left(0.861+\Pr\right)\right]^{0.25}}{\left[1+\left(R_2/R_3\right)^{0.6}\right]^{1.25}} \tag{263}$$

Therefore, the convection heat resistance could be estimated as:

$$R_{CONV\_absb2enlp\_lossvac} = \frac{\left[1+\left(R_2/R_3\right)^{0.6}\right]^{1.25}}{2.425 k_{air} L\left[\Pr Ra_2 / \left(0.861+\Pr\right)\right]^{0.25}} \tag{264}$$

And the Rayleigh number is:

$$Ra_2 = \frac{8 g \beta \left(T_2 - T_3\right) R_2^3}{\alpha \nu} \tag{265}$$

In the loss vacuum condition, the air temperature in the annulus space is high and its pressure is less than atmosphere pressure. The air in the annulus space is regarded as idea gas, therefore,

$$\beta = \frac{1}{T_{avg}} = \frac{2}{T_2 + T_3} \tag{266}$$

Parameters k_{air}, Pr, α and v are estimated at average temperature of T_2 and T_3.

B.1.5.6 Conduction Heat Transfer in Envelope

Similar to conduction heat transfer in absorber, conduction heat flow and heat resistance in envelope are:

$$\dot{q}_{COND\_absb} = \frac{T_4 - T_3}{R_{COND\_enlp}} \tag{267}$$

$$R_{COND\_enlp} = \frac{In\left(R_4 / R_3\right)}{2\pi L k_{enlp}} \tag{268}$$

Where:

$k_{envelope}$ is the conduction of envelope, its value is estimated at temperature (T_3+T_4)/2.

B.1.5.7 Convection Heat Transfer between Envelope and Environment

The convection heat flow between envelope outside and environment describes the heat loss from the envelope's surface to environment caused by convection. The heat flow is:

$$\dot{q}_{CONV\_enlp2env} = \frac{T_4 - T_{air}}{R_{CONV\_enlp2env}} \tag{269}$$

The convection heat resistance is:

$$R_{CONV\_enlp2env} = \frac{T_4 - T_{air}}{\dot{q}_{CONV\_enlp2env}} = \frac{1}{2\pi R_4 L h_{CONV}} = \frac{R_4}{\pi R_4 L k_{air} Nu} \tag{270}$$

Both natural (no wind condition) and force (wind condition) heat transfer conditions are considered.

B.1.5.7.1 Wind Situation

The convection heat transfer mechanism between an envelope and environment is dominated by forced convection if wind exists. Churchill and Bernstein have proposed a single comprehensive equation to estimate *Nu*:

$$Nu = 0.3 + \frac{0.62\,\mathrm{Re}_D^{1/2}\,\mathrm{Pr}^{1/3}}{\left[1+\left(0.4/\mathrm{Pr}\right)^{2/3}\right]^{1/4}}\left[1+\left(\frac{\mathrm{Re}}{282000}\right)^{5/8}\right]^{4/5} \tag{271}$$

All the properties used are estimated at film temperature which is $(T_{env}+T_4)/2$.

B.1.5.7.2 No Wind Situation

In the no wind situation, the convection heat transfer mechanism between envelope and environment is ruled by natural convection. Churchill and Chu have recommended using a single correlation for a wide Rayleigh number range ($Ra < 10^{12}$):

$$Nu = \left\{0.6 + \frac{0.387 Ra_D^{1/6}}{\left[1+\left(0.559/\mathrm{Pr}\right)^{9/16}\right]^{8/27}}\right\}^2 \tag{272}$$

The general heat transfer between an envelope and the environment is determined by both forced and natural heat transfer mechanisms. The general total heat resistance is estimated as:

$$R_{CONV} = \frac{R_{wind} R_{nwind}}{\sqrt{R_{wind}^2 + R_{nwind}^2}} \tag{273}$$

B.1.5.8 Radiation Heat Transfer between Envelope Surface and Environment

Radiation heat flow between envelope's out surface and environment may further subdivide into exchanging energy with the ground or the sky. As shown in Figure 129.

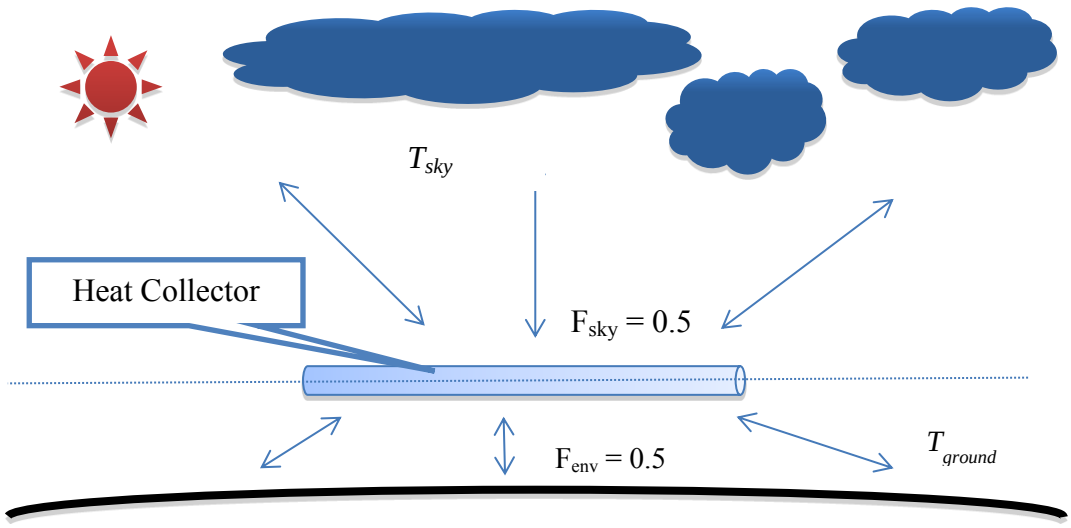

Figure 129: Demonstration of envelope surface radiation heat transfer

And the heat flow and heat resistance are:

$$\dot{q}_{RAD\_enlp2env} = \dot{q}_{RAD\_enlp2env\_grd} + \dot{q}_{RAD\_enlp2env\_sky} \tag{274}$$

$$R_{RAD\_enlp2env} = \frac{T_4 - T_{env}}{\dot{q}_{RAD\_enlp2env}} \tag{275}$$

B.1.5.8.1 Radiation Heat Transfer with Ground or Sky

It supposed that the ground and environment temperatures are identical. Therefore,

$$\dot{q}_{RAD\_enlp2env\_grd} = 2\pi R_4 L F_{enlp2grd} \sigma \varepsilon_4 \left(T_4^4 - T_{env}^4\right) \tag{276}$$

Hence, the heat resistance is calculated as:

$$R_{RAD\_enlp2grd} = \frac{1}{2\pi R_4 L F_{enlp2grd} \sigma \varepsilon_4 \left(T_4 + T_{env}\right)\left(T_4^2 + T_{env}^2\right)} \tag{277}$$

The heat flow and heat resistance for radiation heat exchange with sky is similar. The general heat resistance between the envelope and the environment is

$$R_{RAD\_enlp2env} = \frac{R_{RAD\_enlp2sky} R_{RAD\_enlp2grd}}{R_{RAD\_enlp2sky} + R_{RAD\_enlp2grd}} \tag{278}$$

B.2 HTP Heat Loss Model

Similar to the HCE model, one dimensional physical model is used to simulate transfer pipes' heat loss. Compared with the HCE, the transfer pipe does not collect solar energy and easy to apply thick insulation layer, its heat loss rate is much smaller than HCE.

Figure 130 and Figure 131 shows the diagram of transfer pipe and its heat resistance network.

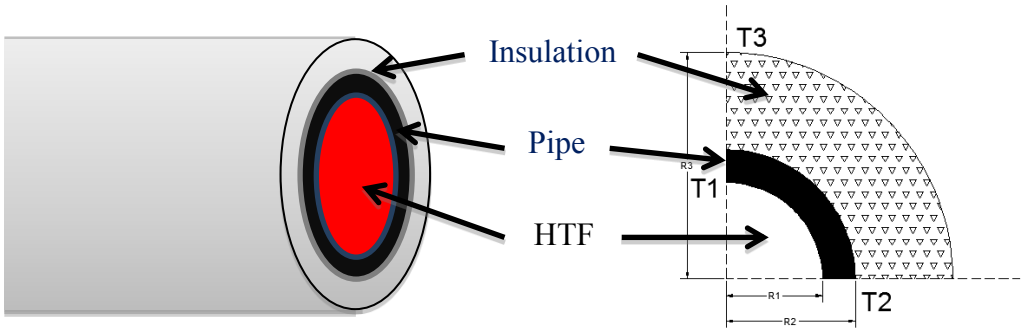

Figure 130: Diagram of the transfer pipe

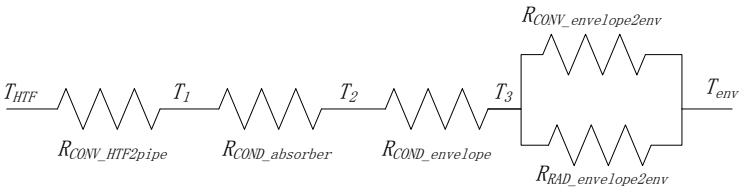

Figure 131: Transfer pipe heat resistance diagram

The HTF temperature is higher than environmental temperature in normal condition. The heat flow is always going from the HTF to the environment. If assumes the pipe and insulation is firmly contacted, then there is no contact heat resistance. The heat flow rate is shown as:

$$\dot{q}_{HTP} = \dot{q}_{CONV\_HTF2pipe} = \dot{q}_{COND\_pipe} = \dot{q}_{COND\_ins} = \dot{q}_{CONV\_ins2env} + \dot{q}_{RAD\_ins2env} \quad (279)$$

The heat transfer rate and heat resistance derived from heat resistance diagram are

$$\dot{q}_{HTP} = \frac{T_{HTF} - T_{env}}{R_{HTF}} \quad (280)$$

$$R_{HTF} = R_{CONV\_HTF2pipe} + R_{COND\_pipe} + R_{COND\_ins} + \left(R^{-1}_{CONV\_ins2env} + R^{-1}_{RAD\_ins2env}\right)^{-1} \quad (281)$$

B.3 Calculation Method

An iterative method is used to calculate the model because it is nonlinear, and some of their inputs are unknown. This method generates a sequence of improving approximate solutions which will converge to solution from initial guess values. The calculation procedure for heat loss model and energy balance is shown in Figure 132.

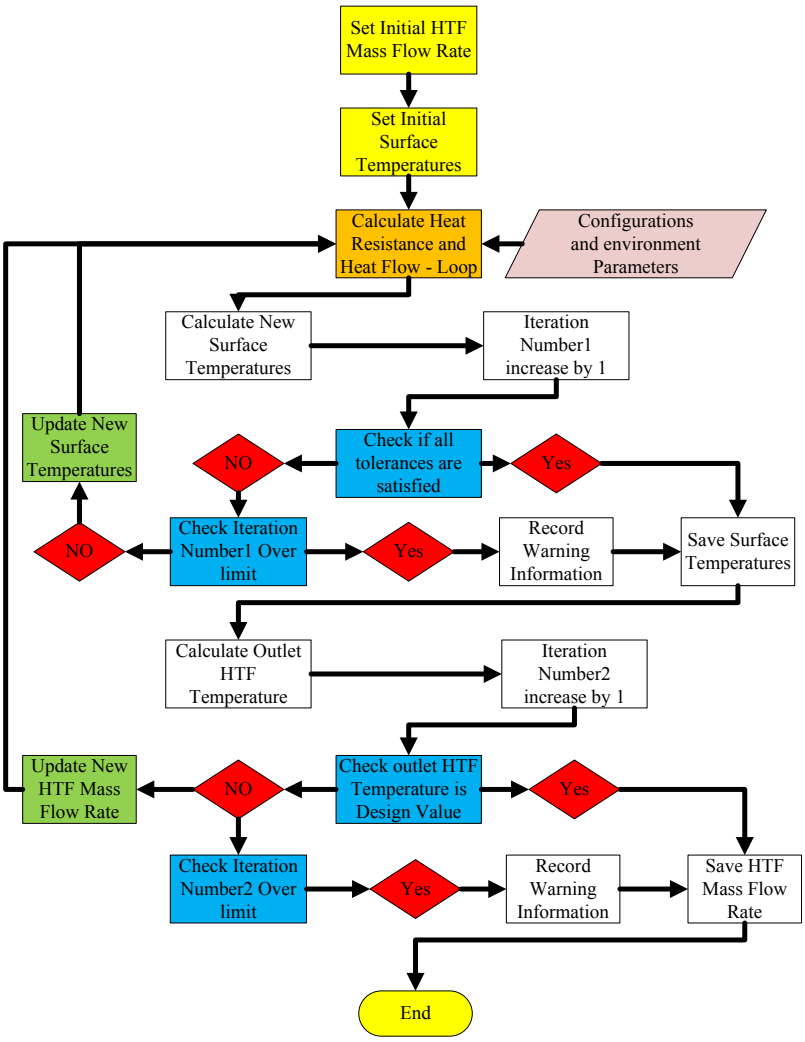

Figure 132: Flow chart of the solar field model

B.4 Storage Tank Heat Loss Estimation

Heat loss occurs in three directions - top surface, tank side and bottom. As shown in Figure 133.

$$\dot{q}_{HL} = \dot{q}_{HL\_top} + \dot{q}_{HL\_side} + \dot{q}_{HL\_btm} \tag{282}$$

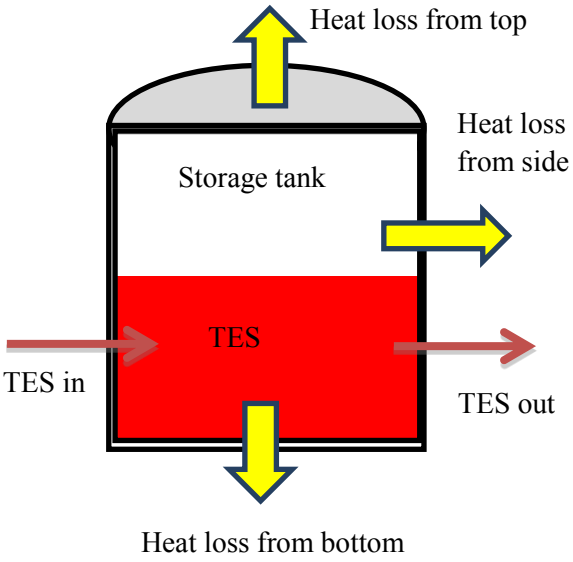

Figure 133: Schematic of the heat loss of a single tank

B.4.1 Heat Loss from Tank's Top Surface

Generally, a storage tank has a self-support dome, as shown in Figure 134.

Figure 134: The two-tank storage system of the Solar Two solar plant[16]

[16] Picture on February 2014, from U.S. Department of Energy, address: http://energy.gov/eere/energybasics/articles/thermal-storage-systems-concentrating-solar-power

The area of dome is:

$$S_{dome} = 2\pi Rh \tag{283}$$

Where

R is the dome's radius;

h is the height of dome;

The dome's height is estimated as 14% of its radius. Therefore, the dome's radius is:

$$R = 3.44r \tag{284}$$

Where r is the radius of tank;

And the dome's surface area is:

$$S_{dome} = 2\pi Rh = 1.02\pi r^2 \tag{285}$$

Since the dome area is very close to flat round surface (only 2% difference), the dome area is treated as flat surface in model.

The heat resistance diagram is illustrated in Figure 135:

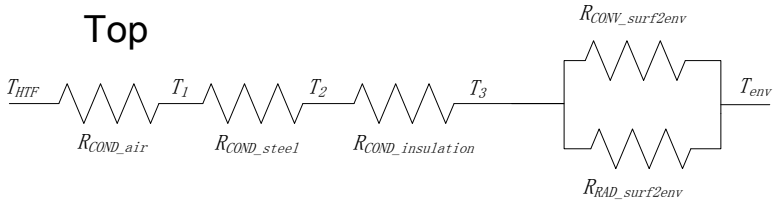

Figure 135: Diagram of the storage tank's top heat resistance

The heat loss rate from the top of tank is calculated as:

$$\dot{q}_{HL\_top} = \frac{T_{TES} - T_{env}}{R_{HL\_top}} \tag{286}$$

$$R_{HL\_top} = R_{COND\_air} + R_{COND\_steel} + R_{COND\_ins} + \frac{R_{CONV\_surf\,2env} \cdot R_{RAD\_surf\,2env}}{R_{CONV\_surf\,2env} + R_{RAD\_surf\,2env}} \tag{287}$$

Heat resistances listed in Figure 135 are shown as following:

$$R_{COND\_air} = \frac{h_{\tan k}\left(1 - f_{vol\_fraction}\right)}{\pi r^2 k_{air}} \tag{288}$$

$$R_{COND\_steel} = \frac{t_{steel\_top}}{\pi r^2 k_{steel}} \tag{289}$$

$$R_{COND\_ins} = \frac{t_{ins\_top}}{\pi r^2 k_{ins}} \tag{290}$$

$$R_{CONV\_surf\,2env} = \frac{L_{character}}{S_{dome} Nuk_{air}} \tag{291}$$

Where $L_{character} = \frac{4r}{\pi}$, this character length is also used to calculate *Re* and *Pr* numbers.

Since the top surface's direction is always facing sky, the radiation heat exchange is only happened with sky.

$$R_{RAD\_surf2env} = \frac{1}{S_{dome}\sigma\varepsilon\left(T_{\tan k\_top} + T_{sky}\right)\left(T_{\tan k\_top}^2 + T_{sky}^2\right)} \tag{292}$$

B.4.2 Heat Loss from Tank's Surround Surface

Similarly, the heat resistance diagram and heat loss rate from the side of tank are:

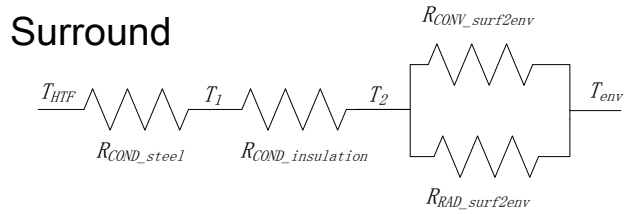

Figure 136: Diagram of the storage tank's surrounding heat resistance

$$\dot{q}_{HL\_surf} = \frac{T_{TES} - T_{env}}{R_{HL\_surf}} \tag{293}$$

$$R_{HL\_top} = R_{COND\_steel} + R_{COND\_ins} + \frac{R_{CONV\_surf2env} \cdot R_{RAD\_sur2env}}{R_{CONV\_surf2env} + R_{RAD\_sur2env}} \tag{294}$$

$$R_{COND\_steel} = \frac{In\left(R_{steel\_out} / R_{steel\_in}\right)}{2\pi h_{\tan k} k_{steel}} \tag{295}$$

$$R_{COND\_ins} = \frac{In\left(R_{ins\_out} / R_{ins\_in}\right)}{2\pi h_{\tan k} k_{ins}} \tag{296}$$

$$R_{CONV\_surf2env} = \frac{1}{\pi h_{\tan k} Nuk_{air}} \tag{297}$$

The surrounding of tank has radiation heat exchange with the sky and the ground. They are assumed to have equal weight, then

$$R_{RAD\_sur2env} = \frac{1}{2\pi r h_{\tan k}\left(h_1 + h_2\right)} \tag{298}$$

$$h_1 = 0.5\sigma\varepsilon\left(T_{\tan k\_surf} + T_{env}\right)\left(T^2_{\tan k\_surf} + T^2_{env}\right) \tag{299}$$

$$h_2 = \frac{0.5\sigma\varepsilon\left(T^4_{\tan k\_surf} + T^4_{sky}\right)}{T_{\tan k\_surf} - T_{env}} \tag{300}$$

B.4.3 Heat Loss from Tanks' Bottom

The heat resistance diagram and heat loss rate from the bottom of tank are:

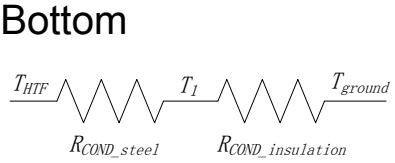

Figure 137: Diagram of the storage tank's bottom heat resistance

$$\dot{q}_{HL\_btm} = \frac{T_{TES} - T_{grd}}{R_{HL\_grd}} \tag{301}$$

T_{grd} is the soil temperature at half meter depth. Its value is obtained from the weather data file.

$$R_{HL\_top} = R_{COND\_steel} + R_{COND\_ins} \tag{302}$$

$$R_{COND\_steel} = \frac{t_{steel\_btm}}{\pi r^2 k_{steel}} \tag{303}$$

$$R_{COND\_ins} = \frac{t_{ins\_btm}}{\pi r^2 k_{ins}} \tag{304}$$